UNIVERSITÀ
DEGLI STUDI
DI TORINO

Unveiling dark matter with cosmic messengers

Approved version by the PhD School of the University of Turin, PhD program in Physics and Astrophysics and the Faculty of Mathematics, Computer Science and Natural Sciences at RWTH Aachen University in order to achieve the doctoral degree

Michael Korsmeier

born in Paderborn, Germany

February 2020

Supervision: Prof. Fiorenza Donato
Prof. Dr. Michael Krämer

This thesis was conducted under the **Agreement for a joint Doctoral Research Thesis** between the University of Turin, RWTH Aachen University, and Michael Korsmeier.

It fulfills the requirements for Dottorato in Fisica e Astrofisica – XXXII cycle – of the Doctoral School of Universitá degli Studi di Torino.

It complies with the doctoral regulations of the Faculty of Mathematics, Computer Science and Natural Sciences of RWTH Aachen University.

Referees appointed by RWTH Aachen University:
Prof. Fiorenza Donato
Prof. Dr. Michael Krämer

Referees appointed by the University of Turin:
Dr. Pasquale Serpico
Dr. Andrew Strong

Members of the PhD defense committee:
Dr. Pasquale Serpico (chair)
Prof. Fiorenza Donato
Prof. Dr. Michael Krämer
Prof. Dr. Philip Mertsch

Date of the oral defense: April 24th, 2020

Michael Korsmeier

michael.korsmeier@to.infn.it

University of Turin
Department of Physics
Via Pietro Giuria, 1
10125 Torino
Italy

korsmeier@physik.rwht-aachen.de

RWTH Aachen University
Institute for Theoretical Particle Physics and Cosmology
Sommerfeldstraße 16
52074 Aachen
Germany

List of publications

This thesis is based on the publications prepared during time of the PhD:

[1] S. Manconi, M. Korsmeier, F. Donato, N. Fornengo, M. Regis and H. Zechlin, *Testing gamma-ray models of blazars in the extragalactic sky*, [1912.0162].

[2] A. Cuoco, J. Heisig, L. Klamt, M. Korsmeier and M. Krämer, *Scrutinizing the evidence for dark matter in cosmic-ray antiprotons*, *Phys. Rev.* **D99** (2019) 103014 [1903.01472].

[3] M. Korsmeier, F. Donato and M. Di Mauro, *Production cross sections of cosmic antiprotons in the light of new data from the NA61 and LHCb experiments*, *Phys. Rev.* **D97** (2018) 103019 [1802.03030].

[4] M. Korsmeier, F. Donato and N. Fornengo, *Prospects to verify a possible dark matter hint in cosmic antiprotons with antideuterons and antihelium*, *Phys. Rev.* **D97** (2018) 103011 [1711.08465].

[5] A. Cuoco, J. Heisig, M. Korsmeier and M. Krämer, *Constraining heavy dark matter with cosmic-ray antiprotons*, *JCAP* **1804** (2018) 004 [1711.05274].

[6] A. Cuoco, J. Heisig, M. Korsmeier and M. Krämer, *Probing dark matter annihilation in the Galaxy with antiprotons and gamma rays*, *JCAP* **1710** (2017) 053 [1704.08258].

[7] F. Donato, M. Korsmeier and M. Di Mauro, *Prescriptions on antiproton cross-section data for precise theoretical antiproton flux predictions*, *Phys. Rev.* **D96** (2017) 043007 [1704.03663].

Previous publications related to the topic of the thesis:

[8] A. Cuoco, M. Krämer and M. Korsmeier, *Novel Dark Matter Constraints from Antiprotons in Light of AMS-02*, *Phys. Rev. Lett.* **118** (2017) 191102 [1610.03071].

[9] M. Korsmeier and A. Cuoco, *Galactic cosmic-ray propagation in the light of AMS-02: Analysis of protons, helium, and antiprotons*, *Phys. Rev.* **D94** (2016) 123019 [1607.06093].

Abstract

In the last decade, space-based experiments like AMS-02 and the Fermi-LAT have turned astroparticle physics of Galactic cosmic rays and gamma rays into a precision discipline. We can use the newly available data to learn more about our Galactic and extragalactic environment. A major motivation to investigate astroparticle messengers is the indirect search for dark matter signatures.

Cosmic-ray antiprotons constitute one very interesting messenger in astroparticle physics. The combination of the antiproton flux data with its parent nuclei, proton and helium, allows to understand cosmic-ray propagation of light nuclei. We perform global fits to the data from AMS-02 and derive constraints on the key parameters of a cosmic-ray propagation model including diffusion and reacceleration. The results are compatible with expectations from other analyses performed on boron-to-carbon ratio.

The analysis of cosmic-ray antiprotons requires precise knowledge of the secondary antiproton production cross sections. We update and compare the most recent cross-section parametrizations by exploiting newly available data from the fixed-target experiments NA61 and LHCb. Furthermore, we derive the uncertainties on these cross-section parametrizations and the secondary antiproton source term. These exceed the uncertainties of the antiproton flux measurement by AMS-02. Consequently, we provide guidelines for future cross-section measurements concerning the most relevant kinematic parameter space.

Cosmic-ray antiprotons are a sensitive probe for dark matter annihilation or decay in our Galaxy. Performing a global fit to the cosmic-ray data of protons, helium, and the antiproton-over-proton ratio, we find a hint for the annihilation of dark matter in the energy spectrum of cosmic-ray antiprotons. The putative dark matter particles have a mass between 30 and 200 GeV and a cross section times velocity at the order of 3×10^{-26} cm^3/s. We investigate how this hint is affected by systematics arising from uncertainties in the production cross sections of secondary antiprotons and correlations in the systematic uncertainties of the cosmic-ray data itself. After accounting for systematic uncertainties, we find a significance of 2.7σ for the dark matter hint. On the other hand, cosmic-ray antiprotons provide strong upper bounds on the annihilation cross section of heavy dark matter particles with masses above 200 GeV. These bounds are competing and complementary to constraints from gamma rays.

A complemental strategy to search for dark matter in cosmic rays is to look for low-energy antinuclei. We explore the prospects to detect a signal in the fluxes of antideuteron or antihelium

corresponding to the dark matter hint in cosmic-ray antiprotons. These fluxes constitute the largest possible dark matter signals in antinuclei which are compatible with cosmic-ray antiprotons. We find that the potential dark matter signal in antideuteron lies within the expected sensitivities of GAPS and AMS-02, while the antihelium signal is significantly below the sensitivity of AMS-02 at all energies. Moreover, we update the predictions of the secondary and tertiary fluxes of antideuteron and antihelium. They are out of reach for both detectors.

Finally, also gamma rays provide an excellent prospect to indirectly search for dark matter. The best prospects to find a signal is to search in regions with either a large dark matter density or a low astrophysical background. Promising sites are the Galactic center, dwarf spheroidal galaxies, or the extragalactic gamma-ray sky. However, a robust understanding of potential dark matter signals requires a good characterization of the background from astrophysical sources. We exploit two unique tools to investigate the properties of gamma-ray sources with small fluxes and at high latitudes: the one-point statistics of photon counts applied to Fermi-LAT data and the recent measurement of the angular correlations in the unresolved gamma-ray background. Within a model of the gamma-ray luminosity function of blazars we compare the properties of the extragalactic gamma-ray sky with resolved blazars at large fluxes. We find that the emission of gamma-rays at high latitudes and small fluxes is consistent with a pure blazar population.

Sommario[1]

Negli ultimi decenni, esperimenti su satelliti come AMS-02 e Fermi-LAT hanno reso la fisica astroparticellare dei raggi cosmici galattici e dei raggi gamma una disciplina di precisione. I nuovi dati sperimentali ci permettono di approfondire la nostra conoscenza dell'ambiente galattico ed extragalattico. Inoltre, una delle motivazioni principali per studiare i messaggeri astrofisici sono le ricerche indirette di segnali di materia oscura.

Tra i raggi cosmici elettricamente carichi, gli antiprotoni sono tra i messaggeri più rilevanti. Combinando le misure dei flussi di antiprotoni e dei suoi nuclei progenitori, protoni ed elio, è possibile studiare la propagazione della componente di nuclei leggeri nei raggi cosmici. Abbiamo realizzato dei fit ai dati di AMS-02 ed ottenuto dei vincoli sui parametri più importanti che determinano la propagazione dei raggi cosmici, includendo la diffusione e la riaccelerazione. I risultati sono compatibili con quelli attesi da analisi basate sulla misura del rapporto boro su carbonio.

Lo studio degli antiprotoni nei raggi cosmici richiede una conoscenza precisa delle sezione d'urto di produzione degli antiprotoni secondari. Abbiamo aggiornato e confrontato le più recenti parametrizzazioni di tali sezioni d'urto utilizzando misure ottenute dall'esperimento a bersaglio fisso NA61e da LHCb. Inoltre abbiamo determinato le incertezze su tali parametrizzazioni e sul termine di sorgente che determina la produzione degli antiprotoni secondari. Tali incertezze superano quelle sul flusso di antiprotoni misurato da AMS-02. Di conseguenza, abbiamo definito delle linee guida per esperimenti futuri di misura di sezione d'urto relativamente allo spazio dei parametri delle variabili cinematiche.

La componente di antiprotoni nei raggi cosmici permette di sondare la presenza di annichilazioni o decadimenti di materia oscura nella nostra Galassia. Attraverso un fit globale alle misure di protoni, elio e rapporto antiprotoni su protoni nei raggi cosmici, abbiamo trovato una possibile evidenza di annichilazioni di materia oscura nello spettro energetico degli antiprotoni. Il segnale è compatibile con particelle di materia oscura con una massa tra 300 GeV e 200 GeV e una sezione d'urto di annichilazione dell'ordine di 3×10^{-26} cm^3/s. Abbiamo analizzato in quale misura questo indizio di eccesso dipenda dalle incertezze sistematiche nella sezione d'urto di produzione degli antiprotoni secondari e dalla correlazione delle incertezze sistematiche nelle misure stesse dei raggi cosmici. Tenendo conto di tali incertezze sistematiche abbiamo quantificato l'evidenza del segnale

[1] Translated to Italian by M. Taoso.

di materia oscura ad un livello di 2.7σ. Per masse delle particelle di materia oscura superiori a 200 GeV, le osservazioni di antiprotoni nei raggi cosmici permettono di ottenere dei limiti molto stringenti sulla sezione d'urto di annichilazione. Questi limiti sono compatibili e complementari a quelli ottenuti attraverso osservazioni dei raggi gamma.

La ricerca di antinuclei a bassa energia costituisce un'ulteriore e complementare ricerca di materia oscura attraverso i raggi cosmici. Abbiamo analizzato la possibilità di rivelare un segnale di materia oscura, corrispondente a quello evidenziato nelle misure di antiprotoni, nei flussi di antideuterio o antielio. Questi sono gli osservabili più promettenti per ricerche di materia oscura attraverso misure di antinuclei, compatibilmente con le osservazioni di antiprotoni. Abbiamo trovato che il segnale di antideuterio si colloca sopra la soglia di rivelabilità attesa per GAPS e AMS-02, mentre il segnale di antielio è sotto la soglia di rivelabilità di AMS-02 a qualunque energia. Inoltre abbiamo aggiornato le predizioni sui flussi secondari e terziari di antideuterio ed antielio. Tali segnali sono fuori dalla possibilità di rivelazione sia per GAPS che per AMS-02.

Anche i raggi gamma possono essere utilizzati per ricerche indirette di materia oscura. La strategia di ricerca più efficace consiste nel focalizzarsi in regioni ad alta densità di materia oscura oppure con una bassa emissione di fondo astrofisica. Regioni promettenti sono il centro galattico, le galassie nane sferoidali o la radiazione di fondo extragalattica. Un requisito fondamentale per effettuare queste ricerche è caratterizzare preventivamente l'emissione di fondo derivante da sorgenti astrofisiche. Abbiamo utilizzato due tecniche per studiare le proprietà delle sorgenti di raggi gamma a basso flusso e situate ad alte latitudini. La prima consiste nel considerare la funzione statistica di correlazione ad un punto, applicata ai conteggi di fotoni misurati da Fermi-LAT. Il secondo metodo considera misure recenti della funzione di correlazione angolare del fondo gamma extragalattico. Utilizzando un modello di luminosità delle sorgenti blazars, abbiamo confrontato le proprietà dell'emissione gamma extragalattica con la popolazione di blazars risolte ed ad alto flusso. Abbiamo concluso che l'emissione gamma ad alte latitudini e a bassi flussi è compatibile con l'ipotesi che tale emissione sia prodotta prevalentemente da sorgenti blazars.

Zusammenfassung

Die genauen Messungen von kosmischer Strahlung und Gammastrahlung durch die Weltraumexperimente AMS-02 und Fermi-LAT haben die Astroteilchenphysik in den letzten zehn Jahren zu einer Präzisionsdisziplin gemacht. Wir nutzen die kürzlich veröffentlichen Daten, um mehr über unsere galaktische und extragalaktische Umgebung zu erfahren. Unsere Hauptmotivation in dieser Arbeit ist die Suche nach Dunkler Materie.

Dabei sind hochenergetische Antiprotonen besonders interessante Botenteilchen. Wenn wir die Informationen von Antiprotonen mit denen von Protonen und Helium kombinieren, können wir mehr über die Propagation kosmischer Strahlung von leichten Kernen lernen. Wir führen globale Parameter-Fits zur Charakterisierung der wichtigsten Parameter im Propagationsmodell, welches Diffusion und Wieder-Beschleunigung erlaubt, durch. Unsere Resultate für die leichten Kerne sind mit den Ergebnissen für schwerere Kerne, wie z.B. aus den Untersuchungen des Verhältnisses von Bor zu Kohlenstoff, kompatibel.

Die Analyse von Antiprotonen in der kosmischen Strahlung setzt die genaue Kenntnis des Wirkungsquerschnitts zur Produktion von sekundären Antiprotonen voraus. Wir vergleichen und verbessern die aktuellen Parametrisierungen des Wirkungsquerschnitts mit Hilfe von neuen experimentellen Daten der Experimente NA61 und LHCb. Dabei bestimmen wir außerdem die Unsicherheit, die sich aus dem Wirkungsquerschnitt auf den Quellterm von kosmischen Antiprotonen ergibt. Diese Unsicherheit übersteigt die der Antiprotonenflussmessung durch das AMS-02 Experiment. Daher erarbeiten wir Richtlinien für zukünftige Experimente zur Messung des Wirkungsquerschnitts für Antiprotonenproduktion. Wir bestimmen den kinematischen Parameterbereich größter Priorität.

Außerdem könnte die Annihilation von möglichen Teilchen Dunkler Materie zu einem zusätzlichen Fluss von Antiprotonen führen. Somit können wir kosmische Antiprotonen dazu nutzen, um indirekt nach Dunkler Materie zu suchen. In unseren Fits an die Daten aus Protonen, Helium und Antiprotonen finden wir einen Hinweis auf die Annihilation von Dunkler Materie. Das mögliche Dunkle-Materie-Teilchen benötigt eine Masse zwischen 30 und 200 GeV und einen Wirkungsquerschnitt für die Annihilation in der Größenordnung von $\langle \sigma v \rangle \sim 3 \times 10^{-26}$ cm^3/s. Wir untersuchen, wie der Hinweis auf dieses mögliche Teilchen von systematischen Unsicherheiten beeinflusst ist. Im Detail schauen wir uns die Unsicherheiten aus dem Wirkungsquerschnitt für die Produktion sekundärer Antiprotonen an und die Auswirkungen von Korrelationen in den AMS-02 Daten. Nach

Berücksichtigung aller Unsicherheiten hat unser Antiprotonsignal für Dunkle Materie eine Signifikanz von 2.7σ. Oberhalb einer Masse von 200 GeV ergeben sich starke obere Schranken für die Größe des möglichen Annihilationwirkungsquerschnitts. Diese sind vergleichbar mit den Schranken aus Gammastrahlung und tragen somit zu einem zuverlässigen Verständnis bei.

Die Suche nach einem niederenergetischen Antiatomkern in kosmischer Strahlung stellt eine komplementäre Strategie dar, um mögliche Signale von Dunkler Materie zu entschlüsseln. Wir untersuchen ob der Hinweis auf Dunkle Materie in den Antiprotonen ein messbares Signal für Antideuterium und Antihelium hinterlassen würde. Ein solches Signal ist der größtmögliche Fluss an Antikernen, der die Beschränkungen aus Antiprotonen nicht verletzt. Nach unseren Berechnungen ist der Fluss von Antideuterium für AMS-02 und das geplante Experiment GAPS in Reichweite, wohingegen wir kein Signal für Antihelium in AMS-02 erwarten. Wir erneuern außerdem die Vorhersagen für den sekundären und tertiären Fluss von beiden Antikernen, diese liegen außerhalb des Messbereichs aktueller Experimente.

Auch Gammastrahlung wird dazu verwendet, um nach Dunkler Materie zu suchen. Dabei konzentriert sich die Suche auf Bereiche, in denen entweder ein großes Signal oder ein kleiner astrophysikalischer Hintergrund erwartet wird. Interessante Bereiche sind das galaktische Zentrum, Zwerggalaxien und die extragalaktische Gammahintergrundstrahlung. Jedoch ist auch hier jeweils eine genaue Betrachtung des astrophysikalischen Hintergrunds vorausgesetzt. Wir nutzen zwei spezielle statistische Methoden, um mehr Informationen über kleine Punktquellen herauszufiltern, die sich weit außerhalb der galaktischen Scheibe befinden. Dazu schauen wir uns zum einen die Statistische Verteilung von Photonen an einem Punkt an und zum anderen interpretieren wir die Winkelkorrelationen in der isotropen Gammahintergrundstrahlung. Unsere Erkenntnisse interpretieren wir in einem Blazarmodell für die Helligkeitskurve von Gammastrahlung. Das Ergebnis zeigt, dass die Gammastrahlung von schwachen Punktquellen konsistent mit einer reinen Population von Blazaren ist.

Acronyms and abbreviations

1pPDF - One-Point Probability Distribution Function
3FHL - Third Catalog of Hard Fermi-LAT sources
4FGL - Fourth Fermi-LAT Catalog
4LAC - Fourth Catalog of Active Galactic Nuclei
AGN - Active Galactic Nucleus
ALEPH - Apparatus for LEP PHysics
AMS-02 - Alpha Magnetic Spectrometer
APS - Angular Power Spectrum
BLLac - BL Lacertae objects
BSM - Beyond the Standard Model of particle physics
CERN - European Organization for Nuclear Research
C.L. - Confidence Level
CM - Center-Of-Mass
CMB - Cosmic Microwave Background
CR - Cosmic Ray or Cosmic-Ray
CREAM - Cosmic Ray Energetics And Mass experiment
DM - Dark Matter
dof - degree of freedom
dSph - Dwarf Spheroidal Galaxy
EGB - Extragalactic Gamma-ray Background
EBL - Extragalactic Background Light
Fermi-LAT - Fermi Large Area Telescope
FLRW - Friedmann–Lemaître–Robertson–Walker
FSRQ - Flat Spectrum Radio Quasar

GAPS - General AntiParticle Spectrometer
GCE - Galactic Center Excess
GLF - Gamma-ray Luminosity Function
GZK - Greisen-Zatsepin-Kuzmin (cutoff in cosmic rays)
H.E.S.S. - High Energy Stereoscopic System
IEM - Interstellar Emission Model
ISM - InterStellar Medium
ISRF - InterStellar-Radiation Field
ISS - International Space Station
ΛCDM - Λ Cold Dark Matter
LDDE - Luminosity-Dependent Density Evolution
LHC - Large Hadron Collider
LHCb - Large Hadron Collider beauty
LIS - Local InterStellar
l.o.s. - line of sight
mAGN - Misaligned Active Galactic Nucleus
MC - Monte Carlo
NFW - Navarro–Frenk–White
gNFW - generalized Navarro–Frenk–White
PAMELA - Payload for Antimatter Matter Exploration and Light-nuclei Astrophysics
PDF - Probability Distribution Function
PSF - Point Spread Function
ROI - Point Spread Function
SED - Spectral Energy Distribution
SFG - Star-Forming Galaxy
SM - Standard Model of particle physics
SNR - Supernova Remnant
TOA - Top Of the Atmosphere
UGRB - Unresolved Gamma-Ray Background
WIMP - Weakly Interacting Massive Particle

Contents

Part I

Introduction

Chapter 1

Motivation

Our fundamental understanding of nature at small scales is based on the Standard Model of particle physics (SM) physics [10–15], which was formulated in the 1960s. The interactions of elementary particles, distinguished into quarks and leptons, are described by quantum field theories respecting gauge symmetries. Here the fundamental forces of electromagnetic, weak, and strong interactions are mediated by gauge bosons. The masses of the elementary particles are introduced through spontaneous symmetry breaking by the Higgs mechanism. The SM has experienced tremendous success in the last 50 years. A huge number of measurements, at various experiments and in a large range of energies are in agreement with SM predictions. Experimentalists and theoreticians have continuously driven the comparison to an increasing precision.

On the other hand, at very large scales the evolution of the Universe is dominated by gravity, which is described by General Relativity. The theory of General Relativity was already formulated at the beginning of the 20th century [16,17]. Also, the story of General Relativity is a long story of success. For example, in the last years the century-old prediction of gravitational waves was confirmed experimentally and very recently the first image of a black hole was recorded. The combination of General Relativity with the cosmological principle, *i.e.* the assumption that the Universe is homogenous and isotropic at large scales, leads to the Friedmann–Lemaître–Robertson–Walker (FLRW) metric and the Friedmann equation [18–24], which describe the expansion of the Universe:

$$H^2(a) = \left(\frac{\dot{a}}{a}\right)^2 = H_0^2 \left[\Omega_{0,r} a^{-4} + \Omega_{0,m} a^{-3} + \Omega_{0,k} a^{-2} + \Omega_{0,\Lambda}\right] \tag{1.1}$$

$$\frac{\ddot{a}}{a} = -\frac{4\pi G}{3}(\rho + 3p) \tag{1.2}$$

Here H is the Hubble rate which is defined in terms of the scale factor a and its time derivative $\dot{a}$. Furthermore, H_0 is the Hubble constant today, G is the gravitational constant, ρ is the energy density and p is the pressure in the Universe. The energy density of the universe can be split into four components i: matter (subscript m), radiation (r), dark energy (Λ), and curvature (k). The coefficients $\Omega_{0,i}$ are defined as the ratios of the energy density of the different components

i with the critical energy density,[1] $\Omega_{0,i} = \rho_{0,i}/\rho_{0,\mathrm{crit}}$. Cosmological observations point to a flat ($\Omega_{0,k} = 0$) Universe. Then, they are well explained within the remaining so-called Λ Cold Dark Matter (ΛCDM) model [25].

One of the main questions in contemporary physics concerns the link between the SM and the theory of gravity. At this moment, the two theories stand separated. While the first is a quantized theory the latter is classical. It is not clear how to combine the two theories into a unified picture. Moreover, the ΛCDM model in cosmology requires that the energy contribution of todays Universe exhibits a contribution of about 25% of so-called Dark Matter (DM) and about 70% of so-called dark energy. However, we lack a fundamental understanding of theses *dark* components in our Universe. In this thesis, we discuss various strategies to unveil the properties of DM with astroparticle messengers.

The remainder of this thesis is structured as follows. In the next section we give a brief introduction to particle DM and in Chapter 2 and 3 introduce Galactic Cosmic Rays (CRs) and gamma rays, respectively. The results of this thesis are presented in Part II. We start with the derivation of antiproton production cross sections in Chapter 4. In Chapter 5 we perform global fits to CR protons, helium and antiprotons in order to constrain CR propagation and learn more about DM. Then, in Chapter 6 we investigate the prospects to observe antinuclei in CRs and in Chapter 7 we use gamma rays to constrain the luminosity function of blazars. Finally, we conclude and give perspectives in Part III.

1.1 Dark Matter

Unveiling the nature of DM poses one of the fundamental open questions in contemporary physics. Despite various hints and anomalies in different observables no clear non-gravitational evidence for DM has been established so far. However, a consistent model of DM is expected to leave characteristic signatures in different observables. By exploiting the complementarity of these different observables, we can obtain a better understanding of the nature of DM which can either lead to improved constraints or, eventually, point to the properties of DM.

1.1.1 Gravitational evidences for dark matter

The gravitational evidence for the existence of DM is overwhelming. The success of DM, with respect to theories of modified gravity is its power to explain at the same time various observations at very different spatial scales. In the following, we shortly review the key observations and refer to [26–28] for more detailed reviews.

The historically first evidence for DM comes from the observation of internal motion in galaxy clusters [29, 30] and in spiral galaxies [31]. Measuring the velocity dispersion of a galaxy cluster, its mass can be estimated from the viral theorem. The estiamted mass typically exceeds the visible baryonic matter by a factor of approximately 5. On the other hand, from classical mechanics[2] the

[1] The critical energy density today is defined as by $\rho_{0,\mathrm{crit}} = 3H_0^2/(8\pi G)$.

[2] In these gravitationally bound systems effects of general relativity can be neglected.

rotational velocity within a spiral galaxy is expected to scale as $v \sim \sqrt{GM(r)/r}$, where r is the distance from the gravitational center, G is the gravitational constant, and $M(r)$ is the total mass enclosed in a sphere of radius r. In particular for distant objects where $M(r)$ exhibits the total mass of the system the velocities are expected to decrease as $v \sim r^{-\frac{1}{2}}$. Instead, measurements of the so-called rotation curves show that the velocities stay mostly constant or even increase. These observations point towards an additional non-visible halo of matter, which extends beyond the scale of the visible baryonic matter.
Another line of evidence comes from the observation of colliding galaxies [32]. After the collision the mass distribution, determined from gravitational lensing, and gas distribution, seen via X-ray emission, do not coincide. The standard explanation is that the gas components interact, slow down, and emit X-rays, while the non-interacting (or at most weakly interacting) DM component continues uninfluenced.
Furthermore, structure formation points to the existence of DM. In order to explain the amount of structures observed in the current Universe requires a dominant amount of DM. The amount of structure in the Universe is encoded in the matter power spectrum. On large scales, this matter power spectrum can be derived from linear perturbation theory and compared to data [33,34], while, at smaller, non-linear scales, N-body simulations are performed. Also these simulations are only able to reproduce the structure of the Universe if there is a dominant contribution of DM [35,36].
Finally, the observations of temperature fluctuations in the Cosmic Microwave Background (CMB) are extremely well reproduced in the ΛCDM model. The CMB exhibits photons which arrive from the last scattering surface at recombination of electrons and protons in the early Universe at a redshift of $z \approx 1100$. A fit of the ΛCDM model to the latest measurements of temperature fluctuations in the CMB by the Planck satellite shows that 84% of the matter in our Universe today is categorized as DM [25,37].

In summary, these observations point to DM candidates with some generic properties: A good DM candidate should be cold, *i.e.* non-relativistic, (or act like a cold particle) and provide the correct relic density observed today. It should be neutral and stable, exhibit a small self-interaction, and can not have a large coupling to the SM. The candidate has to comply with several constraints from astroparticle physics, particle physics, and cosmology.

1.1.2 Dark matter distributions

Cold DM is expected to form hierarchical structures. Over-dense regions of matter are able to decouple from the cosmic expansion and collapse into gravitationally bound regions, which are called DM halos. A DM halo can contain substructures of DM clumps, also called sub-halos. The properties of DM halos are expected to be (almost) independent of their size. To first approximation DM halos are spherically symmetric and described by the radial energy density profile. We distinguish two different types of profiles which are commonly studied in the literature. The first type is cored DM density profile like the Burkert profile [38]:

$$\rho_{\text{Burkert}}(r) \quad = \quad \frac{\rho_c}{(1 + r/r_c)(1 + r^2/r_c^2)}, \tag{1.3}$$

which is flat towards the halo center and decreases with r^{-3} at $r \gg r_c$. So, the core radius r_c determines the radial extension of the flat core at the halo center. These cored profiles are the preferred DM distributions from the observation of rotation curves in dwarf galaxies. On the other hand, N-body simulations [35, 36] prefer a cuspy DM density profile with a slope of the order of $\sim r^{-1}$ towards the halo center. There are three different parametrizations which are frequently used in literature. The Navarro–Frenk–White (NFW) profile [39] is a broken power law where the radial density profile evolves exactly with r^{-1} for radii smaller than the characteristic halo radius r_h and with r^{-3} for $r \gg r_h$:

$$\rho_{\mathrm{NFW}}(r) = \rho_h \frac{r_h}{r} \left(1 + \frac{r}{r_h}\right)^{-2}. \tag{1.4}$$

In a generalized version of the NFW (gNFW) profile, the density in the inner halo scales with $r^{-\gamma}$, while the behavior in the outer part remains fixed to r^{-3}:

$$\rho_{\mathrm{gNFW}}(r) = \rho_h \left(\frac{r_h}{r}\right)^{\gamma} \left(1 + \frac{r}{r_h}\right)^{-3+\gamma}. \tag{1.5}$$

An alternative profile, which also describes well the results of N-body simulation, is the Einasto profile [40]:

$$\rho_{\mathrm{Einasto}}(r) = \rho_a \exp\left(-\frac{2}{\alpha}\left[\left(\frac{r}{r_a}\right)^{\alpha} - 1\right]\right). \tag{1.6}$$

It is typically slightly softer towards the very central region of the DM halo.

We can use the Galactic DM halo for a comparison of the different profiles. The local DM density at the position of the sun can be derived from the motion of local stars and from the mapping of the rotation curve as function of galactocentric radius. In [41], it is determined to $\rho_{\mathrm{sun}} = 0.43^{+0.11}_{-0.10}$ GeV/cm^3. We show the different DM density profiles[3] in Fig 1.1.

1.1.3 Dark matter candidates

Theoretically motivated models of DM range from extremely light particles, like fuzzy DM ($\sim 10^{-22}$ eV) or axions ($\sim 10^{-5}$ eV), to primordial black holes (up to 10^{65} eV). The enormous freedom in the DM mass spanning 80 orders of magnitude reflects the lack of non-gravitational evidence for DM.

The baryonic matter in our Universe is described by the SM. One apparent reasoning for the nature of DM is to explain it by a yet undiscovered elementary particle which could be weakly coupled to the SM. Some DM candidates have an additional motivation from particle physics. For example, the axion provides a viable DM candidate and, at the same time, solves the strong CP problem in quantum chromodynamics [42–45]. Another prominent example is supersymmetry [46, 47], which is an extension of the SM where each SM fermion (boson) receives a partner boson

[3] In Fig 1.1 we adopt the following parameters. NFW: $r_h = 20$ kpc; gNFW: $r_h = 20$ kpc, $\gamma = 1.2$; Einasto: $\alpha = 0.17$, $r_a = 28.44$ kpc; Burkert: $r_c = 5$ kpc or $r_c = 5$ kpc.

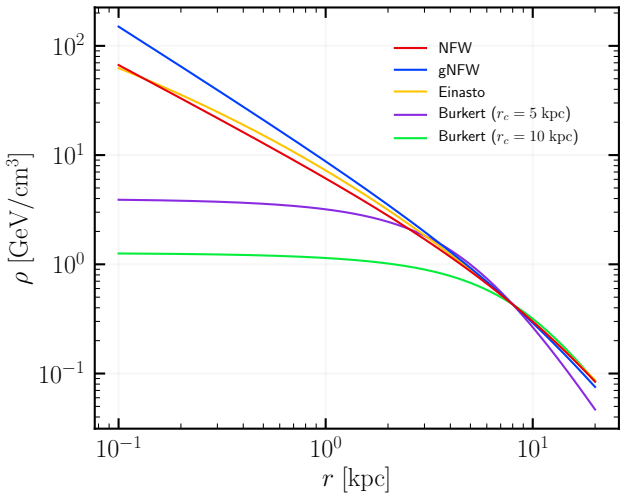

Figure 1.1: We compare different DM density profiles. They are normalized to a local DM density of $0.43\,\mathrm{GeV/cm^3}$ at the solar position of $r_{\mathrm{sun}} = 8$ kpc.

(fermion). From a particle physics perspective the supersymmetry could solve the hierarchy problem between the electroweak and the Planck scale. Furthermore, supersymmetry allows to achieve a unification of gauge couplings at high energies. If the lightest supersymmetric particle is stable, it represents a suitable DM candidate. There are many further well motivated DM candidates. For a more complete review we refer to [48–50] and references in there.
Independently from the specific Beyond the Standard Model of particle physics (BSM) realization, one of the most attractive class of DM candidates are the so-called Weakly Interacting Massive Particle (WIMP)s which have masses from a few GeV to 100 TeV and annihilation cross section at the scale of the SM weak interaction. The appeal of these candidates is that a WIMP mass and cross section automatically leads to the freeze-out of the DM particles in the early Universe and gives the correct DM relic density observed today. The formalism is detailed in the next section.

1.1.4 Dark matter relic density and the freeze-out mechanism

The freeze-out mechanism for DM is the one of the most popular mechanisms to explain the relic DM density which is observed today. Here we present the mechanism for a cold DM particle, which is non-relativistic at the time of freeze-out. A more general derivation of the mechanism is given in [26]. We assume that the DM particles interact frequently with other particles from the SM model in the early Universe DM. The annihilation of the DM particle χ and its antiparticle $\bar{\chi}$ into (at least) one of the SM particles X and its antiparticle $\bar{X}$ is denoted as

$$\chi + \bar{\chi} \leftrightarrow X + \bar{X}. \tag{1.7}$$

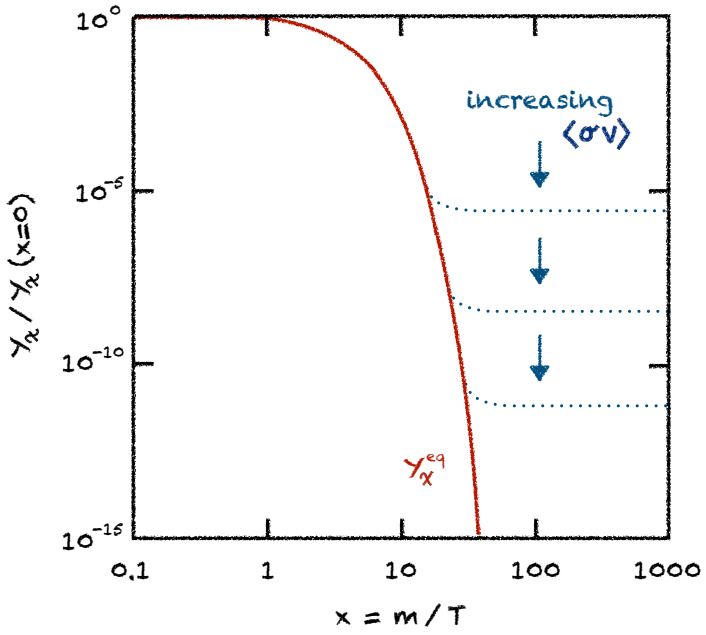

Figure 1.2: Sketch of the solution of Eq. (1.12) to visualize the freeze-out mechanism.

We note that this reaction can occur in both directions. The number density, n_χ, of the DM particles is described by a Bolzmann equation, which takes the following form in the FLRW metric:

$$\frac{\mathrm{d}n_\chi}{\mathrm{d}t} + 3Hn_\chi = \langle\sigma v\rangle \left[n_\chi^2 - (n_\chi^{\mathrm{eq}})^2\right], \tag{1.8}$$

where H is the Hubble parameter, $\langle\sigma v\rangle$ is the thermally averaged cross section times velocity of the reaction in Eq. (1.7), and n_χ^{eq} is the density of the DM particle in thermal equilibrium. We assume that the effects of Bose condensation or Fermi degeneracy can be neglected such that the equilibrium density is given by a Bolzmann distribution,[4]

$$n_\chi = g\left(\frac{m_\chi T}{2\pi}\right)^{\frac{3}{2}} \exp\left(-\frac{m_\chi}{T}\right), \tag{1.9}$$

where g is the internal degree of freedom (dof) of χ, m_χ its mass, and T is the average temperature in the Universe. We expect that in the early Universe the interaction rate, $\Lambda = \langle\sigma v\rangle\, n_\chi$, dominates over the expansion rate H and enforces the DM density to stay close to the equilibrium density, $n_\chi \approx n_\chi^{\mathrm{eq}}$. As the Universe expands the density n_χ and consequently the interaction rate quickly decreases. At some point, the right-hand side of Eq. (1.8) can be neglected. In this case, the DM density per co-moving volume becomes constant, $n_\chi/a^3 = \text{const}$, in other words, DM freezes out.

[4] We remind that we assume the non-relativistic limit, $T \ll m_\chi$.

Now we will quantify the freeze-out a bit better. In the radiation dominated Universe, we can link temperature and time by using the Friedmann Eqs. (1.1) and (1.2) equations:[5]

$$t = \sqrt{\frac{45}{16\pi^3 g_*}} m_{\rm P} T^{-2}. \tag{1.10}$$

Here g_* is the effective dof of the sum of all relativistic particles. It is common to rewrite the Bolzmann equation in terms of the dimensionless quantities $x = T/m$ and $Y = n/s$, where s is the entropy density given by:

$$s = \sqrt{\frac{2\pi^2}{45}} g_{*s} T^3. \tag{1.11}$$

Here g_{*s} denotes the effective dof for the entropy evolution in the Universe.[6] A short calculation yields:

$$\frac{{\rm d}Y_\chi}{{\rm d}x} = -\langle\sigma v\rangle \frac{g_{*s}}{\sqrt{g_*}} m_\chi m_{\rm P} \sqrt{\frac{\pi}{45}} \left[Y_\chi^2 - (Y_\chi^{\rm eq})^2\right]. \tag{1.12}$$

Furthermore, it is useful to rewrite this differential equation in terms of the difference $\Delta = Y_\chi - Y_\chi^{\rm eq}$:

$$\frac{{\rm d}\Delta}{{\rm d}x} = -\frac{{\rm d}Y_\chi^{\rm eq}}{{\rm d}x} - \langle\sigma v\rangle \frac{g_{*s}}{\sqrt{g_*}} m_\chi m_{\rm P} \sqrt{\frac{\pi}{45}} \Delta \left[\Delta + 2Y_\chi^{\rm eq}\right]. \tag{1.13}$$

We can solve this equation in two limits, before and after freeze-out, which occurs at $x = x_f$:

- At early times ($x < x_f$), the DM particles are at equilibrium with the other particles and we expect $Y_\chi \approx Y_\chi^{\rm eq}$ and ${\rm d}\Delta/{\rm d}x \approx 0$. In this limit we deduce from Eq. (1.13):

$$\Delta \approx \frac{\sqrt{g_*}}{g_{*s}} \frac{1}{\langle\sigma v\rangle m_\chi m_{\rm P}} \sqrt{\frac{45}{\pi}} \frac{x^2}{2}. \tag{1.14}$$

- After freeze out ($x > x_f$), we can neglect the equilibrium density $Y_\chi^{\rm eq} \ll Y_\chi$. By integrating Eq. (1.13) from $x = x_f$ to infinity we obtain[7]:

$$Y_\chi(x = \infty) \approx \frac{\sqrt{g_*}}{g_{*s}} \frac{1}{\langle\sigma v\rangle m_\chi m_{\rm P}} \sqrt{\frac{45}{\pi}} x_f. \tag{1.15}$$

  We can estimate x_f from the condition $\Delta(x_f) \approx Y_\chi^{\rm eq}(x_f)$ in Eq. (1.14), which gives:

$$x_f \approx \log\left(\frac{2\sqrt{45}}{(2\pi)^{\frac{7}{2}}} m_\chi m_{\rm P} \langle\sigma v\rangle\right). \tag{1.16}$$

[5] We have to use $\rho_r = \pi^2/30\, g_* T^4$, $p_r = \rho_r/3$, and $a(t) \sim t^{\frac{1}{2}}$.
[6] In the early Universe, we can approximate $g_* = g_{*s}$.
[7] We assume that $\langle\sigma v\rangle$ does not depend on velocity or temperature, as expected for s-wave annihilation.

For a typical DM particle with a mass of $m_\chi = 100$ GeV and a cross section at the order of the SM weak interaction of $\langle \sigma v \rangle = 3 \times 10^{-26}$ cm^2/s we obtain $x_f \approx 26$ and[8]

$$Y_\chi(x = \infty) \approx \frac{11}{\langle \sigma v \rangle m_\chi m_{\rm P}} \,. \tag{1.17}$$

Finally, the relic density of today is given by:

$$\Omega_{0,\chi} = \frac{s_0}{\rho_{0,\rm crit}} Y_\chi \Big|_{x=\infty} \approx 0.25 \tag{1.18}$$

where s_0 is the entropy density today[9] and $\rho_{0,\rm crit}$ is the critical energy density of the Universe. The obtained relic density[10] of $\Omega_{0,\chi} h^2 = 0.12$ matches very well the relic density observed by the Planck satellite which is also 0.12 [25]. A sketch of the solution of the Bolzmann Eq. (1.12) is shown in Fig. 1.2.

The coincidence that a SM weak annihilation cross section for a DM particle with a mass of between a few GeV and ~ 100 TeV gives automatically the correct DM relic density is known as *WIMP miracle*. Finally, we note that the thermally averaged cross section $\langle \sigma v \rangle$ is similar but not necessarily identical to the annihilation cross section for the indirect search of DM. The velocity distribution at DM at freeze-out and in the Galactic halo today differs considerably. If the DM annihilation cross section depends on velocity, $\langle \sigma v \rangle$ at freeze-out and $\langle \sigma v \rangle$ today can be significantly different. Nonetheless, the thermally averaged annihilation cross section of freeze-out gives an orientation for the order of magnitude of relevant annihilation cross section for indirect detection.

1.1.5 Strategies to search for particle dark matter

The search for DM is an interdisciplinary effort and an unambiguous answer concerning the nature of DM can only be achieved by combining the information of different observations from particle physics, astrophysics, and cosmology. The search for particle DM is typically structured into three different strategies: direct, indirect, and collider-based searches. In the first case, the idea is to investigate the possibility of a direct interaction between a DM particle and a nucleus. The cross section of this interaction strongly depends on the coupling of the DM particle to the SM: in particular on differentiates between spin-dependent and spin-independent coupling which lead to sizeable differences in the cross-section constraints. Various underground experiments try to measure the recoil energy of nuclei due to the scattering off DM. The second option is to search for indirect signatures of DM in astrophysical observables. The hypothesis is that DM can either decay or self-annihilate into SM final states. In both cases one expects characteristic signatures in gamma rays, CRs, and neutrinos. The expected signatures strongly depend on the mass of the potential DM particle and the SM final states. The question which cosmic messengers are most promising to find or constrain a DM model depends on the discrete BSM realization. Finally, the DM particles might be produced directly in collider experiments, as for example at the Large Hadron Collider (LHC).

[8] We use $g_*(x_f) = g_{*s}(x_f) \approx 80$.

[9] The entropy density is given by Eq. (1.11) with values of today, $g_{*s} = 3.94$ and $T = 2.73$ K.

[10] We use the typical notation in cosmology with $h = H_0/(100\,\text{km}/(\text{s}\,\text{Mpc})) \approx 0.7$.

Typical signature of a BSM model are events with missing transverse energy due to the escape of DM particles or resonances at the mass of mediator particles. Closely related to the production of DM at colliders is the production of DM in the early Universe.

Schematically, the three strategies are summarized in Fig. 1.3, which displays a Feynman diagram for the interaction between a DM particle χ and some SM particle X. The diagram can be read in three directions corresponding to collider searches (right to left), indirect detection (left to right), and direct detection (bottom to top). The diagram nicely visualizes the connection between the different search strategies. However, the explicit connection depends on the concrete BSM models which then determine the interaction hidden in the blob of Fig. 1.3. In this thesis, we will mainly focus on indirect detection strategies of DM which are discussed for CRs and gamma rays in Secs. 2.5 and 3.2, respectively.

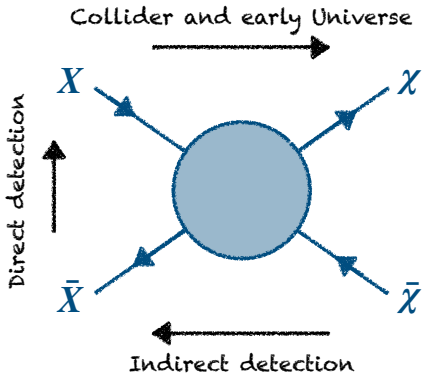

Figure 1.3: Feynman diagram showing a generic interaction of DM particles χ with SM particles X.

Chapter 2

Astroparticle physics of Galactic cosmic rays

CRs are high-energy charged particles originating from Galactic and extragalactic sources. They propagate in the turbulent magnetic field and on their journey may interact with the (extra-)galactic distribution of gas and the background fields of radiation. Today, CRs are measured over roughly 13 orders of magnitude in energy spanning form a few tens of MeV to above 10^{19} eV. In first approximation, above ~ 10 GeV the flux of CRs follows a steeply falling power law with a spectral index varying between 2.7 and 3.1. Figure 2.1 summarizes some recent flux measurements of individual CR species at low energies and the over-all particle flux at higher energies.

The extraterrestrial origin of cosmic-rays was established in 1912 by Victor Hess who conducted balloon flight to altitudes above 5 km. Thereby, he measured an increase of the ionization with altitude [51]. Today, this increase of ionization is understood as the effect of CR air showers produced by the interaction of very high-energy particles with the atmosphere of the Earth. At the time of Victor Hess, however, it was not yet clear that the "cosmic radiation" was actually due to charged particles. It was only by 1932 that CRs could be identified as charged particles due to the latitude effect [52]. It was realized that the ionization was minimal at the equator and then increased towards the north and the south poles due to the latitude-dependent deflection in the Earth's magnetic field. From those years on, CR became a very interesting field of research. At that time, CRs were the only source of high-energy particles and therefore exploited to study particle physics. Many particles were first discovered in CRs; among them the positron in 1932 [53], the muon in 1937 [54], and later also pions and kaons [55, 56].

There are two fundamentally different strategies to measure the spectrum of CRs. At low energies, up to a few hundred TeV, it is possible to perform a direct measurement of the CR fluxes above the Earth's atmosphere. Detectors are either sent to extremely high altitudes in balloon experiments or directly sent to space and mounted on satellites or the International Space Station (ISS). Typically, those detectors are spectrometers, calorimeters, Cerenkov counters, and/or transition-radiation detectors. Although each individual strategy is sufficient to obtain CR energy spectra, modern experiments like PAMELA and AMS-02 exhibit a combination of these sub-detectors to

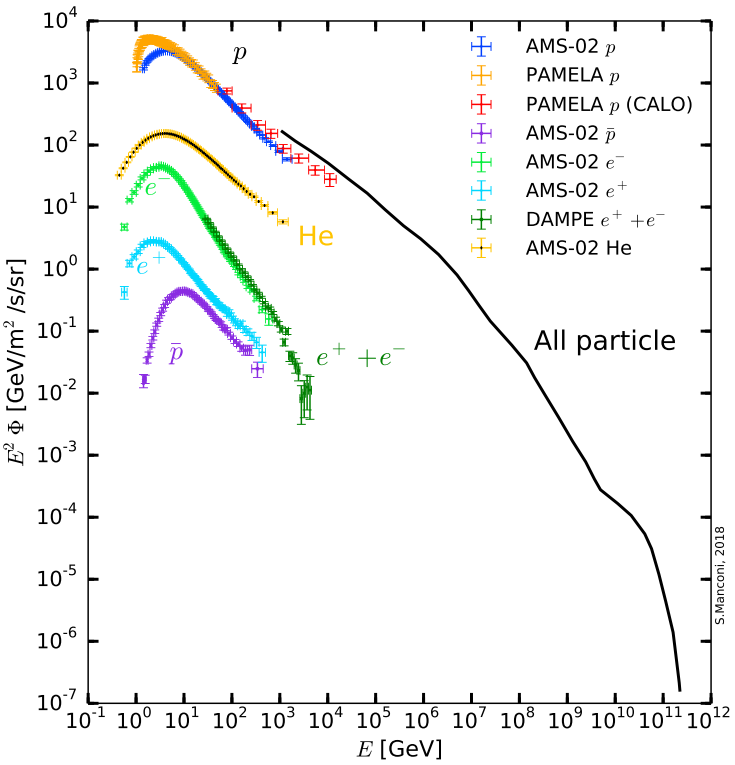

Figure 2.1: Summary of Glactic CR fluxes. Below an energy of few TeV there are direct and precise measurements of individual scpecies. We show the measurement of some nuclei [57–59] and leptons [60, 61] by AMS-02, PAMELA and DAMPE. Furthermore, we display the antiproton measurement by AMS-02. At high energies the identification of individual species is far more challenging. The black line summarize the trend of the all-particle flux [62], which at the highest energies is of extragalactic origin. The figure is taken from [63].

exploit the advantages of cross-calibrating the instruments. Furthermore, the combination of the various sub-detectors allows a precise determination of the flux of individual CR species and isotopes. We note that the magnets on-board the modern experiments provide an important advantage compared to older experiments. Figure 2.1 shows that the CR flux drastically drops when going to higher energies. While at 10 GeV there are 25 particles per square meter and second in an energy bin with a width of 10%, this number drops to roughly 1 particle per hour at 10 TeV. At the highest energies above 1 EeV the flux drops below 1 particle per square kilometer and year. The restrictions in size and weight of space-based experiments result in upper limits for the acceptance of those detectors. Thus, the detection strategy at above a few hundred TeV is very different. One exploits the Earth's atmosphere as a calorimeter and measures either the ultra violet light emitted along the shower using fluorescence detectors or the electromagnetic and muonic component of the shower with (typically Cerenkov) detectors at the surface. A good example is the Pierre Auger Observatory

in Argentina which uses both strategies to determine the CR fluxes up the highest energies.

In general one distinguishes Galactic and extragalactic CRs by the features in the energy spectrum of Fig. 2.1. Below 10 GeV CRs are strongly affected by solar wind, the so-called solar modulation effect, which we will discuss in a few more details below. Then, between 10 GeV and about 10 PeV the spectrum (of the dominant proton and helium fluxes) follows a single power law with spectral index about 2.7. Above 10 PeV the CR spectrum softens. The transition is commonly known as CR-knee. The physical origin of the knee is under discussion. The most favoured explanations are that either the Galactic sources of CRs are not able to accelerate particles to higher energies and/or the Galactic magnetic fields are not strong enough to contain the CRs within the Galaxy. In any case, CRs below the knee are considered to be Galactic. Above a few EeV the spectrum hardens again, commonly called ankle. At these extremely high energies the spectrum is considered to be of pure extragalactic origin. Finally, there is a sharp cutoff at $\sim 5\ 10^{19}$ eV. A cutoff around this energy is expected because those extremely high-energy particles start to interact with CMB photons. For example, a CR proton interacting with a CMB photon can produce a Δ^+ or Δ resonance which then decays, respectively, into a proton or neutron and a pion:

$$p + \gamma_{\mathrm{CMB}} \longrightarrow \Delta^+/\Delta \longrightarrow p'/n + \pi^0/\pi^+.$$

The effect was first discussed by Greisen, Zatsepin, and Kuzmin and is often called Greisen-Zatsepin-Kuzmin (cutoff in cosmic rays) (GZK) cutoff [64, 65]. The energy threshold for the interaction is inferred from the fact that the Center-Of-Mass (CM) energy has to be larger than the sum of proton and pion masses. A short calculation for head-on collisions yields:

$$\begin{aligned} \underline{p}_p + \underline{p}_\gamma &= \underline{p}_{p'} + \underline{p}_\pi \\ \Rightarrow (E_\gamma + E_p)^2 - (E_\gamma - p_p)^2 &= s \geq (m_p + m_\pi)^2 \\ \Rightarrow \qquad E_p &\gtrsim \frac{m_\pi^2 + 2 m_p m_\pi}{4 E_\gamma}. \end{aligned} \tag{2.1}$$

Here E_i, p_i, and m_i are energy, momentum and mass of the contributing particles, respectively, while $\underline{p}_i$ denotes a four-vector. In the last line we used that $p_p \approx E_p$ and $E_\gamma \ll E_p$. With a photon energy of $E_\gamma = 0.23\,\mathrm{meV} \hat{=} 2.7\,\mathrm{K}$ and proton/pion masses of 940/140 MeV, the cutoff energy is estimated to approximately 300 EeV. Note that this is only a first-order estimate. More detailed calculations have to account for the energy spectrum of the CMB photons. Finally, we note that it is very difficult to distinguish the GZK cutoff from a cutoff due to the maximal acceleration power of astrophisical sources. In the literature, both scenarios are discussed.

2.1 Galactic cosmic rays

In the remainder of this chapter we will focus on Galactic CRs, more specifically, on CRs in the range between the GeV level and a few hundred TeV. In the last decade, space-based experiments like PAMELA and AMS-02 provided measurements of CR leptons [60, 66–70] and nuclei [57–59, 71–74] with unprecedented precision in this energy range making astrophysics of CRs a precision discipline. For many species, the measurement accuracy is pushed to the level of a few percent. The

most precise measurement of CR antiprotons [75] is provided by AMS-02 with a precision below 5% between 2 GeV and 100 GeV. On the one hand, the precise data offers the unique opportunity to improve our knowledge and modeling of CR sources and propagation, even allowing to investigate unconventional scenarios like non-power-law and non-isotropic diffusion. On the other hand, systematic uncertainties in the modeling become substantially important since they potentially bias our conclusions. Systematics arise, for example, from the scarcity and lack of precision of secondary production cross sections, uncertainties in the gas densities and composition of the InterStellar Medium (ISM), and our limited understanding of solar modulation. Technically, one distinguishes between particles which are accelerated at astrophysical sources, so called primaries, and those produced by interactions with the ISM during propagation, so called secondaries. Electrons, protons, helium and also carbon and oxygen mostly belong into the first category, while lithium, beryllium, boron, and the antinuclei are prominent representatives of the secondaries. In principle, all secondaries are expected to contain a small primary contribution from the spallation of the heavier primaries within the astrophysical sources, however, from the analysis of the CR this contribution has to be small and until now there is no clear evidence for such a contribution. The composition of Galactic CRs is dominated by protons with about 90% and helium which contributes roughly 10%. The fraction of leptons and heavier nuclei is much smaller, both give approximately a contribution of 1%.

Before describing in more detail the various concepts of modeling Galactic CRs we define the CR flux, which is the number-flux of particles through an area A per time t, in the total energy interval E to $E + \mathrm{d}E$, and arriving from the solid angle $\mathrm{d}\Omega$:

$$\phi_E(\boldsymbol{x}, E, t, \theta, \phi) = \frac{\mathrm{d}^4 N}{\mathrm{d}A\,\mathrm{d}t\,\mathrm{d}E\,\mathrm{d}\Omega}. \tag{2.2}$$

We use the subscript E to denote that we mean the energy-differential flux. In addition to this definition there are two further definitions of the flux which are very commonly used in this field: (i) a flux which is differential in kinetic-energy per nucleus, T/n, and (ii) a flux which is differential in rigidity, $R = p/|Z|$. Depending on the application either of the definitions can be advantageous. For example, if a primary CR spallates to a secondary on the ISM the kinetic-energy per nucleon remains constant. On the other hand, the propagation of CRs in magnetic fields depends on the rigidity of a particle. From a measurement point of view, spectrometers (like AMS-02 or PAMELA) determine the rigidity of the CR while calorimeters (like CREAM) determine the total energy of a particle. We shortly summarize the relations:

$$\phi_{T/n} = \frac{\mathrm{d}E}{\mathrm{d}(T/n)}\phi_E = A\,\phi_E, \tag{2.3}$$

$$\phi_R = \frac{\mathrm{d}E}{\mathrm{d}R}\phi_E = |Z|\frac{p}{E}\,\phi_E, \tag{2.4}$$

$$\phi_R = \frac{\mathrm{d}(T/A)}{\mathrm{d}R}\phi_{(T/n)} = \frac{|Z|}{A}\frac{p}{E}\,\phi_{(T/n)}. \tag{2.5}$$

Here A and Z are mass and charge number of the CR species. Sometimes, in the following, we will drop the subscripts E, R, and T/n to avoid an overload of notation. In those cases the functional dependence of the flux indicates which of the three definitions is intended.

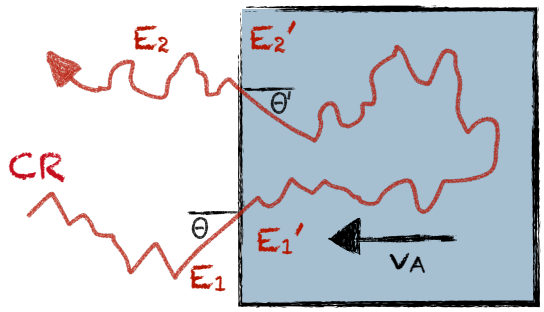

Figure 2.2: Sketch of the scattering of a CR on a magnetic wave leading to the second order Fermi acceleration.

2.2 Cosmic-ray acceleration

The steep power, observed in the local CR spectrum, suggests that the injected energy spectrum already at at the sources follows a power law. Moreover, the observation of a power law hints that the underlying acceleration mechanism is scale-invariant. Today, the generally accepted mechanism as first described by Fermi [76] relies on an iterative scattering of the CRs on magnetic waves. We assume that the energy gain at each scattering is proportional to the energy before scattering. So, at each iteration step we obtain: $E_{i+1} = (1+\xi)E_i$. Furthermore, the probability $P_{\rm esc}$ of the CR to escape the acceleration process after each iteration step is constant. Then, the number of particles with an energy larger than $E_n = E_0 \cdot (1+\xi)^n$ is given by

$$N(>E_n) \quad \sim \sum_{k=n}^{\infty} (1-P_{\rm esc})^k \sim (1-P_{\rm esc})^n \sim E_n^{-\alpha} \tag{2.6}$$

and $\alpha = -\frac{\log(1-P_{\rm esc})}{\log(1+\xi)}$. Hence, the energy-differential flux is proportional to a power law with a spectral index of

$$\gamma = 1+\alpha = 1 - \frac{\log(1-P_{\rm esc})}{\log(1+\xi)} \approx 1 + \frac{P_{\rm esc}}{\xi}. \tag{2.7}$$

Now we first relate the energy gain ξ and the scattering on magnetic waves moving at the Alfven speed, $v_{\rm A}$. In Fig. 2.2 the situation is sketched for a CR which enters the system of the wave under an incident angle θ and then scatters to an angle θ' before leaving the wave. Note that the angle θ' for convenience is defined in the rest frame of the wave while θ is the angle in the system of the Galaxy. We perform the following calculation in the limit where the CR is relativistic ($p \approx E$) and the velocity of the wave is very small compared to the speed of light ($\beta = v_{\rm A}/c \ll 1$). Then, the energies and angles before and after the scattering are related by:

$$\begin{aligned} E_1' &= \gamma(E_1 + \beta p_{1,\parallel}) \approx \gamma E_1 \gamma\,[1+\beta\cos(\theta)] \\ E_2 &= \gamma(E_2' + \beta p_{2,\parallel}') \approx \gamma E_2' \gamma\,[1+\beta\cos(\theta')]. \end{aligned} \tag{2.8}$$

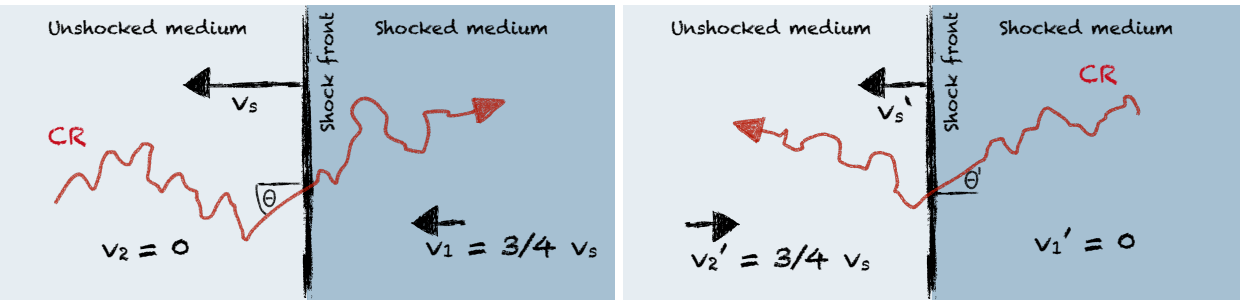

Figure 2.3: Sketch of diffusive shock acceleration of CRs as viewed from an observer in the unshocked medium (left) and an observer moving with the shocked medium (right).

Since the scattering is magnetic the energy in the system of the wave is unchanged, $E_1' = E_2'$, and we obtain:

$$\xi = \frac{E_2 - E_1}{E_1} = \gamma\,[1 + \beta\cos(\theta)]\,[1 + \beta\cos(\theta')] - 1 \approx \beta[\cos(\theta) + \cos(\theta')] + \beta^2[1 + \cos(\theta)\cdot\cos(\theta')]. \tag{2.9}$$

To obtain the average gain in the Galaxy we have to average over the two angles θ and θ'. Since θ' is randomly distributed after the scattering we expect $\langle cos(\theta')\rangle = 0$. On the other hand, the rate of particle entering in the system of the wave depends on the relative velocity of the CR and of the wave and the probability distribution for $\cos(\theta)$ becomes $P(\cos\theta) = 1/2\,(1 + v_\mathrm{A}/v_\mathrm{CR}\cos(\theta)) \approx 1/2\,(1 + \beta\cos(\theta))$, which results in $\langle\cos(\theta)\rangle = \beta/3$. Finally, the energy gain per scattering is given by:

$$\langle\xi\rangle \approx \frac{4}{3}\beta^2. \tag{2.10}$$

This scattering is known as *second order Fermi mechanism* since it is proportional to v_A^2. For characteristic Alfven velocities of to 50 km/s and structures of the magnetic field such that a scattering occurs at the parsec scale (about every 3 years) the acceleration of a CR from 1 GeV to 10 PeV (CR knee) would take more than 1 billion years, which is several orders of magnitude above the escape time of CRs in the Galaxy. In summary, the second order Fermi mechanism is not responsible for the acceleration of CRs to the highest energies. However, it can reaccelerate CRs during the propagation. As discussed in more details below this can affect the CR spectrum below a few tens of GeV.

The acceleration of CRs at astrophysical sources occurs in a special environment at shock fronts. In this environment, the acceleration is more efficient since backwards scattering ($\cos(\theta) < 0$) is impossible. Shock fronts are for example observed around Supernova Remnants (SNRs). Figure 2.3 shows the situation from an observer at rest in the shocked and in the unshocked medium. From both perspectives, the medium on the opposite side of the shock front is moving towards the observer. So, only forward scattering is allowed, which has to be encoded when averaging over $\cos(\theta)$ and

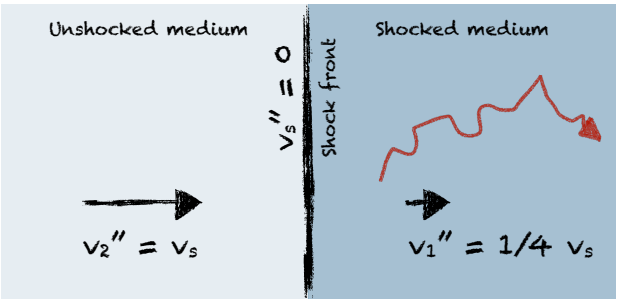

Figure 2.4: Sketch of diffusive shock acceleration of CRs as viewed from an observer on the shock front.

$\cos(\theta')$. The probability densities are given by $P(\cos\theta) = 2\cos(\theta)$ and $P(\cos\theta') = 2\cos(\theta')$ while $\cos(\theta)$ and $\cos(\theta')$ are restricted to be larger than 0. So, $\langle\cos(\theta)\rangle = \langle\cos(\theta')\rangle = 2/3$ and we obtain:

$$\langle\xi\rangle \approx \frac{4}{3}\beta. \tag{2.11}$$

Since in this case ξ depends linearly on β it is also called *first order Fermi acceleration*. Finally, we have to determine the escape velocity. Looking at Fig. 2.4 we see that the shocked medium is moving away from the shock front at $v_1'' = 1/4\, v_s$. Hence, in the shocked medium the CR tends to drift away from the shock front. The escape probability is then given by the ratio of the drift rate and the rate of crossing the shock front. The crossing rate is proportional to the CR speed divided by 4. The factor 4 arises from averaging the CRs moving towards the shock front over $\cos(\theta'')$. Since the CR speed is approximately equal to the speed of light, the escape probability is given by

$$P_{\rm esc} = \frac{4\, v_1''}{c}. \tag{2.12}$$

Inserting Eq. (2.11) and (2.12) into the Eq. (2.7) results in

$$\gamma = 1 + \frac{4\frac{v_1''}{c}}{\frac{4}{3}\beta} = 1 + \frac{3}{v_2''/v_1'' - 1}. \tag{2.13}$$

In the last step, we have replaced β by the difference of v_2'' and v_1''. In a perfect shock, the kinetic gas theory dictates that the ratio v_2''/v_1'' is equal to 4 and that γ becomes 2. In practice, if the shock is not ideal, γ can be slightly larger than 2.

For further details on this topic we refer to [77–79] and references therein.

2.3 Cosmic-ray propagation

In the following we explain how the propagation of CRs in our Galaxy is typically described. We are usually not interested in a single particle but rather in the phase-space density $f_i(\boldsymbol{x}, \boldsymbol{p}, t)$ of each

CR species i, namely, the number of particles per volume and momentum, $\mathrm{d}^6N/\mathrm{d}^3x\mathrm{d}^3p$. We are interested in the evolution of the phase-space density given by the Liouville's theorem which states that the phase-space density is constant along its trajectory up to a potential source term, q_i:

$$\frac{\mathrm{d}f_i(\boldsymbol{x},\boldsymbol{p},t)}{\mathrm{d}t} = \frac{\partial f_i}{\partial t} + \boldsymbol{v}\cdot\frac{\partial f_i}{\partial \boldsymbol{x}} + \dot{\boldsymbol{p}}\cdot\frac{\partial f_i}{\partial \boldsymbol{p}} = q_i(\boldsymbol{x},\boldsymbol{p},t) \qquad \dot{\boldsymbol{p}} = q_i\left(\boldsymbol{E}(\boldsymbol{x},t) + \frac{\boldsymbol{v}\times\boldsymbol{B}(\boldsymbol{x},t)}{c}\right). \tag{2.14}$$

Here $\dot{\boldsymbol{p}}$ is given by the Lorentz force. Notice that in practice there are no electric fields, $\boldsymbol{E}$, in our Galaxy. They are cancelled immediately by the charged particles in the plasma. However, the motion of the charged plasma particles creates magnetic fields, $\boldsymbol{B}$. They are described by the Maxwell equations. It is immediately obvious that this set of coupled differential equations is highly non-linear and the solution of the system is non-trivial. The Eq. (2.14) in combination with the Maxwell equations is well known in literature as Vlasow equation. Typically, it is necessary to either fix the electric and magnetic field to infer the behavior of single particles and the phase-space density or to fix the phase-space density to infer properties of the electromagnetic fields.

2.3.1 Diffusion equation of cosmic rays

We now take the pragmatic and phenomenological approach and describe CR propagation by diffusion. Intuitively, this can be justified since CRs undergo a random walk in the turbulent component of the Galactic magnetic fields. On average, one expects that the flux of CRs is negatively proportional to gradient of the CR density:

$$\boldsymbol{j}_i(\boldsymbol{x},\boldsymbol{p},t) = -D\,\boldsymbol{\nabla} f_i(\boldsymbol{x},\boldsymbol{p},t). \tag{2.15}$$

If we combine this equation with current conservation,

$$\frac{\partial f_i(\boldsymbol{x},\boldsymbol{p},t)}{\partial t} + \boldsymbol{\nabla}\cdot\boldsymbol{j}_i(\boldsymbol{x},\boldsymbol{p},t) = \tilde{q}_i(\boldsymbol{x},\boldsymbol{p},t), \tag{2.16}$$

we obtain the diffusion equation:

$$\frac{\partial f_i(\boldsymbol{x},\boldsymbol{p},t)}{\partial t} - \boldsymbol{\nabla}\cdot D\,\boldsymbol{\nabla} f_i(\boldsymbol{x},\boldsymbol{p},t) = \tilde{q}_i(\boldsymbol{x},\boldsymbol{p},t). \tag{2.17}$$

Here D is the diffusion coefficient. In principle, D can be time, position, and momentum dependent. Furthermore, if diffusion is not isotropic D might be a matrix,

$$D = \begin{pmatrix} D_\perp & D_A & 0 \\ -D_A & D_\perp & 0 \\ 0 & 0 & D_\parallel \end{pmatrix}. \tag{2.18}$$

In this case, $D_\parallel$ describes the diffusion parallel to a regular magnetic field, $D_\perp$ perpendicular to the field, and D_A would account for possible drift effects. However, for CR nuclei it is often sufficient to assume an isotropic and spatially homogeneous diffusion coefficient. The most commonly adapted form of the diffusion coefficient is a power law in rigidity:

$$D = \beta D_0 \left(\frac{R}{R_0}\right)^\delta. \tag{2.19}$$

Here D_0 is the normalization of the diffusion coefficient and β is the velocity divided by the speed of light. The spectral index, δ, characterizes the energy-dependence of the diffusion coefficient. In general, we expect a rise of the diffusion coefficient with energy ($\delta > 0$) since the trajectories of higher-energy particles are less bent in magnetic fields. Consequently, diffusion has to proceed faster. The exact value of δ depends on the spectrum of turbulence of the magnetic field. The two most common theories of magnetic turbulence are Kolmogorov or Kraichnan and predict a value of $\delta = 0.33$ and 0.5, respectively. These values should be taken as indications, while the exact value of δ has to be inferred from CR measurements, see discussion below.

Most attempts to describe CR propagation in our Galaxy rely on an modified version of the diffusion Eq. (2.17). This approach goes back to the Galactic halo model proposed by Ginzburg and Syrovatskii [80]. The adjustments account for further processes that CRs might encounter in the Galaxy [81]. An extensive discussion of CR diffusion is found in [82]. We will now state the full diffusion equation and then discuss the meaning of every single term:

$$\begin{aligned}\frac{\partial \psi_i(\boldsymbol{x},p,t)}{\partial t} &= \underbrace{q_i(\boldsymbol{x},p)}_{\text{(i)}} \underbrace{+\boldsymbol{\nabla}\cdot D_{xx}\boldsymbol{\nabla}\psi_i}_{\text{(ii)}} \underbrace{-\boldsymbol{\nabla}\cdot(\boldsymbol{V}\psi_i)}_{\text{(iii)}} \\ &\underbrace{+\frac{\partial}{\partial p}p^2 D_{pp}\frac{\partial}{\partial p}\frac{1}{p^2}\psi_i}_{\text{(iv)}} \underbrace{-\frac{\partial}{\partial p}\left(\frac{\mathrm{d}p}{\mathrm{d}t}\psi_i\right)}_{\text{(v)}} \underbrace{-\frac{\partial}{\partial p}\left(\frac{p}{3}(\boldsymbol{\nabla}\cdot\boldsymbol{V})\psi_i\right)}_{\text{(vi)}} \underbrace{-\frac{1}{\tau_{f,i}(\boldsymbol{x},p)}\psi_i - \frac{1}{\tau_{r,i}(p)}\psi_i}_{\text{(vii)}}\,.\end{aligned} \tag{2.20}$$

Here we already assumed that the phase-space density mentioned above is isotropic in momentum, $f_i(\boldsymbol{x},\boldsymbol{p},t) \to f_i(\boldsymbol{x},p,t)$. Local measurements of Galactic CRs confirm this isotropy. The CR density ψ_i is related to the phase-space density f_i by $\psi_i(\boldsymbol{x},p,t) = 4\pi p^2 f_i(\boldsymbol{x},p,t)$. In detail, the various terms of Eq. (2.20) describe:

(i) The **source term** specifies the location and energy spectrum of CRs injected in our Galaxy. This includes the astrophysical sources of primary CRs, which are typically characterized as (broken) power laws in rigidity. Furthermore, the source term includes the injection of secondary CRs which are produced by the interaction of primary CRs with the ISM. The source term of secondaries, therefore, depends on the density of the ISM, the primary CR flux, and the production or fragmentation cross section. We will discuss secondary CR and their importance in more detail below.

(ii) **Spatial diffusion** is the heart of the diffusion equation. D_{xx} is the diffusion coefficient discussed above, which is typically a power law in rigidity. The subscript xx is used to distinguish it from reacceleration which is described by the diffusion in momentum space.

(iii) During propagation CRs might be **reaccelerated** in the turbulent magnetic fields. Effectively, this can be described by diffusion in the CR momentum. The coefficient of diffusive reacceleration D_{pp} is related to the spatial diffusion D_{xx} via the velocity v_A of Alfven magnetic waves [83, 84] as

$$D_{pp} = \frac{4\,(p\,v_\mathrm{A})^2}{3(2-\delta)(2+\delta)(4-\delta)\,\delta\,D_{xx}}. \tag{2.21}$$

It was noted in [85] that this process inserts a significant amount of energy into the CR system, which might damp the turbulence of the magnetic fields. This damping could lead effectively to an increase of the spatial diffusion coefficient as already suggested in [86].

(iv) **Convective winds** drive CRs away from the Galactic plane. The winds introduce a current $\boldsymbol{V}(\boldsymbol{x})\,\psi(\boldsymbol{x},p,t)$. Together with the current conservation we obtain the term $\boldsymbol{\nabla}\cdot\boldsymbol{V}(\boldsymbol{x})\,\psi(\boldsymbol{x},p,t)$. Typically, we assume that the convective winds are perpendicular to the Galactic plane since they are generated by astrophysical sources in the Galactic plane like supernova explosions.

(v) **Continuous energy losses** are described by the term $dp/dt = \sum_k dp_k/dt$, summing over the various contributions k. The dominant processes of energy losses depend on the CR energy and the species. In particular, energy losses are very different for nuclei and leptons. More details are given below.

(vi) **Adiabatic energy loss** are caused by a non-zero divergence of $\boldsymbol{V}(\boldsymbol{x})$.

(vii) The catastrophic loss of particles by **decay** or **fragmentation** with decay and interaction times τ_r and τ_f, respectively. Note that the mean fragmentation time depends on the density of the ISM and the inelastic cross section resulting in a space and energy dependence. The proper decay time, on the other hand, depends only on energy.

Equation 2.20 provides a chain of coupled differential equations. The fragmentation of heavier primary nuclei on the ISM produces secondary CRs. Thus, the source term of the secondaries depends on the flux of the heavier primary CRs. In practice, one solves the chain of equations from heavy elements to lighter elements. Often one assumes that the CRs in our Galaxy are in a steady state, i.e. ψ_i is time-independent. Then the left-hand side of Eq. (2.20) becomes zero. Usually, one adopts cylindrical boundary conditions at which the CRs escape from the so-called diffusion halo, practically, this means to enforce $\psi = 0$ at the boundary. The CR density ψ is related to the CR flux by

$$\phi_R(\boldsymbol{x},R,t) = \frac{\mathrm{d}N}{\mathrm{d}A\,\mathrm{d}t\,\mathrm{d}R\,\mathrm{d}\Omega} = \frac{\beta c}{4\pi}\psi(\boldsymbol{x},p(R),t)\,\frac{\mathrm{d}p}{\mathrm{d}R} = \frac{\beta c}{4\pi|Z|}\psi(\boldsymbol{x},p(R),t). \tag{2.22}$$

The solution of the CR diffusion equation can be obtained by using numerical codes like GALPROP [87,88], DRAGON [89], or PICARD [90]. Alternatively, it is possible to solve simplified approximations of Eq. (2.20) analytically or to exploit semi-analytical tools like USINE [91].

2.3.2 Analytic solution of the diffusion equation

It is very instructive to solve a simplified version of the diffusion equation analytically to get an idea of the generally expected behaviours of the full equation. If we concentrate on CR nuclei, we might neglect energy losses and reacceleration at first approximation. Furthermore, we assume that the convection velocity is constant and perpendicular to the Galactic disc. We adopt one-dimensional diffusion model, namely, we assume an infinity expanded disk at $z = 0$ and a boundary condition with free escape at $z = \pm L$. The one-dimensional model is a reasonable approximation for CRs at

the solar position which is at 8 kpc Galactocentric radial distance while typical boundaries of the diffusion halo in two-dimensional models are at about 20 kpc.On the other hand, typical values for the height of the diffusion halo, L, range from 2 to 15 kpc. Since, the height of the Galactic disc, h, is very small compared to L it is possible to compress the fragmentation to $z = 0$, namely,

$$\begin{aligned}\Gamma_f(\boldsymbol{x}, p) &= \sum_{i\in\mathrm{H,He}} n_{\mathrm{ISM,i}}(\boldsymbol{x}) v \sigma_{\mathrm{in,CR}+i}(p) \\ &\longrightarrow 2h\delta(z) \underbrace{\langle n_{\mathrm{ISM,H}} v\rangle (\sigma_{\mathrm{in,CR+H}}(p) + 0.1\cdot\sigma_{\mathrm{in,CR+He}}(p))}_{=\Gamma_f(p)},\end{aligned} \tag{2.23}$$

[1]

where n_{ISM} denotes the density of Hydrogen or helium, σ_{in} is the inelastic cross section, and h is the height of the Galactic disc. Similarly the source term is confined to the disk. Finally, assuming steady-state we obtain:

$$D\cdot\nabla^2\psi(z) - \partial_z\left(\mathrm{sign}(z) v_c \psi(z)\right) = 2h\delta(z) q_0(R) - 2h\delta(z)\Gamma_f(p)\psi(z). \tag{2.24}$$

In the following, we will sketch the analytic solution, taking advantage of the symmetry with respect to the Galactic plane, $f(z) = f(-z)$. First, let us note that we have removed all energy-changing processes form the equation, so we can suppress the energy-dependence of ψ in our notation. Note, however, that an energy-depend diffusion coefficient, D, and energy-dependent fragmentation cross section will induce a *parametric* energy dependence of ψ. For $z > 0$ the equation reduces to $\partial_z^2\psi(z) - v_\mathrm{c}/D\,\partial_z\psi(z) = 0$, which is solved by

$$\psi(z) = A + B\left[\exp\left(\frac{v_\mathrm{c}|z|}{D}\right) - 1\right]. \tag{2.25}$$

The two coefficients A and B are fixed through the boundary conditions

$$\psi(z = L) = 0 \qquad \text{and} \tag{2.26}$$

$$[\![\partial_z\psi(z)]\!]\big|_{z=0} = \lim_{\epsilon\to 0}\int_{-\epsilon}^{\epsilon} \mathrm{d}z\, \partial_z^2\psi(z) = \frac{2}{D}\left[(v_\mathrm{c} + h\Gamma_f)\psi(0) - q_0 h\right]. \tag{2.27}$$

Here $|[\partial_z\psi(z)]|_{z=0}$ denotes the jump condition in the first derivative of $\psi(z)$. In the second step of Eq. (2.27) we have inserted Eq. (2.24) and assumed that ψ is continuous and bounded at $z = 0$. It is easy to show that these two conditions lead to

$$A = \frac{q_0}{\frac{v_\mathrm{c}}{h} + \frac{v_\mathrm{c}}{h}\frac{1}{\exp(v_\mathrm{c}L/D)-1} + \Gamma_f} \qquad \text{and} \tag{2.28}$$

$$B = -\frac{1}{\exp(v_\mathrm{c}L/D) - 1}\, A. \tag{2.29}$$

Note that the flux at $z = 0$ is given by $\phi(0) = A$. Let us investigate three limits:

[1] Compared to Eq. (2.20) we replaced the mean fragmentation time by the fragmentation rate $\Gamma_f = 1/\tau_f$. In the second step of Eq. (2.23) we assumed that the helium density in the ISM is 10% of Hydrogen density.

- **Diffusion domination:** In this limit, we can expand A around $v_c D/L \ll 1$ and then neglect fragmentation and convection. We obtain $\psi(0) = q_0\, hL/D$. The ratio of phase-space density ψ and source term q_0 determines a characteristic time scale for diffusion of CRs in the Galaxy, we define $\tau_{\rm diff} = hL/D$. If diffusion is the dominant process affecting CRs this coincides with the escape time of the CRs from our Galaxy, which is true for nuclei above approximately 10 GV. For typical values of the diffusion coefficient at 10 GV of $D = 0.3$ kpc^2/Myr and a halo (disc) height of 10 kpc (0.1 kpc) the diffusion time is $\tau_{\rm diff} = 3.3$ Myr. Since D increases with energy the diffusion time decreases and vice versa. These time scales can be understood as mean residual time of the CR in the Galaxy.

- **Convection domination:** In this case, we obtain $\tau_{\rm conv} = h/v_c$. For typical convection velocities of 15 km/s ≈ 0.015 kpc/Myr we obtain $\tau_{\rm conv} = 6.6$ Myr. So, convection might become the dominant process at low energies when $\tau_{\rm conv}$ drops below $\tau_{\rm diff}$.

- **Fragmentation domination:** This means that we can neglect convection and diffusion. We obtain $\tau_f = 1/\Gamma_f$. Also, these losses due to fragmentation are typically only important at low energies. We note that it strongly depends on the nucleus if and at which energies fragmentation domination is reached. In general, heavier nuclei are much more affected by fragmentation since inelastic cross sections grow roughly with A^{D_1} with D_1 between 2/3 to 1.0. We note that at low energies of about 1 GeV/n the fragmentation of nuclei is very important. As a result, different nuclei probe different volumes in the diffusion halo [92].

From Eq. (2.28) we understand that the total escape time of all relevant sub-processes is approximately obtained by

$$\frac{1}{\tau_{\rm esc}} \approx \sum_k \frac{1}{\tau_k}. \tag{2.30}$$

Then the CR flux is given by $\phi(R) = q_0(R)/\tau_{\rm esc}(R)$. Sometimes the escape time is also called effective propagation time and denoted $\tau_{\rm eff}$. In the literature, the approximation $\phi(R) = q_0(R)/\tau_{\rm esc}(R)$ is discussed as the so-called *leaky box* model [82, 93]. We note that the local CR flux depends only on the ratio of D/L in this simplified model, so it is not possible to constrain the diffusion coefficient and halo height separately. To lift the degeneracy it is necessary to exploit the information of radioactive CR isotopes which decay at time scales comparable to the escape time.

It is also possible to find analytic solutions of the two-dimensional setup. One adopts cylindrical symmetry with Galactocentric radial distance, r and distance from the Galactic plane z and uses boundary condition with free escape at $r = r_{\rm max}$ and $z = \pm L$. For a more detailed discussion on different analytic solutions refer to [94]. Here we repeat only the solution which will be used later in Chapter 6. The diffusion equation in cylindrical coordinates reads

$$\frac{\partial \psi(r,z)}{\partial t} - D \cdot \boldsymbol{\nabla}^2 \psi(r,z) + \partial_z \left(\mathrm{sign}(z)\psi(r,z)v_c\right) = q(r,z) - 2h\delta(z)\Gamma_f \psi(r,z) \tag{2.31}$$

$$\text{and} \qquad \boldsymbol{\nabla}^2 = \frac{1}{r}\,\partial_r^2\, r + \partial_z^2$$

The solution at the solar position is given in terms of Bessel functions by:

$$\psi(r,z)\Big|_{r=r_{\rm sun},z=0} = \sum_{n=1}^{\infty} J_0\left(\xi_n \frac{r_{\rm sun}}{r_{\rm max}}\right) \exp\left(-\frac{v_{\rm c} L}{2D}\right) \frac{y_n(L)}{A_n \sinh(S_n L/2)} \tag{2.32}$$

with

$$\begin{aligned} Q_n &= \frac{4}{J_1^2(\xi_n) r_{\rm max}^2} \int_0^{r_{\rm max}} dr\, r J_0(\xi_n r/r_{\rm max}) q(r,z), \\ y_n &= \int_0^{Z} dz\, \exp\left(\frac{v_{\rm c}(Z-z)}{2D}\right) \\ &\qquad \times \sinh(S_n(Z-z)/2) Q_n, \\ A_n &= 2h\Gamma_f + v_{\rm c} + D S_n \coth(S_n L/2), \\ S_n &= \left(v_{\rm c}^2/D^2 + 4\xi_n^2/r_{\rm max}^2\right)^{1/2}. \end{aligned} \tag{2.33}$$

Here J_0 and J_1 are the zero- and first-order Bessel functions, while ξ_n is the n-th zero of J_0. We stress that this solution allows sources located in the disc of the Galactic plane as well as in the diffusion halo.

2.4 Nuclei in cosmic rays and the role of secondaries

The most important process affecting the propagation of CR nuclei can be understood from the time scales of the single processes in Eq. (2.20). In Fig. 2.5 we show the time scales for the propagation of CR protons. The propagation parameters are inferred from the fit of an analytic one-dimensional model to the recent CR data of the boron-to-carbon ratio provided by the AMS-02 experiment [74]. Details on this fit are provided in [95]. This model allows for diffusion, reacceleration, and convection. Furthermore, losses from nuclear interaction are taken into account. As expected, at high energies diffusion dominates all other processes and convection becomes important below a kinetic energy of $T_p \lesssim 10$ GeV. Only, at very small energies of $T_p \lesssim 0.2$ GeV the continuous energy losses due to Coulomb scattering and ionization become relevant ($\tau_{\rm loss}$). Diffusive reacceleration ($\tau_{\rm DR}$) is sub-dominant at all energies. Note, however, that the conclusion on reacceleration depends on the exact realization of the CR diffusion model. If the model would allow for larger values of Alfven velocities, diffusive reacceleration would be more important at low energies. The effective propagation time, $\tau_{\rm eff}$, which comprises all subprocesses, is on the order of Myrs.

2.4.1 Primaries versus secondaries

Primary CRs are accelerated and injected into the diffusion halo at astrophysical sources. For nuclei, SNRs are the supposed dominant source of primary CRs. At the shock front of the SNR CRs can be accelerated up the observed energies. The energy budget of CRs can be sustained with

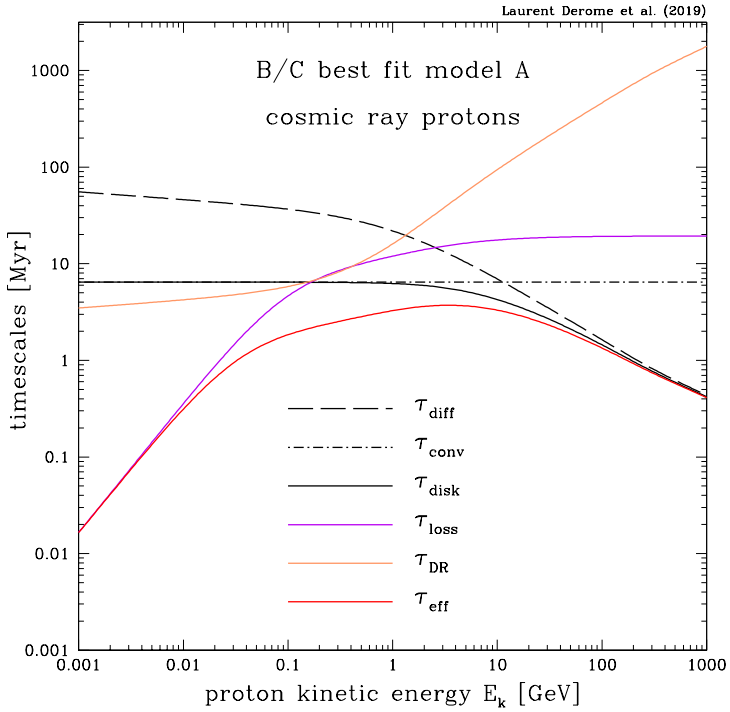

Figure 2.5: Comparison of the characteristic time scales of various relevant processes for the propagation of CR protons. The figure is taken from [95].

the observed rate of supernova explosion of approximately three per century. Therefore, the source term of primary CR nuclei is expected to follow the distribution of SNR in our Galaxy. Usually one assumes that an effectively time-independent source term can be separated into an energy-dependent component and a spatial component, $q(\boldsymbol{x}, p) = q_{xx}(\boldsymbol{x})q_p(p)$. If we furthermore assume that the source distribution is cylindrically symmetric it can be parametrized by

$$q_{xx}(r, z) \quad = \quad \left(\frac{r}{r_0}\right)^{\alpha} \exp\left(-\beta\frac{r - r_0}{r_0}\right) \exp\left(-\frac{|z|}{z_0}\right), \tag{2.34}$$

which follows the observed radial distibution of SNR in our Galaxy [96, 97]. Typical parameter values are $\alpha \sim 1.6$, $\beta \sim 4$ with a flattening above $r \gtrsim 10$ kpc and a cutoff above $r \gtrsim 30$ kpc. Moreover, the sources are exponentially constrained to the disk with a mean width of $z_0 \sim 0.2$ kpc. The energy-dependent part q_p is typically modeled as (broken) power law in rigidity but the exact spectral index and potential breaks are not known from first principles and have to be inferred from data.

Secondary CRs are not produced at the astrophysical sources. We can identify them by comparing the abundance of elements in CRs with the abundance in the solar system. Figure 2.6 shows the relative abundances of all elements from protons to iron compared to silicon. For primary elements

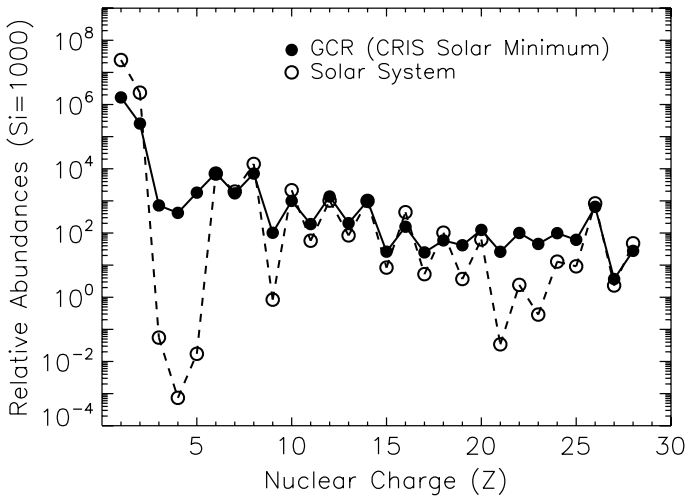

Figure 2.6: Comparison of nuclei abundances in CRs and the solar system. The figure is taken from [98].

the two abundances agree with each other while for secondary elements the CR abundance significantly exceeds the solar abundance. The reason is that the secondary elements are not produced during thermonuclear fusion in the stellar cycle. Hence, they are far less abundant in the solar system. In CRs, however, the secondaries can be produced by the interaction of primary CRs with the ISM Therefore, their abundance is increased. From Fig. 2.6 we identify that p and He as well as C, N, and O are primary CRs while Li, Be, and B are secondary. Furthermore, some of the sub-iron elements are secondaries.
The source term of secondaries is given by:

$$q_i(T_i) \quad = \quad \sum_{k>i} \sum_{j=\{\mathrm{p,He}\}} 4\pi\, n_{\mathrm{ISM},j}\, \phi_k(T_k)\, \sigma_{k+j\to i}(T_k) \Big|_{\frac{T_k}{A_k}=\frac{T_i}{A_i}} \tag{2.35}$$

Here $\sigma_{k+j\to i}$ denotes the fragmentation cross section of species k into i on the ISM component j, ϕ_k is the CR primary flux, and $n_{\mathrm{ISM},j}$ is the density of the ISM. We have assumed that the kinetic energy per nucleon (T/A) is constant during the fragmentation, which is a good approximation up to a few percent precision [99]. At large energies the cross section is approximately independent of energy. Then the source term of the secondary CRs equals the energy behaviour of the parent flux. Consequently, the secondary source term adopts the energy spectrum of the propagated primary CR flus and thus it is harder than the primary source term. The cross sections for secondary production are measured at high-energy experiments, however, the precision of these cross sections lags behind the precision of recent CRs observations by AMS-02 [100].

Note that when we talk about primary CRs we mean "dominantly primary". All primary nuclei contain also a secondary component from the fragmentation of heavier elements. Furthermore, there are speculations about a primary component in typical secondary species. They would be

produced by spallation of the primaries directly at the vicinity of the sources and then participate in the acceleration process [101–104]. Typically, this kind of primary component is not supported by the B/C ratio but it could become important at high energies at the order of one TV because the primary source terms are softer than the secondary source terms [105, 106].

2.4.2 Primary-to-secondary ratios

Primary-to-secondary ratios in CRs constrain the behaviour of propagation. To understand the principle let us take another a look at the analytic one-dimensional diffusion model discussed above. At high energies, where diffusion is dominant, the flux of primaries is given by

$$\phi_{\mathrm{prim}}(T/A) \approx \frac{c}{4\pi A} \frac{q_{\mathrm{prim}}(T/A)\, h\, L}{D(T/A)}. \tag{2.36}$$

Then source term and flux of the secondary become

$$q_{\mathrm{sec}}(T/A) \approx 4\pi\, n_{\mathrm{ISM}}\, \phi_{\mathrm{prim}}(T/A) \sigma_{\mathrm{prim}\to\mathrm{sec}} \quad \text{and} \tag{2.37}$$

$$\phi_{\mathrm{sec}}(T/A) \approx \frac{c}{A} \frac{n_{\mathrm{ISM}}\, \phi_{\mathrm{prim}} \sigma_{\mathrm{prim}\to\mathrm{sec}}(T/A)\, h\, L}{D(T/A)}, \tag{2.38}$$

such that the secondary-to-primary ratio turns out to be

$$\frac{\phi_{\mathrm{sec}}(T/A)}{\phi_{\mathrm{prim}}(T/A)} \approx \frac{c}{A} \frac{n_{\mathrm{ISM}}\, \sigma_{\mathrm{prim}\to\mathrm{sec}}\, h\, L}{D(T/A)}. \tag{2.39}$$

The standard ruler to constrain propagation parameters in the diffusion models is the boron-to-carbon ratio. Boron is produced from the spallation of carbon and heavier species on the ISM. AMS-02 has measured the B/C ratio with high precision between 2 GeV and a few TeV [72]. It roughly follows a power law above a few tens of GeV with a spectral index between -0.3 and -0.5. We can conclude that the diffusion coefficient behaves as $D \sim R^{\delta}$ with δ in the range of 0.3 to 0.5, which is in agreement with the theoretical expectations. In more detailed analyses it is possible to infer not only the diffusion coefficient but it also possible to constrain further processes like convection, reacceleration, and potential breaks in the diffusion coefficient. Recent analyses of the AMS-02 data require a detailed understanding of the various systematic uncertaintes as for example discussed in [95, 107].

2.4.3 Cosmic-ray clocks

Radioactive isotopes in CRs can be used to break the degeneracy of L and D. They are also called CR clocks. To understand how this works we go back to our simple analytic one-dimensional diffusion equation, Eq. (2.24). In the limit of only diffusion and decay it reads $D \cdot \nabla^2 \psi(z) = 2h\delta(z) q_0(R) - \Gamma_r(p)\psi(z)$. The solution at $z = 0$ is given by

$$\psi(z)\big|_{z=0} = \frac{q_0\, h}{\sqrt{\Gamma_r D}} \tanh\left(\frac{\Gamma_r L^2}{D}\right). \tag{2.40}$$

In a decay dominated regime the characteristic decay time is $\tau_{\rm decay} = h/\sqrt{\Gamma_r D}$. The decay rate Γ_r is energy-dependent because of the time dilation of the relativistically moving CRs. If $\gamma = E/m$ is the Lorentz factor and $\tau_{0,r}$ the mean decay time of the CR species at rest, the decay rate is $\Gamma_r = 1/(\gamma\tau_{0,r})$. The ^{10}Be isotope is radioactive and has a lifetime about 2 Myr, which is suitable to constrain the halo size. Historically, the ratio of ^{9}Be/^{10}Be is considered as standard ruler, however, the experimental measurements of this ratio are scarce and restricted to very low energies.[2] We stress that solid conclusions at low energies are difficult since many propagation effects become important such as cross section, solar modulation, reacceleration, and convection. An alternative might be to consider the Be/B ratio which is measured precisely by AMS-02 [72]. A recent analysis hints towards $L \sim 6$ kpc. However, this result might be affected by systematic uncertainties in the Be production cross section [110]. Taking this systematic uncertainties into account the result becomes less reliable, although remaining compatible with standard assumptions for L. In particular, it still excludes very small halo heights of $L \lesssim 2$ kpc.

2.4.4 Observation of the spectral break at 300 GeV

The precise measurement of the CR proton and helium fluxes by PAMELA [57] revealed a spectral break in the power law at a rigidity of about 300 GV. This observation is confirmed by the AMS-02 experiment [58,59]. Moreover, AMS-02 has acquired sufficient statistics to observe a similar break in the heavier primary spectra of carbon and oxygen [73]. The difference of spectral indices above and below the break is approximately 0.1. On the other hand, the secondary fluxes of lithium, beryllium, and boron exhibit a break at the same rigidity, but the change of spectral index is roughly twice as large as for the primaries. This can be explained by a break in the diffusion coefficient [111]. In principle, a break in the energy spectra of CRs could originate from the injection spectrum or from diffusion coefficient. The generic argument to support the latter is that the break in the secondaries is more pronounced than in the primaries. This is expect if there is a change in the diffusion coefficient since secondaries *experience diffusion twice*, once as primary and a second time as secondary, *i.e.* after spallation.
The observation of this break in the diffusion coefficient could be explained within models of self-generated turbulence [112, 113] due to the streaming instability of CRs. This would decrease the diffusion coefficient at low energies, below the observed break, and leave it unchanged above. Because of the decreased diffusion coefficient at low energies advection of CRs becomes more important (at about 10 GV) which would lead to another break in the observed spectrum. So, effectively this models would lead to two breaks in the propagation processes of CRs. Recently, it was noted that a model of self-generated diffusion could also be used to explain the origin of a diffusion halo with a half-height at the order of a few kpc [114].

[2] We note that also some further radioactive nuclei are explored in literature. In particular, the ratios of ^{26}Al/^{27}Al, ^{36}Cl/Cl, and ^{54}Mn/Mn are considered [108, 109].

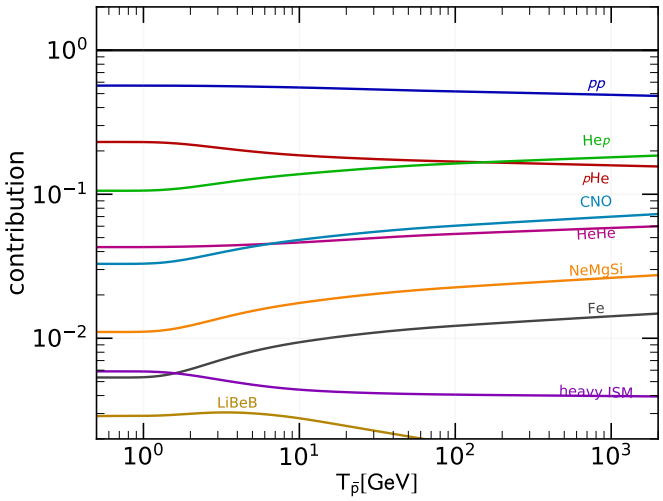

Figure 2.7: Relative contribution of various channels to the total secondary antiprotons source term in CRs as function of the antiproton kinetic energy, $T_{\bar{p}}$. The dominant contributions are given by the pp, pHe, and Hep channels. More details on how to obtain this results are given in Sec 4, see Fig. 4.6. The figure is taken from [3].

2.5 The special role of cosmic-ray antiprotons

Antiprotons take a special role in the ensemble of CRs. Their dominant production mechanism is of secondary origin, namely, antiprotons are produced by the interaction of primary CRs with the ISM. However, the production mechanism differs significantly from the production of secondary nuclei like lithium or boron. The latter are produced by fragmentation of heavier nuclei on the ISM. In these fragmentation reactions the kinetic energy-per-nucleon of the secondary and primary stays constant as discussed in the previous section. Antiparticles, on the other hand, have to be created in pair of particle and antiparticle. The dominant production reactions of CR antiprotons are the inelastic interaction of CR protons or helium on the ISM which consists of hydrogen and helium. In the following, we will call antiprotons produced in the interaction of the CR species i and the ISM component j "produced in the ij channel". Explicitly, antiprotons produced from a CR proton and ISM Hydrogen are attributed to the proton-proton (pp) channel and the underlying reaction is $p+p \to \bar{p}+X$. Figure 2.7 shows the relative contribution of the different production channels to the total antiproton source term. The pp channel makes up 50% to 60% of the total antiproton source term, while the pHe and Hep channels each contribute 15% to 20%. The production of antiprotons by heavier CR nuclei or the heavier components in the ISM give only a small and almost negligible contribution at the percent level.

Before we give a more detailed derivation of the antiproton source term, we have to remark on one subtlety: In the total source term of antiprotons, we count not only the antiprotons directly

produced at the interaction vertex of CR and ISM particles, commonly called *prompt* antiprotons, but also all particles which decay into antiprotons within typical propagation time-scales of CRs. In particular, this includes antineutrons and antihyperons. It will be discussed below how to relate antineutrons and antihyperons to the prompt antiproton production.

2.5.1 Derivation of the antiproton source term

The source term of CR antiprotons in the ij channel, namely, the number of antiprotons produced per time, volume, and energy in the interaction of a CR species i and an ISM component j, is given by [7, 115, 116]:

$$q_{ij}(T_{\bar{p}}) \quad = \quad \int_{T_{\rm th}}^{\infty} \mathrm{d}T_i \; 4\pi \, n_{{\rm ISM},j} \, \phi_i(T_i) \, \frac{\mathrm{d}\sigma_{ij}}{\mathrm{d}T_{\bar{p}}}(T_i, T_{\bar{p}}). \tag{2.41}$$

Here T_i and $T_{\bar{p}}$ are the kinetic energy of the CR projectile and the produced antiproton, respectively. Furthermore, $n_{\rm ISM}$ is the ISM density, ϕ_i is the CR flux, and $\mathrm{d}\sigma_{ij}/\mathrm{d}T_{\bar{p}}$ is the energy-differential antiproton production cross section in the ij channel. The factor 4π corresponds to an angular integration of the isotropic CR flux. The lower bound, $T_{\rm th}$, in the energy integration is the threshold energy to produce a proton-antiproton pair in the CR-ISM collision, which, in the case of the pp channel, this energy is given by $T_{\rm th} = 6\, m_p \approx 5.63$ GeV.

The energy-differential antiproton production cross section in Eq. (2.41) can be related to the fully-differential cross section measured in high-energy experiments. These cross sections are typically stated in the Lorentz-invariant form

$$\sigma_{\rm inv} = E\frac{d^3\sigma}{dp^3}(\sqrt{s}, x_f, p_{\rm T}), \tag{2.42}$$

where E is the total energy and p the momentum of the produced antiproton. The production cross section depends on three kinematic variables: The CM energy of the collision, $\sqrt{s}$, and two parameters to state the energy and direction of the produced antiproton.[3] Commonly used parameters are the so-called Feynman scaling variable $x_f = 2p_L^*/\sqrt{s}$ and the transverse momentum p_T. The superscript * denotes that a variable is taken in the CM frame. In some cases, we will replace the Feynman scaling x_f with the radial scaling $x_{\rm R} = E_{\bar{p}}^*/E_{\bar{p}}^{\rm max,*}$, with the maximal antiproton energy given by $E_{\bar{p}}^{\rm max,*} = (s - 8m_p^2)/(2\sqrt{s})$. [4]

To obtain the energy-differential cross section in Eq. (2.41) from the Lorentz-invariant cross section in Eq. (2.42) we, first, have to relate the kinematic variables from the CM frame, $\{\sqrt{s}, x_f, p_{\rm T}\}$, to kinetic variables in the ISM frame. The standard choice of variables are the kinetic energy-per-nucleon of the projectile, T_i/A, the kinetic energy of the produced antiproton $T_{\bar{p}}$, and the angle of the produced antiproton with respect to the incoming projectile, θ.

[3] Note that the cylindrical symmetry of the collision reduce the kinematic parameters of the produced antiproton from 3 to 2.

[4] A derivation of this formula is given in the App. A of [7].

Let us for a moment focus on the pp channel. Then, the Lorentz transformation between the CM and ISM frame relating the energy and the longitudinal momentum of the antiproton is given by:

$$\begin{pmatrix} E_{\bar{p}} \\ p_{\bar{p},L} \end{pmatrix} = \begin{pmatrix} \gamma^* & \gamma^*\beta^* \\ \gamma^*\beta^* & \gamma^* \end{pmatrix} \begin{pmatrix} E^*_{\bar{p}} \\ p^*_{\bar{p},L} \end{pmatrix}. \tag{2.43}$$

Here β^* is the velocity of (each of) the proton(s) in the CM frame and $\gamma^* = \left((1-(\beta^*)^2\right)^{-1/2}$ is the corresponding Lorentz factor. In terms of proton energy and momentum of the projectile proton, the two variables can be expressed as

$$\begin{aligned} \beta^* = p^*_p/E^*_p &= \sqrt{\frac{E_p - m_p}{E_p + m_p}} = \sqrt{\frac{s-4m_p^2}{s}} \qquad \text{and} \\ \gamma^* = E^*_p/m_p &= \sqrt{\frac{E_p + m_p}{2m_p}} = \frac{\sqrt{s}}{2m_p}, \end{aligned} \tag{2.44}$$

and the CM energy is given by

$$s = 4E^*_p = 2E_p m_p + 2m_p^2. \tag{2.45}$$

More details are given in App. B of [7].
After the Lorentz transformation the energy-differential cross section is obtained by an angular integration:

$$\frac{\mathrm{d}\sigma}{\mathrm{d}T_{\bar{p}}}(T_p, T_{\bar{p}}) = \int \mathrm{d}\Omega \; \frac{\mathrm{d}^3\sigma}{\mathrm{d}E_{\bar{p}}\mathrm{d}\,\Omega}(T_p, T_{\bar{p}}, \theta) = \int \mathrm{d}\Omega \; p_{\bar{p}}^2 \frac{\mathrm{d}p_{\bar{p}}}{\mathrm{d}E_{\bar{p}}} \frac{d^3\sigma}{p_{\bar{p}}^2 \,\mathrm{d}p_{\bar{p}}\,\mathrm{d}\Omega} = p_{\bar{p}} \int \mathrm{d}\Omega \, \sigma_{\mathrm{inv}}(T_p, T_{\bar{p}}, \theta). \tag{2.46}$$

Here $\mathrm{d}\Omega = \mathrm{d}\varphi\mathrm{d}(\cos\theta)$ denotes the integral over the solid angle. In the last step we used the relation $\mathrm{d}p_{\bar{p}}/\mathrm{d}E_{\bar{p}} = E_{\bar{p}}/p_{\bar{p}}$. If the angular integral has to be evaluated numerically it is preferable to replace the angle θ with the pseudo-rapidity η using $\cos\theta = \tanh\eta$.

In Fig. 2.8 we show the energy-differential antiproton production cross section as function of the kinetic energy of the proton projectile and the antiproton product. As expected, the antiprotons are produced only above a threshold in the proton energy of 5.63 GeV and they respect energy conservation, namely, the antiproton energy always stays below the energy of the projectile proton. Furthermore, at $T_{\bar{p}} \lesssim 1$ GeV the production of antiprotons from protons with low energies (close to T_{th}) is suppressed because of a decreasing phase space.

2.5.2 A comment on the contribution of antineutrons and antihyperons

As already mentioned above, antiprotons in CRs can originate from the decay of an intermediate antineutron or antihyperons ($\bar{\Lambda}$ and $\bar{\Sigma}$) with typical mean lifetimes of 881.5 s and $\sim 10^{-10}$ s, respectively, which are negligibly small compared to the time scales of CR propagation at the order of a few Myrs, see above. Therefore, the production cross section in Eq. (2.46) has to refer to

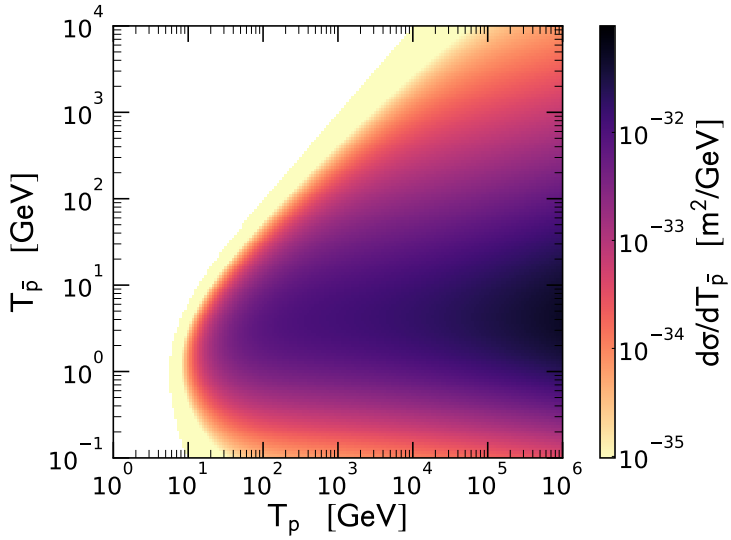

Figure 2.8: Energy-differential antiproton production cross section in the pp channel as function of proton and antiproton kinetic energies. The cross section is derived from the parametrization of Ref. [117]. The figure is taken from [7].

the sum of antiprotons, antineutrons, and antihyperons. However, at the fully-differential cross section level only the prompt antiproton component is measured. We assume that the production of antineutrons and antihyperons is proportional to the antiproton production which is a reasonable assumption given their similar baryonic structure. Traditionally, the production of antiprotons and antineutrons was considered to be identical, until an enhancement of antiproton production was observed in the reaction of $p + n \to \bar{p} + X$ with respect to $p + p \to \bar{p} + X$ [118]. As argued in [117], due to symmetry, the same enhancement of about 30%±20% is expected in $p + p \to \bar{n} + X$ with respect to $p + p \to \bar{p} + X$. We denote the enhancement of antineutron production with respect to antiproton production with Δ_{IS}. This so-called isospin violation was further studied and compared to data sets at various CM energies by [119] as displayed in the left panel of Fig. 2.9. According to this analysis the enhancement is 10% to 20% at low energies and decreases to 0 at high energies.

On the other hand, the production ratio of $\bar{\Lambda}/\bar{p}$ increases from 30% at $\sqrt{s} \leq 10$ GeV to 60% at $\sqrt{s} \geq 100$ GeV, see right panel of Fig. 2.9. To obtain the number of antiprotons from the decay of antihyperons we assume a constant production ratio of $\bar{\Sigma}/\bar{\Lambda} \approx= 0.33$ and branching ratios of $\mathrm{Br}(\bar{\Lambda} \to \bar{p} + \pi) = 0.64$ and $\mathrm{Br}(\bar{\Sigma} \to \bar{p} + \pi) = 0.52$. Then the enhancement of antiproton production due to an antihyperon contribution is given by $\Delta_\Lambda = 0.81 \cdot \bar{\Lambda}/\bar{p}$. Finally, if we assume that antiproton and antineutron production from antihyperons are equal, the total cross section for antiproton production in our Galaxy is related to the prompt antiproton production cross section by

$$\sigma_{\mathrm{inv}}^{\mathrm{Galaxy}} = \sigma_{\mathrm{inv}} \cdot (2 + \Delta_{\mathrm{IS}} + 2\Delta_\Lambda). \tag{2.47}$$

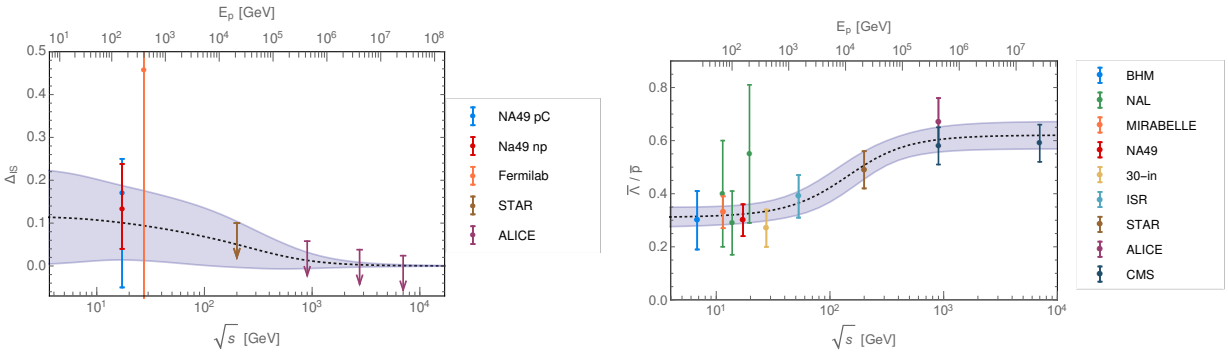

Figure 2.9: The left panel shows the enhancement of antineutron production with respect to antiproton production, $\Delta_{\rm IS}$, as function of CM energy, while the right panel shows the ratio of anti-Λ-to-antiproton production. Both figures are taken from [119].

2.5.3 Scaling of the proton-proton to the proton-nucleus channels

In principle, we would like to have independent determinations of antiprotons in the pp and the significantly contributing pHe, Hep and HeHe channels. Unfortunately, there are not enough cross section measurements to follow this procedure in the pHe channels. Only very recently the first ever measurement of antiproton production cross sections on He was provided by the LHCb experiment. They used a fixed He target and proton projectiles at 6.5 TeV to measure antiprotons produced at momenta between 12 and 110 GeV and transverse momenta between 0.4 and 4.0 GeV [120]. The contribution of this parameter space to the source term of CR antiprotons is very small. Therefore, the common approach is to rescale the pp channel to pA and AA. To understand the relation between the pp channel and the channels including a heavier nucleus as projectile and/or target we use the picture that a nucleus is built from a number of A nucleons. Then, the production of antiprotons can be traced back to an interaction of a single nucleon in the target with a single nucleon in the projectile. Therefore, at very first approximation one expects a scaling of the cross section which is linear in A for both, projectile and target (*c.f.* [3] and references in there):

$$\sigma_{\rm inv}^{A_1 A_2}(\sqrt{s}, x_f, p_{\rm T}) \approx A_1\, A_2 \sigma_{\rm inv}^{pp}(\sqrt{s}, x_f, p_{\rm T}). \tag{2.48}$$

From the above picture, it is obvious that the appropriate CM frame is the nucleon-nucleon frame and that the kinematic variables $\sqrt{s}$ and x_f refer to this nucleon-nucleon frame.[5] In practice, there are shielding effects such that the scaling is slightly smaller than linear. We will discuss this in more detail in Chapter 4.

Historically, there have been different strategies to determine the rescaling factor. In Ref. [121] the authors performed a fit to various data sets from pBe up to pPb interactions. However, for the purpose of antiproton production in CRs we are interested in the scaling factor of pHe which might differ significantly from the scaling of pPb given the large difference in mass number: $A_{\rm He} = 4$ and

[5] Specifically, this means that in Eqs. (2.44) and (2.45) the energy E_p and the momentum of the p_p of the projectile (in the ISM frame) have to be replaced by E_A/A and p_A/A.

$A_{\mathrm{Pb}} = 208$. In Ref. [119] the author relies solely on the rescaling to pC for which precise data is available from the NA49 experiment [122]. We will adopt this procedure and in Chapter 4 and, furthermore, include the first-ever measurement in the pHe channel by LHCb to cross check our approach.

2.5.4 The energy-differential antiproton production cross section

There are mainly two different methods to obtain the energy-differential antiproton production cross section. The first method exploits analytic parametrizations of the Lorentz invariant cross section, Eq. (2.42). The analytic parametrizations are fitted to various data sets of antiproton production cross sections in proton-proton, proton-nucleus, and nucleus-nucleus collisions. The energy-differential cross section is derived as described in the previous paragraph. Historically, this approach was introduced by the Tan& Ng [123] in 1983 and since then continuously improved by various groups [116, 117, 119, 121].[6] The two latest parametrizations were stimulated by the very precise new measurements of the antiproton production cross sections in the pp channel by the NA49 experiment at CERN [124]. Apart from the NA49 data, the parametrizations are adjusted to several data sets from fixed-target and collider experiments over a large range of CM energies spanning from about 6 GeV up to 2.7 TeV, which allows a robust prediction of the antiproton source term from 1 GeV up to the TeV range. In Chapter 4 we will provide an update of the two latest parametrizations including new cross section measurements by NA61 [125] in the pp channel and LHCb [120] in the pHe channel.

The second option is to tune Monte Carlo (MC) event generators to the available cross section data, and then to extract the energy-differential cross section directly from running the MC. This was, for example, performed with DTUNUC [126,127] which was designed specifically to take effects at low energies into account and provided the cross sections for the pp, pHe, Hep, and HeHe. More recently Kachelriess *et al.* [128,129] (hereafter KMO) exploited the MC generators EPOS-LHC and QGSJET-II-04 to obtain the cross sections for all pp, p-nucleus (pA), and nucleus-nucleus (AA) channels. These MC generators were originally developed for very high energy interaction as, for example, occurring in CR air showers or at the LHC at CERN. Therefore, the authors specifically trained their MC to describe also the data of the NA49 experiment which are taken at a CM energy of 17.3 GeV (158 GeV proton energy in the ISM frame). This allows robust predictions of the antiproton source term down to an energy of approximately $T_{\bar{p}} \sim 10$ GeV. However, there is a clear disadvantage with respect to the analytic parametrizations which can be trusted down to the level of 1 GeV.

In Fig. 2.10 we present a comparison of the different methods and parametrizations to obtain the energy-differential cross section. The three panels show that there are significant deviations between the various cross section determinations. While at intermediate projectile energies of $T_p \sim 100$ GeV and antiproton energies of $T_{\bar{p}} \sim 20$ GeV the cross sections agree reasonably at the level of 30% to 50%, the deviation for $T_p \geq 1$ TeV increase above a factor of 2. Furthermore, there is a significant deviation of the cross sections at low antiproton energies, $T_{\bar{p}} \leq 1$ GeV, where the deviation can increase to a factor of a few. Finally, we observe that the KMO cross section at low $T_{\bar{p}}$ always

[6] Note that [119] is an update of [116].

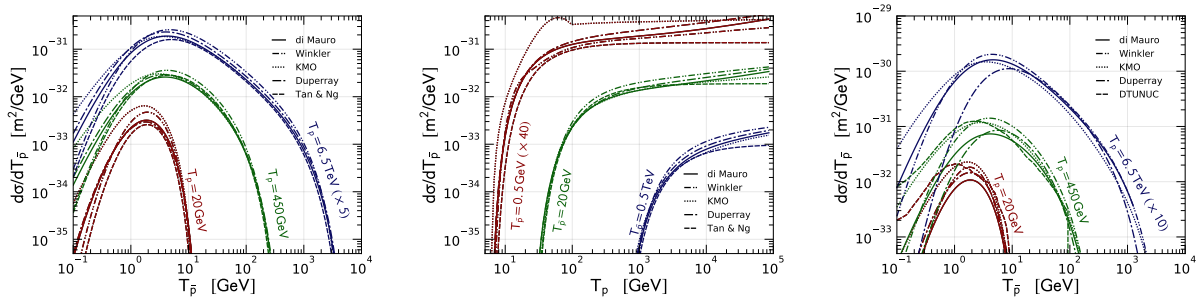

Figure 2.10: Comparison of the energy-differential antiproton production cross section of different analytic parametrizations from di Mauro [117], Winkler [116], Duperray [121], and Tan&Ng [123] with the MC approach of KMO [128]. The left panel shows the cross section in the pp channel as function of $T_{\bar{p}}$ at three fixed T_p of 20 GeV, 450 GeV, and 6.5 TeV, while the central panel shows the same cross section as function of T_p at fixed $T_{\bar{p}}$ of 0.5 GeV, 20 GeV and 0.5 TeV. The right panel is equivalent to the left panel, but for the pHe channel. The figures are taken from [7].

overpredicts the antiproton production cross section with respect to the analytic parametrizations and we remind again that at this energies the MCs are not tuned to data. Therefore, the analytic approaches are more trusted.

2.5.5 Feynman and radial scaling invariance of the cross section

By radial scaling we mean that the inclusive cross section to produce a single particle a becomes independent of $\sqrt{s}$ at large $\sqrt{s}$ if expressed as function of $x_R = E_a^*/E_a^{*,\max}$ and p_T, more specifically:

$$\sigma_{\text{inv}}(\sqrt{s}, x_{\text{R}}, p_{\text{T}}) \xrightarrow[s\to\infty]{} \sigma_{\text{inv}}(x_{\text{R}}, p_{\text{T}}). \tag{2.49}$$

This hypothesis was studied in detail in [130] for different inclusive cross section in proton-proton collisions to pion, kaons, protons, and antiprotons. They concluded that radial scaling works well above $\sqrt{s} \gtrsim 10$ GeV. Furthermore, they compare radial scaling to the previously suggested Feynman scaling [131], namely:

$$\sigma_{\text{inv}}(\sqrt{s}, x_f, p_{\text{T}}) \xrightarrow[s\to\infty]{} \sigma_{\text{inv}}(x_f, p_{\text{T}}). \tag{2.50}$$

As discussed in [130], at high $\sqrt{s}$ Feynman scaling and radial scaling coincide, but radial scaling is valid down to lower energies. Therefore, radial scaling is commonly used to parametrize the antiproton production cross sections since it was introduced by Tan&Ng [123].

However, in the latest update of [119] it was shown that the scaling invariance of the antiproton production cross section is broken above $\sqrt{s} \gtrsim 50$ GeV for two reasons: Firstly, the total inelastic cross section in pp keeps rising and does not reach a plateau at high $\sqrt{s}$, in contrast to Feynman's assumption. Secondly, above $\sqrt{s} \gtrsim 50$ GeV the p_T-distribution of the cross section becomes softer as demonstrated in Fig. 2.11. Only by modeling both of these effects the total antiproton cross section is correctly reproduced.

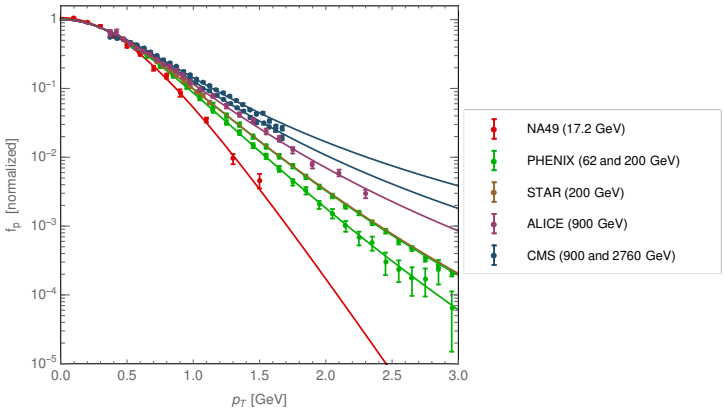

Figure 2.11: Transverse momentum distribution of the prompt antiproton production cross section at different CM energies. The distribution continuously softens with increasing $\sqrt{s}$. The figure is taken from [119].

2.5.6 Signatures of dark matter in cosmic-ray antiprotons

Next to the secondary component there might be a primary contribution of CR antiprotons due to the annihilation or decay of a DM particle into SM particles. As discussed in Sec. 1.1 our Galaxy is surrounded by a DM halo which extends significantly beyond the diffusion volume of CR. If the annihilation or decay occurs inside the diffusion halo we might expect a antiproton signature. In principle, one expects a contribution also in all other species but the signal-to-background ratio for antiprotons is superior compared to most other species. The reason is simple: while primaries, as for example, protons are accelerated and injected by astrophysical sources like SNR, antiprotons are secondary and dominantly produced by interaction of protons with the ISM. The ratio of antiprotons-to-protons in CRs is about 10^{-4}. So, if protons and antiprotons are produced by DM annihilation or decay in similar amounts the signal in protons would be suppressed with respect to antiprotons at the level of 10^{-4}.
The search for DM with CR belongs into the branch of indirect detection. In the case of annihilating DM particles, the source term of antiprotons is given by:

$$q_{\bar{p}}^{(\mathrm{DM})}(\boldsymbol{x}, R) = \frac{1}{2}\left(\frac{\rho(\boldsymbol{x})}{m_{\mathrm{DM}}}\right)^2 \sum_f \langle\sigma v\rangle_f \frac{\mathrm{d}N_{\bar{p}}^f}{\mathrm{d}R}. \tag{2.51}$$

Here m_{DM} and $\rho(\boldsymbol{x})$ are DM mass and energy-density, respectively. The sum runs over all possible DM annihilations channels into SM final states. Then $\langle\sigma v\rangle_f$ denotes the corresponding velocity averaged annihilation cross section and $\mathrm{d}N_{\bar{p}}^f/\mathrm{d}R$ is the rigidity spectrum for a single DM in the channel f. We note that the factor $1/2$ corresponds to Majorana fermion DM. In case of Dirac fermions it would be replaced by $1/4$. Furthermore, the rigidity spectra $\mathrm{d}N_{\bar{p}}^f/\mathrm{d}T$, depend on the DM mass as well as on the details of kinematics, fragmentation and decay of the annihilation products.

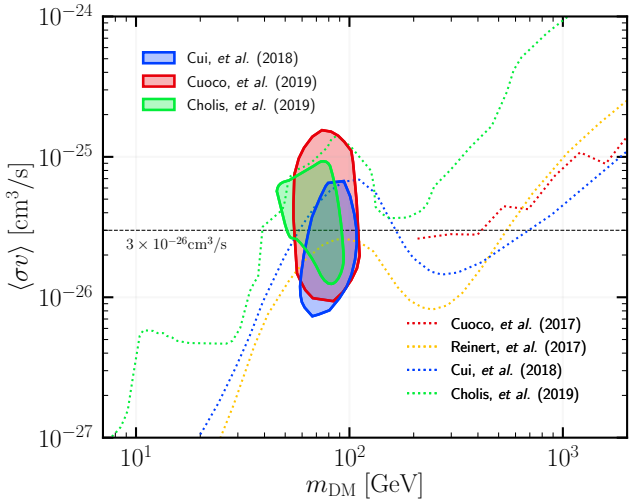

Figure 2.12: Comparison of a hint for DM annihilation into a pair of $b\bar{b}$ quarks from different analysis [2,134,135] and limits on the DM annihilation cross section [5,136]. For more details refer to the text. This figure is taken from [137].

The challenge in CRs is that it is not possible to distinguish individual sources. Due to propagation of CRs in the turbulent magnetic fields of the Galaxy all directional information is lost. Hence, the local flux observed at Earth is almost isotropic. Thus, searching for DM comes back to the investigation of specific features in the energy spectrum. Moreover, due to diffusion CRs mostly probe the local DM density. They are not sensitive to the shape of the DM density profile at the Galactic Center (or other DM subhalos) [5,132,133] which can be an advantage compared to the indirect search of DM with gamma-rays. While the pointing towards expected high DM densities with gamma-rays increases the signal-to-background ratio also the model dependence on the DM density profile at the halo center becomes significant. On the other hand, the size of potential DM signals strongly depend on the half-height of the diffusion halo, L. In this sense, the search for DM with CRs and gamma-rays provides an important complementarity.

Antiprotons have been suggested and used to search and constrain DM by several groups in the past [133,138–150]. Recently, a potential signal of DM was observed in the CR antiproton spectrum measured by AMS-02 [8,134–136,151]. The current situation is summarized in Fig. 2.12. The best-fit region for the potential DM particle points to a DM mass, $m_{\rm DM}$, around 80 GeV and velocity averaged annihilation cross section, $\langle\sigma v\rangle$, close to the thermal cross section around 3×10^{-26} cm^3/s, if we assume that two DM particles annihilate into a pair of $b\bar{b}$ quarks. The contours in Fig. 2.12 display the 2σ best fit region[7] in the plane of DM mass and annihilation cross section for three

[7] We note that the contour of Cui, *et al.* (2018) [134] refers to a 95% Confidence Level (C.L.), which is approximately 2σ.

recent analysis [2, 134, 135]. Furthermore, we display the DM limits for each analysis framework.[8] Additionally, we display the limit on DM annihilation from Reinert, *et al.* (2017) [136]. This analysis does not find a significant hint for a DM annihilation but the limit around $m_{\rm DM} \sim 80$ GeV increases significantly, such that all contours lie (at least partly) below the limit. The contours and limits have been rescaled to a local DM density of $\rho_{\rm sun} = 0.3$ GeV/cm^3. Finally, we note that the comparison should still be viewed as approximate since the different analyses adopt slightly different values for the halo half-height, L, which affects the value of $\langle \sigma v \rangle$. In [135] the halo height is fixed to three different values between 3 kpc and 6 kpc, while [134] and [2] marginalize over L in a fit. For example, in [2] L can vary freely in the range from 2 kpc to 10 kpc, while in [136] L is fixed to 4.1 kpc. A recent analysis [152] finds that antiprotons are consistent with a pure secondary origin based on the argument of goodness of fit.[9] We note however the difficulty to correctly estimate the correlated uncertainties involved and the fact that the analysis does not explicitly insert a DM signal to investigate a potential improvement between prediction and data. We will discuss the potential DM signal and important systematic uncertainties in more details in chapter 5.

2.6 Antideuteron and antihelium in cosmic rays

In principle, one we might observe also charged antinuclei, like antideuteron or antihelium, in CRs. However, no antinuclei have been detected so far. We do not expect primary astrophysical sources to produce antinuclei. At the same time, the expected secondary signals, namely, due to production by the interaction of CR proton and helium with the ISM, are below current experimental sensitivities. Next to this secondary component we will discuss potential DM signals. These are very interesting for antinuclei. At low energies, we expect a very good DM signal to secondary background ratio for antinuclei, much better than for antiprotons. Therefore, the potential observation of a low-energy antinucleus is often considered as *smoking gun* to find DM signals in CRs.

The coalescence model for the nucleon fusion was first applied to antimatter production in our Galaxy by [153]. Shortly later the potential to probe DM with low-energy antideuteron was suggested in [154]. Since then antideuteron and antihelium have been studied extensively in literature and the production mechanisms for DM signal as well as for the secondary background was continuously refined in [155–164]. The propagation of antideuteron in our Galaxy was carefully studied in [165]. The current most constraining limits for the flux of antideuteron in CRs are provided by BESS experiment [166]. The upper limit on the flux is at 1.9×10^{-4} m^{-2} s^{-1} sr^{-1} (GeV/n)$^{-1}$ at low energies around 1 GeV/n. The limits on the antihelium-to-helium flux ratio are at 6.9×10^{-8} between 1 and 14 GV rigidity [167]. This situation will change in the next years. The AMS-02 detector born on the ISS is expected to improve significantly the limits for antideuteron and antihelium. However, we stress that the analysis of AMS-02 data is very challenging since an extremely good background suppression is required. A dedicated experiment to search for low-energy antideuteron, the GAPS experiment [168–170], is expected to perform the first balloon flights in Antarctica in the season 2021/2022. The GAPS experiment is based on a unique detection technique for antineuclei

[8] The DM limit from Cuoco, *et al.* (2017) is taken from Ref [5].
[9] The goodness of fit in this analysis refers to a chi-squared test.

which relies on the intermediate formation of an exotic atom. The de-excitation and subsequent annihilation of the exotic atom inside the detector provides a very characteristic signal.

2.6.1 The coalescence model for antinuclei

In the following, we review the analytic coalescence model which in the context of CRs was first discussed in [153]. The coalescence model is the same for secondary production and production from DM annihilation or decay. The formalism and all equations shown in this paragraph apply to the most simple case, *i.e.* antideuteron production. We will state explicit formulas for antihelium in the next paragraphs. Our general picture for the production of antideuteron is that we produce one pair of $p\bar{p}$ and a second pair of $n\bar{n}$. In the analytic model, we assume that these pairs are produced independently from each other. After production the $\bar{p}$ and $\bar{n}$ can coalesce to $\bar{D}$ if they have very similar momenta.

Let us introduce a short notation for the Lorentz invariant multiplicity:

$$E\frac{\mathrm{d}^3N}{\mathrm{d}k^3}(\sqrt{s},\vec{k}) = f(\sqrt{s},\vec{k}). \tag{2.52}$$

At this moment, this notation might apply for the production of either $\bar{p}$, $\bar{n}$, or $\bar{D}$. In any case, E denotes the total energy of the produced particle and $\vec{k}$ its three-momentum. Furthermore, $\sqrt{s}$ is the CM of the process. Hence, $f(\sqrt{s},\vec{k})d^3k$ indicates the number of particles produced in a single interaction. Then, the number of antideuterons produced in this interaction will be given by the product of the antiproton and the antineutron production cross section convoluted with a factor $\mathcal{C}(\vec{k}_{\bar{p}},\vec{k}_{\bar{n}})$, describing the coalescence probability:

$$f_{\bar{D}}(\sqrt{s},\vec{k}_{\bar{D}})\mathrm{d}k^3_{\bar{D}} = \int \mathrm{d}k^3_{\bar{p}}\mathrm{d}k^3_{\bar{n}}\ \mathcal{C}(\vec{k}_{\bar{p}},\vec{k}_{\bar{n}}) f_{\bar{p}}(\sqrt{s},\vec{k}_{\bar{n}}) f_{\bar{n}}(\sqrt{s},\vec{k}_{\bar{n}}). \tag{2.53}$$

Here the integration has to be carried out such that the differential $\mathrm{d}k^3_{\bar{D}}$ remains on the right-hand side of Eq. (2.53). We will specify what this means in a moment. Momentum conservation during coalescence dictates $\vec{k}_{\bar{D}} = \vec{k}_{\bar{p}} + \vec{k}_{\bar{n}}$. The appropriate linearly independent variable is the difference of proton and neutron momentum, $\vec{k}_{\bar{p}} - \vec{k}_{\bar{n}} = \vec{\Delta}$. Note that the functional determinant of the transformation $(\vec{k}_{\bar{p}},\vec{k}_{\bar{n}}) \to (\vec{k}_{\bar{D}},\vec{\Delta})$ is equal to $1/8$.[10] Hence, we rewrite $\mathrm{d}k^3_{\bar{p}}\mathrm{d}k^3_{\bar{n}} = 1/8\,\mathrm{d}k^3_{\bar{D}}\mathrm{d}\Delta^3$. Now, it is clear that the integral in Eq. (2.53) is meant to be taken over $\mathrm{d}\Delta^3$. If we assume that coalescence is homogeneous, we obtain

$$f_{\bar{D}}(\sqrt{s},\vec{k}_{\bar{D}})\mathrm{d}k^3_{\bar{D}} = \mathrm{d}k^3_{\bar{D}} \int \mathrm{d}\Delta^3\, \frac{\mathcal{C}(\vec{\Delta})}{8}\, f_{\bar{p}}(\sqrt{s},\vec{k}_{\bar{D}}/2+\vec{\Delta})\, f_{\bar{n}}(\sqrt{s},\vec{k}_{\bar{D}}/2-\vec{\Delta}). \tag{2.54}$$

We remind that coalescence takes places if $\vec{k}_{\bar{p}} \approx \vec{k}_{\bar{n}}$. So, the coalescence factor, $\mathcal{C}(\vec{\Delta})$, has to be 0 for large $|\vec{\Delta}|$. In practice, we can approximate $|\vec{\Delta}| \ll |\vec{k}_{\bar{D}}|$ which leads to

$$E_{\bar{D}}\, f_{\bar{D}}(\sqrt{s},\vec{k}_{\bar{D}}) = \left\{ \int \mathrm{d}\Delta^3\ \frac{E_{\bar{D}}}{E_{\bar{p}}E_{\bar{n}}}\frac{\mathcal{C}(\vec{\Delta})}{8} \right\} E_{\bar{p}}\, f_{\bar{p}}(\sqrt{s},\vec{k}_{\bar{D}}/2)\ E_{\bar{n}}\, f_{\bar{n}}(\sqrt{s},\vec{k}_{\bar{D}}/2). \tag{2.55}$$

[10] In literature there is a second common definition $\vec{k}_{\bar{p}} - \vec{k}_{\bar{n}} = 2\vec{\Delta}'$. With this definition the functional determinant is equal to 1. We will come back to this at the end of this section.

Note that the term in the curly brackets of Eq. (2.55) is Lorentz invariant, because the left-hand side is Lorentz invariant as well as the term $E_{\bar{p}}\, f_{\bar{p}}\, E_{\bar{n}}\, f_{\bar{n}}$ on the right-hand side. We choose now to calculate this integral in the $\bar{D}$ rest frame. Since $|\vec{\Delta}| \ll m_p \approx m_n$ we can assume $E_{\bar{p}} \approx m_p$ and $E_{\bar{n}} \approx m_n$. By definition we can use $E_{\bar{D}} = m_D$. In the rest frame of $\bar{D}$ we expect the coalescence factor to be isotropic, $\mathcal{C}(\vec{\Delta}) = \mathcal{C}(|\vec{\Delta}|)$. If, finally, we approximate this coalescence factor with a step function, which is equal to 1 for $|\vec{\Delta}| < p_{\mathcal{C}}$ and 0 otherwise, we obtain:

$$f_{\bar{D}} = \left\{ \frac{m_{\bar{D}}}{m_{\bar{p}} m_{\bar{n}}} \frac{4\pi}{3} \frac{p_{\mathcal{C}}^3}{8} \right\} f_{\bar{p}}\, f_{\bar{n}}. \tag{2.56}$$

The parameter $p_{\mathcal{C}}$ is commonly called coalescence momentum. Its physical interpretation is the following: if the $\bar{p}$ and the $\bar{n}$ are produced with a momentum difference smaller than $p_{\mathcal{C}}$ they always coalesce and form $\bar{D}$, while for a momentum difference larger than $p_{\mathcal{C}}$ the two antinucelons never coalesce. Finally, we address one subtlety which concerns the conservation of energy. If the $p\bar{p}$ pair is produced from a CM energy of $\sqrt{s}$ the available energy to produce the $n\bar{n}$ pair has to be reduced, and *vice versa*. We can take this into account at a superficial level by assuming that the two pairs are created after each other. Explicitly, we define

$$f_{\bar{p}}\, f_{\bar{n}} = \frac{1}{2} \left(f_{\bar{p}}(\sqrt{s}, \vec{k}_{\bar{D}}/2)\; f_{\bar{n}}(\sqrt{s} - 2E_{\bar{p}}, \vec{k}_{\bar{D}}/2) + (\bar{p} \leftrightarrow \bar{n}) \right) \tag{2.57}$$

We note that Eq. (2.57) is symmetric under the exchange of $\bar{p}$ and $\bar{n}$. The value for the coalescence momentum has to be derived from measurements. Typical values of $p_{\mathcal{C}}$ in the analytic coalescence model vary between 160 MeV and 250 MeV.

2.6.2 Secondary production of antinuclei

We now adapt the coalescence model discussed in the previous section in order to give explicit equations for the secondary production of antinuclei. We start with the most simple case of antideuteron production in the interaction of a CR proton with a proton of the ISM. The Lorentz-invariant cross section is linked to the multiplicity defined in Eq. (2.52) by

$$E \frac{\mathrm{d}^3\sigma}{\mathrm{d}k^3}(\sqrt{s}, \vec{k}) = \sigma_{\mathrm{tot}} f(\sqrt{s}, \vec{k}). \tag{2.58}$$

If we insert Eq. (2.58) into Eq. (2.56) we obtain:

$$E_{\bar{D}} \frac{\mathrm{d}^3\sigma_{\bar{D}}}{\mathrm{d}k_{\bar{D}}^3} = \frac{1}{\sigma_{\mathrm{tot}}} \left\{ \frac{m_{\bar{D}}}{m_{\bar{p}} m_{\bar{n}}} \frac{4\pi}{3} \frac{p_{\mathcal{C}}^3}{8} \right\} E_{\bar{p}} \frac{\mathrm{d}^3\sigma_{\bar{p}}}{\mathrm{d}k_{\bar{p}}^3} E_{\bar{n}} \frac{\mathrm{d}^3\sigma_{\bar{n}}}{\mathrm{d}k_{\bar{n}}^3}. \tag{2.59}$$

Above we have considered only the reaction $p + p \to \bar{D} + X$. If we replace either the projectile or the target by a heavier nucleus the antiproton and the antineutron productions are enhanced, both roughly by a factor $A^{0.7}$. However, if the antineutron and the antiproton are be produced from different nucleons inside heavier projectile or target, they would be too far separated to coalesce.

Therefore, it is reasonable to assume that the production of antideuteron is enhanced only by a single factor of approximately $A^{0.7}$. Actually, this result is also obtained by simply replacing all pp cross section in Eq. (2.59) with pA cross section. We note the factor $1/\sigma_{\rm tot}$ which rescales approximately with $A^{-0.7}$. In Fig. 2.13 we show the $\bar{D}$ source term from the most important CR + ISM $\rightarrow \bar{D} + X$ channels. The dominant channel is the pp channel, but also the pHe and Hep channels are important. The ranking is equivalent to the antiproton production discussed in the previous section.

Furthermore, we might produce secondary antideuterons from CR antiprotons. If we replace the CR projectile by an antiproton, we have to replace all $p+p \rightarrow \bar{p}+X$ cross sections by $\bar{p}+p \rightarrow \bar{p}+X$. Due to the lack of measurements, the latter is often approximated with the $p + p \rightarrow p + X$ cross section. In general, the antiproton channel is suppressed by the small $\bar{p}/p$ ratio in CRs which is of the order of 10^{-4}. Nonetheless, this channel is important at low energies because the pp and pA channels are kinematically suppressed. Figure 2.13 shows that the antideuteron production in the antiproton channel is important below ~ 1 GeV/n, while it is negligible above a few GeV/n.

The generalization of the coalescence model to heavier antinuclei is straight forward. We only state the explicit result for antihelium, $^3\overline{\rm He}$, (or equivalently tritium) which is the next-heavier

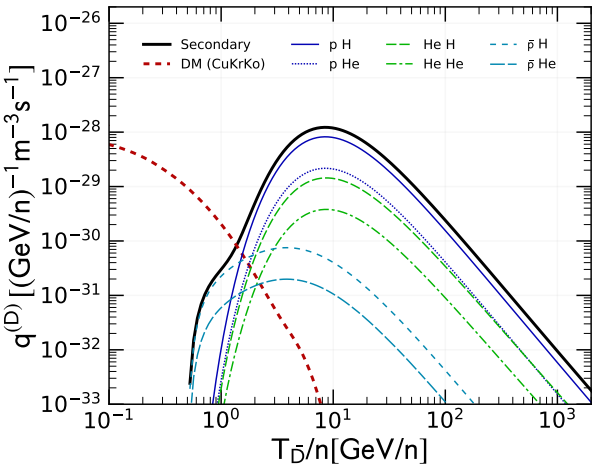

Figure 2.13: Source term for antideuterons as function of kinetic energy per nucleon derived in the analytic coalescence model. We show separately the contribution from different production channels. The figure is taken from [4].

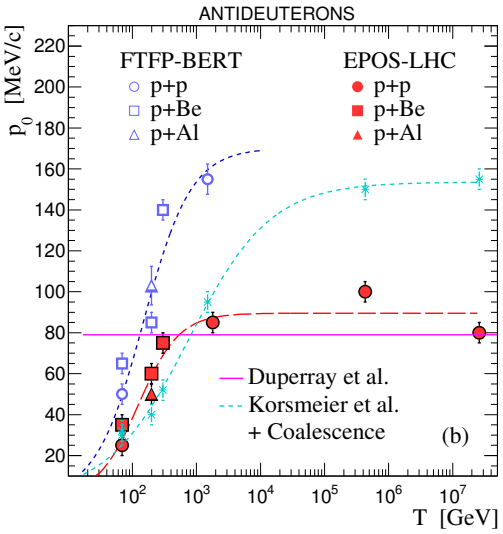

Figure 2.14: Potential energy dependence of the coalescence momentum (p_0), which is obtained from the comparison of two MC-based coalescence models and one analytic model with $\bar{D}$ production data at different energies; T is the kinetic energy of the proton projectile in a fixed-target experiment. The figure is taken from [171].

antinucleus:

$$E_{\overline{\mathrm{He}}}\frac{\mathrm{d}^3\sigma_{\overline{\mathrm{He}}}}{\mathrm{d}k^3_{\overline{\mathrm{He}}}} = \frac{m_{\mathrm{He}}}{m_{\bar{p}}^2 m_n}\left(\frac{1}{\sigma_{\mathrm{tot}}}\frac{4\pi}{3}\frac{p_C^3}{8}\right)^2 E_{\bar{p}}\frac{\mathrm{d}^3\sigma_{\bar{p}}}{\mathrm{d}k^3_{\bar{p}}}\, E_{\bar{p}}\frac{\mathrm{d}^3\sigma_{\bar{p}}}{\mathrm{d}k^3_{\bar{p}}}\, E_{\bar{n}}\frac{\mathrm{d}^3\sigma_{\bar{n}}}{\mathrm{d}k^3_{\bar{n}}}, \tag{2.60}$$

where antiproton and antineutron cross sections are evaluated at $\vec{k}_{\bar{p}} = \vec{k}_{\bar{n}} = \vec{k}_{\overline{\mathrm{He}}}/3$. The generalization of Eq. (2.57) to ${}^3\overline{\mathrm{He}}$ is given by:

$$\begin{aligned}\frac{\mathrm{d}^3\sigma_{\bar{p}}}{\mathrm{d}k^3_{\bar{p}}}\frac{\mathrm{d}^3\sigma_{\bar{p}}}{\mathrm{d}k^3_{\bar{p}}}\frac{\mathrm{d}^3\sigma_{\bar{n}}}{\mathrm{d}k^3_{\bar{n}}} &= \frac{1}{3}\Bigg[\frac{\mathrm{d}^3\sigma_{\bar{p}}}{\mathrm{d}k^3_{\bar{p}}}\left(\sqrt{s},\vec{k}_{\bar{p}}\right)\frac{\mathrm{d}^3\sigma_{\bar{n}}}{\mathrm{d}k^3_{\bar{n}}}\left(\sqrt{s}-2E_{\bar{p}},\vec{k}_{\bar{n}}\right)\frac{\mathrm{d}^3\sigma_{\bar{p}}}{\mathrm{d}k^3_{\bar{p}}}\left(\sqrt{s}-2E_{\bar{p}}-2E_{\bar{n}},\vec{k}_{\bar{p}}\right)\\ &\quad + (\bar{p}\leftrightarrow\bar{n}\,\bar{p}) + (\bar{p}\,\bar{n}\leftrightarrow\bar{p})\Bigg].\end{aligned} \tag{2.61}$$

We note that for an arbitrary antinucleus the production cross section scales approximately with coalescence factor

$$B_A = \frac{m_A}{m_p^A}\left(\frac{1}{\sigma_{\mathrm{tot}}}\frac{4\pi}{3}\frac{p_C^3}{8}\right)^{(A-1)}. \tag{2.62}$$

Beside the analytic coalescence model, an alternative approach is discussed in literature, which is based on MC generators. Typically, these MC generator do not directly provide the yield of antideuterons. Instead the coalescence has to be implemented as an afterburner to the MC. In more details, this means that one checks on an event-by-event basis whether an antiproton and antineutron are close enough in momentum space. Again, if the difference is less than a threshold coalescence momentum an antideuteron is formed. The advantage of a MC coalescence model is that correlations between antiproton and antineutron production are taken into account. We note, however, that the standard MC generators are not tuned to correctly reproduce these correlation and, therefore, might be wrong. Indeed, different MC generators can produce different results. In any case, the coalescence momentum in MC-based approach has to be tuned to data. It is not a first-principle method. We stress that a certain coalescence momentum should not be taken from one (for example the analytic) and then be used in another (for example MC-based) model. Recently, the coalescence momentum has been tuned to a large set of pp and pA data [171]. The authors find that the coalescence momentum is energy-dependent, *c.f.* Fig. 2.14. They explore different MC generators and find a good agreement between data and MC for EPOS-LHC and FTFP-BERT. Furthermore, they explore one analytic coalescence model. We note, however, that the two MC generators are tuned to higher energies than those relevant for CRs. Furthermore, in the analytic model the CM correction of Eq. (2.57) is not applied in the analysis of [171]. Neglecting this correction could explain (a part of) the energy-dependence seen in Fig. 2.14.

Finally, we remind that definition of $\vec{\Delta}$ is a pure convention. If instead we would define $2\,\vec{\Delta}' = \vec{k}_{\bar{p}} - \vec{k}_{\bar{n}}$ the factor $1/8$ would disappear in Eq. (2.59). Since, however, the physical result must be independent of our convention we have to redefine also the coalescence momentum accordingly, $p'_C = p_C/2$. In literature, both conventions are used.

2.6.3 Antinuclei from dark matter annihilation

The antideuteron yield from DM decay or annihilation is expected to peak at low energies, where the secondary production of antideuteron is kinematically forbidden. In order to produce an antideuteron in a pp collision we have to create a $p\bar{p}$ and a $n\bar{n}$ pair. The minimal requirement for the CM energy is therefore $\sqrt{s} \geq 6m_p$ and subsequently $E = (s - 2m_p^2)/(2m_p) \geq 17m_p$ in the fixed-target frame. Note that this threshold is much larger compared to the antiproton production threshold at $E \geq 7m_p$. On the other hand, DM annihilation or decay is expected to take place at rest. Hence, low energies are not suppressed.

The source term of antideuterons from annihilating DM particles is given by Eq. (2.51) if we replace the energy spectrum $\mathrm{d}N_{\bar{p}}^f/\mathrm{d}R$ by $\mathrm{d}N_{\bar{D}}^f/\mathrm{d}R$. As usual, $\mathrm{d}N_i^f/\mathrm{d}R$ and $\mathrm{d}N_i^f/\mathrm{d}E$ are related by the factor $\mathrm{d}R/\mathrm{d}E = 1/|Z|\, E/p$. We can adapt and rephrase the formalism of the previous paragraph to obtain this energy spectrum if we rewrite

$$\frac{\mathrm{d}^3N}{\mathrm{d}k^3} = \frac{1}{4\pi k^2}\frac{\mathrm{d}E}{\mathrm{d}k}\frac{\mathrm{d}N}{\mathrm{d}E} = \frac{1}{4\pi kE}\frac{\mathrm{d}N}{\mathrm{d}E}. \tag{2.63}$$

Inserting this relation into Eq. (2.59) reveals

$$\frac{\mathrm{d}N_{\bar{D}}}{\mathrm{d}E_{\bar{D}}} = \frac{m_D}{m_p m_n}\frac{4}{3}\frac{p_C^3}{8k_{\bar{D}}}\frac{\mathrm{d}N_{\bar{p}}}{dE_{\bar{p}}}\frac{\mathrm{d}N_{\bar{n}}}{dE_{\bar{n}}}. \tag{2.64}$$

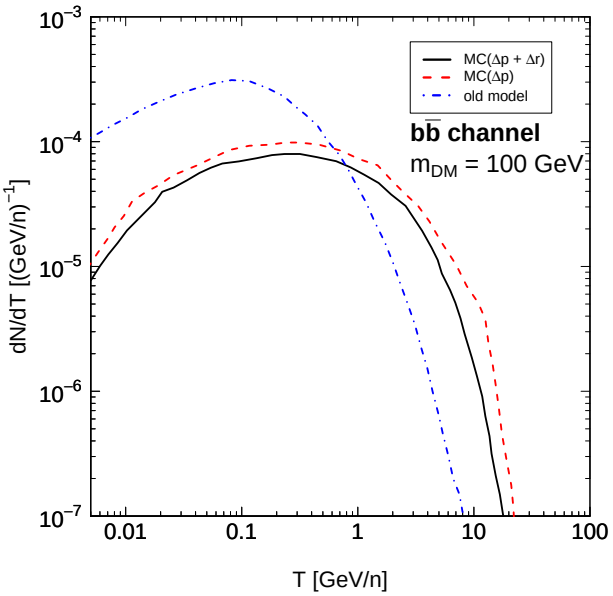

Figure 2.15: Comparison of the DM energy spectrum derived from the analytic coalescence model (blue dashed-dotted line) with two MC-based approaches (solid black and red dashed lines). In this example, the energy spectrum, which is proportional the source term, is derived for DM annihilation with $m_{\mathrm{DM}} = 100$ GeV into a pair of $b\bar{b}$-quarks. The figure is taken from [159].

The equivalent result for antihelium three is given by:

$$\frac{\mathrm{d}N_{\overline{\mathrm{He}}}}{\mathrm{d}E_{\overline{\mathrm{He}}}} = \frac{m_{\mathrm{He}}}{m_{\bar{p}}^2 m_n} 3 \left(\frac{p_C^3}{8 k_{\overline{\mathrm{He}}}} \right)^2 \frac{\mathrm{d}N_{\bar{p}}}{\mathrm{d}E_{\bar{p}}} \frac{\mathrm{d}N_{\bar{p}}}{\mathrm{d}E_{\bar{p}}} \frac{\mathrm{d}N_{\bar{n}}}{\mathrm{d}E_{\bar{n}}}. \tag{2.65}$$

Figure 2.13 displays the DM source term for a typical WIMP annihilation. More precisely, in this case the DM source term corresponds to the DM hint found in CR antiprotons. We use a DM mass of 71 GeV and a velocity averaged annihilation cross section of $\langle \sigma v \rangle = 2.6^{-26}$ cm^3/s. Note that propagation will enhance the DM term with respect to the secondary term.

Finally, we want to elaborate again a bit more on the difference between the analytic coalescence model and a MC-based approaches. The analytic approximation is expected to work reasonably well whenever the antiproton and antineutron production is roughly spherical. But this is not the case for DM annihilation or decay in all SM final states. For example, when DM annihilation produces a pair of Z or W bosons the antiproton and antineutron production will be boosted along the direction of the bosons and the spherical approximation, applied in Eq. 2.63, does not work well. On the other hand, the spherical approximation is expected to work reasonably for the annihilation into light quarks or b-quarks. In the context of DM, the analytic and MC-based approaches have been compared extensively in [159]. An example is shown in Fig. 2.15. The energy spectra can have a very different shape. We note, however, that the $\bar{D}$ yield between 0.1 GeV/n and 1 GeV/n, where the experiment GAPS will conduct measurements, is very similar. This similarity is expected since both coalescence models are tuned to data from the ALEPH experiment, which measured antideuteron production from the Z-boson decay [172] with momenta between 0.62 and 1.03 GeV, *i.e.* a very similar energy range. Finally, we remark that the results derived from MC generators suffer from uncertainties. For example, the DM energy spectra derived with Pythia and Herwig can give results [173] different up to a factor of a few.

2.7 Solar Modulation

At low energies of $E \lesssim 50$ GeV CRs are deflected and decelerated by solar modulation. The effect on the CR spectrum strongly depends on energy. While the CR fluxes at low energies are strongly affected by solar modulation the effect becomes smaller with increasing energy. Furthermore, the strength of solar modulation depends on the activity of the sun which which undergoes a 11-year cycle. Furthermore, at each peak of the solar cycle the magnetic field of the sun reverses its direction. Solar modulation can be described by a Fokker-Planck equation which is adjusted to the solar environment and solar magnetic field. These equations are typically solved by numerical codes [174–176]. Recent progress in the better understanding of solar modulation is achieved by two experimental observations. First, the VOYAGER probe has left the heliosphere and measured the Local InterStellar (LIS) of various CR species at low energies. The combination of this data with the modulated data taken at the Top Of the Atmosphere (TOA) by AMS-02 and PAMELA strongly constrains the properties of solar modulation. Secondly, the measurement of time-dependent CR fluxes released by PAMELA [177, 178] and recently also by AMS-02 [179, 180]. In particular, we remark that these observations revealed a charge-sign dependence of the solar modulation.

Despite of the success of numerical codes to describe solar modulation, a common approach when studying Galactic CR is to use the so-called force-field approximation [181]. In this approximation, one assumes that the propagation of CRs in the heliosphere is dominated by diffusion and solar winds. Under the further assumption of spherical symmetry and neglecting adiabatic energy losses, one obtains the steady state solution of the Fokker-Planck equation:

$$E = E_{\rm LIS} - |z|e\varphi \tag{2.66}$$

$$\phi_E(E) = \frac{E^2 - m^2}{E_{\rm LIS}^2 - m^2}\phi_{E,\rm LIS}(E_{\rm LIS}), \tag{2.67}$$

Here z is the charge number,[11] e the elementary charge, and m the mass of the CR. The force-field approximation describes solar modulation by a single effective parameter φ, commonly called Fisk potential or solar modulation potential. Since solar modulation is time-dependent we expect that φ is a function of time. Then, the modulation potential can be approximately derived from the anticorrelation between the solar activity and the neutron flux at Earth [182, 183]. Nonetheless, this procedure is affected by large systematic uncertainties, in particular, originating from different assumptions on the LIS spectra of CRs.

Recently, also semi-analytical models are proposed to, on the one hand, capture more details of the solar environment achieving a physically motivated and better description of solar modulation and, on the other hand, still profit from fast evaluation which are required in global fits in large parameter scans [184].

[11] In this thesis, we focus on nuclei and, therefore, typically do not distinguish between charge number z and atomic number Z.

Chapter 3

Astroparticle physics of gamma rays

3.1 Origin of gamma rays

Gamma rays up to an energy of about 1 TeV are precisely measured by satellite-based experiments [185–188]. The Fermi-LAT [188] experiment provides the most recent and precise measurement. It has been taking data for more than 10 years and covers the entire sky. At higher energies up to ~ 100 TeV, the gamma-ray measurements can be complemented with ground-based observations from Cherenkov telescopes [189–191]. The observed gamma-ray emission can be explained by the sum of (i) Galactic diffuse emission, (ii) Galactic and extragalactic resolved (mostly point-like) sources, and (iii) the Unresolved Gamma-Ray Background (UGRB), which remains after subtracting (i) and (ii) from the total gamma-ray emission.[1] The Galactic diffuse emission of gamma rays is caused by the interaction of CRs with the interstellar gas and radiation fields. The dominant production mechanisms of the diffuse emission are the decay of π^0 mesons and bremsstrahlung [192]. Furthermore, various individual astrophysical objects are able to produce gamma rays. They are detected as (mostly) point-like sources. The Fermi-LAT experiment has detected a total number of 5065 sources in an energy range between 50 MeV and 1 TeV. They are listed in the most recent Fourth Fermi-LAT Catalog (4FGL) catalog which is based on eight years of data and contains all sources detected at a C.L. above 4σ [193]. The most numerous Galactic point sources are Pulsars and SNRs, while blazars (see Sec. 3.3 for more details) comprise the largest population of resolved extragalactic sources. For convenience, we define the Extragalactic Gamma-ray Background (EGB), which includes all extragalactic point sources and the UGRB. Next to blazars, the Fermi-LAT has detected Misaligned Active Galactic Nucleus (mAGN), radio galaxies, and Star-Forming Galaxy (SFG)s [193, 194]. In particular, mAGN and SFG are intrinsically faint but extremely numerous. Observations of these sources at other wavelengths and extrapolations to gamma rays suggest that these objects can contribute significantly to the observed UGRB [195–201].

[1] In literature, the UGRB is often called isotropic gamma-ray background (IGRB) because at first glance it is almost isotropic. We instead refer to the UGRB since in Sec. 3.5 we use use the measurement of the angular power spectrum of the UGRB, *i.e.* small anisotropies, to learn more about its properties.

3.2 Dark matter searches with gamma rays

If DM particles can annihilate into SM particles we expect a gamma-ray signal. The signal will strongly depend on the fundamental interaction between the DM particles and the SM. Unless the DM particles directly annihilate or decay into gamma rays, the dominant production arises from pion decays. We note that there can be indirect production of gamma-rays, in particular, for leptonic final states. In this case, gamma-rays might be produced from synchrotron or inverse Compton processes. For these production mechanisms, we expect a broad energy spectrum. On the other hand, if the DM particles directly annihilate or decay into a pair of gamma rays we would try to observe a so-called gamma-ray line, *i.e.* a very strongly peaked (line-like) signatures at $E = m_{\rm DM}$ or $E = m_{\rm DM}/2$ for annihilating or decaying DM, respectively. The strategies to search for DM with gamma rays is different compared to charged CRs: gamma rays point towards the direction of their source since they are not deflected by the Galactic magnetic fields. Therefore, the search can be focussed on selected environments, where a large DM signal is expected. We will briefly discuss two attractive environments in the following paragraphs, first the Galactic center and second the so-called Dwarf Spheroidal Galaxys dSphs.
The expected gamma-ray flux per energy arriving from a specific Point Spread Function (ROI) is given by:

$$\frac{\mathrm{d}S}{\mathrm{d}E} = \frac{1}{2m_{\rm DM}^2} \sum_f \frac{\mathrm{d}N_\gamma^f}{\mathrm{d}E} \frac{\langle \sigma v \rangle_f}{4\pi} \underbrace{\int_{\rm ROI} \mathrm{d}\Omega \int_{\rm l.o.s.} \mathrm{d}s\, \rho^2\left(s, \theta, \phi\right)}_{J\text{-factor}}, \tag{3.1}$$

where $m_{\rm DM}$ is the DM mass, f the SM final state, $\langle \sigma v \rangle$ the velocity averaged annihilation cross section, and ρ is the DM energy density. If s denotes the distance from the observer, the DM density can be expressed as a function of the distance s and two angles, θ and ϕ. The factor $1/2$ corresponds to self-conjugate DM and the factor $1/4\pi$ arises from the distance correction of the flux. Note that the flux seen by an observer at the distance s is given by $S_0/(4\pi s^2)$, if S_0 is the flux emitted by a source. The factor s^2 cancels with the functional determinant, $\mathrm{d}V = s^2\,\mathrm{d}s\mathrm{d}\Omega$. Equation (3.1) is applicable only for Galactic (or close by) sources. For far away, extragalactic sources it is necessary to take redshift effects on the photon energy into account and to consider the absorption of high-energy gamma rays by the Extragalactic Background Light (EBL). The ROI and line of sight (l.o.s.) integrals in Eq. (3.1) is commonly called J-factor. The result of the J-factor can depend significantly on the assumption of the DM density profile of the considered source. A cuspy density profile, like the NFW or the Einasto profile, often gives very different result compared to cored density profiles, like a Burkert profile (see Eqs. 1.4 to 1.3). This is very important for analyses which focus on the central region of a DM halo, as for example Galactic center.

3.2.1 Dwarf spheroidal galaxies

A dSph is a low-luminosity galaxy with an old star population and a small contribution of dust. Typically, it exhibits a spheroidal shape and contains a large DM contribution compared to baryonic matter. This DM contribution can be deduced from the stellar motion in the dSph. Because of the relatively high DM density, dSphs present a good target to search for DM signals in gamma rays.

The non-observation of such signals places strong constraints on DM annihilation [202–205]. The best limits on the DM annihilation cross section are derived from recent Fermi-LAT data by using the methods of template fitting [205]. These are templates for the gamma-ray background derived from the modeling of the Galactic gamma-ray sources, which take into account all the astrophysical processes as for example arising from diffuse emission of pion decays or bremsstrahlung, and a DM template, which is a function of $m_{\rm DM}$, $\langle\sigma v\rangle$, and SM final state. A combined fit of the background nuisance parameters and the two DM parameters for each final state provides the DM limit. In the analysis, the Fermi-LAT collaboration marginalizes the fit-likelihood over the J-factor uncertainty of each dwarf. Along with this analysis [205], the Fermi-LAT collaboration published for each dSph, k, the likelihoods to observe a specific energy flux. In total, the Fermi-LAT collaboration analyzed 45 dSphs (28 kinematically confirmed dwarfs and 17 candidates). These likelihoods as a function energy-flux, $S_{E,i}$, are provided in 24 energy bins, i. The likelihood for each dSph is denoted with $\mathcal{L}^{(k)}(E_i, S_{E,i})$. We can use this likelihoods derive DM limits as follows. The energy-flux in each energy bin is given by:

$$S_{E,i}^{(k)}\Big(m_{\rm DM}, \langle\sigma v\rangle, J^{(k)}\Big) = \int_{E_{{\rm min},i}}^{E_{{\rm max},i}} {\rm d}E\, \frac{{\rm d}S}{{\rm d}E}\Big(E, m_{\rm DM}, \langle\sigma v\rangle, J^{(k)}\Big), \tag{3.2}$$

where ${\rm d}S/{\rm d}E$ is defined in Eq. (3.1). It is common practice to take the uncertainty of the observed J-factors, $J_{\rm obs}^{(k)}$, into account. Following the analysis in [204], we define:

$$\tilde{\mathcal{L}}^{(k)}\Big(m_{\rm DM}, \langle\sigma v\rangle, J^{(k)}\Big) = \mathcal{L}_J\Big(J^{(k)}, J_{\rm obs}^{(k)}, \sigma_{J,k}\Big) \cdot \prod_{i=1}^{24} \mathcal{L}^{(k)}\Big(E_i, S_{E,i}(m_{\rm DM}, \langle\sigma v\rangle, J^{(k)})\Big) \tag{3.3}$$

with

$$\mathcal{L}_J\Big(J^{(k)}, J_{\rm obs}^{(k)}, \sigma_{J,k}\Big) = \frac{1}{\ln(10) J_{\rm obs}^{(k)} \sqrt{2\pi}\sigma_{J,k}} \exp\left[-\frac{1}{2}\left(\frac{\log(J^{(k)}/J_{\rm obs}^{(k)})}{2\sigma_{J,k}}\right)^2\right]. \tag{3.4}$$

Here, $\sigma_{J,k}$ is the normalization uncertainty of the observed J-factor. Finally, the combined likelihood of multiple dSphs is given by the product of the individual likelihoods, where each likelihood is marginalized over the J-factor:

$$\mathcal{L}_{\rm dSphs}\big(m_{\rm DM}, \langle\sigma v\rangle\big) = \prod_k \tilde{\mathcal{L}}^{(k)}\Big(m_{\rm DM}, \langle\sigma v\rangle, J^{(k)}\Big)\Big|_{J^{(k)}=J_{\rm max}^{(k)}}. \tag{3.5}$$

In other words, $J_{\rm max}^{(k)}$ maximizes each individual likelihood $\tilde{\mathcal{L}}^{(k)}$ for fixed $m_{\rm DM}$ and $\langle\sigma v\rangle$. More information about the J-factors is given in [206–208]. In practice, it is sufficient to use the 5–10 dSphs with the largest J-factors to derive the DM limits, since the remaining dwarfs give almost no additional constraining power. We remark that using the published likelihoods provided by the Fermi-LAT collaboration gives only an approximate description of the full likelihood which would be obtained from the template fit as described above. But the approximate method based

on the provided likelihoods was shown empirically to give the same results as those obtained with the full template fit [205]. The analysis by the Fermi-LAT collaboration focuses on a ROIs of $10^\circ \times 10^\circ$ around each dSph. This is large enough to include the entire DM halos around the dSphs. Therefore, the J-factor does not depend much on the adopted DM density profile. We note that, four of the dSphs (Reticulum II, Tucana III, Tucana IV, Indus II) show small excesses at the level of $\sim 2\sigma$ (local). These excesses are compatible with a DM particle annihilating with a thermal cross section [205, 209, 210].
Finally, we note that the DM limits from dSphs are affected by systematic uncertainties. For example, more freedom in the background flux estimation can significantly weaken the DM limits, especially for heavy DM particles [211, 212].

3.2.2 The Galactic center excess

Several groups have reported an excess of the gamma-ray flux from the Galactic center [213–215]. The energy spectrum of the Galactic Center Excess (GCE) peaks at about 2 GeV (in the usual flux times energy squared representation) and quickly drops to 0 below 1 GeV and above a few tens of GeV. Spatially the GCE coincides with the direction of the Galactic center and follows a steep radial profile below a few degrees. The signal extends to at least 10° away from the Galactic center and is approximately circular. The analyses to detect the GCE typically rely on the method of template fitting, namely, the observed gamma-ray map at the vicinity of the Galactic center is fitted with spatial and spectral templates. The templates contain the diffuse emission which is produced by bremsstrahlung and π^0 decay, inverse Compton emission, the Fermi Bubbles (depending on the ROI), and an isotropic diffuse background. In addition there is one template which describes the excess. In the template fit the normalizations of the individual templates are slightly adjusted to match the data. Resolved sources are usually masked during this fit. We note that the GCE is subdominant with respect to the Galactic contributions. For an ROI of 10° the GCE only produces about 10% of the gamma-ray flux, while the dominant flux is provided by bremsstrahlung, π^0 decay, and inverse Compton emission.

There are different attempts to explain the origin of the GCE. One possible scenario are the annihilations of potential DM particle in the Galactic halo. This option has been studied extensively in literature [213–228]. The GCE is fitted well by DM annihilation of a typical WIMP with masses between a few GeV and 200 GeV and thermal annihilation cross sections between 10^{-27} GeV/cm^3 and 10^{-25} GeV/cm^3. The exact DM masses and cross sections depend on final states of the elementary annihilation process. In the case of DM annihilation, the spatial morphology of the GCE is well described by a gNFW DM density profile (see Eq. 1.4) with $\gamma \sim 1.2$ [214]. Apart from DM, several astrophysical origins of the excess have been discussed, such as an unresolved population of point sources [218, 223, 227, 229–235]. One appealing possibility is a population of unresolved (millisecond) pulsars. Intriguingly, the energy spectrum of gamma rays emitted from a pulsar and the spectrum of a ~ 40 GeV WIMP annihilating into a pair of bottom-quarks look extremely similar [218]. Two different techniques have been explored to support the point-source hypothesis. The first technique is based on the so-called wavelet mechanism [236], which allows to test if the flux from the Galactic center is as homogeneous as expected from DM annihilation, and the second technique is based on photon-count statistics [237] to identify unresolved point

sources (see also Sec. 3.4). We note that, recently, the stability of the second method is discussed controversially [238, 239].

There are different methods proposed to search for counterpart signatures of a putative point source population, e.g. one might search for the expected radio signals of a pulsar distribution [240] or for the gravitational-wave signal produced by binary objects at the Galactic center [241]. An alternative to the *traditional* template fitting was discussed in [242], which uses a sky factorization with adaptive constrained templates. This method allows to compensate imperfections in the adopted templates which might arise from an incomplete modeling. We note that this method finds a preference for a bulge-like shape of the GCE which would point to a stellar origin [243]. Further discussed scenarios include an enhanced diffuse emission from the Galactic center due to an increased abundance of leptons [244–248] or molecular clouds at the vicinity of the Galactic center [249].

3.3 Active galactic nuclei

An Active Galactic Nucleus (AGN) is the central region of a galaxy with a tremendous amount of non-stellar emission at various wavelengths, including gamma rays [193, 196, 250–253]. At the center of an active galaxy a supermassive black hole accretes surrounding matter which is located in a disc. The available energy is then emitted in the form of two relativistic jets. Depending on the orientation of these jets we divide AGNs into two classes: if one of the relativistic jets points towards us, we call it a blazar, while we talk about a mAGN otherwise [254]. Blazars constitute the most numerous population of individually resolved extragalactic gamma-ray sources of the Fermi-LAT [193]. In general blazars are sub-divided into two categories, Flat Spectrum Radio Quasars (FSRQs) and BL Lacertae objectss (BLLacs). The first exhibit a high radio luminosity, which originates from the edge-elongated radio lobes [255], while the latter have a low radio luminosity, which is produced mostly in the center and the jets. In gamma rays, the two populations have slightly different spectral indices. The energy spectrum of FSRQ is a slightly softer ($\Gamma \sim 2.4$) compared to BLLacs ($\Gamma \sim 2.1$) [198].

3.3.1 Gamma-ray luminosity function and spectral energy distribution of blazars

We model blazars and their emission of gamma rays by the Gamma-ray Luminosity Function (GLF), which is the number of blazars per unit of luminosity L, co-moving volume V_c, and photon spectral index, Γ:

$$\Phi(L, z, \Gamma) = \frac{\mathrm{d}N_{\mathrm{BL}}(L, z, \Gamma)}{\mathrm{d}L\, \mathrm{d}V_c\, \mathrm{d}\Gamma}. \tag{3.6}$$

The GLF then depends on luminosity, redshift, and photon spectral index. Note that in a homogeneous and isotropic Universe the redshift dependence of the GLF should be understood as an evolution of the blazar distribution in time rather than in space. We define in the following the GLF and Spectral Energy Distribution (SED) in the specific model suggested in [201]. This model does not distinguish between the two blazar classes (BLLac and FSRQ) in order to have a larger sample

and better constrain the GLF. After discussing the specific model we will give some comments how to generalize.

The SED, $\mathrm{d}N/\mathrm{d}E$ is defined as the number of photon in the energy bin $[E, E+\mathrm{d}E]$ which would be observed at our detector per unit time and unit area, if there was no absorption of gamma-ray photons by the EBL. We assume that this SED follows a smoothly broken power law in energy

$$\frac{\mathrm{d}N}{\mathrm{d}E}(E) = K \left[\left(\frac{E}{E_b} \right)^{\gamma_a} + \left(\frac{E}{E_b} \right)^{\gamma_b} \right]^{-1} , \tag{3.7}$$

where E_b is the break position and γ_a (γ_b) is the spectral photon index below (above) the break. Moreover, E is the observed energy of the photon. In our specific model the three parameters γ_a, γ_b, and E_b are tuned to the Fermi-LAT observations. The two spectral indices γ_a and γ_b are fixed to 1.7 and 2.6, respectively and the break position is related to the observed photon spectral index by $\log(E_b/(\mathrm{GeV}) = 9.25 - 4.11\,\Gamma$. From Eq. (3.7) we conclude that the flux of observed photons in the energy bin $[E_{\mathrm{min}}, E_{\mathrm{max}}]$ is given by:

$$S(E_{\mathrm{min}}, E_{\mathrm{max}}) = \int_{E_{\mathrm{min}}}^{E_{\mathrm{max}}} \mathrm{d}E \, \frac{\mathrm{d}N}{\mathrm{d}E} \exp\left(-\tau[E\,(1+z), z]\right). \tag{3.8}$$

Now, the last factor of the integrand takes into account the absorption of photons in the EBL.
It is useful to define the photon energy in the rest frame of the source, $E_r = (1+z)\,E$. The luminosity, L, in the rest frame of the blazar and in the energy range 0.1 GeV to 100 GeV is defined as

$$L = \int_{0.1\ \mathrm{GeV}}^{100\ \mathrm{GeV}} \mathrm{d}E_r \, E_r \, \frac{\mathrm{d}\mathcal{N}_\gamma(E_r)}{\mathrm{d}E_r}, \tag{3.9}$$

where $\mathrm{d}\mathcal{N}_\gamma/\mathrm{d}E_r$ is the number of emitted photons by the blazar per unit time and per rest-frame energy. It is related to the SED through

$$\frac{\mathrm{d}\mathcal{N}_\gamma(E_r)}{\mathrm{d}E_r} = 4\pi\chi^2 \frac{\mathrm{d}N(E)}{\mathrm{d}E}\Big|_{E=\frac{E_r}{1+z}} , \tag{3.10}$$

where χ is the co-moving distance defined as $\chi = \int_0^z \mathrm{d}z'/H(z')$. In a flat and homogenous Universe, the Hubble rate $H(z)$ is given by $H(z) = H_0\,[\Omega_{0,r}(1+z)^4 + \Omega_{0,m}(1+z)^3 + \Omega_{0,\Lambda}]^{1/2}$. Here $\Omega_{0,i}$, $i \in \{r, m, \Lambda\}$ denote the radiation, matter, and dark energy density in the Universe of today and H_0 is the current Hubble rate. Note that in Eq. (3.10) the factor $(1+z)$ which arises from the transformation of $E \to E_r$ cancels with a second factor from the change of frequency between rest and observer frame.[2]

According to [201] the parametrization of the GLF is factorizable into a redshift dependent and a redshift independent part, such that we may write:

$$\Phi(L, z, \Gamma) = \Phi(L, 0, \Gamma) \times e(L, z). \tag{3.11}$$

[2] In our compact notation we hide that both, N and $\mathcal{N}$, are differential in time.

Here we adopt the Luminosity-Dependent Density Evolution (LDDE) of the GLF, $e(L, z)$, although, we note that this is not the only modeling used in literature. At redshift $z = 0$, the GLF is parametrized as a broken power law in luminosity and it follows a Gaussian distribution in photon spectral index:

$$\Phi(L, 0, \Gamma) = \frac{A}{\ln(10) L} \left[\left(\frac{L}{L_0} \right)^{\gamma_1} + \left(\frac{L}{L_0} \right)^{\gamma_2} \right]^{-1} \exp \left[-\frac{(\Gamma - \mu(L))^2}{2\sigma^2} \right] , \tag{3.12}$$

The parameter A is an overall normalization factor, the indices γ_1 and γ_2 govern the power-law behavior in luminosity and $\mu(L)$ and σ are the mean and dispersion of the distribution in Γ, respectively. The mean spectral index is allowed to have a logarithmical dependence on luminosity:

$$\mu(L) = \mu^* + \beta \left[\log \left(\frac{L}{\text{erg s}^{-1}} \right) - 46 \right] . \tag{3.13}$$

For the LDDE we adopt the functional form:

$$e(L, z) = \left[\left(\frac{1+z}{1+z_c(L)} \right)^{-p_1(L)} + \left(\frac{1+z}{1+z_c(L)} \right)^{-p_2(L)} \right]^{-1} \tag{3.14}$$

with

$$z_c(L) = z_c^* \, (L/10^{48})^{\alpha}, \tag{3.15}$$

$$p_1(L) = p_1^* + \tau \, (\log(L) - 46), \tag{3.16}$$

$$p_2(L) = p_2^* + \delta \, (\log(L) - 46). \tag{3.17}$$

The GLF and SED models contain a large number of free parameters. In [201] these parameters are determined by fitting the model to the Fermi-LAT catalog data, which is complemented with redshift information of follow-up observations of the blazars in the catalog.

We conclude this section with a few comments:

- Next to the LDDE in literature two further redshift evolutions are investigated. They are called primarily luminosity evolution and primarily density evolution. The result of Ref. [201] is that in the context of gamma rays the LDDE provides the best description of the available data.
- In literature, the SED is sometimes modeled as a simple power law, which is a slight simplification compared to the model presented above. In this case one replaces the SED in Eq. (3.7) by $\mathrm{d}N/\mathrm{d}E = K \, E^{-\Gamma}$.
- The model above attempts to combine FSRQs and BLLacs into a single framework. Sometimes it might be better to separate the two source classes into two different models. Then, the functional form of each model typically resembles the combined model discussed in this section, but the adopted parameter values may differ significantly.
- For a more general overview on the topic we refer to the review [256] and references therein.

3.4 Photon statistics

The statistics of gamma-ray point sources can be used to constrain the source-count distribution below the flux threshold for the detection of individual sources. The method is commonly used in X-ray astronomy [259–263]. Its prospects to distinguish blazars from a potential DM signal was studied in [264]. Then, it was first applied to gamma-ray data in [257] and later refined by [258,265]. The typical goal pursued with the One-Point Probability Distribution Function (1pPDF) method is to constrain the source-count distribution of extragalactic point sources.

Before giving a detailed description of the method in the next section, we will briefly summarize the main idea. If the gamma rays were solely produced by diffuse processes, we would expect that the probability distribution for the observation of photons in each pixel of the sky would be governed by a Poisson statistics. If, however, the detected gamma rays (partly) originate from point sources, we expect that the Probability Distribution Function (PDF) is distorted with respect to Poisson distribution. In particular, this distortion leads to a higher probability to observe a large number of photons in a single pixel. The best way to visualize this effect is to count the number of pixels with a certain number of photons, k, and then produce a histogram of the results as function of k. This histogram is an estimator for the 1pPDF. An example is displayed in Fig. 3.1 where the histogram is deduced from Fermi-LAT data. The analysis is restricted to high latitudes to minimize the effect of Galactic foregrounds. The various lines in Fig. 3.1 show different components

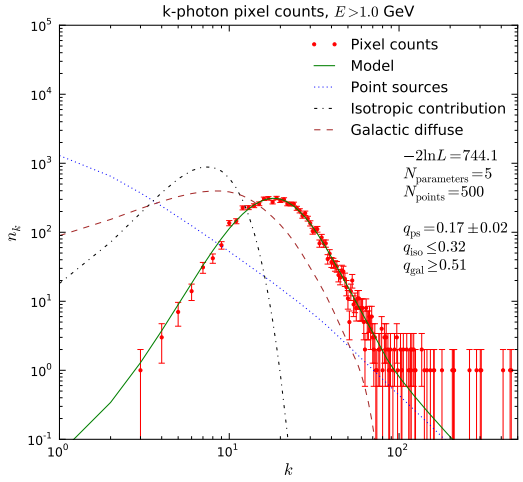

Figure 3.1: Histogram showing the number of pixels n_k with exactly k observed photons as function of k as measured by the Fermi-LAT detector. For a description of the model we refer to the text. The figure is taken from [257].

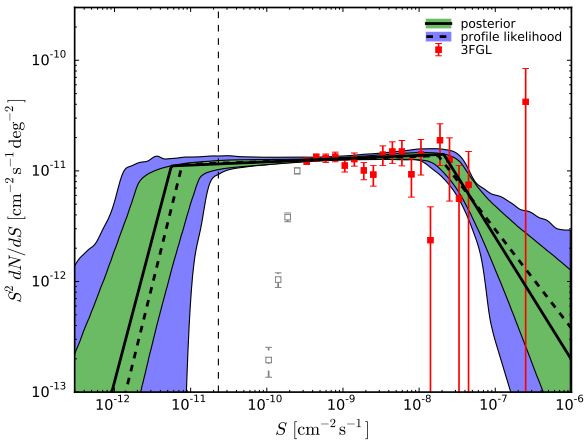

Figure 3.2: Measurement of the source count distribution exploiting the 1pPDF method with the Fermi-LAT detector. The $\mathrm{d}N/\mathrm{d}S$ in the energy bin from 1 GeV to 10 GeV is modeled as a multiple-broken power law. The figure is taken from [258].

of the model which was fitted in order to reproduce the observed histogram. The model takes into account Galactic diffuse emission, an isotropic background flux, and an extra-galactic source-count distribution shaped as a broken power law. The final PDF (green line) is the convolution of the three distinct components. We note that the point sources are in particular constrained by the tail of the distribution at large k.

The important refinement of [258, 265] is that the theoretical model is no longer fitted to a histogram but the PDF is evaluated individually for each pixel. This allows to properly take into account small variations of the PDF which may arise from the pixel-dependence of the detector acceptance and from the pixel-dependence of the strength of the Galactic foreground emission. Figure 3.2 shows an important result of [258], which is the measurement of the source-count distribution, $\mathrm{d}N/\mathrm{d}S$, as a function of flux, S. It is very well visible that the method of photon statistics is capable of constraining the source-count distribution to approximately one order of magnitude smaller fluxes with respect to standard techniques for individual source detection. The $\mathrm{d}N/\mathrm{d}S$ of individually detected point sources (red and grey data points) quickly drops below a threshold of $S \sim 2 \cdot 10^{-10}$ cm^{-2}s^{-1} while photon statistics still constrain the $\mathrm{d}N/\mathrm{d}S$ down to $S \sim 2 \cdot 10^{-11}$ cm^{-2}s^{-1}.

Finally, we note that the method of photon statistics was also applied to the Galactic center to infer information about the origin of the GCE [237]. However, the stability of the method in the complicated environment of the Galactic center is still under discussion [239, 266]. We note that for the extragalactic sky the method was extensively tested and found to provide stable results [258, 265, 267].

3.4.1 Formalism of the one-point probability density function

The formalism of the 1pPDF is summarized in [257, 258]. We present a personal adaptation of the formalism. In the following we want to answer the question: What is the probability to observe exactly k photons in a certain pixel? Here a pixel is a very small fraction of the observed gamma-ray sky. The symbol k is a random variable and our goal in the following is to relate the probability to observe exactly k photons, typically denoted p_k, to the probability distribution function of of photon sources. We will start to explore some simple examples and, then, step-by-step arrive at a more realistic description which can be applied to the gamma-ray sky.

1. First, we imagine that there is only a single source class. This is an artificial class which only exists in a thought experiment. We assume that each source in this class always contributes exactly one photon in our detector. Furthermore, the number of sources n_1 per pixel shall follow a PDF which is Poisson distributed. The mean of the Poisson distribution is denoted

x_1.[3] So, the probability to observe exactly n_1 sources in one pixel is given by:

$$P(n_1) = \frac{(x_1)^{n_1}}{n_1!} \exp(-x_1). \tag{3.18}$$

Since our source class is constructed such that each source contributes exactly one photon, the number of observed photons is equal to the number of sources. The random variables k and n_1 are related by $k = n_1$. Consequently, the probability to observe exactly k photons is given by:

$$P(k) = p_k^{(1)} = \frac{(x_1)^k}{k!} \exp(-x_1). \tag{3.19}$$

2. Now, we imagine to have two source classes, both of them contributing exactly one photon. The number of sources for each class, $n_1^{(1)}$ and $n_1^{(2)}$, follows a Poisson distribution with mean values $x_1^{(1)}$ and $x_1^{(2)}$, respectively. The probability to observe exactly $k = n_1^{(1)} + n_1^{(2)}$ photons is the convolution of the two Poisson distributions:

$$p_k^{(1+2)} = \sum_{k'=0}^{k} p_{k'}^{(1)} p_{k-k'}^{(2)} = \sum_{k'=0}^{k} \frac{\left(x_1^{(1)}\right)^{k'}}{k'!} \exp\left(-x_1^{(1)}\right) \cdot \frac{\left(x_1^{(2)}\right)^{(k-k')}}{(k-k')!} \exp\left(-x_1^{(2)}\right). \tag{3.20}$$

At this step it is convenient to introduce the *generating function* $\mathcal{P}(t)$ which contains all the information of the PDF. We define

$$\mathcal{P}(t) = \sum_{k=0}^{\infty} p_k \cdot t^k \tag{3.21}$$

such that we can obtain p_k by

$$p_k = \frac{1}{k!} \frac{\mathrm{d}^k \mathcal{P}(t)}{\mathrm{d}t^k}\bigg|_{t=0}. \tag{3.22}$$

With the generating function we can rewrite Eq. (3.20) as

$$\mathcal{P}_{(1+2)}(t) = \mathcal{P}_{(1)}(t) \cdot \mathcal{P}_{(2)}(t) = \sum_{k=0}^{\infty} p_k^{(1)} t^k \cdot \sum_{k'=0}^{\infty} p_{k'}^{(2)} t^{k'} = \sum_{k=0}^{\infty} \left[\sum_{k'=0}^{k} p_{k'}^{(1)} p_{k-k'}^{(2)} \right] t^k, \tag{3.23}$$

where in the last step we have applied the Cauchy product.

[3] We provide an explicit example for a *source class* which emits exactly one photon per source. Let us say our *source class* is the sum of all inverse Compton events. Then, the number of inverse Compton events pointing towards a single pixel, namely the number of *sources*, follows a Poisson distribution. Hence, the number of photons from inverse Compton events in each pixel follows the same Poisson distribution. In the 1pPDF formalism, we denote the number of sources with n_1 and the mean of the Poisson distribution with x_1. In this example the number of *sources* and observed photons is identical.

3. Let us take again one source class. However, now each source in this class contributes exactly m photons in our detector. The number of sources n_m again follows a PDF which is Poisson distributed and has a mean value denoted x_m. Then, the number of observed photons is $k = m\,n_m$ and the probability to observe exactly k photons is given by:

$$p_k^{(m)} = \begin{cases} \frac{(x_m)^{(k/m)}}{(k/m)!}\exp(-x_m) & , k = 0, m, 2m, 3m, ... \\ 0 & , \text{otherwise.} \end{cases} \tag{3.24}$$

In terms of generating functions we can write

$$\mathcal{P}_{(m)}(t) = \sum_{n_m=0}^{\infty} p_{n_m}^{(m)} t^{m\,n_m} = \sum_{n_m=0}^{\infty} \frac{(x_m)^{n_m}}{(n_m)!}\exp(-x_m)\,(t^m)^{n_m} = \exp\left(x_m\,t^m - x_m\right). \tag{3.25}$$

4. Finally, we can move to the general case where we allow, at the same time, to have sources with any number of m photons per pixel. The number of sources n_m in each class is Poisson distributed with mean x_m, respectively. Hence, the total number of observed photons in a pixel is $k = \sum_m m \cdot n_m$. We saw in *example 2* that we can write the generating function of the final PDF as the product of the individual PDFs. Therefore, we obtain:

$$\mathcal{P}(t) = \prod_{m=0}^{\infty} \mathcal{P}_{(m)}(t) = \exp\left(\sum_m \left[x_m\,t^m - x_m\right]\right). \tag{3.26}$$

This is a very important result. We have reduced our original question for the probability to observe k photons to the determination of the expectation values x_m. The calculation of x_m is straightforward as soon as we have a source-count distribution.

In the following, our goal is to give an explicit formula for x_m, which is the mean number of sources per pixel emitting exactly m photons. With this, at least formally, our problem is solved since we can calculate the probabilities p_k from Eqs. (3.22) and (3.26). We note, however, that calculating the k-th derivative becomes computationally very expensive for large k[4]. In practice, it is better to calculate p_k from a recursive scheme, *i.e* the generalization of (3.20):

$$q_k^{(1)} = p_k^{(1)} \tag{3.27}$$

$$q_k^{(m)} = \sum_{\substack{k'=0 \\ \text{step } m}}^{k} p_{k'}^{(m)} q_{k-k'}^{(m-1)}. \tag{3.28}$$

Then, p_k is given by the limit $p_k = \lim_{m\to\infty} q_k^{(m)}$, which in practice can be truncated as soon as m is larger than the largest relevant k. Below, we introduce a superscript (p) to denote the pixel dependence of our quantities. Let S be the flux, namely, the number of photons in the energy bin $[E_{\min}, E_{\max}]$ traversing a unit area per unit time. The differential source-count distribution $\mathrm{d}N/\mathrm{d}S$

[4]The number of terms in in the k-th derivative grows approximately with 2^k.

denotes the number of sources per solid angle in the flux bin $[S, S + \mathrm{d}S]$. We assume that $\mathrm{d}N/\mathrm{d}S$ is isotropic for extragalactic sources and, therefore, does not depend on the pixel. However, the number of photon counts $\mathcal{C}^{(p)}(S)$ may depend on the pixel, since the exposure of the detector can depend on the pixel. The probability that a source with flux S emits exactly m photons follows a Poisson statistics:

$$p_m(S) = \frac{[\mathcal{C}^{(p)}(S)]^m}{m!} \exp(-\mathcal{C}^{(p)}(S)). \tag{3.29}$$

Hence, the expectation value x_m is given by

$$x_m = \Omega_{\mathrm{pix}} \int_0^\infty \mathrm{d}S \, \frac{\mathrm{d}N(S)}{\mathrm{d}S} \, p_m(S), \tag{3.30}$$

where Ω_{pix} is the pixel size in steradian. For completeness, we define $\mathcal{C}^{(p)}(S)$ which depends on the exposure, $\mathcal{E}^{(p)}(E)$:

$$\mathcal{C}^{(p)}(S) = \int_{E_{\mathrm{min}}}^{E_{\mathrm{max}}} \mathrm{d}E \, \frac{\mathrm{d}S(E)}{\mathrm{d}E} \cdot \mathcal{E}^{(p)}(E) \approx S \, \frac{\int_{E_{\mathrm{min}}}^{E_{\mathrm{max}}} \mathrm{d}E \, E^{-\Gamma} \cdot \mathcal{E}^{(p)}(E)}{\int_{E_{\mathrm{min}}}^{E_{\mathrm{max}}} \mathrm{d}E \, E^{-\Gamma}}. \tag{3.31}$$

In the last step, we have approximated the energy-differential flux by a power law with spectral index Γ. For practical calculations this approximation with $\Gamma = 2.4$ is sufficient.

There are two subtleties which have not yet been addressed. First, the finite angular resolution of the detector means that only a fraction f of the flux is observed in one pixel while the remainder is detected in neighboring pixels. To take this effect into account we have to know the average distribution function of the fractional photon flux, $\rho(f)$. The behavior of $\rho(f)$ depends on the pixel size and the Point Spread Function (PSF) (angular resolution) of the detector. We remark that the PSF is usually energy-dependent and, therefore, also $\rho(f)$ adopts this energy dependence. The distribution $\rho(f)$ peaks at smaller f if the pixel size is reduced or the PSF worsens. This effect of angular resolution can be taken into account by convolving Eq. (3.30) with $\rho(f)$:

$$x_m = \Omega_{\mathrm{pix}} \int_0^\infty \mathrm{d}S \int_0^1 \mathrm{d}f \, \rho(f) \, \frac{\mathrm{d}N(S)}{\mathrm{d}S} \, \frac{[f \, \mathcal{C}^{(p)}(S)]^m}{m!} \exp(-f \, \mathcal{C}^{(p)}(S)). \tag{3.32}$$

We note that $\rho(f)$ should be normalized such that the sum of all fraction is equal to 1, namely, $\int_0^1 \mathrm{d}f \, \rho(f) = 1$. To obtain the average distribution function one conducts a simple MC simulation, where one simulates sources at random positions in the sky, folds the arriving photons with the PSF, and counts the fraction of photons from each source arriving in the same pixel.

Let us now address the second subtlety. So far, we assumed that the gamma-ray sky solely contains point sources. However, in practice there is also diffuse emission from the interaction of Galactic CRs and, potentially, a Galactic and/or extragalactic isotropic component. We have already discussed all the relevant formalism to include the diffuse emission. To make this explicit we remind that from

our statistical perspective a diffuse emission is nothing else than a distribution of sources which emit exactly one photon per pixel. In our formalism, the diffuse components can simply be added to x_1 (footnote[3] explains the relation for the inverse Compton emission). For completeness, we define the additional component:

$$x_{\mathrm{diff}}^{(p)} = \int\limits_{\Omega_{\mathrm{pix}}} \mathrm{d}\Omega \int\limits_{E_{\mathrm{min}}}^{E_{\mathrm{max}}} \mathrm{d}E \, \frac{\mathrm{d}S_{\mathrm{diff}}(E)}{\mathrm{d}E} \cdot \mathcal{E}^{(p)}(E) \tag{3.33}$$

In the following, we will shortly discuss two models for the source-count distribution. First, a generic phenomenological model where the number of sources as function of flux follows a power law and then, in a second step, we will introduce a more physically motivated model where the number of point sources per flux interval is given by the GLF of blazars.

Source-count distribution modeled as multiple-broken power law

One possibility is to assume that the source-count distribution is given by a power law in the flux, S, with multiple breaks. If we allow for a number of N_{b} breaks located at $S_{\mathrm{b}j}$, $j = 1, 2, \ldots, N_{\mathrm{b}}$, the multiple-broken power law is defined as

$$\frac{\mathrm{d}N}{\mathrm{d}S}(S) \propto \begin{cases} \left(\frac{S}{S_0}\right)^{-n_1} & , S > S_{\mathrm{b1}} \\ \left(\frac{S_{\mathrm{b1}}}{S_0}\right)^{-n_1+n_2} \left(\frac{S}{S_0}\right)^{-n_2} & , S_{\mathrm{b2}} < S \leq S_{\mathrm{b1}} \\ \quad \vdots \qquad \vdots & \\ \left(\frac{S_{\mathrm{b1}}}{S_0}\right)^{-n_1+n_2} \left(\frac{S_{\mathrm{b2}}}{S_0}\right)^{-n_2+n_3} \cdots \left(\frac{S}{S_0}\right)^{-n_{N_{\mathrm{b}}+1}} & , S \leq S_{\mathrm{b}N_{\mathrm{b}}} \end{cases} \tag{3.34}$$

where S_0 is a normalization constant. Moreover, n_j are the indices of the power-law components. To complete the definition of the multiple-broken power law we define the overall normalization factor A_{S} such that $A_{\mathrm{S}} = \mathrm{d}N/\mathrm{d}S\,(S_0)$. Note that in order to obtain a finite total flux we have to impose $n_1 > 2$ and $n_{N_{\mathrm{b}}+1} < 2$.

Source-count distribution derived from the gamma-ray luminosity function of blazars

A more physically motivated approach is to use the blazar GLF and SED to model the source-count distribution:

$$\frac{\mathrm{d}N_{\mathrm{BL}}}{\mathrm{d}S} = \frac{1}{4\pi} \int \mathrm{d}z \int \mathrm{d}\Gamma \, \frac{\mathrm{d}N_{\mathrm{BL}}(S, z, \Gamma)}{\mathrm{d}S \, \mathrm{d}z \, \mathrm{d}\Gamma}. \tag{3.35}$$

The factor $1/4\pi$ appears because conventionally, although suppressed in the notation, $\mathrm{d}N/\mathrm{d}S$ is differential in solid angle. We can relate Eq. (3.35) to the blazar GLF as defined in Eq. (3.6) through

$$\frac{\mathrm{d}N_{\mathrm{BL}}(S, z, \Gamma)}{\mathrm{d}S \, \mathrm{d}z \, \mathrm{d}\Gamma} = \left| \frac{\partial(L, V_c, \Gamma)}{\partial(S, z, \Gamma)} \right| \, \Phi(L, z, \Gamma) = \frac{\mathrm{d}V_c}{\mathrm{d}z} \, \frac{\mathrm{d}L}{\mathrm{d}S} \, \Phi(L, z, \Gamma), \tag{3.36}$$

where $\partial(L, V_c, \Gamma)/\partial(S, z, \Gamma)$ is the Jacobian matrix. In a flat and homogeneous Universe, co-moving volume and redshift are related by $dV_c/dz = 4\pi\chi^2(z)/H(z)$. Furthermore, we obtain $\mathrm{d}L/\mathrm{d}S = L/S$. To understand the last relation we remind that both, L and S, are strictly proportional to one single free parameter, K from Eq. (3.7).

3.5 Angular correlation of gamma rays

Above we explained the 1-point PDF method for gamma rays which derives the probability to observe a certain number of photons in a specific pixel. However, the 1-point PDF discards all the directional information of the extragalactic sources contained in the gamma-ray map. The next logical step is to investigate angular correlations and the power spectrum. The power spectrum is known to be a very powerful tool to compare physics models with theoretical prediction. The most prominent example is probably the power spectrum of the CMB which is extremely important to constrain cosmological models [25]. Although, the gamma-ray flux is measured much less precisely compared to the temperature fluctuations of the CMB, we can still obtain a deeper insight when investigating the Angular Power Spectrum (APS) of gamma rays. The APS is expected to contain signatures of astrophysical sources and potentially from DM annihilation or decay. The expected signals from DM were first calculated in [268] while the importance of astrophysical sources was realized slightly later in [269, 270]. The formalism to calculate the expected signals, in particular of DM, relies on the halo model [271, 272]. In the halo model one approximates the DM distribution by an ensemble of spherical DM halos which follow the linear power spectrum of matter with a certain bias. The approximation is arranged such that the true power spectrum of matter (as for example obtained from numerical simulations) is well reproduced by the halo model. In the last years, due to the increased precision of the gamma-ray data provided by the Fermi-LAT experiment the APS and cross correlations have become a popular object of study. In this context, the APS has been used to provide constraints on DM annihilation and decay [273]. The most recent measurement of the APS by the Fermi-LAT is provided in [274]. This updates the previous measurements [275, 276]. The formalism to calculate the APS of gamma rays from DM is well summarized in [277]. Our focus in the next section lies on the derivation of the APS in gamma rays for the astrophysical sources such as blazars which are the dominant source of the observed APS in gamma rays. However, before focussing on astrophyscial sources, we note that the cross-correlation of the gamma-ray flux with other observables, in particular, gravitational tracers of the matter distribution in our Universe is a powerful tool to search for DM [277–280]. This is a very interesting and active field of research since a lot of precise new data is becoming available from cosmology experiments [281].

3.5.1 Formalism to calculate auto- and cross-correlation signals

In the following we will explain the general formalism to calculate the auto- and cross-correlation of astrophysical sources. All equations are first given for the specific example of the gamma-ray flux and the cross-correlation in different energy bins. For simplicity, we consider a single source class which, in practice, for example could be blazars. At the end of this section we will generalize to more than a single source class. The gamma-ray flux in the energy bin $[E_{\mathrm{min}}, E_{\mathrm{max}}]$ arriving from the

direction $\vec{n}$ is given by:

$$S(\vec{n}) = \int \mathrm{d}\chi \underbrace{\chi^2}_{(i)} \int \mathrm{d}L \underbrace{\frac{\mathrm{d}^2 N_{\mathrm{BL}}}{\mathrm{d}V_c \, \mathrm{d}L}(\vec{x},\chi,L)}_{(ii)} \times \int_{E_{\min}(1+z)}^{E_{\max}(1+z)} \mathrm{d}E_r \underbrace{\frac{\mathrm{d}\mathcal{N}_\gamma}{\mathrm{d}E_r}(E_r,L)}_{(iii)} \underbrace{\frac{1}{4\pi\chi^2(1+z)}}_{(iv)} \underbrace{\exp\big[-\tau\,(E_r,z)\big]}_{(v)} . \tag{3.37}$$

Here χ denotes the co-moving radial distance which is used interchangeably with redshift z or time. The integrand has to be evaluated at $\vec{x} = \chi\vec{n}$. The different factors arise as follows:

- (i) This is the typical factor which appears in the l.o.s. integral. The number of sources in a small cone with opening angle $\mathrm{d}\Omega$ increases with distance squared. We note again that the flux $S(\vec{n})$ is differential in $\mathrm{d}\Omega$.
- (ii) We assume that the distribution of blazars depends on the gamma-ray luminosity, L. Then, the differential distribution of blazars, namely, the number per volume and luminosity, is labeled by $\mathrm{d}^2N_{\mathrm{BL}}/\mathrm{d}V_c\mathrm{d}L$. The subscript c is used to denote the co-moving volume.
- (iii) Number of photons per energy and unit time interval emitted by a single source. For sources which are far away from the position of the detector we have to take into account that the energy changes with redshift. The rest-frame energy, E_r, is is then related to the observed energy, E, by $E_r = (1+z)E$. The energy spectrum may depend on the luminosity of the source since the relation between luminosity and energy spectrum is given by:
$$L = \int \mathrm{d}E_r \; E_r \; \mathrm{d}\mathcal{N}_\gamma/\mathrm{d}E_r. \tag{3.38}$$
- (iv) This factor captures two effect. Firstly, the flux decreases with the distance of the source leading to the factor $4\pi\chi^2$. The factor $1+z$ takes into account that the time interval between emission and detection changes.
- (v) For high-energy photons the Universe becomes opaque. This term describes the absorption of photons as function of redshift (distance) and emitted energy.

We note that in literature often the product of (iii) and (iv) is called $\mathrm{d}N/\mathrm{d}E_r = 1/(1+z)\mathrm{d}N/\mathrm{d}E$ (*c.f.* Eq. (3.10)). However, this is a constructed quantity: It describes the number of photons per energy, unit area, and time which would be observed at the detector if no photons were absorbed in the EBL. Reordering Eq. (3.37) we obtain:

$$S(\vec{n}) = \int \mathrm{d}\chi\mathrm{d}L \underbrace{\frac{\mathrm{d}^2 N_{\mathrm{BL}}}{\mathrm{d}V_c\mathrm{d}L}(\vec{x},\chi,L)}_{=g(\vec{x},\chi,L)} \underbrace{\frac{1}{4\pi\,(1+z)} \int_{E_{\min}(1+z)}^{E_{\max}(1+z)} \mathrm{d}E_r \, \frac{\mathrm{d}\mathcal{N}_\gamma}{\mathrm{d}E_r}(E_r,L) \exp\big[-\tau\,(E_r,z)\big]}_{=\tilde{W}(\chi,L)} . \tag{3.39}$$

The integrand in Eq. (3.39) can be divided into the *source field*, $g(\vec{x},\chi,L)$, and the *window function*, $\tilde{W}(\chi,L)$. We stress that only the source field depends on space (or direction), while the window function depends only on redshift and luminosity. Furthermore, the window function is up to a normalizing factor $1/\chi^2$ equal to the flux of a single source with luminosity L at co-moving distance χ. We define $S_s(\chi,L) = \tilde{W}(\chi,L)/\chi^2$. Here we are mainly interested in the fluctuation of the gamma-ray flux, $\delta S(\vec{n}) = S(\vec{n}) - \bar{S}$, where $\bar{S} = \langle S(\vec{n})\rangle$ denotes the ensemble average. In practice, due to the homogeneity and isotropy of the Universe this is equal to averaging the flux over the whole sky. We note that $\bar{S}$ does not depend on direction. We expand the flux fluctuations in spherical harmonics:

$$\delta S(\vec{n}) \;=\; \bar{S}\sum_{\ell=0}^{\infty}\sum_{m=-\ell}^{\ell} a_{\ell m}Y_{\ell m}(\vec{n}). \tag{3.40}$$

Consequently, the coefficients $a_{\ell m}$ are defined by:

$$\begin{aligned} a_{\ell m} &= \frac{1}{\bar{S}}\int \mathrm{d}^2\vec{n}\;\delta S(\vec{n})Y^*_{\ell m}(\vec{n}) \\ &= \frac{1}{\bar{S}}\int \mathrm{d}^2\vec{n}\,\mathrm{d}\chi\,\mathrm{d}L\;\underbrace{\frac{g(\vec{x},\chi,L)-\bar{g}(\chi,L)}{\bar{g}(\chi,L)}}_{=f(\vec{x},\chi,L)}\underbrace{\bar{g}(\chi,L)\tilde{W}(\chi,L)}_{=W(\chi,L)}Y^*_{\ell m}(\vec{n}). \end{aligned} \tag{3.41}$$

In Eq. (3.41), we have defined the normalized source field $f(\vec{x},\chi,L)$ and the normalized window function $W(\chi,L)$. Next, we replace the normalized source field with by its Fourier transform, $f(\vec{x},\chi,L) = \int \frac{\mathrm{d}^3\vec{k}}{(2\pi)^3}\,\hat{f}(\vec{k},\chi,L)\,\exp(i\vec{k}\cdot\vec{x})$, and use the Rayleigh expansion, $\exp(i\vec{k}\cdot\vec{x}) = 4\pi\sum_{\ell' m'} i^{\ell'} j_{\ell'}(k\cdot\chi)Y^*_{\ell' m'}(\hat{k})Y_{\ell' m'}(\vec{n})$, where j_ℓ are the spherical Bessel functions. From Eq. (3.41), we obtain:

$$a_{\ell m} \;=\; \frac{i^\ell}{\bar{S}}\int \mathrm{d}\chi\mathrm{d}L\;\frac{\mathrm{d}^3\vec{k}}{2\pi^2}\hat{f}(\vec{k},\chi,L)\;j_\ell(k\cdot\chi)\;W(\chi,L)Y^*_{\ell m}(\hat{k}). \tag{3.42}$$

If we consider two different energy bins $[E^{(i)}_{\min},E^{(i)}_{\max}]$ and $[E^{(j)}_{\min},E^{(j)}_{\max}]$, we can define the APS as the expectation value of $\langle a^{(i)}_{\ell m}a^{(j)*}_{\ell m}\rangle$:

$$\begin{aligned} C^{(ij)}_\ell = \frac{1}{\bar{S}_i\bar{S}_j}\int \mathrm{d}\chi\,\mathrm{d}\chi'\,\mathrm{d}L\,\mathrm{d}L'\,\frac{\mathrm{d}^3\vec{k}}{2\pi^2}\frac{\mathrm{d}^3\vec{k'}}{2\pi^2}\,\Big\langle\hat{f}(\vec{k},\chi,L)\hat{f}^*(\vec{k'},\chi',L')\Big\rangle Y^*_{\ell m}(\hat{k})Y_{\ell m}(\hat{k'}) \\ \times j_\ell(k\cdot\chi)\;j_\ell(k'\cdot\chi')\;W^{(i)}(\chi,L)\;W^{(j)}(\chi',L')Y^*_{\ell m}(\hat{k})Y_{\ell m}(\hat{k'}). \end{aligned} \tag{3.43}$$

In our specific case, the blazars which are the *source* of the flux in the energy bin i are also the *source* of the flux in the energy bin j. Therefore, we do not use any superscript on f, which is however important if i and j have different sources fields. We define the power spectrum $P(k,\chi,\chi',L,L')$ of two individual sources with luminosities L, L', and at distances χ, χ' by

$$\langle\hat{f}(\vec{k},\chi,L)\hat{f}^*(\vec{k'},\chi',L')\rangle = (2\pi)^3\delta(\vec{k}-\vec{k'})P(k,\chi,\chi',L,L'), \tag{3.44}$$

where δ denotes the Dirac delta function. If we insert Eq. (3.44) into Eq. (3.43) we obtain:

$$\begin{aligned} C_\ell^{(ij)} &= \frac{1}{\bar{S}_i \bar{S}_j} \frac{2}{\pi} \int \mathrm{d}\chi \, \mathrm{d}\chi' \, \mathrm{d}L \, \mathrm{d}L' \, \mathrm{d}^3\vec{k} \; j_\ell(k\chi) \; j_\ell(k\chi') \; W^{(i)}(\chi,L) \; W^{(j)}(\chi',L') \; P(k,\chi,\chi',L,L') Y^*_{\ell m}(\hat{k}) Y_{\ell m}(\hat{k}) \\ &= \frac{1}{\bar{S}_i \bar{S}_j} \frac{2}{\pi} \int \mathrm{d}\chi \, \mathrm{d}\chi' \, \mathrm{d}L \, \mathrm{d}L' \, \mathrm{d}k \; j_\ell(k\chi) \; j_\ell(k\chi') \; W^{(i)}(\chi,L) \; W^{(j)}(\chi',L') \; P(k,\chi,\chi',L,L') \underbrace{\delta_{\ell\ell} \delta_{mm}}_{=1} . \end{aligned} \tag{3.45}$$

Finally, we use the Limber approximation [282] and obtain:

$$C_\ell^{(ij)} = \frac{1}{\bar{S}_i \bar{S}_j} \int \frac{\mathrm{d}\chi}{\chi^2} \, \mathrm{d}L \, \mathrm{d}L' \; W^{(i)}(\chi,L) \; W^{(j)}(\chi,L') \; P(k=\ell/\chi,\chi,L,L'). \tag{3.46}$$

From the last equation we see that the calculation of the APS requires the knowledge of the normalized window functions and the power spectrum of individual sources. The normalized window functions are already defined in Eq. (3.41).

Let us investigate now the power spectrum and write down explicitly the ensemble average $\langle f(\vec{x},\chi,L) f(\vec{x}',\chi,L') \rangle$. Since both fields, f, are evaluated at the same co-moving distance, χ, we will subsume this dependence in the following.

$$\left\langle f(\vec{x},L) f(\vec{x}',L') \right\rangle = \frac{\left\langle g(\vec{x},L) g(\vec{x}',L') \right\rangle}{\bar{g}(L) \bar{g}(L')} - 1. \tag{3.47}$$

We can assume that blazars are point sources and write the source field $g(\vec{x},L)$ as a sum of point-like seeds at positions $\vec{x}_a$:

$$g(\vec{x},L) = \sum_a \delta(\vec{x} - \vec{x}_a) \delta(L - L_a). \tag{3.48}$$

With Eq. (3.48) we can write the two-point correlation function as:

$$\begin{aligned} \left\langle g(\vec{x},L) g(\vec{x}',L') \right\rangle &= \left\langle \sum_a \delta(\vec{x} - \vec{x}_a) \delta(L - L_a) \sum_b \delta(\vec{x}' - \vec{x}_b) \delta(L' - L_b) \right\rangle \\ &= \left\langle \sum_a \delta(\vec{x} - \vec{x}_a) \delta(L - L_a) \delta(\vec{x}' - \vec{x}_a) \delta(L' - L_a) \right\rangle \\ &\quad + \left\langle \sum_a \delta(\vec{x} - \vec{x}_a) \delta(L - L_a) \sum_{b \neq a} \delta(\vec{x}' - \vec{x}_b) \delta(L' - L_b) \right\rangle \\ &= \bar{g}(L) \; \delta(\vec{x} - \vec{x}') \; \delta(L - L') \quad + \quad \bar{g}(L) \; \bar{g}(L') \; \left[1 + \xi^{(2)}(\vec{x},\vec{x}',L,L') \right]. \end{aligned} \tag{3.49}$$

In the last line, we have defined the two-point correlation function of two different sources $\xi^{(2)}(\vec{x},\vec{x}',L,L')$. Often, one uses the simplifying assumption that the correlation function is proportional to the linear correlation function of matter. The normalization factor, also called bias and denoted $b(L)$, may

depend on the luminosities of the sources. We rewrite $\xi^{(2)}(\vec{x},\vec{x}',L,L') \approx b(L)\, b(L')\, \xi_{\rm lin}(|\vec{x}-\vec{x}'|)$. Inserting everything into Eq. (3.47) we obtain:

$$\left\langle f(\vec{x},L) f(\vec{x}',L') \right\rangle \;=\; \frac{1}{\bar{g}(L)}\, \delta(\vec{x}-\vec{x}')\, \delta(L-L') \quad + \quad b(L)\, b(L')\, \xi_{\rm lin}(|\vec{x}-\vec{x}'|). \tag{3.50}$$

Finally, using the Fourier transform of Eq. (3.50) the power spectrum of Eq. (3.46) becomes:

$$P(k,\chi,L,L') \;=\; \frac{1}{\bar{g}(L)}\, \delta(L-L') \quad + \quad b(L)\, b(L')\, P_{\rm lin}(k{=}\ell/\chi), \tag{3.51}$$

where $P_{\rm lin}(k)$ is the linear power spectrum of matter. Putting everything together we obtain:

$$\begin{aligned} C_\ell^{(ij)} \;=\; & \frac{1}{\bar{S}_i \bar{S}_j} \int {\rm d}\chi\, {\rm d}L\, g(L,\chi)\, \chi^2\, S_s^{(i)}(L,\chi) S_s^{(j)}(L,\chi) \\ & + \frac{1}{\bar{S}_i \bar{S}_j} \int {\rm d}\chi\, \chi^2 \left[\int {\rm d}L\, b(L)\, S_s^{(i)}(L,\chi)\right] \left[\int {\rm d}L'\, b(L')\, S_s^{(j)}(L',\chi)\right] P_{\rm lin}(k{=}\ell/\chi). \end{aligned} \tag{3.52}$$

For the gamma-ray flux of blazars, at $\ell \gtrsim 50$ the second term in Eq. (3.51) is negligible. Astrophysical sources are point-like and, therefore, the probability to find two sources at a specific distance is relatively small. On the other hand, for extended sources (like DM halos) this probability is boosted and the so-called 2-halo term is important. Here, the dominant first term is also called Poisson noise, which is independent of ℓ. We denote this constant term by $C_P^{(ij)}$. In the case of astrophysical sources and gamma-ray fluxes, the ensemble average of the source field is usually called GLF denoted with $\phi(L,\chi)$, which we will adopt in the following. If we change the integration variable form co-moving distance to redshift and use ${\rm d}\chi = 1/H(z)\, {\rm d}z$ the Poisson noise is given by:

$$C_P^{(ij)} \;=\; \frac{1}{\bar{S}_i \bar{S}_j} \int {\rm d}z\, \underbrace{\frac{\chi^2(z)}{H(z)}}_{=\frac{1}{4\pi}\frac{{\rm d}V_{\rm c}}{{\rm d}z}} \int {\rm d}L\, \phi(L,z)\, S_s^{(i)}(L,z) S_s^{(j)}(L,z). \tag{3.53}$$

Several comments are in order:

- Typically, the GLF of astrophysical sources depends not only on the luminosity and redshift but also on at least one additional parameter characterizing the spectral energy distribution of the sources. The most common parameter is the index, Γ, of the spectral energy distribution which is often modeled as simple power law: ${\rm d}N/{\rm d}E \sim E^{-\Gamma}$. The extension of the formalism is trivial. Each function which depends on L also depends on Γ. Moreover, every integral in L is replaced by an integral in L and Γ, every Dirac delta functions in L is replaced by the product of delta functions in L and Γ.
- If the seeds of the source filed in Eq. (3.48) are not point-like, we would write $g(\vec{x},L) = \sum_a \int {\rm d}^3y\, \delta(\vec{y}-\vec{x}_a)\delta(L-L_a) g_s(\vec{x}-\vec{y},L)$. The final results of in Eq. (3.53) would then contain factors of the Fourier transform of g_s. For example, DM halos are not point-like but extended sources.

- The formalism is also used to calculate the flux of DM annihilation or decay. In the so-called halo model the DM density is approximated by the sum of DM halos which, in that case, form the seeds of the source field. Then, the GLF is replaced by the halo-mass function $\mathrm{d}N/\mathrm{d}m$ and the luminosity, L, by the halo mass, m. The separation of the power spectrum into two terms, cf. Eq. (3.51), are commonly denoted *1-halo* and *2-halo* term. An explicit derivation of the formalism for DM is used for example in Ref. [277].
- For the cross-correlation of different sources, each (normalized) source field carries an index i or j.
- If the APS contains more than one relevant source class the total power spectrum is given by the sum of auto- and cross-correlation. Explicitly, for two source classes i and j the total C_ℓ would be written as $C_\ell = C_\ell^{(ii)} + C_\ell^{(jj)} + 2\,C_\ell^{(ij)}$.

Part II

Results

Chapter 4

Antiproton production cross sections in cosmic rays

In Sec. 2.5 we discussed the special role of antiprotons in CRs. They are produced by the interaction of the primary p and He flux with p and He in the ISM. One main ingredient, and consequently also source of uncertainty, to predict the antiproton flux or its progenitor the antiproton source term is the production cross sections of antiprotons in the nuclear interactions $\mathrm{CR} + \mathrm{ISM} \to \bar{p} + X$. In the following, we will first update and compare the latest analytic cross section parametrizations by [117] and [119] in the pp channel. Here, we use the newly available data by the NA61 experiemnt [125]. Afterwards, we update the rescaling of the pp to the pA channel where we include for the first time the recent measurement of antiproton production in the pHe channel by LHCb [120, 283]. Finally, we derive the uncertainty on the antiproton source term due to nuclear cross sections and derive the interesting parameter space which should be covered by future high-energy experiments to improve predictions for the antiproton source term. The results of this section are based on the papers [3, 7].

4.1 Fitting the proton-proton channel

4.1.1 Parametrization of the antiproton production cross section

We exploit in the following fits: i) the parametrization by Di Mauro *et al.* [117] (their Eq. (12) , hereafter Param. I) and ii) the parametrization by Winkler [119] (Param. II). Both parametrizations are provided for the Lorentz invariant cross section, Eq. (2.42), as function of the kinematic variables $\sqrt{s}$, x_R, and p_T. We remind that these kinetic variables refer to the CM frame. Param. I depends on 8 free parameters, denoted as $\mathcal{C} = \{C_1 ... C_8\}$

$$\begin{aligned} \sigma_\mathrm{inv}(\sqrt{s}, x_\mathrm{R}, p_\mathrm{T}) &= \sigma_\mathrm{in}(1 - x_\mathrm{R})^{C_1} \exp(-C_2 x_\mathrm{R}) \\ &\quad \times \left[C_3 \left(\sqrt{s}\right)^{C4} \exp(-C_5 p_\mathrm{T}) + C_6 \left(\sqrt{s}\right)^{C7} \exp\left(-C_8 p_\mathrm{T}^2\right) \right] . \end{aligned} \tag{4.1}$$

Here σ_in is the total inelastic cross section which depends on the CM energy as stated in [117] (Appendix B). We note that this parametrization does not strictly enforce radial scaling invariance

at high energies. It incorporates the increase at large $\sqrt{s}$ dictated by the total inelastic cross section and it allows for some freedom in p_T as function of $\sqrt{s}$. On the other hand, Param. II depends on 6 parameters $\mathcal{C} = \{C_1 ... C_6\}$. It is given by

$$\sigma_{\text{inv}}(\sqrt{s}, x_{\text{R}}, p_{\text{T}}) \quad = \quad \sigma_{\text{in}} R\, C_1 (1 - x_{\text{R}})^{C_2} \left[1 + \frac{X}{\text{GeV}}(m_T - m_p)\right]^{-\frac{1}{C_3 X}}, \tag{4.2}$$

where the transverse mass is defined as $m_T = \sqrt{p_T^2 + m_p^2}$. We use the parametrization of the total inelastic cross section stated in [119]:

$$\sigma_{\text{in}} \quad = \quad c_{\text{in},1} + c_{\text{in},2} \log\left(\sqrt{s}\right) + c_{\text{in},3} \log^2\left(\sqrt{s}\right), \tag{4.3}$$

with the best-fit parameters $c_{\text{in},1} = 30.9$ mb, $c_{\text{in},2} = -1.74$ mb, and $c_{\text{in},3} = 0.71$ mb. The factor R changes the cross section behavior at small $\sqrt{s} < 10$ GeV, explicitly it is given by

$$R \quad = \quad \begin{cases} 1 & , \sqrt{s} \geq 10\,\text{GeV} \\ \left[1 + C_5 \left(10 - \frac{\sqrt{s}}{\text{GeV}}\right)^5\right] \exp\left[C_6 \left(10 - \frac{\sqrt{s}}{\text{GeV}}\right)^2 (x_{\text{R}} - x_{R,\text{min}})\right] & , \text{elsewhere} \end{cases} \tag{4.4}$$

with $x_{R,\text{min}} = m_p / E_{\bar{p}}^{\text{max}*}$[1]. Finally, the parameter X is defined as

$$X \quad = \quad C_4 \log^2\left(\frac{\sqrt{s}}{4 m_p}\right). \tag{4.5}$$

At this point, it is interesting to comment again on the radial scaling invariance and its regime of validity. For low energies, $\sqrt{s} < 10$ GeV, the scaling is broken explicitly by the $\sqrt{s}$ dependence of the factor R in Eq. (4.4). Then up to about 50 GeV scaling invariance is restored. To verify this from Eq. (4.2), we have to note that the last factor in the limit of small $\sqrt{s}$ (equivalently small X) behaves as

$$\left[1 + \frac{X}{\text{GeV}}(m_T - m_p)\right]^{-\frac{1}{C_3 X}} \xrightarrow[X \to 0]{} \exp\left(-\frac{m_T - m_p}{C_3}\right) \left[1 + \frac{(m_T - m_p)^2}{2 C_3} \frac{X}{\text{GeV}} + \mathcal{O}(X^2)\right]. \tag{4.6}$$

So, for small $\sqrt{s}$ and small p_{T} one obtains the typical exponential behavior in $m_T - m_p$. At a value of $p_T = 1.0$ GeV the correction from the exponential behavior reaches 10% at approximate $\sqrt{s} = 50$ GeV. This correction increases for larger $\sqrt{s}$ and larger p_{T}. However, the dominant amount of antiprotons is produced at small p_T as we will see in Sec. 4.4. The second violation of scaling invariance at high energies is due to the increase of σ_{in} with CM energy, cf. Eq. (4.3). In the following, we will update Param. II at low energies using the newly available data from NA61 which are taken at a $\sqrt{s}$ between 7.7 and 17.3 GeV. Since, this data is not expected to modify the

[1] Note that this parametrization of R differs from the parametrization used in [119] where the bracket $(x_{\text{R}} - x_{R,\text{min}})$ is squared. However, the effect of using or not using the square is very small down to $T_{\bar{p}}$ of 1 GeV. Furthermore, we refit the parametrization in the following and we find a good agreement with the available data. Also below $\sqrt{s} = 10$ GeV.

behavior at high energies we fix the parameter $C_4 = 0.038$, which is responsible for the breaking of scaling invariance above $\sqrt{s} \gtrsim 50$ GeV, to the best-fit value of [119]. The remaining five parameters will be varied freely in the fit.

If we want to calculate the total source term in our Galaxy we have to add antineutrons and antihypereons which subsequently decay into antiprotons. Following the analysis of [119] we take this into account by rescaling the prompt production cross section as stated in Eq. (2.47). For completeness we repeat the formulae for isospin asymmetry and hyperon production factor. They are explicitly given by

$$\Delta_{\mathrm{IS}} = \frac{c_1^{\mathrm{IS}}}{1 + (s/c_2^{\mathrm{IS}})^{c_3^{\mathrm{IS}}}}, \tag{4.7}$$

with $c_1^{\mathrm{IS}} = 0.114$, $c_2^{\mathrm{IS}} = (144\,\mathrm{GeV})^2$, and $c_3^{\mathrm{IS}} = 0.51$ and

$$\Delta_{\Lambda} = 0.81 \left(c_1^{\Lambda} + \frac{c_2^{\Lambda}}{1 + (c_3^{\Lambda}/s)^{c_4^{\Lambda}}} \right), \tag{4.8}$$

with $c_1^{\Lambda} = 0.31$, $c_2^{\Lambda} = 0.30$, $c_3^{\Lambda} = (146\,\mathrm{GeV})^2$, and $c_4^{\Lambda} = 0.9$. We adopt this rescaling for both, Param. I and Param. II.

4.1.2 Data sets to constrain antiproton production in the proton-proton channel

At intermediate energies, where the radial scaling is expected to work well, the cross section $p+p \to \bar{p}+X$ is constrained best by the data from NA49 [124] and NA61 [125]. Both experiments take data at $\sqrt{s} = 17.3$ GeV and their measurement agrees within uncertainty. However, while NA49 only provides data at this single energy, NA61 additionally provides measurements of the cross section at $\sqrt{s} = 7.7$ GeV, 8.8 GeV, and 12.3 GeV. These additional measurements allow, first, to verify our assumption of scaling invariances down to 10 GeV and, second, to constrain a part of the behavior at $\sqrt{s} < 10$ GeV, where the radial scaling is violated. However, the lowest cross section measurement of NA61 is taken at 7.7 GeV. The gap between this measurement and the production threshold at $4m_p = 3.75$ GeV should be constrained by additional data. So, we complement the NA49 and NA61 measurements with the data taken by Dekkers *et al.* [284] at $\sqrt{s} = 6.1$ and 6.7 GeV. Furthermore, in the case of Param. I, we add the data taken by the BRAHMS experiment at $\sqrt{s} = 200$ GeV [285] in order to fix the cross section behavior at high energies. On the other hand, for Param. II we only use NA49, NA61, and Dekkers since the high-energy behavior is kept fixed.

Finally, we have to address one subtlety: the modern experiments NA49 and NA61 provide a measurement of the prompt antiproton production cross section. In other words, they correct their measurement by excluding the contribution from intermediate hyperon states which decay inside of the detector volume, but have displaced vertices. However, for older measurements the situation is less clear. The typical assumption is that this kind of correction was not applied. To account for the effect in our analysis we subtract the antihyperon contribution $\Delta_{\Lambda}(\sqrt{s})$ from the Dekkers and BRAHMS data before fitting the cross section parametrizations. A similar treatment for antineutrons is not required. Because of their large lifetime of 881.5 s they always decay outside the detector. All data sets we use in the fit of the *pp* channel are summarized in Tab. 4.1.

Table 4.1: Summary of all *pp* data sets, their available CM energies, and references. Furthermore, we explicitly state for which parametrization (I and/or II) the data set will be used in the fit and which scale uncertainty σ_{scale} is adopted.

Experiment	$\sqrt{s}$ [GeV]	σ_{scale}	I	II	Ref.
NA49	17.3	6.5%	×	×	[124]
NA61	7.7, 8.8, 12.3, 17.3	5%	×	×	[125]
Dekkers *et al.*	6.1, 6.7	10%	×	×	[284]
BRAHMS	200	10%	×		[285]

4.1.3 Methods to fit the cross section parametrization to the proton-proton channel

In order to fit the two parametrizations to the available data sets listed in Tab. 4.1 we perform a χ^2-fit. The MINUIT package from the ROOT[2] software framework is used to minimize the χ^2 and to obtain the correlated uncertainties in the form of a covariance matrix. In the fit, we account for the statistical and systematic uncertainty which are added in quadrature, and an additional scale uncertainty σ_{scale}. The scale uncertainty allows to move up or down all the data points of each experiment simultaneously. For the NA49 experiment the scale uncertainty is 6.5%. It originates from the luminosity uncertainty of the proton beam. We assume that all other data sets are affected by a similar uncertainty. The adopted scale uncertainty for each experiment are stated in Tab. 4.1. If this uncertainty is not stated with the measurement it is estimated from the mean size of the systematic uncertainty. In order to map the scale uncertainty into the χ^2-definition we introduce a scale factor ω_k for each data set k. These parameters acts as nuisance parameters in the fit.

The total χ^2 as function of cross section parameters $\mathcal{C}$ and nuisance parameters $\boldsymbol{\omega}$ consist of two terms

$$\chi^2(\mathcal{C},\boldsymbol{\omega}) \;=\; \chi^2_{\text{stat}}(\mathcal{C},\boldsymbol{\omega}) + \chi^2_{\text{scale}}(\boldsymbol{\omega}), \tag{4.9}$$

where the first term contains the χ^2 of each single data point and the second term determines the constraints on the nuisance parameters $\boldsymbol{\omega}$ according to the scale uncertainties. Explicitly, the first term is given by

$$\chi^2_{\text{stat}}(\mathcal{C},\boldsymbol{\omega}) \;=\; \sum_{k=1}^{L}\sum_{i_k} \frac{\left(\omega_k\sigma_{\text{inv},i_k} - \sigma_{\text{inv}}(\mathcal{C},\sqrt{s}^{(i_k)},{x_{\text{R}}}^{(i_k)},{p_{\text{T}}}^{(i_k)}\right)^2}{\omega_k^2\sigma_{i_k}^2}. \tag{4.10}$$

Here i_k denotes the i-th data point of the data set k. Consequently, σ_{inv,i_k} is the Lorentz invariant cross section measured at this data point and σ_{i_k} is the corresponding quadratic sum of statistical and systematic uncertainty. Furthermore, $\sigma_{\text{inv}}(\mathcal{C},\sqrt{s}^{(i_k)},{x_{\text{R}}}^{(i_k)},{p_{\text{T}}}^{(i_k)}$ denotes the evaluation of the cross section parametrization (I or II) at the kinematic variables of the data point i_k. Note that each

[2] https://root.cern.ch

Table 4.2: Fit quality of the two fits in the *pp* channel of Param. I and II. The first row reports the χ^2 and the dof of the complete fit, while the additional rows show the contribution to the χ^2 of each single data sets.

	with Param. I	with Param. II
χ^2/dof	534.7/411	464.7/394
χ^2_{BRAHMS} (data points)	27.6 (21)	-
χ^2_{Dekkers}(data points)	9.8 (10)	8.3 (10)
χ^2_{NA49} (data points)	211.4 (143)	179.0 (143)
χ^2_{NA61} (data points)	286.0 (249)	277.4 (249)

data set is rescaled by the factor ω_k. In order to constrain this factor within the scale uncertainty $\sigma_{\text{scale},k}$ we use the second term of Eq. (4.9):

$$\chi^2_{\text{scale}}(\boldsymbol{\omega}) \quad = \quad \sum_{k=1}^{L} \frac{(\omega_k - 1)^2}{\sigma^2_{\text{scale},k}}. \tag{4.11}$$

4.1.4 Results on the antiproton production in the proton-proton channel

We fitted the Param. I and II to the data sets summarized in Tab. 4.1 accounting for the statistical, systematic and scale uncertainties as described above. Both parametrization provide a good fit to the available data sets. They result into a χ^2/dof of 1.30 and 1.18 for Param. I and II, respectively. We note that the reduced χ^2s for all the individual data sets converge to values close to 1. The exact values are stated in Tab. 4.2.
The best-fit parameters and the 1σ uncertainty for both parametrizations are summarized in Tab. 4.2. Moreover, the table contains the best-fit values of the scale parameters ω_k for each data set k. To obtain the full covariance matrix of all cross section and nuisance parameters we use the HESSE algorithm of the MINUIT package. The matrices are provided in the Appendix of Ref. [3]. We note that the NA61 data tends to converge to a scale factor slightly smaller than 1, while all other experiments have a scale factor which is slightly larger than 1. These nuisance parameters are expected to be compatible with 1 within the scale uncertainties $\sigma_{\text{scale},k}$. This is the case for both fits and all data sets. The posterior uncertainties of the nuisance parameters are only slightly smaller than $\sigma_{\text{scale},k}$, hinting that there is no tension among the various data sets. Therefore, we conclude that both parametrizations result in a good fit of available and most relevant data sets in the *pp* channel.

Now, we can use the two cross section parametrizations to derive the energy-differential cross section for antiproton production in the *pp* channel. The comparison of our refitted parametrizations with the original parametrizations, Refs. [117, 119], and the MC approach KMO [128] is shown in Fig. 4.1. The cross section is given as function of the kinetic energy of the antiproton, $T_{\bar{p}}$, at three fixed proton energies of $T_p = 20$ GeV, 450 GeV, and 6.5 TeV. All lines correspond to the prompt production of antiprotons in the *pp* channel, i.e. they do not include antineutrons or antihyperons. In order to obtain the uncertainty at the cross section level, we exploit the covariance matrix of

Table 4.3: Best-fit parameters and uncertainties for the fit of Param. I and II of the $p+p \to \bar{p}+X$ cross section. The full correlation matrices are provided in the appendix of [3].
$^{(*)}$ We remind that the parameter C_4 is fixed, *i.e.* not included in the fit, in Param. II (see text for details).

	with Param. I	with Param. II
C_1	3.50 ± 0.64	$(5.02 \pm 0.22) \times 10^{-2}$
C_2	5.59 ± 0.85	7.790 ± 0.077
C_3	$(4.00 \pm 0.73) \times 10^{-2}$	$(1.649 \pm 0.012) \times 10^{-1}$
C_4	-0.251 ± 0.071	$(3.800 \pm 0.057) \times 10^{-2}$ $^{(*)}$
C_5	2.651 ± 0.097	$(4.74 \pm 2.59) \times 10^{-4}$
C_6	$(3.78 \pm 0.53) \times 10^{-2}$	3.70 ± 0.64
C_7	$(4.3 \pm 4.3) \times 10^{-2}$	-
C_8	2.695 ± 0.047	-
ω_{BRAHMS}	1.115 ± 0.079	-
ω_{Dekkers}	1.051 ± 0.068	1.090 ± 0.090
ω_{NA49}	1.059 ± 0.039	1.061 ± 0.044
ω_{NA61}	0.936 ± 0.036	0.932 ± 0.038

each fit. For example, to obtain our 2σ band we sample 1000 realizations of the cross section and nuisance parameters, $\mathcal{C}$ and $\boldsymbol{\omega}$. Then, we insert each parameter realization into Eq. (4.9) and compute the χ^2. If the χ^2 difference with respect to the best-fit χ^2 is smaller than 4, we compute the energy-differential cross section as given by Eq. (2.46). The 2σ uncertainty band is the envelope of all realizations with $\Delta\chi^2 \leq 4$. We observe that the two parametrizations agree well within the uncertainties bands. Also, the original analytic parametrizations show a reasonable agreement with the refitted parametrizations. However, the MC approach by KMO significantly differs from all other parametrization at small energies, $T_{\bar{p}} \lesssim 10$ GeV and $T_p \lesssim 20$ GeV. This deviation was already noted in the introduction, Sec. 2. We remind again than at small energies of $\sqrt{s} < 10$ GeV the MC generators are not tuned to data and, therefore, should be less trusted.

Finally, we compute the local source term of CR antiprotons in the pp channel by solving the integral of Eq. (2.41). We assume a hydrogen density of $n_{\text{ISM}} = 1$ cm^{-3}. The local proton flux is taken from a fit of the measured proton flux by AMS-02 [58]. Solar modulation is demodulated within the force-field approximation for which we adopt a Fisk potential of $\varphi = 600$ MV. Note that antiprotons are only produced by CR protons above the threshold energy $T_p \geq 6m_p$. In Fig. 4.2 we compare the source term of prompt antiprotons for our two parametrizations and the same literature estimations as before. The shaded band again denotes the 2σ uncertainty from our fit of the cross sections. The lower panel of Fig. 4.2 displays the ratio of the source terms with respect to the best fit of Param. II. We observe that Param. I and II agree well within uncertainties. The agreement is particularly good between $T_{\bar{p}} = 10$ GeV and a few hundred GeV. Towards lower energies the deviation between the two parametrizations increases to 10% at 1 GeV, and similarly above 1 TeV the deviation increases to 10%. Note that at very high energies, $T_{\bar{p}} \gtrsim 1$ TeV, Param. II is more

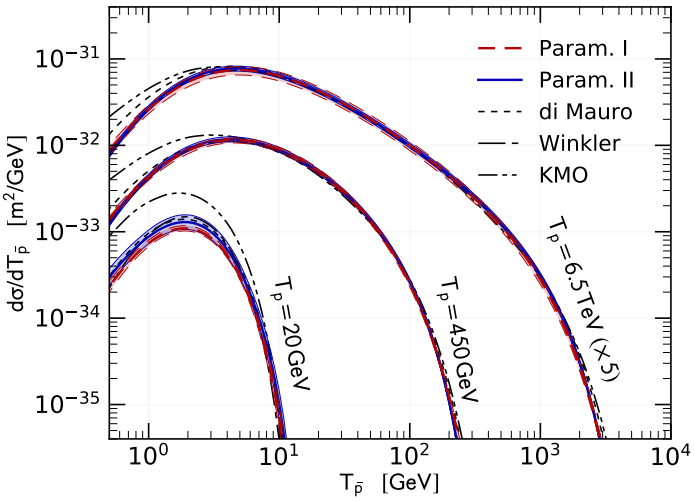

Figure 4.1: The energy-differential cross section $d\sigma/dT_{\bar{p}}(p + p \to \bar{p} + X)$ for prompt antiproton production at fixed proton energies, $T_p = 20$ GeV, 450 GeV and 6.5 TeV. The dashed (solid) line and the red (blue) band are the result of our analysis for Param. I and Param. II. The shaded uncertainty band displays the 2σ confidence interval. We report for comparison some literature estimations: di Mauro [117], Winkler [119], and KMO [128]. The figure is taken from Ref. [3].

trustworthy. It is specifically tuned to data up to CM energies of 2.7 TeV and takes violations of the radial scaling invariance explicitly into account, while Param. I is only fitted to data sets up to $\sqrt{s} = 200$ GeV. It was already noted in [117] that Param. I should be trusted up to $T_{\bar{p}} \sim 500$ GeV The uncertainty bands of both parametrizations are about 8% between $T_{\bar{p}} = 10$ GeV and a few hundred GeV and then increase at smaller or larger $T_{\bar{p}}$. In particular, we note that the uncertainty band of Param. II increases to 15% at 1 GeV. The reason for this increase at low energies is that the cross section shape is no longer determined by the radial scaling invariance since the invariance is broken at $\sqrt{s} < 10$ GeV. The uncertainty in the shape of the cross section translates into a shape uncertainty at the source term level. On the other hand, the uncertainty of the bands at high energies, $T_{\bar{p}} \gtrsim 10$ GeV is mostly a normalization factor. The original analytic parametrizations agree with our updates within uncertainties. Again, we note that the MC approach KMO significantly overpredicts the antiproton source term at $T_{\bar{p}} \lesssim 10$ GeV.

4.2 Fitting the proton-nucleus channel

In Sec. 2, we showed the contributions of the various channels to the total source term of CR antiprotons. The pp channel dominates with a contribution of 50% to 60% at all energies, while the rest is provided by pA channels. In practice, the most important proton-nucleus channels are the pHe and Hep channels, they make up 15% to 20% each. Heavier channels contribute at the percent

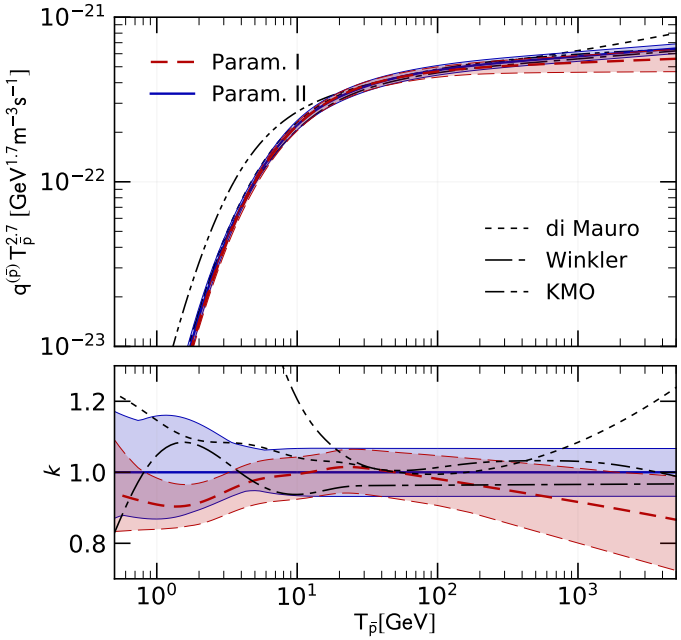

Figure 4.2: Antiproton source term in pp channel and its uncertainty from nuclear cross sections derived from our fits of Param. I (red dashed) and Param. II (blue solid), respectively. For comparison, we show the antiproton source term from previous parametrizations (cf. Fig 4.1). The shaded uncertainty bands display the 2σ uncertainty. In the lower panel we show the ratio of the source term to the best fit of Param. II. So, by definition the solid blue line is equal to 1. The figure is taken from Ref. [3].

level. Thus, our goal in the following is to find a good parametrization for the pHe and Hep. Since data is very scarce we cannot find a standalone parametrization of these channels. Instead, we rely on a rescaling from the pp channel exploiting the very precise data in the pC data by NA49 and the recent measurement in the pHe channel by LHCb. We will not include data of heavier nuclei as done in [121], since our focus lies on the light nuclei relevant in CRs. If, on the other hand, a precise determination of cross section with heavier nuclei like iron or lead is required this analysis should be redone including further data sets.

4.2.1 Rescaling of the proton-proton to the proton-nucleus channels

Before going into details, we remind our simple picture for the parametrization of pA channels that in practice the scattering occurs between the projectile proton and either one proton or one neutron in the nucleus. Therefore, in the following all kinematic variables and the definition of the CM frame refer to the nucleon-nucleon frame. One important difference between the pp channel and the

pA channel (or better proton-nucleon channel) are symmetries. Both reaction establish a cylindrical symmetry around the beam axis. However, only the pp channel is symmetric under reflection along the beam axis in the CM frame. The shielding effects in the pA channel and enhancements in the pn channel with respect to pp due to isospin violations break the reflection symmetry. Therefore, the appropriate kinematic variables in the pA channel is not the radial scaling, x_{R}, since the use of x_{R} indirectly assumes reflection symmetry. In other words, we cannot distinguish between antiproton production in forward or backward direction using x_{R}. Therefore, instead of x_{R} we will the Feynman scaling x_f which is proportional to the longitudinal momentum and, hence, distinguishes forward ($x_f > 0$) and backward ($x_f < 0$) production. The cross-section asymmetry is actually visible in the NA49 pC data [122]. To describe this asymmetry we use the fact that the antiproton production can be split into two contributions, one originating from the projectile and the other originating from the target nucleon. The consequence is that the projectile produces antiprotons mostly in forward direction and the target mostly in backward direction. This kind of splitting is observed also in pion production. The so-called projectile overlap function F_{pro} characterizes the fraction of particles produced from the projectile. It depends only on x_f and was measured and tabulated in [122] from pion production. We repeat the definition of $F_{\mathrm{pro}}(x_f)$ for completeness in Tab. 4.4. The target overlap function is inferred by $F_{\mathrm{tar}}(x_f) = 1 - F_{\mathrm{pro}}(x_f) = F_{\mathrm{pro}}(-x_f)$. Separately, adjusting the projectile and target overlap function in the pA channels allows to incorporate an effective forward-backward asymmetry. This approach was already pursued in [119]. Finally, we define our rescaling factor for the pA channel. The rescaling is done at the level of the fully-differential Lorentz-invariant cross section:

$$\sigma_{\mathrm{inv}}^{pA}(\sqrt{s}, x_f, p_{\mathrm{T}}) \quad = \quad f^{pA}(A, x_f, \mathcal{D})\ \sigma_{\mathrm{inv}}^{pp}(\sqrt{s}, x_{\mathrm{R}}, p_{\mathrm{T}}). \tag{4.12}$$

Table 4.4: Definition of the projectile overlap function $F_{\mathrm{pro}}(x_f)$. The table is copied from [122].

x_f	F_{pro}	x_f	F_{pro}
-0.250	0.0000	0.250	1.0000
-0.225	0.0003	0.225	0.9997
-0.200	0.0008	0.200	0.9992
-0.175	0.0027	0.175	0.9973
-0.150	0.010	0.150	0.990
-0.125	0.035	0.125	0.965
-0.100	0.110	0.100	0.890
-0.075	0.197	0.075	0.803
-0.050	0.295	0.050	0.705
-0.025	0.4	0.025	0.6
		0.000	0.5

Table 4.5: Data sets used to fit the antiproton production in the pA channel. We compare the CM energies, $\sqrt{s}$, and scale uncertainties σ_{scale}. Furthermore we state which data set is used in the four fits discussed in the result section and give references.

	$\sqrt{s}$ [GeV]	σ_{scale}	I-A	I-B	II-A	II-B	Ref.
NA49	17.3	6.5%	×	×	×	×	[122]
LHCb	110	6.0%		×		×	[120]

Here A is the mass number of the nucleus and $\mathcal{D} = \{D_1, D_2\}$ are the two fit parameters which will be adjusted to data in the following. Explicitly, the factor f^{pA} is given by:

$$f^{pA} = A^{D_1}\left[A^{D_2}\left(1+\frac{N}{A}\Delta_{\text{IS}}\right)F_{\text{tar}}(x_f) + F_{\text{pro}}(x_f)\right]. \tag{4.13}$$

The first factor A^{D_1} determines the overall enhancement of the pA cross section with respect to the pp case. In our simple picture, where individual nucleons interact and produce the antiprotons, we expect D_1 to be close to 1. On the other hand, A^{D_2} gives the enhancement of the target production with respect to the projectile. The summand $\frac{N}{A}\Delta_{\text{IS}}$ corrects for the fact that the production of antiprotons in a pn interaction is enhanced with respect to pp. N is the number of neutrons in the target nucleus.

The fit procedure is analogous to the procedure described in the pp channel. The definition of χ^2 can be copied from Eqs. (4.9) to (4.11), if the fit parameters $\mathcal{C}$ are replaced by $\mathcal{D}$. We note that in the following fits the parameters $\mathcal{C}$ are fixed to the best-fit values of the previous section and only the two new parameters $\mathcal{D}$ are included in the fit. Consequently, the sum over data sets k runs only over the new pA data. As in the pp case we allow one nuisance parameter, ω, to rescale each data set.

4.2.2 Data sets to constrain antiproton production in the proton-nucleus channels

We use the data of NA49 in the pC channel and the LHCb data in the pHe channel. They are both fixed-target experiments where the projectile proton is accelerated to 158 GeV and 6.5 TeV, respectively. Both experiments provide very precise data of the prompt antiproton production, namely, any contribution from antihyperons has been removed. The two data sets are summarized in Tab. 4.5.

4.2.3 Results on the antiproton production in the proton-nucleus channels

In this section we discuss the result of four fits of the factor f^{pA}. Our goal is, first, to determine a good parametrization of f^{pA} for Param. I and II and, second, to determine the impact of the newly available LHCb data. In detail, the four fit setups differ in the parametrization of the pp channel (I and II) and the data included in the fit. We will refer to the fit as I-A or II-A if it includes only the pC data of NA49, while we will refer to I-B and II-B if it contain additionally the LHCb data.

The results of all four fits are summarized in Tab. 4.6 and 4.7. Let us first focus on the fits I-A and II-A, without LHCb data. We see that the rescaling of both parametrizations provides a good fit of the pC data. The reduced χ^2s are 1.3 and 1.1, respectively. The parameters of D_1 and D_2 are almost independent of the parametrizations and converge to 0.83 and 0.15. This meets our expectations that D_1 is close to 1 and D_2 a small asymmetry (see above).

Now, we would like to determine the impact of the LHCb data. The first step is to use our fit results I-A and II-A to predict the cross section at the kinematic variables where LHCb takes its data points. Then we use the prediction to calculate the χ^2 of the LHCb data set. Our results are $\chi^2_{\text{LHCb}} = 1266$ and 212 for Param. I-A and II-A, respectively, for 136 data points. Here it is already visible that Param. II fits the LHCb data much better than Param. I. In fact, this result is not very much surprising. The LHCb data is taken at very large $\sqrt{s} = 110$ GeV. At those energies we are far beyond the regime where radial scaling is applicable. So, the observation that Param. II fits better with the LHCb data is probably due to the fact that the underlying pp cross section at $\sqrt{s} = 110$ GeV works better for Param. II than for Param. I. To strengthen our conclusion that Param. II works better with LHCb data we now look at the results of the fits I-B and II-B which include the LHCb data in the fit setup. We obtain reduced χ^2s of 8.4 and 1.4, respectively, for Param. I-B and II-B. The large χ^2 of I-B is due to the LHCb data. A closer look at the comparison of the best-fit parametrizations I-B and II-B with the LHCb data, as presented in Fig. 4.3, reveals

Table 4.6: Summary of the fit quality of f^{pA} for the different Param. I and II, and for the different data sets A (NA49 pC) and B (NA49 pC, LHCb pHe). The first row contains the χ^2 and the dof, while the second and third rows show the separate contributions from the pC and pHe data sets. The number of data points for each data set is displayed in brackets. The italic numbers are not the result of the fit but a χ^2 calculation of the predicted cross section where the parameters $\mathcal{D}$ are fixed to the best-fit of Param. I-A and II-A.

	Param. I		Param. II	
	A	B	A	B
χ^2/dof	153.0/118	1296.3/253	131.2/118	326.3/253
χ^2_{NA49}	153.0 (121)	155.3 (121)	131.2 (121)	131.8 (121)
χ^2_{LHCb}	*1266 (136)*	1141 (136)	*212.4 (136)*	194.5 (136)

Table 4.7: Fit results of the four different fits discussed in the result section.

	Param. I		Param. II	
Parameter	A	B	A	B
D_1	0.830 ± 0.012	0.825 ± 0.012	0.825 ± 0.012	0.828 ± 0.012
D_2	0.149 ± 0.013	0.167 ± 0.012	0.154 ± 0.013	0.145 ± 0.012
ω_{NA49}	1.000 ± 0.025	1.001 ± 0.024	1.000 ± 0.025	0.997 ± 0.024
ω_{LHCb}	-	0.900 ± 0.015	-	1.034 ± 0.018

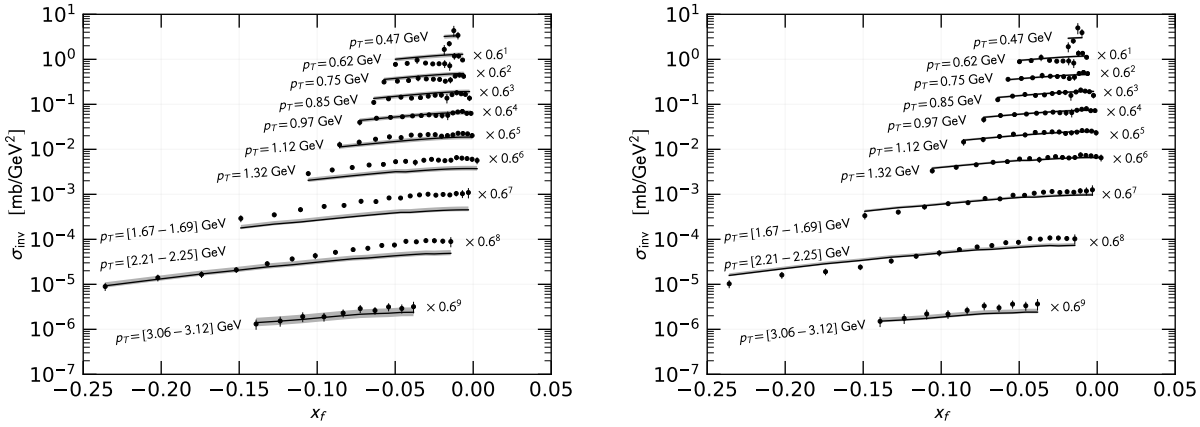

Figure 4.3: Comparison of LHCb data to the fit with Param. I-B (left) and Param. II-B (right). The grey band corresponds to 2σ uncertainty in the fit. The LHCb data agree better with Param. II and, therefore, they select this model for the high-energy behavior of the Lorentz invariant cross section. The figure is taken from Ref. [3].

that the problem is related to the $p_{\rm T}$-shape of the underlying pp parametrizations[3]. For Param. II-B the LHCb data is fitted reasonably at all $p_{\rm T}$, while for Param I-B there is a significant mismatch between best fit and data at $p_{\rm T} \sim 1.5$ GeV. We observe that the best-fit parameters D_1 and D_2 are not largely affected by adding the LHCb data. Consequently, we infer that in general the rescaling of pp to pHe and pC works as expected. The important point however, is that before LHCb data we entirely relied on an interpolation between pp and pC. Here, with the new data, we show for the first time that this interpolation is correct for pHe. This is a very important conclusion of this analysis, although the kinetic parameter space in which LHCb takes its measurements is only marginally relevant for CRs. Finally, we note that the LHCb select the cross-section parametrization (Param. II) which has the slightly harder trend at high energies. This is an important conclusion of this chapter.

Before calculating the energy-differential cross section and the source terms in the pHe and Hep channels we would like to extend Eq. (4.13) to the more general case of nuclei as projectile. The straight forward extension[4] is

$$f^{A_1A_2} = A_1^{D_1} A_2^{D_1} \left[A_1^{D_2} \left(1 + \frac{N_1}{A_1} \Delta_{\rm IS} \right) F_{\rm pro}(x_f) + A_2^{D_2} \left(1 + \frac{N_2}{A_2} \Delta_{\rm IS} \right) F_{\rm tar}(x_f) \right], \quad (4.14)$$

where the subscript 1 denote the projectile and 2 the target. We checked that the parametrization of Eq. (4.14) is self-consistent within the current uncertainties. Namely, we calculated the resulting

[3]The $p_{\rm T}$ shape is not changed by f^{pA}.

[4]Note that there is actually one subtlety in the extension. It is not certain how (or if) the antiproton production in neutron-neutron scattering is enhanced with respect to the proton-proton case. In the formula the neutron-neutron scattering is enhanced by the isospin asymmetry twice. We will not elaborate this issue further, since the effect is very much suppressed. It appears only in the HeHe channel and even heavier channels.

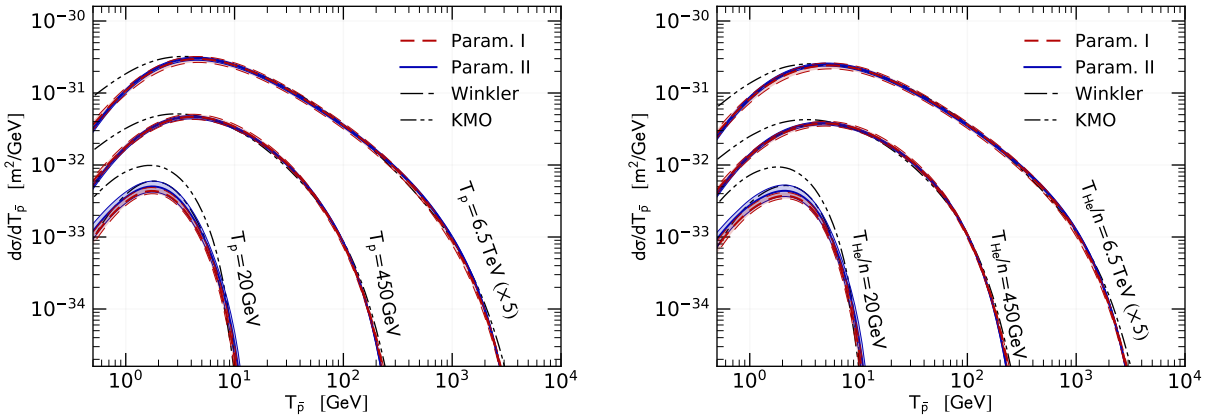

Figure 4.4: Energy-differential antiproton production cross section in the pHe (left) and Hep (right) channels. All lines correspond to the prompt antiproton production. The cross section are shown as function of antiproton kinetic energy for three representative fixed projectile kinetic energies per nucleon, $T_{\rm pro}/n = 20$ GeV, 450 GeV, and 6.5 TeV. The dashed red line and solid blue correspond to our Param. I-B and II-B. The shaded bands denote the 2σ statistical uncertainty of our fit. We compare with predictions from literature of Winkler [119] and KMO [128]. The figure is taken from Ref. [3].

antiproton source term of the Hep channel in two different ways. The first way is to use Eq. (4.14). The second way (which is the "correct" and self-consistent way) is more involved: we used the cross-section parametrization of the pHe channel and transformed this to the ISM frame. Then to get the Hep channel we performed a Lorentz transformation to the frame where the p is at rest. Finally, we performed the integrations to obtain the energy-differential cross section and source term. Compared to the cross section induced uncertainty of the source term the deviation between the two methods is negligible. All plots in the following exploit on the first way which requires less computation.

Figure 4.4 shows the energy-differential cross section for prompt antiproton production in the pHe (left) and the Hep (right panel) channel as obatained from our fit. We compare with the literature estimations from [119, 128]. As before the MC approach deviates significantly at $T_{\bar{p}} \lesssim 10$ GeV. The uncertainty bands of our fits display the 2σ uncertainty. To obtain the band we proceed as follows. We sample 1000 realizations of the full parameter set $(\mathcal{C} + \mathcal{D})$ from the covariance matrices. From there we compute the total χ^2, which is the sum of the pp and the pA fit. Finally, we require that the total χ^2 difference is smaller or equal to 4 and individually that the χ^2 of the pp channel is smaller than 4. In this way we ensure that the pp fit remains a prior to the pA fit, or in other words, we make sure that the $\mathcal{C}$ parameters in the band are not driven by the pA data. The size of the uncertainty band is similar to the pp case. This is expected since the pp channel is the prior of all heavier channels. Note that all uncertainties from pp directly translate into the heavier channels.

We calculated the source term of prompt CR antiprotons in the pHe and Hep channels from the

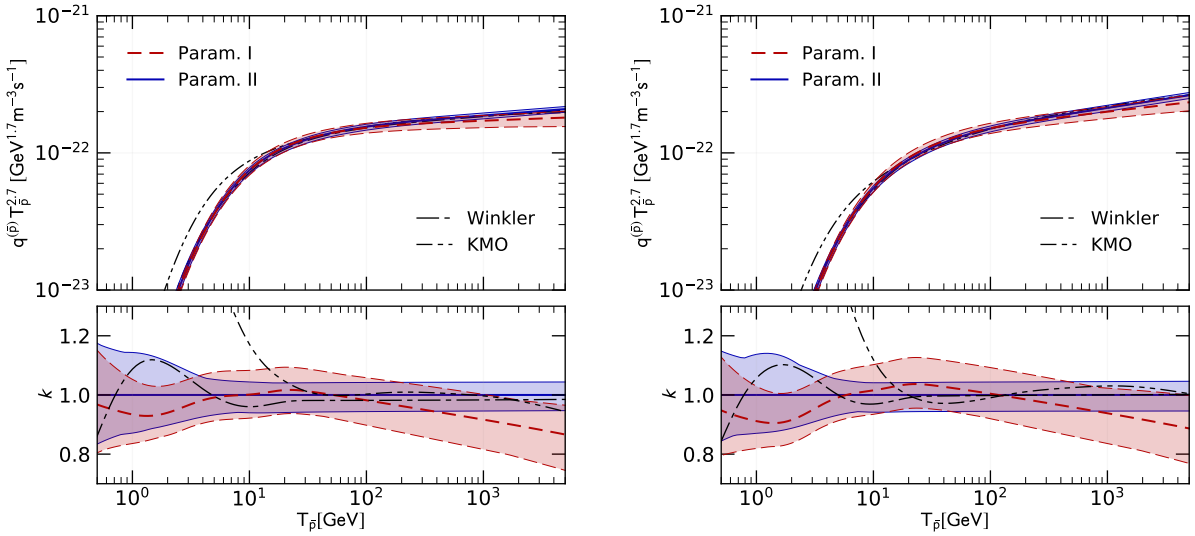

Figure 4.5: Source term of CR antiprotons in the pHe (left panel) and Hep (right panel) channels. We show the best fit of Param. I-B and II-B. Uncertainties are given at the 2σ confidence interval. For details on the literature comparison refer to Fig. 4.4. The figure is taken from Ref. [3].

energy-differential cross section of Fig. 4.4. The results are shown in Fig. 4.4 which is very similar to the pp channel, Fig. 4.2. In the calculation of the pHe channel, we use an ISM density of He which is 0.1 cm^{-3}, while in the Hep channel we use a fit of the helium flux measured by AMS-02 [59] and corrected for solar modulation in the force-field approximation as before. In our calculation we assume that the helium flux is 100% ^{4}He, which is of course an approximation. In reality a fraction of 10–15% of the helium flux is ^{3}He. Finally, we note that the source term in the Hep channel is softer than in the pp and pHe channel. This is related to the fact that the proton flux is harder compared to the helium flux measured by AMS-02.

4.3 The total antiproton source term

In this paragraph, we will derive the total source terms of CR antiprotons. We use all the information of the previous paragraphs on the prompt antiproton production cross section and then add the contribution from antineutrons and antihyperons as discussed in Sec. 2.5. Here we calculate the source term of various CR-ISM combinations, in particular, also combination with heavier nuclei in the CR species. The results are shown in Fig. 4.6. The four dominant channels, pp, pHe, Hep, and HeHe, are given individually, while the contribution of heavier channels are grouped into: all channels with CNO, MgNeSi, LiBeB, or Fe in the CR initial state. The CR fluxes in the calculation are taken from [74] (Li, Be and B), [73] (C and O), [286] (N). For all heavier nuclei we use the

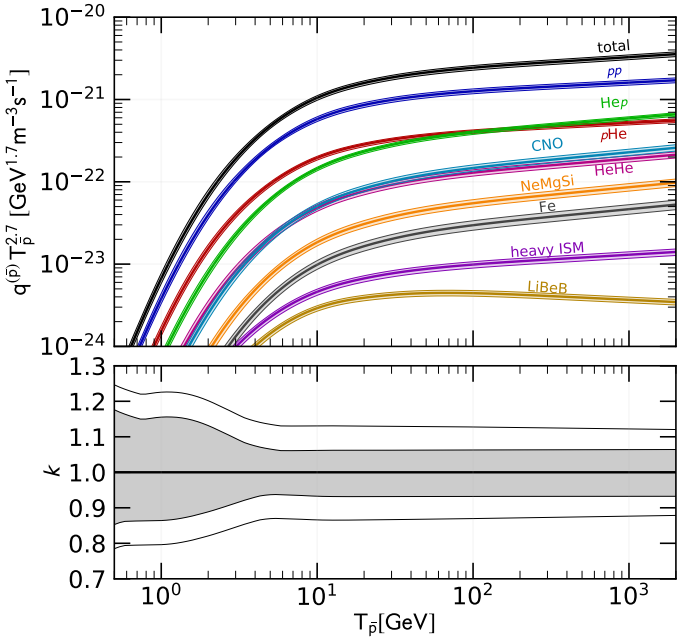

Figure 4.6: Source terms of CR antiprotons and separate CR-ISM contributions, derived from Param. II-B. The shaded bands denote the 2σ uncertainty due to prompt antiproton production cross sections. The lower panel shows the relative uncertainty of the total source term. The shaded band is again the 2σ uncertainty due to prompt antiproton production cross sections, while the open band shows the additional uncertainty from isospin violation and hyperon decay. Fig 2.7 is derived from this plot. The figure is taken from Ref. [3].

oxygen ratios in [287] and multiply with the oxgen flux from AMS-02. The local ISM density contribution from nuclei heavier than He is taken from [288]. We observe that all CNO channels are equally important as the HeHe channel. This is interesting since the HeHe channel is usually taken into account in analyses of CR antiprotons while the CNO channels are often neglected. Even the contribution of MgNeSi and Fe are above 1%. While the contribution of heavier ISM or the secondaries LiBeB are in principle interesting since they result in a different shape of the source term, they are always reduced to 1%.
In the lower panel of Fig. 4.6 we show the relative uncertainty of the total cross section. At the 2σ level the uncertainty from the prompt cross-section parametrization is $\pm 8\%$ at $T_{\bar{p}} \gtrsim 5$ GeV. It increases to $\pm 15\%$ at 1 GeV (shaded band). To obtain the total uncertainty due to cross section (open band) we have to add uncertainty of the antihyperon factor and the isospin violation term. These uncertainties are taken from [119] (cf. also to Fig. 2.9). All in all, we obtain an uncertainty on the total source term of $\pm 20\%$ at 1 GeV and $\pm 12\%$ at $T_{\bar{p}} \gtrsim 5$ GeV.

4.4 Requirements for future cross section measurements

In the previous section we fitted the antiproton production cross section and derived the uncertainties which are imposed on the source term. If we now compare the uncertainties of the antiproton flux measured by the AMS-02 experiment with the uncertainties of the source term we realize that there is a mismatch in accuracy[5]. AMS-02 measures antiprotons with an accuracy of about 5% between 1 GeV and 100 GeV, while the source term uncertainties range from 12% to 20% depending on the exact energy. This simple argument shows that further effort is required to improve our knowledge on antiproton production cross sections if we do not want to be limited in the interpretation of the current antiproton flux measurements by nuclear physics.

In this section we will answer the question at which energies and which transverse momenta (or equivalently angles) future measurements should be performed. The answer will be guided by two principles:

1. The uncertainty on the source term (and consequently on the flux) of CR antiprotons shall be equal or smaller than the uncertainty of the currently best measurement of the flux by the AMS-02 experiment.

2. The cross section should be measured first and most precise in the kinetic parameter space which gives the largest contribution to the source term.

However, before really going to the topic it is instructive to first analyse the fraction of the source term which is covered by current cross-section experiments. We first focus on the pp channel and comment on the pA channels towards the end of this section.

4.4.1 Fractional contribution of the source term

Here we derive the fraction of the source term which is determined by the measurement of a given experiment. We call this fraction *source term contribution* in the following. To obtain this quantity we calculate the source term (in the pp channel) while restricting the kinetic variables $\sqrt{s}$, x_f, and p_T to the parameter space which is covered by the experiment. Explicitly, this restricted source term $q_{pp,\mathrm{exp}}$ is obtained by replacing the energy-differential cross section in Eq. (2.41) by

$$\left(\frac{\mathrm{d}\sigma_{pp}}{\mathrm{d}T_{\bar{p}}}\right)_{\mathrm{exp}}(T_i, T_{\bar{p}}) = p_{\bar{p}} \int \mathrm{d}\Omega \left(E\frac{\mathrm{d}^3\sigma_{ij}}{\mathrm{d}p^3}\right)(p_i, p_{\bar{p}}, \eta)\, \omega_{\mathrm{exp}}(\sqrt{s}, x_f, p_\mathrm{T}). \tag{4.15}$$

Note that this equation is equivalent to Eq. (2.46) apart from the factor $\omega_{\mathrm{exp}}(\sqrt{s}, x_f, p_\mathrm{T})$ which is equal to 1 if the kinematic variables ($\sqrt{s}$, x_f, p_T) are within the region measured by the experiment and 0 otherwise. Then the source term contribution of an experiment is defined as the ratio of the restricted source term and the total source term, $q_{pp,\mathrm{exp}}/q_{pp}$. From the previous section we know that the NA61 experiment provides the most precise and relevant data in the pp channel. The source term contribution of this experiment is shown in Fig. 4.7. The NA61 experiment helps to

[5]Note that the relative uncertainty of source term and propagated flux are identical at first approximation. This will be addressed more carefully in the following.

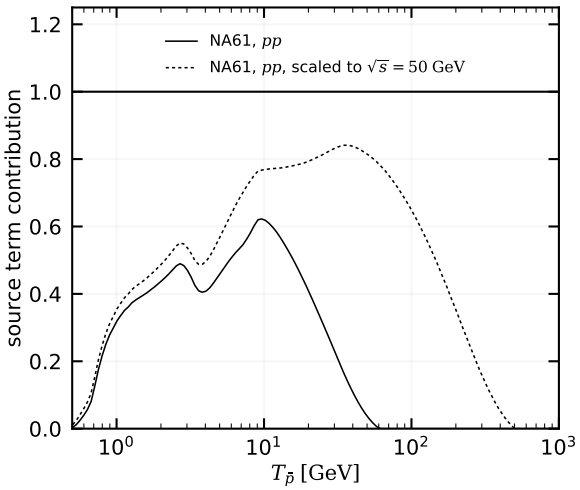

Figure 4.7: The solid line shows the source term contribution of the NA61 experiment in the pp channel. If we assume that the Lorentz invariant cross section does not depend on $\sqrt{s}$ between 10 GeV and 50 GeV (radial or Feynman scaling [119]), we obtain the dotted contribution.

determine the source term between $T_p \sim 0.5$ GeV to 60 GeV. The contribution shows two peaks at 2.5 GeV and 10 GeV with a contribution of ∼50% and 60%, respectively. Between the two peaks the contribution drops to 40%. The peak at $\sim$ 10 GeV comes from the parameter space which is directly measured by the NA61 experiment. Since, the pp channel is symmetric in under $x_f \to -x_f$ we obtain the second peak at 2.5 GeV[6]. The fact that the source term contribution at low energies is smaller than at higher energies can be explained from kinematics. Antiprotons at very small $T_{\bar{p}} \sim 1$ GeV can be produced in the interaction of protons with almost any energy above T_{th}. On the other hand, antiprotons at higher energies are more constrained by $T_{\bar{p}} < T_p$. It is instructive to take another look at Fig. 2.8. The dotted line in Fig. 4.7 gives the contribution if we use additionally to the NA61 measurement the theoretical argument of radial scaling. In this case, we can extend the "measured" parameter space of NA61 from $\sqrt{s} = 17.3$ GeV to 50 GeV, which is the upper CM energy to which radial scaling invariance is valid. We observe an improvement, in particular, of the source term contribution of the second, high-energy peak. The source term fraction probed by the NA61 data is now approximately 80% between 10 GeV and 100 GeV. Note that from this exercise we can understand very well why the uncertainty of the source term in Fig. 4.6 increases significantly below $T_{\bar{p}} \lesssim 5$ GeV: This kinematic regime is not well covered by the precise measurement of NA61. So, already at this point we have the hint that additional measurements at CM energies below 7.7 GeV (NA61 lowest $\sqrt{s}$) would be important to obtain a more precise source term at $T_{\bar{p}} \lesssim 5$ GeV.
The only measurement in the pHe channel is currently provided by the LHCb experiment. Here

[6]The source term contribution of the NA61 experiment shown in [3] differs from this figure, since there the x_f symmetry was not exploited.

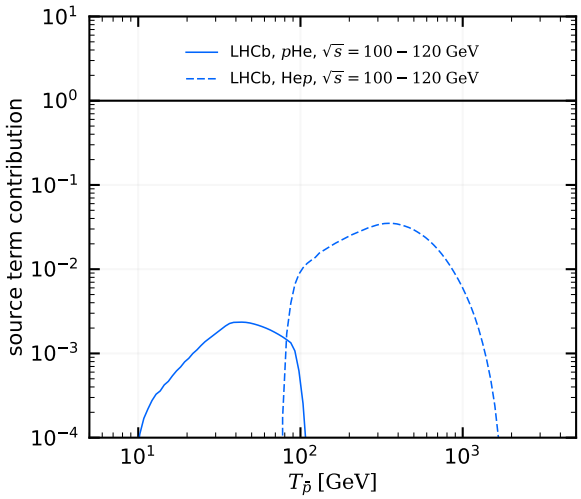

Figure 4.8: The solid (dashed) line shows the source term contribution of the LHCb experiment to the pHe (Hep) channel. The experiment measures antiprotons produced in the interaction at single $\sqrt{s} = 110$ GeV. We assume that it possible to extrapolate the knowledge of the source term to a range from 100 GeV to 120 GeV.

antiproton data is taken at $p_{\bar{p}}$ between 10 GeV and 110 GeV for production in a collision of 6.5 TeV protons on fixed-target helium. In the proton-nucleus channels the x_f symmetry is broken, but we can use the fact that the transformation $x_f \to -x_f$ relates the pHe channel with the Hep channel. In other words, we can take the measurement in the pHe channel as an indirect constraint of the Hep channel. The source term contribution of the LHCb experiment to the total source term in the pHe and Hep channel are shown in Fig. 4.4 (note the logarithmic y-axis). As expected, the contribution in the pHe peaks between $T_{\bar{p}} = 10$ GeV and 110 GeV. It reaches a maximum of 2.5 pre-mill. The contribution in the Hep channel peaks at 80 GeV and 2 TeV and reaches at most 3.5%. This shows the importance of additional measurements in the helium channels if we do not want to rely on rescaling from carbon or on large extrapolations in the kinematic parameter space.

4.4.2 Prescriptions on antiproton cross-section data for precise theoretical antiproton flux predictions

In the following, we will systematically answer the question which cross-section measurement are required if we want to fully exploit the information of the currently most precise antiproton flux measurement by AMS-02. In other words, we want to determine the antiproton production cross section at least as precise the CR antiproton flux measurement by AMS-02. We will give advice on the kinetic parameter space which should be covered and on the accuracy which should be reached. To obtain this answer we invert the calculation of the source term from the Lorentz invariant cross section. At each step of the calculation we keep track of the uncertainty we want to obtain which

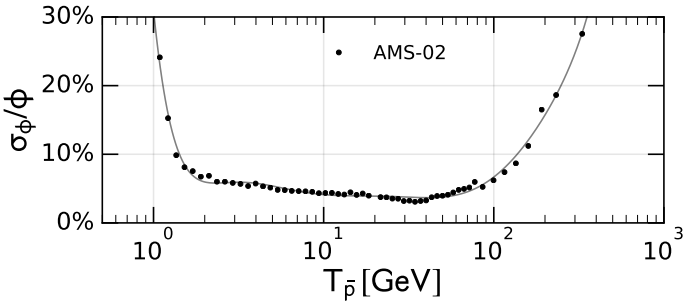

Figure 4.9: Relative uncertainty of the CR antiproton flux measurement by the AMS-02 experiment [75]. We add statistical and systematic uncertainties in quadrature. The figure is taken from Ref. [7].

is guided by the accuracy of the AMS-02 flux measurement.

To start our discussion we have a closer look at the precision of the AMS-02 measurement of CR antiprotons. Figure 4.9 shows the relative uncertainty of the AMS-02 measurement as function of $T_{\bar{p}}$. The data points and uncertainties are taken from [75]. We account for statistical and systematic uncertainties by adding them in quadrature. The antiproton flux is measured at an accuracy of about 5 percent between $T_{\bar{p}} = 2$ GeV and 100 GeV. It increases to 30% at 1 GeV and at 350 GeV. For the following calculation we parametrize this relative uncertainty with the solid black line. Note that the relative uncertainty of the CR flux and the source term are identical at first order. This can be seen from the theoretical description of Galactic CRs. The source term and local interstellar flux are related by propagation which is typically described in terms of a diffusion equation. This equation (Eq. (2.20)) links the source term and the flux linearly, namely, an increase of the source term by 5% will increase the flux by 5%. At low energies this simple argument only works approximately since reacceleration and energy losses might smear out a bit the relative uncertainty. We checked this potential effect by propagating source terms with peaked Gaussian energy spectra using GALPROP[7] [87, 88]. We found that the approximation of constant relative uncertainty for the source term and flux

$$\sigma_q^{\mathrm{rel}}(T_{\bar{p}}) \equiv \frac{\sigma_q(T_{\bar{p}})}{q(T_{\bar{p}})} \approx \frac{\sigma_{\phi_{\bar{p}}}(T_{\bar{p}})}{\phi_{\bar{p}}(T_{\bar{p}})}, \tag{4.16}$$

is valid in the energy range above 1 GeV. However, one subtlety arises from solar modulation. The link between flux and source term established above is valid for the local interstellar flux while AMS-02 measures the TOA flux which is affected by solar modulation. If we treat solar modulation in the force-field approximation we can correct the effect on the relative uncertainty. It amounts to a shift in energy: $\sigma_q^{\mathrm{rel}}(T_{\bar{p}}) = \sigma_\phi^{\mathrm{rel}}(T_{\bar{p}} + e \cdot \varphi)$, where $T_{\bar{p}}$ is the flux measured by AMS-02 and φ is the Fisk potential. We fix $\varphi = 600$ MV.

In the following, we will derive the maximal allowed uncertainty of the cross-section measurement such that we do not overshoot $\sigma_q^{\mathrm{rel}}(T_{\bar{p}})$ as dictated by the AMS-02 experiment. The first question

[7] http://galprop.stanford.edu/

which has to be answered is how to distribute the relative uncertainty on the various CR-ISM channels. We decide that all channels should be measured with the same relative accuracy:

$$\sigma_q^{\mathrm{rel}}(T_{\bar{p}}) = \sigma_{q_{ij}}^{\mathrm{rel}}(T_{\bar{p}}). \tag{4.17}$$

With this information we can focus on the pp channel and extend to the pA channels at the end of this section. We begin by deriving the contribution of the source term from each parameter point. The relation of the source term and the invariant cross section is given by:

$$q(T_{\bar{p}}) = \int_{\log(T_{\mathrm{th}})}^{\infty} \mathrm{d}\log(T) \int_{0}^{\infty} \mathrm{d}\eta \underbrace{\frac{8\pi^2\, p_{\bar{p}}\, n_{\mathrm{ISM}}\, T\, \phi(T)\, \sigma_{\mathrm{inv}}(T_{\bar{p}}, T, \eta)}{\cosh^2(\eta)}}_{\equiv I(T_{\bar{p}}, T, \eta)}. \tag{4.18}$$

From here we define the containment

$$x(T_{\bar{p}}, T, \eta) = \frac{1}{q(T_{\bar{p}})} \int_{I(T_{\bar{p}}, T', \eta') > I(T_{\bar{p}}, T, \eta)} d\log(T') d\eta'\; I(T_{\bar{p}}, T', \eta'), \tag{4.19}$$

which by definition varies between 0 and 1. Let us understand the meaning of the containment x at an example. The parameter space with $x(T_{\bar{p}}, T, \eta) < 0.9$ contains 90% of the source term. This argument can be inverted: if a one searches a volume which contains 90% of the source term, we can select $x(T_{\bar{p}}, T, \eta) < 0.9$. Note that here the definition of the volume is defined through Eq. (4.19). In general, there are infinitely many different volumes which contain 90% of the source term. The definition of x selects a specific volume, which minimizes the area in the $\log(T)$-η-plane for each fixed $T_{\bar{p}}$. Certainly, this choice is a bit arbitrary, but the two variables $\log(T)$ and η respect the natural scaling of the cross section and the CR proton flux. Furthermore, the integrand $I(T_{\bar{p}}, T, \eta)$ is strongly peaked in one single maximum. Using different variables could change the volume slightly, but not drastically. In practice, we compute $x(T_{\bar{p}}, T, \eta)$ on a 3-dimensional grid with 400 grid points in each direction. It was checked that the results are not affected by the choice of the gird. Figure 4.10 visualizes the containment x at one fixed $T_{\bar{p}} = 50$ GeV. We show the isocontours at $x = 0.9$, 0.99, and 0.999. In the calculation, we used the cross-section parametrization of [117], but the results do not depend on the parametrization (see below). From Fig. 4.10 we understand that 90% of the antiprotons at $T_{\bar{p}} = 50$ GeV are produced from protons with energies of T_p from 90 GeV to 3 TeV and with a pseudorapidity η between 4.1 and 7.1. As expected, the isocontours increase while x increases until at $x = 1$ the entire plane is covered.

Now, we want to connect the relative uncertainty of the source term with the accuracy requirement on the Lorentz invariant cross section. Our guiding idea for this connection is the principle (2) from the beginning of this section, Sec. 4.4. We want to measure the cross section well where the contribution to the source term is large. Note the containment function x provides the possibility to implement this requirement. We simply have to define a connection between x and $\sigma_{\mathrm{inv}}^{\mathrm{rel}}$ such that $\sigma_{\mathrm{inv}}^{\mathrm{rel}}$ increases while x increases. At this point, we have to decide a functional form for $\sigma_{\mathrm{inv}}^{\mathrm{rel}}(x)$ which is almost arbitrary up to the fact that it should be monotonically increasing . Furthermore,

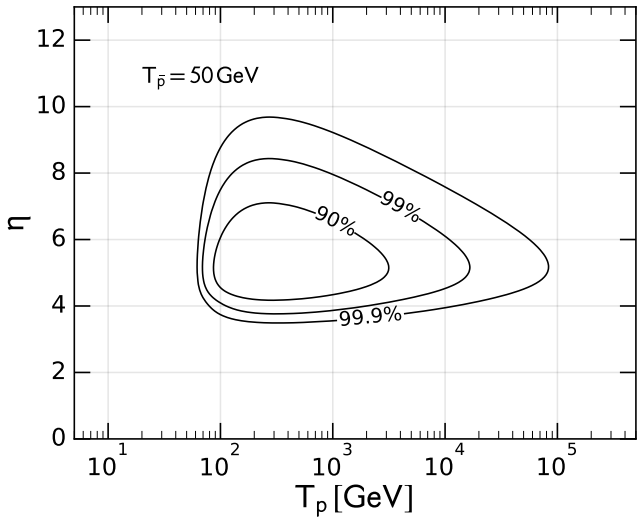

Figure 4.10: Isocontours of the containment function $x(T_{\bar{p}}, T, \eta)$ at fixed antiproton kinetic energy of 50 GeV. The three contours correspond to $x = 0.9$, 0.99 and 0.999. More details on the interpretation are given in the text. The figure is taken from Ref. [7].

there is our principle (1) which requires

$$\int_0^1 \mathrm{d}x \; \sigma^{\mathrm{rel}}_{\sigma_{\mathrm{inv}}}(x, T_{\bar{p}}) = \sigma^{\mathrm{rel}}_{q}(T_{\bar{p}}). \tag{4.20}$$

The integral over x is a short notation for the integration over T_p and η.
We choose the functional form of $\sigma^{\mathrm{rel}}_{\mathrm{inv}}(x)$ to be a step function:

$$\sigma^{\mathrm{rel}}_{\sigma_{\mathrm{inv}}}(x, T_{\bar{p}}) = \begin{cases} 3\% & x < x_t(T_{\bar{p}}) \\ 30\% & \text{elsewhere.} \end{cases} \tag{4.21}$$

It means that we want the measure the cross section with a 3% accuracy at the most relevant parameter space and with 30% accuracy everywhere else. The threshold value x_t for the transition of $\sigma^{\mathrm{rel}}_{\mathrm{inv}}$ from 3% to 30% is fixed by the requirement of Eq. (4.20). The step-values of 3% and 30% are guided by the smallest uncertainties which we currently find in cross-section measurement of NA49 or NA61 and the spread of different cross-section parametrizations, respectively. Nonetheless, we will discuss how our results depend on the choice of the step-values. Finally, we have all the ingredients to compute $\sigma^{\mathrm{rel}}_{\mathrm{inv}}(T_{\bar{p}}, T_p, \eta)$. The result will be a contour in the 3-dimensional parameter space where the $\sigma^{\mathrm{rel}}_{\mathrm{inv}}$ changes from 3% to 30%. In the first step, these kinematic variables correspond to the ISM frame or in the context of cross-section measurement fixed-target experiments. To obtain $\sigma^{\mathrm{rel}}_{\mathrm{inv}}$ as function of CM variables, either $\sqrt{s}$, p_{T}, x_{R} or $\sqrt{s}$, p_{T}, x_f, we simply transform the contours

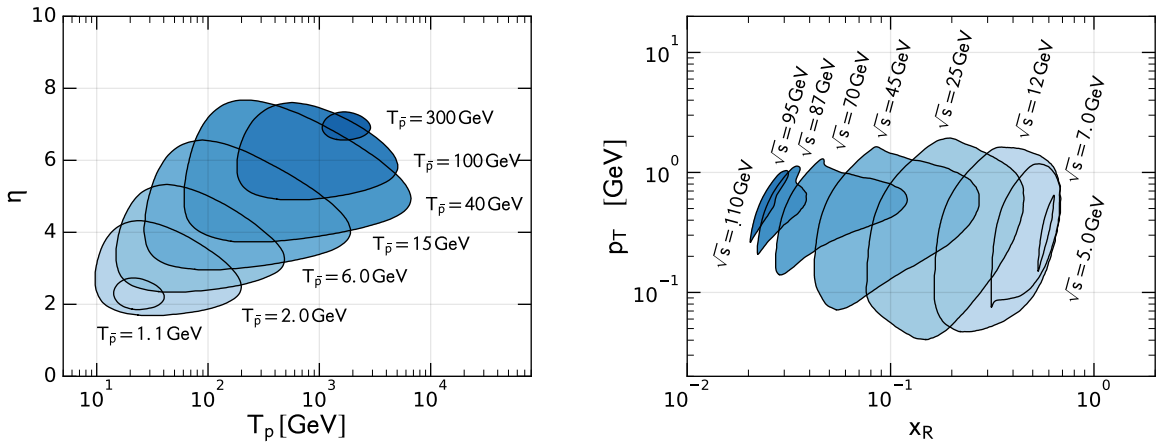

Figure 4.11: Parameter space of the $p + p \to \bar{p} + X$ cross section which should be determined by cross-section experiments in order to reach the accuracy of the recent antiproton flux measurement of AMS-02. The cross section should be measured with 3% accuracy within the blue contours and known with 30% accuracy outside. The two panels contain the same information, but the left panel uses the fixed-target kinetic variables and the right panel CM frame variables. The figure is taken from Ref. [7].

to the new kinetic variables. Here one has to pay attention when transforming to x_{R}: The relation between T_p, $T_{\bar{p}}$, η and $\sqrt{s}$, p_{T}, x_{R} is not bijective. As discussed before x_{R} does not differentiate between forward and backward production of antiprotons. The transformation of one contour from T_p, $T_{\bar{p}}$, η leads to two contours in $\sqrt{s}$, p_{T}, x_{R}. In practice, these overlap and can be merged to a single contour which will be shown in the results.

4.4.3 Results

Figure 4.11 shows the parameter space in the pp channel which should be covered by (future) cross-section measurements to predict the antiproton flux with an uncertainty which is equal to or smaller than the uncertainty of the recent AMS-02 flux measurement. To achieve this the cross section should be measured with an accuracy of 3% within the blue contours and 30% outside the contours. The contours are provided for kinetic variables in the fixed target frame (left panel) and in the CM frame (right panel). In a fix target experiment, the beam energy of the protons should vary from 10 GeV to 7 TeV and antiprotons should be measured in the range between 1 GeV and 300 GeV with a pseudorapidity between 2 and 8. We observe that with increasing antiproton energy the experiment should use larger beam energies and cover larger values of pseudorapidity, i.e. antiprotons which are more forward directed. This is expected since $T_p > T_{\bar{p}}$ and the larger the proton energy the more pronounced is the peaks of the cross section in forward direction. The contours at $T_{\bar{p}} = 1.1$ GeV and above 100 GeV become smaller since there the relative uncertainty of the AMS-02 flux measurement increases to about 30%. In the CM frame the experiments should

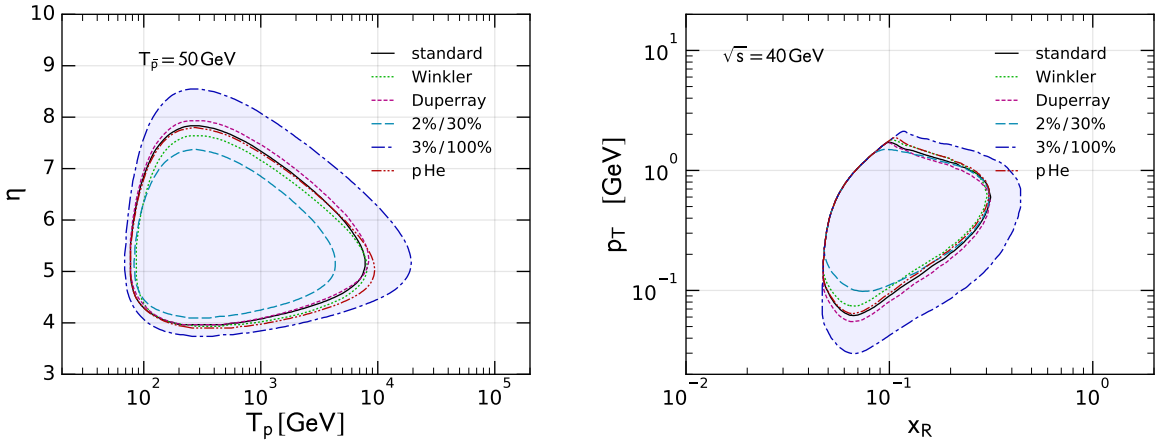

Figure 4.12: Effect of different systematics on the contours in Fig. 4.11 in the fixed target frame, exemplary shown at $T_{\bar{p}} = 50$ GeV in the fixed target frame (left panel) and fixed $\sqrt{s}$ in the CM frame (right panel). The standard setup (cross-section parametrization from [117] and inner/outer uncertainty of 3%/30%) is compared to: (i) changing the default cross-section parametrization to Winkler [119] or Duperray [121], (ii) changing the inner/outer uncertainties to 2%/30% or 3%/100%, and (iii) performing the analysis in the pHe channel. The figure is taken from Ref. [7].

cover a $\sqrt{s}$ from 5 GeV to 110 GeV. Then the antiprotons should be measured with a transverse momentum between 0.4 GeV and 2 GeV and x_R should vary be between 0.02 and 0.8.

The results can be affected by different systematic uncertainties. Our first check is the dependence of the results on the cross-section parametrization adopted in the calculation. Next to our default [117] we test two further parametrizations from [119, 121]. The comparison is displayed in Fig. 4.12, where we show the effect of various systematics on, exemplary, the contour at $T_p = 50$ GeV in the fixed target frame (left panel) or a contour at fixed $\sqrt{s} = 40$ GeV (right panel). As expected, different cross-section parametrizations affect our results only marginally. On the other hand, different choices of the inner/outer uncertainties can increase or decrease the contours significantly. By increasing the uncertainty of the outer regime the contour increases while decreasing the uncertainty in the inner regime decrease the size of the contour. We not that this increase and decrease is more pronounced at the upper boundary of both η and T_p. In the CM frame the contours changes only at the boundary of large x_R.

One of the currently most precise determination of the antiproton production cross section is provided by the NA49 experiment. The best measured data points reach a statistical uncertainty below 3%. In Fig. 4.13 we compare the NA49 data points which are taken at $\sqrt{s} = 17.3$ GeV with our requirements derived above. We observe that the measurement of NA49 covers a large fraction of our requirement contour. In particular, the more important part of the contour at large x_R and intermediate p_T is covered well. But overall only three data points stay below our requirement of 3%. Some of the other points inside the contour even exceed 30% uncertainty. Note that on top of the statistical uncertainty there is a 6.5% scale uncertainty for all the points. If this scale uncertainty

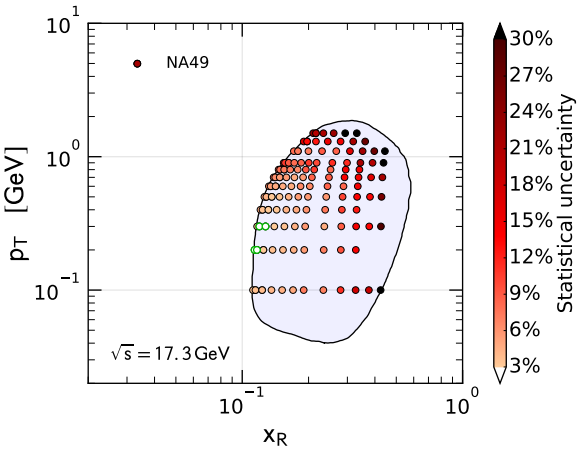

Figure 4.13: Statistical measurement uncertainty of the experiment NA49 [124] compared to our standard requirement, 3% accuracy inside the contour and 30% outside. The points with green border color fulfil our 3% requirement.

was included in the plot none of the points would fulfil our requirements. The comparison of further data sets with our requirements is given in the appendix of Ref. [7]. We conclude that the precision of current experiments is not yet sufficient to predict the CR antiproton source term at the same accuracy as the AMS-02 flux measurement. This conclusion is in agreement with the result of the cross section fits in the first part of this chapter.

Finally, let us extend our result to the case of the pA (and AA) channels. We expect that the results from the pp channel are directly applicable to all pA channels. The reason is that at first order the antiproton production can be viewed as pp for each pair of two nucleons from projectile and target. This is confirmed in Fig. 4.12 for the pHe channel. Note, however, that there is one subtlety for the pA channels in the CM frame. Since the pA is not necessarily symmetric each point in the x_R-p_T plane corresponds actually to two experimental measurement points, one in forward and one in backward scattering. Alternatively, to break this degeneracy we can view the parameter space in the x_f-p_T plane as shown in Fig. 4.14. All these results are also valid in the most general case of the AA channel, if in Fig. 4.11 the kinetic energy of the proton is replaced by the kinetic energy-per-nucleon of the projectile nucleus.

4.5 Forecasts for cross-section measurements by COMPASS++/AMBER

The COMPASS experiment is a multipurpose experiment build to investigate the hadron structure by performing hadron spectroscopy with high-intensity muon and hadron beams. It is located at CERN and uses the particle beams of the Super Proton Synchrotron (SPS), which is the preaccelerator to the Large Hadron Collider. Recently, it was noted that the detector is capable to measure

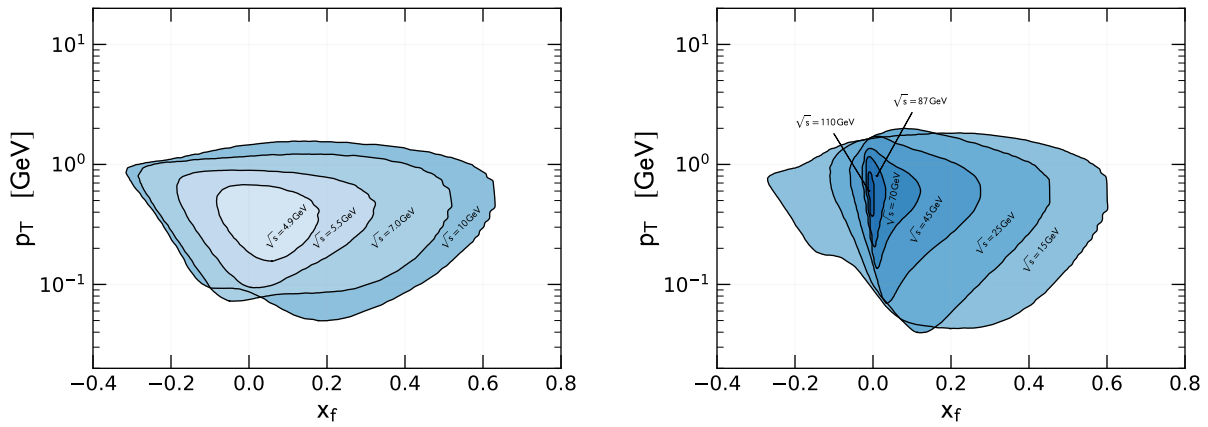

Figure 4.14: Same results as in Fig. 4.11 (right panel) but presented in the p_T-x_f plane instead of the p_T-x_R plane. This presentation has advantages if the results are used in the pA channels. The figure is taken from Ref. [3].

the antiproton production cross section of nuclear collisions in the pp and the pHe channel. The available proton beam in the fixed-target experiment reaches from $\sqrt{s} = 50$ GeV to 280 GeV. For all CM energies, antiprotons can be identified in a momentum range from 10 GeV to 45 GeV. The angular distribution might be determined up to a maximal pseudorapidity of $\eta = 5.5$. The minimal pseudorapidity is approximately $\eta = 2$[8]. With this information we can forecast how valuable a future cross-section measurement by the COMPASS++/AMBER collaboration would be in order to improve the determination of the antiproton production cross section. The first feasibility study of the COMPASS collaboration was performed this year and a *Letter of Intent* to which I contributed will be published at the beginning of this year. In case of approval, the COMPASS++/AMBER collaboration could perform measurement starting from 2022.

The pp the measurements by COMPASS++/AMBER will be in a similar kinetic parameter space as NA49 and NA61. Therefore, we do not expect large improvements in the determination of the cross section and its uncertainty in this channel. Nevertheless, a measurement in this channel would provide an important independent cross check of the previous determinations by NA49 and NA61. More important is the fact that COMPASS can provide measurements also in the pHe channel. Figure 4.15 shows the expected source term contribution of COMPASS++/AMBER for various detector setups in which the cross section would be measured in different ranges of proton beam momenta of i) 100 GeV to 190 GeV, ii) 50 GeV to 190 GeV, and iii) the full range from 50 GeV to 250 GeV. We observe that COMPASS++/AMBER would determine the source term in the pHe channel at a level up to 70% between an antiproton energy of about 10 GeV to 100 GeV. This is a significant improvement compared to the current only measurement of LHCb which only covers a per-mill level at this energies. Note that the energy range of 10 GeV to 100 GeV is particular

[8]This information was provided in private communication with Michela Chiosso and Paolo Zuccon.

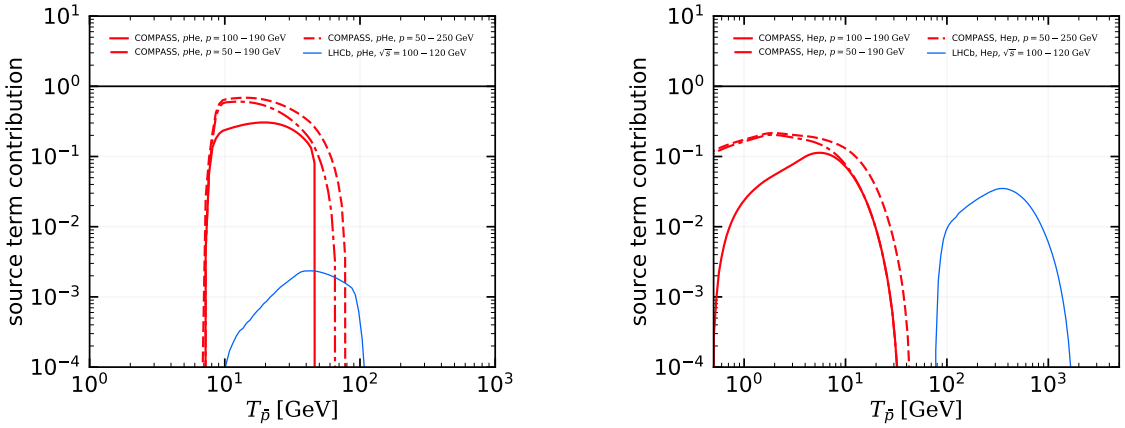

Figure 4.15: Source term contribution in the pHe (left) and Hep (right) channel which could be reached with a cross-section measurement in the future by the COMPASS++/AMBER collaboration. For comparison we display the source term contribution of the LHCb experiment (Fig. 4.8).

important for CRs which are measured precisely by AMS-02 in this regime. In the Hep channel the measurement could cover 20% of the source term below $T_{\bar{p}} \lesssim 10$ GeV, which is fully complementary to the LHCb constraints which cover $T_{\bar{p}}$ between 100 GeV and 2 TeV. Finally, we note that the best coverage of the source term is obtained if COMPASS++/AMBER measures the antiproton production cross section down to a proton beam momentum of $p = 50$ GeV. So, achieving this low-energy measurement should be given priority. On the other hand, measuring the cross section additionally at $p = 250$ GeV improves the coverage only marginally.

Chapter 5

A closer look at dark matter signatures in cosmic-ray antiprotons

The space-based experiments PAMELA and AMS-02 with a precision at a level of a few percent have pushed CR physics into a precision discipline. The CR fluxes of nuclei and leptons are provided with a precisions at the percent level which is a challenge for our theoretical modeling, but at the same time opens the possibility to understand further details about CR propagation and the opportunity to search for new phenomena such as DM. Global fits have proven great potential to study CR propagation models and simultaneously searches of exotic sources like the annihilation of a potential DM candidate. In this chapter, we will focus on the role of CR antiprotons. It is generally accepted that the bulk of antiprotons observed by the AMS-02 experiment is in good agreement with the prediction of secondary antiprotons originating form the spallation of CR proton and helium on the ISM [149, 152]. However, it was pointed out in previous analyses that there is a small anomaly in the antiproton flux measured by AMS-02 at $T_{\bar{p}}$ of about 10 GeV to 20 GeV [6,8,151]. This anomaly could be explained by the annihilation of DM into hadronic SM final states. Depending on the exact final state the mass of the potential DM candidate can vary between 40 GeV and 130 GeV. For all final states the thermally-averaged annihilation cross section, $\langle \sigma v \rangle$, is of the order of 3×10^{-26} cm^3/s which is in agreement with the typical expectation for a thermal WIMP. Beside the potential DM signal at $\sim$ 100 GeV, the precise antiproton data can be used to derive strong constraints on DM annihilation cross section in our Galaxy. These constraints are competitive and complementary to constraints from gamma-ray observations of dSphs or the Galactic center.

In Sec. 5.1, we specify the model to describe CR propagation in our Galaxy and the methods adopted to perform global fits to CR data sets. We define a default setup for two fits to the CR data of proton, helium, and antiproton-over-proton. In the first fit our CR model does not include antiprotons from DM annihilation and in the second model antiprotons from DM annihilation are included. We present the result of the fits in the default setup, which then serve as reference point for further investigations. In the default setup we find a $\sim 3\sigma$ hint for a DM signal in CR antiprotons. In Sec. 5.2, we investigate how the potential DM signal in CR antiprotons is affected by systematic uncertainties. We will focus on two effects: first, the systematics due to the uncertainties

in the production cross sections of secondary antiprotons and, second, the uncertainty originating from the correlations of systematic uncertainties in the AMS-02 data itself. In Sec. 5.3 we test the compatibility of the DM hint in antiprotons with the GCE and interpret the results within the singlet scalar Higgs portal model. In Sec. 5.4 we will adopt a more conservative approach and interpret results in terms of upper limits on the annihilation cross section of DM. We will briefly discuss an application of these limits in the case of a specific, so-called *minimal DM* model. This chapter is based on the three papers [2, 5, 6].

5.1 Global fits to cosmic-ray proton, helium, and antiproton data

In this section, we perform a total of four fits to the data of CR protons, helium and antiproton-over-proton ratio. These fits correspond to two different setups which we label *default setup* and *extended setup*. In each setup, we will perform one fit in which our CR model includes a flux of antiprotons from DM annihilation and one fit without DM annihilation. We label these fits *default setup with DM*, *default setup without DM*, *extended setup with DM*, and *extended setup without DM*. There are two main goals of this section. First, we want to derive constraints on CR propagation parameters and, second, we want to investigate the properties of a potential DM particle annihilating into CR antiprotons. Constraints on CR propagation from antiprotons have also been derived in [9, 289]. In the default setup, we will use data of the AMS-02 experiment [58, 59, 75] in a combination with recent data from the VOYAGER probe [290]. The combination of AMS-02 and VOYAGER data allows to disentangle CR propagation and solar modulation effects at low energies. In the extended setup, we will complement the proton and helium data with measurements by the CREAM experiment [291] at high energies. We summarize the four fits and the exploited data sets in Tab. 5.1. In Sec. 5.1.1 we present the CR model, in Sec. 5.1.2 we present the technical details of the fit setups, and in Sec. 5.1.3 we present the fit results.

Before going to the details of the fit, we briefly justify the choice of data sets. Protons, helium and antiprotons form an almost independent subset within the CR nuclei. We note that our setups include secondary antiprotons[1], protons, deuterons, and ^{3}He. Antiprotons are predominantly produced by the spallation of CR protons and helium. The contribution from nuclei like CNO are subdominant at the percent level. Furthermore, the secondary components of proton (or deuteron) and helium from the spallation of nuclei heavier than He is fairly negligible. Secondary protons have

[1] We also include tertiary antiprotons, which are inelastically scattered secondary antiprotons.

Table 5.1: Summary of CR data sets used in the four fits of Sec. 5.1.

	AMS-02			VOYAGER		CREAM	
fit name	p	He	$\bar{p}/p$	p	He	p	He
default setup without DM	×	×	×	×	×		
default setup with DM	×	×	×	×	×		
extended setup without DM	×	×	×	×	×	×	×
extended setup with DM	×	×	×	×	×	×	×

no contribution from heavier nuclei, they are inelastically scattered protons, which lost a significant amount of their original energy by scattering off the ISM. The contribution of the secondary ^{3}He is mostly due to the spallation of ^{4}He. Only a fraction of up to 30% is expected to originate from heavier CRs. Thus, in the total He flux, where the contribution of ^{3}He always stays below 15%, the fraction of secondary He from spallation is below 5%. Deuteron is produced by spallation of ^{4}He. All in all, the secondary components of protons, helium, and antiprotons from elements heavier than ^{4}He are only at the level of a few percent. Unless specified differently, in the following of this chapter the proton flux denotes the sum of primary protons, secondary protons and deuterons, and the helium flux is the sum of ^{3}He and ^{4}He.

5.1.1 Model for cosmic-ray propagation and solar modulation

The propagation of CRs in our Galaxy is described by diffusion as encoded in Eq. (2.20). We assume a cylindrical symmetry of the Galaxy and, consequently, use the two spatial coordinates r and z which are the Galactocentric radial distance and the distance from the Galactic plane, respectively. The source term of the primary protons and helium is divided into a spatial and an energy-dependent part. The spatial part is parametrized by Eq. (2.34) with the parameters $\alpha = 0.5$, $\beta = 2.2$, $r_0 = 8.5$ kpc, and $z_0 = 0.2$ kpc.[2] For the energy-depend part of the source term we adopt a broken power law in rigidity

$$q_R(R) \quad = \quad \left(\frac{R}{R_0}\right)^{-\gamma_1} \left(\frac{R_0^{1/s} + R^{1/s}}{2\, R_0^{1/s}}\right)^{-s(\gamma_2-\gamma_1)} . \tag{5.1}$$

Here R_0 is the position of the break and γ_1 and γ_2 are the spectral indices below and above the break, respectively. The parameter s regulates the smoothing of the break: the larger s the smoother is the break. In our setup, spatial diffusion is isotropic and homogeneous. The rigidity-dependent diffusion coefficient D_{xx} is taken as broken power law in rigidity:

$$D_{xx}(R) \quad = \quad \begin{cases} \beta D_0 \left(\frac{R}{4\,\mathrm{GV}}\right)^{\delta} & \text{if } R < R_1 \text{ and} \\ \beta D_0 \left(\frac{R_1}{4\,\mathrm{GV}}\right)^{\delta} \left(\frac{R}{R_1}\right)^{\delta_2} & \text{otherwise}\,, \end{cases} \tag{5.2}$$

where δ and δ_2 are the indices below and above the break positioned at the rigidity R_1. Furthermore, D_0 is the overall normalization and $\beta = v/c$ the velocity of the CRs. This break allows to describe the CR softening observed by PAMELA and AMS-02 at a rigidity of about 300 GV. As discussed in Sec. 2.3 data favours to have this break in diffusion rather than in the injection spectrum since the break is more enhanced in secondaries compared to primary CRs. We allow for reacceleration which is parametrized in terms of the speed of Alfven magnetic waves, cf. Eq. (2.21). We note that this formula shows an explicit dependence on the spectral index of the diffusion coefficient. We use the value δ (not δ_2) at all rigidities. Moreover we allow convection perpendicular to the Galactic plane.

[2] This are the default values of Galprop v56. They differ slightly from the values obtained in the analysis of SNRs [96, 97]. However, it was shown in [9] that the spatial dependence of the source term distribution has only a negligible effect on the local CR fluxes.

It is described by a constant convection velocity, $\boldsymbol{V}(\boldsymbol{x}) = \mathrm{sign}(z)\, v_{0,\mathrm{c}}\, \boldsymbol{e}_z$.[3] Finally, we remind that CRs are affected by various continuous, adiabatic, and catastrophic energy losses. Their description follows the default implementation in GALPROP.

We use a modified version of GALPROP 56.0.2870 and GALTOOLLIBS 855[4] to derive steady state solutions of the diffusion equation. We assume free escape of the CRs at the boundaries of the diffusion halo at $r = 20$ kpc and $z = \pm z_{\mathrm{h}}$[5]. The solution of the diffusion equation is calculated on a three-dimension grid in r, z, and kinetic energy-per-nucleon. We adopt grid steps of $\Delta r = 1\,\mathrm{kpc}$ and $\Delta z = 0.1\,\mathrm{kpc}$. The grid in kinetic energy-per-nucleon extends from 1 MeV to 10^7 MeV and changes logarithmically with a constant step factor of 1.4. The most important modification we have done to the GALPROP code concerns the antiproton production cross sections. We include the cross-section parametrizations of di Mauro et al. [117] (referred to as Param. MD in the following) and Winkler [119] (Param. MW) We exploit the updated parameter values derived in the previous chapter. The required energy-differential cross section $\mathrm{d}\sigma_{ij}(T_i, T_{\bar{p}})/\mathrm{d}T_{\bar{p}}$ can either be read from a table or calculated from the analytic parametrizations on the fly. Furthermore, we implement the option to use a smoothly-broken power law for the injection spectra of CR primaries, see Eq. (5.1).

Besides the standard astrophysical CR production we allow for a primary contribution of CR antiprotons from DM. Its source term is given by Eq. (2.51). In the first part of this chapter, we will consider the generic example of pure annihilation of DM particles into bottom quarks, DM DM $\to b\bar{b}$, which serves as an illustrative example. The antiproton energy spectra in Eq. (2.51) are taken from [292], which we implemented in GALPROP. We assume that the DM distribution in our Galaxy follows an NFW density profile (see Eq. 1.4) with a characteristic halo radius of $r_h = 20\,\mathrm{kpc}$. The profile is normalized to a local DM density $\rho_{\mathrm{sun}} = 0.43\,\mathrm{GeV/cm^3}$ [41] at the solar position $r_{\mathrm{sun}} = 8\,\mathrm{kpc}$.

At low energies, CRs are affected by solar modulation. We describe this phenomenon within the force-field approximation in which the solar effect on the flux is described by a single, time-dependent parameter, φ. The local CR fluxes are linked to the TOA fluxes by Eq. (2.66). Since recent observation revealed a charge-sign dependence of solar modulation we adopt two independent solar modulation potentials, one value for proton and helium and a second value for antiprotons. Furthermore, in our default setup we restrict the fit to rigidities above 5 GV, since these rigidities are not so strongly affected by solar modulation. For example, below 3 GV the time dependent helium-to-proton ratio measured by AMS-02 shows an increase after May 2015 which is not expected and cannot be described within the force-field approximation. Furthermore, the time-dependent proton flux reveals crossings of fluxes at different times, e.g. at 4 GeV for Bartels Rotation 2460 (November 2013) and Bartels Rotation 2476 (March 2015), which is also not expected within the force-field approximation.

[3] We note that the discontinuous parametrization of the convection velocity formally leads to a non-conservation of the flux at $z = 0$. But the parametrization can be seen as an approximation of a continuous parametrization like $\mathrm{sign}(z) \approx \tanh(az)$ for $a \gg 1$.

[4] https://galprop.stanford.edu/download.php

[5] In Chapter 2, the halo height was typically called L, while in this chapter we will denote it with z_h.

5.1.2 Technical details of the default setup

The default setup of our fits is similar to the setups already used in [8, 9]. Here we repeat the key ingredients and point out some important differences. Our fit includes the AMS-02 flux data of protons and helium [58, 59] measured in the period from May 2011 until November 2013 and the antiproton-to-proton ratio [75] measured over a period from May 2011 until May 2015. The data sets are complemented with the proton and helium data taken by VOYAGER [290] and, in some cases, also with the data taken by CREAM [291]. The log-likelihood of the CR fit is given by the sum of the log-likelihoods of the single experiments e and species s:

$$-2\,\log(\mathcal{L}_{\rm CR}) = \chi^2_{\rm CR} = \sum_{e,s}\sum_{i,j}\left(\phi^{(e)}_{s,i} - \phi^{(\rm m)}_{s,e}(R_i)\right)\left(\left(\mathcal{V}^{(e,s)}\right)^{-1}\right)_{ij}\left(\phi^{(e)}_{s,j} - \phi^{(\rm m)}_{s,e}(R_j)\right)\,. \tag{5.3}$$

Here $\phi^{(e)}_{s,i}$ denotes the CR flux of species s measured by the experiment e at the rigidity point R_i and $\phi^{(\rm m)}_{s,e}(R_i)$ is the same flux calculated in our model. The superscript m encodes the dependence of this flux on the model parameters (more details given below) for both, CR propagation and solar modulation. The subscript e and s denote the dependence of the model flux on the experiment and the species. For example, when fitting the VOYAGER data the solar modulation potential is always 0, while for AMS-02 it takes different values for proton and helium, on the one hand, and antiprotons, on the other hand. Finally, $\mathcal{V}^{(e,s)}_{ij} = \delta_{ij}\left[\sigma^{(e)}_{s,i}\right]^2$ is the covariance matrix of the experimental uncertainties. In the default setup, we assume that the systematic uncertainties of all experimental data points are uncorrelated, namely, the matrix is diagonal (δ_{ij} denotes the Kronecker delta). Systematic and statistical uncertainties are added in quadrature: $\sigma^{(e)}_{s,i} = \sqrt{\left(\sigma^{(e)}_{s,i,\rm stat}\right)^2 + \left(\sigma^{(e)}_{s,i,\rm sys}\right)^2}$.

Our CR model contains in total 15 (17) free parameters in the default fit without (with) DM. The free parameters and the fit ranges are summarized in Tab. 5.2. Six parameters are used to describe the energy spectra of the source terms of primary protons and helium. They adjust the smoothly broken power laws of Eq. (5.1). The spectral indices above and below the break, $\gamma_{1,p}$, γ_1, $\gamma_{2,p}$, γ_2, are varied individually for protons (subscript p) and helium (no subscript), while both injection spectra share a common break at rigidity R_0 and a common smoothing parameter s. CR propagation is described by five parameters. These are normalization of the diffusion coefficient, D_0, and the spectral index, δ, at rigidities below the break R_1. In the default setup, we restrict the fit to rigidities between 5 GV and 300 GV. In this case, the parameters R_1 and δ_2 are not included as fit parameters. Instead, they are fixed to $R_1 = 300$ GV and $\delta_2 = \delta - 0.12$, respectively. The further free parameters are the convection velocity, $v_{0,c}$, the velocity of Alfven magnetic waves, $v_{\rm A}$, and the half-height of the diffusion halo z_h. If DM is included in the fit the two additional parameters are the DM mass, $m_{\rm DM}$, and the velocity averaged annihilation cross section, $\langle\sigma v\rangle$. These 11–13 parameters discussed above are sampled with the MultiNest package [293]. Therefore, we call them MultiNest parameters in the following. We exploit flat priors except for $m_{\rm DM}$ and $\langle\sigma v\rangle$, which adopt priors proportional to $1/m_{\rm DM}$ and $1/\langle\sigma v\rangle$, respectively[6]. In the standard case, we use 500 live points, an enlargement factor of EFR=0.7, and a stopping criterion of TOL=0.1. A single fit in this setup requires about

[6]Note that these priors imply flat priors in log of the corresponding variable.

Table 5.2: Summary of free fit parameters and the corresponding fit ranges.

parameter	fit range	default setup without DM	default setup with DM	extended setup without DM	extended setup with DM
γ_1	1.2 – 1.8	×	×	×	×
$\gamma_{1,p}$	1.2 – 1.8	×	×	×	×
γ_2	2.3 – 2.6	×	×	×	×
$\gamma_{2,p}$	2.3 – 2.6	×	×	×	×
R_0, [GV]	1.0 – 10.0	×	×	×	×
s_0	0.1 – 0.9	×	×	×	×
D_0, $[10^{28}\,\mathrm{cm}^2/\mathrm{s}]$	0.5 – 10.0	×	×	×	×
δ	0.2 – 0.5	×	×	×	×
v_A, [km/s]	0.0 – 30.0	×	×	×	×
$v_{0,\mathrm{c}}$, [km/s]	0.0 – 60.0	×	×	×	×
z_h, [kpc]	2.0 – 7.0	×	×	×	×
m_DM, [GeV])	$10 - 10^5$		×		×
$\langle\sigma v\rangle$, $[\mathrm{s}/\mathrm{cm}^3]$)	$10^{-27} - 10^{-23}$		×		×
δ_2	0.3 – 0.6			×	×
R_1, [GV]	100 – 500			×	×
$\varphi_{\mathrm{SM,AMS\text{-}02},p,\mathrm{He}}$, [MV]	> 0	×	×	×	×
$\varphi_{\mathrm{SM,AMS\text{-}02},\bar{p}}$, [MV]	> 0	×	×	×	×
A_p	> 0	×	×	×	×
A_He	> 0	×	×	×	×
$A_{p,\mathrm{CREAM}}$	> 0			×	×
$A_{\mathrm{He,CREAM}}$	> 0			×	×

200 000 evaluations of the likelihood function. The remaining four fit parameters are treated in a different way in order to speed up the fitting procedure. The flux prediction for those parameters is decoupled from the MultiNest parameters. Therefore, it is possible to marginalize the likelihood in these so-called *linear parameters* on-the-fly for each fixed set of MultiNest parameters. In detail, the four parameters are: the solar modulation potential for proton and helium, $\varphi_{\text{SM,AMS-02},p,\text{He}}$, the modulation potential for antiprotons, $\varphi_{\text{SM,AMS-02},\bar{p}}$, and two normalizations of the proton and helium fluxes, called A_p and A_{He}, respectively. Note that a re-normalization of the proton and helium flux by A_p and A_{He} can approximately be absorbed into the isotopic abundance, namely, the normalization of the primary source term.[7] During the on-the-fly marginalization we impose a weak Gaussian constraint on the difference of $\varphi_{\text{SM,AMS-02},p,\text{He}} - \varphi_{\text{SM,AMS-02},\bar{p}}$ of 100 MV. Otherwise, no constraints on the values for solar modulation or normalization are assumed. We will interpret the results of our fits in the frequentist framework.[8] Uncertainties on single parameters will be calculated from the one-dimensional likelihood profile. The 1σ ($n\sigma$) confidence level then corresponds to the condition $\Delta\chi^2 = 1$ ($\Delta\chi^2 = n^2$) with respect to the minimum χ^2. Furthermore, we will derive likelihood contours for each combination of two fit parameters given by the two-dimensional χ^2-distribution. The 1, 2, and 3σ C.L.s are given at $\Delta\chi^2 = 2.30$, 6.18, and 11.83. Finally, we remark on a subtlety concerning solar modulation. We use the proton, helium and antiproton-over-proton data in our fit. The proton flux appears twice, first directly and a second time in the antiproton-to-proton ratio. Since the two data sets correspond to (slightly) different measurement periods, in principle, one would have to allow for two different solar modulation potentials. However, we use the $\bar{p}$ flux and the $\bar{p}/p$ ratio of [75] to obtain the proton flux in the same period. Then, we fit the ratio of this proton flux and the *original* proton flux with a smooth function. To obtain the *effective* proton and helium flux which correspond to the same period as the $\bar{p}/p$ ratio, we multiply both fluxes with the smooth function. In this way, we are able to reduce the number of required solar modulation potentials to two, as already assumed during all the discussion above. For more details we refer to [2].

5.1.3 Results of the fits in the default and extended setup

We perform two fits in the default setup, one with and another one without DM. The results of theses two fits are summarized in Figs. 5.1 to 5.3. In more detail, the Fig. 5.1 shows the best-fit result of our default fit without DM for the proton and helium flux compared to the AMS-02 and VOYAGER data. Furthermore, we display the residuals of the AMS-02 data points in the lower panels. The AMS-02 data are very well fitted in the rigidity range from 5 GV to 300 GV. Furthermore, the VOYAGER data points agree well with the LIS flux, i.e. the flux without solar modulation. We note that the plots of the corresponding fit with DM look very similar to the shown

[7] We note that there is a subtle difference between the isotopic abundances and the normalization factors A_p and A_{He}. While the first act only on the primary proton and helium fluxes the latter also change the normalization of secondary proton and helium. Therefore, the isotopic abundances of proton and helium where adjusted in an iterative procedure to obtain $A_p \approx 1$ and $A_{\text{He}} \approx 1$.

[8] We note that intrinsically MultiNest is a Bayesian tool. In [9], we have compared the frequentist and Bayesian interpretation of on CR fit and found that the conclusion are not affected by the framework. Concerning the size of uncertainties the frequentist approach is slightly more conservative.

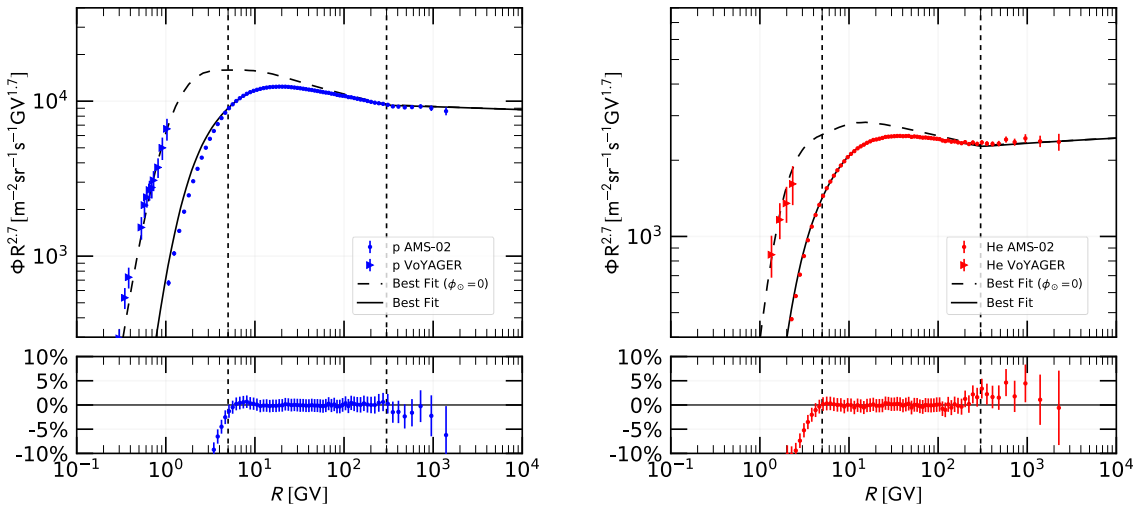

Figure 5.1: Comparison of the best-fit proton and helium fluxes with AMS-02 and VOYAGER data. The two plots are taken from a fit setup without DM. The rigidity range of the fit for AMS-02 data is restricted from $R = 5$ to 300 GV (between the dotted lines). The dashed line labeled $\phi_\odot = 0$ marks the CR fluxes without solar modulation which should be compared with the VOYAGER data. The lower panel shows the residuals of the AMS-02 data with respect to our best fit. The figure is taken from [2].

plots without DM and, we, therefore, do not show the plots explicitly. Taking a closer look at the residuals reveals a common problem when fitting the CR data of AMS-02. The agreement between data and model is too good when looking at the sizes of the data point's uncertainties. In other words, the χ^2/dof is significantly smaller than 1. The most probable solution for this issue is that the systematic uncertainties of the AMS-02 data points are correlated, although, this correlation is not provided by the experiment. We will discuss possible correlations and potential effects on the significance of the DM hint in the following section.

In Fig. 5.2 we display the comparison of our best-fit results of the antiproton-over-proton ratio in the setup without DM (left panel) and and with DM (right panel). In general, we note that the AMS-02 data is fitted well within our model in both cases. However, the measured flux in the fit without DM shows a small excess between 10 and 20 GV, which is in particular visible in the residuals. The right panel shows that this excess can be filled with a potential DM signal. This signal corresponds to a DM mass of about 75 GeV and a thermal cross section, $\langle \sigma v \rangle = 3 \times 10^{-26}$ cm^3/s. These values are obtained for a DM particle annihilating into a $b\bar{b}$ pair. However, we note that the annihilation of DM into all hadronic channels exhibits similar features. Indeed, it is possible to fit the antiproton excess in all hadronic channels if one allows to slightly adjust the DM mass. For a more detailed discussion we refer to Sec. 5.3. The statistical significance of the potential DM signal can be inferred from the χ^2 difference. In this case, we obtain a $\Delta\chi^2$ of 12.7 which corresponds to a frequentist significance of 3.1σ. We remark that the search for a DM signal in the antiproton data relies on

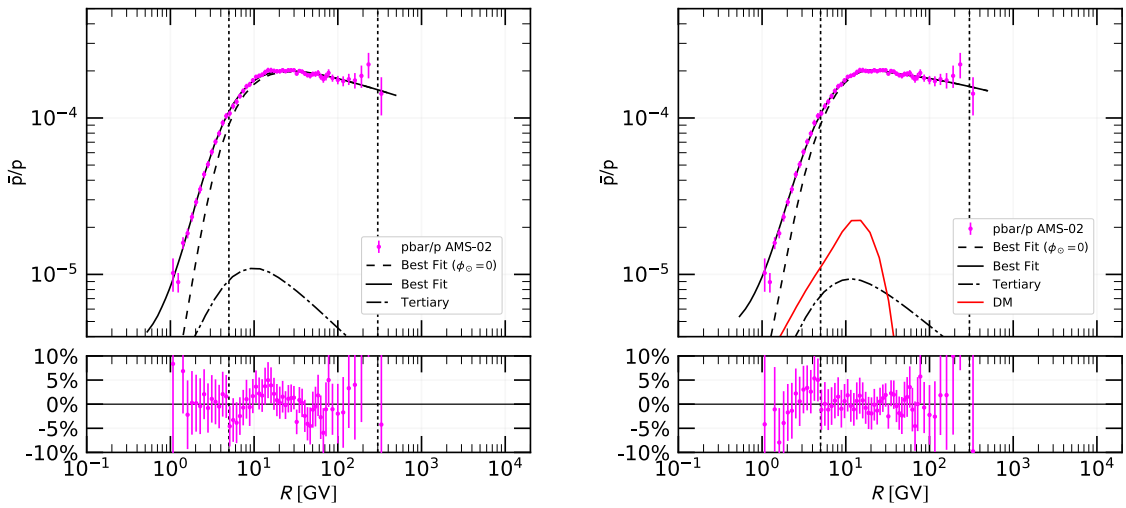

Figure 5.2: Same as Fig. 5.1 but for the antiproton-to-proton ratio. The left (right) panel shows the case without (with) DM. Furthermore, we show the individual contribution from tertiary antiprotons and DM. The figure is taken from [2].

the characteristic shape of the DM energy spectrum which for our best-fit DM mass shows a sharp cut-off at about 20 GV. Such a sharp signature is not expected in the secondary or tertiary fluxes of astrophysical origin.

In Fig. 5.3 we display a triangle plot which shows the best-fit values and uncertainties of all free model parameters in the fit. On the diagonal, we show the χ^2-profile for all the MultiNest parameters. The two inlaid plots show the χ^2-profile for the solar modulation potential of p and He as well as the difference between the p and He potential with respect to the $\bar{p}$ potential. The panels below the diagonal show the best-fit regions for each combination of two parameters. The contours display the 1, 2, and 3σ regions derived from the two-dimensional χ^2 distribution as explained above. The results are shown and compared for the fit with (red) and without (black contours and line) DM. We note that the two fits prefer a very similar best-fit region which is expected since DM is a subdominant contribution to the $\bar{p}$ spectrum. Our fits prefer to have no or only a very small amount of convection which is limited to $v_{0,c} \lesssim 10$ km/s, while they require reacceleration. The Alfven velocities converge to about 20 km/s. The half-height of the diffusion halo z_h and normalization of the diffusion coefficient D_0 are not constrained individually, but, as expected (see Sec. 2.3), their ratio is well constrained to ~ 0.028 kpc/My. This value agrees well with the constraints from CR antiprotons found in [289]. Recent analysis of the B/C data find values of $D_0/z_h \sim 0.017$ [107, 136] which is a 40% below our values. We stress however that differences of this size can easily arise from differences in the (radial) source distribution and the description of the interstellar gas distribution. The spectral index of the diffusion coefficient δ converges to values between 0.3 and 0.45, which is roughly in agreement with expectations from the B/C ratio which points to values between 0.4 and 0.5 [107, 294, 295]. We note that the fit with DM prefers

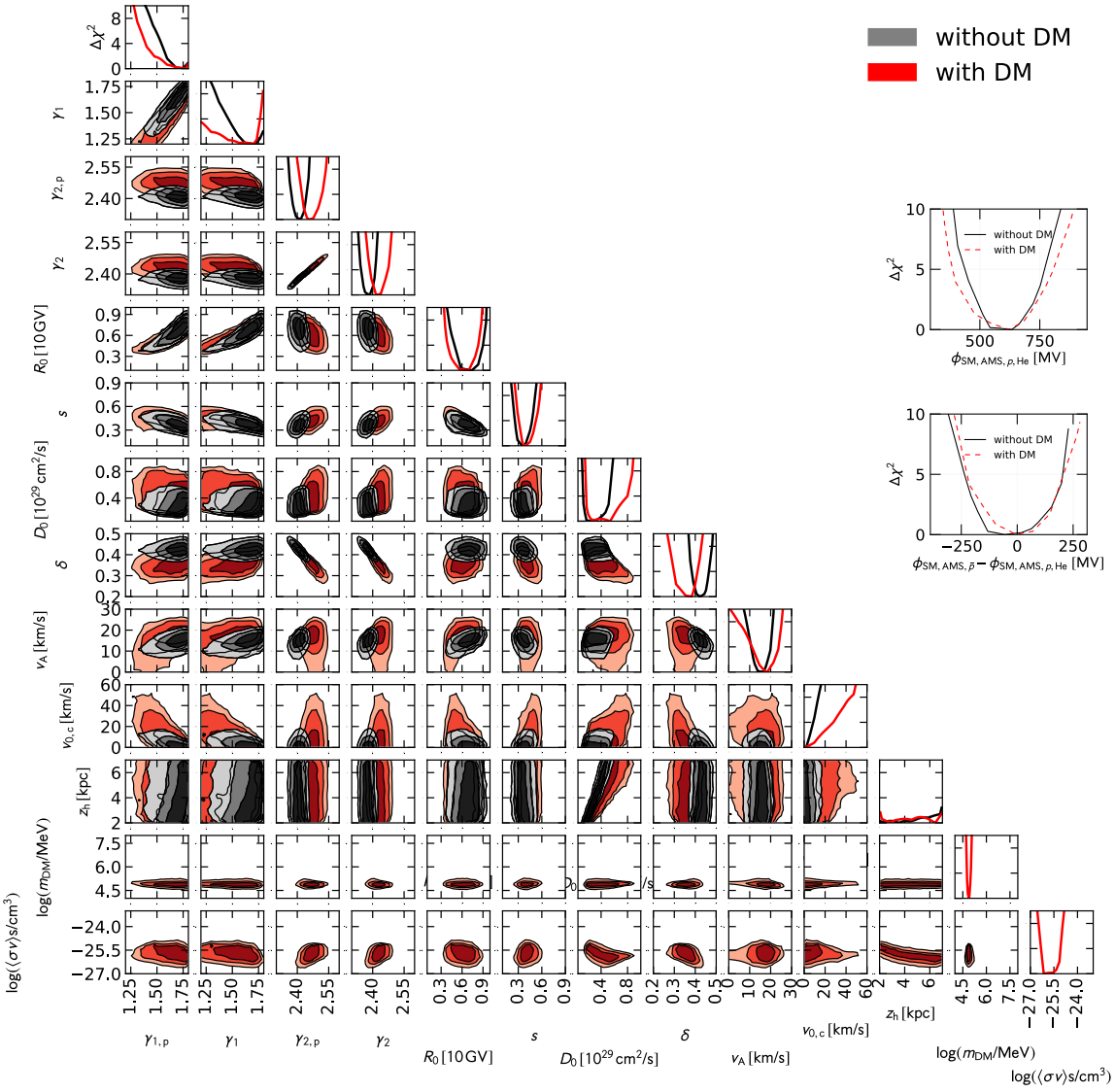

Figure 5.3: Triangle plot containing the results of the two fits in the default setup with and without DM. The black and red contours show the 1σ to 3σ regions of the fits without and with DM, respectively. The diagonal shows the χ^2 profiles plotted each single fit parameter. The two inlaid plots display the χ^2 profiles of the solar modulation potential for AMS-02 p, He and its difference to the potential of $\bar{p}$, respectively. The figure is taken from [2].

slightly smaller values of δ compared to the fit without DM. The values of δ and γ_2 (or $\gamma_{2,p}$) are strongly correlated. We remind that the CR flux behavior at high energies follows $\phi \sim R^{-\gamma_2-\delta}$. So, the precise measurements of the proton and helium fluxes basically fix the sum of $\gamma_2 + \delta$. This also

explains why the fit converges to different values for $\gamma_{2,p}$ and γ_2, the difference $\gamma_{2,p} - \gamma_2 \approx 0.05$ agrees with the difference in slope measured for the proton and helium flux by AMS-02. The slopes γ_1 and $\gamma_{1,p}$ below R_0 are less well constrained because the behavior of the fluxes at low energies is more degenerate with the various propagation effects. Finally, we note that the solar modulation potentials of protons/helium and antiprotons converge to the same value within uncertainties. If any, there is a slight preference for $\varphi_{\mathrm{SM,AMS-02},\bar{p}} \lesssim \varphi_{\mathrm{SM,AMS-02},p,\mathrm{He}}$. From a theoretical point of view, the charge-sign dependence of solar modulation is expected to depend on the polarity of the solar magnetic field. Since there is a change of the polarity in 2013, which is in the middle of the measurement period of AMS-02, it is not entirely clear whether to expect a smaller or a larger value of the solar modulation potential for protons or antiprotons.

Finally, we remind that the analysis discussed here is an update of the previous analysis [8] which found a larger statistical significance for a DM signal of 4.5σ. We will now list the most important differences with respect to this analysis and step-by-step discuss the impact on the significance. In detail, we

(i) removed the CREAM data from our default setup and restricted the fit range of the AMS-02 data to a maximal rigidity of 300 GV,

(ii) changed the default antiproton production cross section from Tan&Ng [123] to the Param. MW [119] which shows a much better agreement with data in particular at high energies,

(iii) introduced two different solar modulation potentials for p and He, on the one hand, and $\bar{p}$, on the other hand, in order to take the charge-sign dependence of solar modulation into account.

Step-by-step these changes affect the $\Delta\chi^2$ between the fit with and without DM as follows: the $\Delta\chi^2$ is (i) reduced from 25 to 21, (ii) reduced from 21 to 11, and (iii) finally increased again from 11 to 12.7. We note that the most severe change of significance is obtained when updating the Tan&Ng cross-section parametrization with the more recent Param. MW. This demonstrates the importance of the secondary antiproton production cross sections for the correct interpretation of the AMS-02 data. We will continue the discussion in the next section.

Concerning the compatibility of AMS-02 and CREAM data (point (i)) we conducted one further test. We included again the CREAM and the AMS-02 data above 300 GV in the fit, but at the same time allowed a bit more freedom in the setup. This is the so-called *extended* setup. We included four additional parameters in the fit which modify the behavior at high rigidity: Firstly, we allowed the parameters R_1 (break position in the diffusion coefficient) and δ_1 (spectral index above R_1) to vary freely. Furthermore, we allowed a free normalization for the proton and helium data of CREAM. The physical motivation for a slightly normalization of AMS-02 and CREAM data is the uncertainty of the energy scale measurement, in particular, for the calorimetric measurement of CREAM. The results of this *extended setup* show, firstly, that CREAM and AMS-02 data are in good agreement if the energy-scale uncertainties are included in the fit and, secondly, they justify the values adopted for R_1 and δ_1 in the default setup. The $\Delta\chi^2$ between the fit with and without DM is 15.1 corresponding to a significance of 3.5σ. We summarize the results of all four fits in the default setup and the extended setup in Tab. 5.3. Finally, we study how the significance for DM is affected by the AMS-02 data below 5 GV by gradually decreasing the cut rigidity R_{cut} from 5 GV

Table 5.3: The best-fit parameters of the fits with and without DM in the default and extended setup. More details are given in the text.

parameter	**default setup**		**extended setup**	
XS parametrization	Param. MW		Param. MW	
DM	incl.	excl.	incl.	excl.
γ_1	$1.71^{+0.02}_{-0.25}$	$1.72^{+0.04}_{-0.12}$	$1.64^{+0.05}_{-0.12}$	$1.72^{+0.02}_{-0.11}$
$\gamma_{1,p}$	$1.78^{+0.003}_{-0.19}$	$1.75^{+0.03}_{-0.10}$	$1.73^{+0.04}_{-0.06}$	$1.73^{+0.05}_{-0.07}$
γ_2	$2.41^{+0.03}_{-0.002}$	$2.38^{+0.01}_{-0.02}$	$2.44^{+0.01}_{-0.02}$	$2.38^{+0.01}_{-0.01}$
$\gamma_{2,p}$	$2.45^{+0.03}_{-0.002}$	$2.42^{+0.01}_{-0.02}$	$2.48^{+0.01}_{-0.02}$	$2.41^{+0.01}_{-0.01}$
R_0, [MV]	6950^{+330}_{-1640}	7380^{+910}_{-1450}	6519^{+1045}_{-824}	7695^{+563}_{-1375}
s_0	$0.38^{+0.06}_{-0.04}$	$0.34^{+0.05}_{-0.04}$	$0.38^{+0.06}_{-0.01}$	$0.37^{+0.04}_{-0.03}$
D_0, [$10^{28}\,\mathrm{cm}^2/\mathrm{s}$]	$5.43^{+0.45}_{-3.17}$	$2.90^{+1.33}_{-1.21}$	$3.46^{+2.46}_{-1.19}$	$1.97^{+1.27}_{-3.81}$
δ	$0.38^{+0.01}_{-0.03}$	$0.42^{+0.02}_{-0.01}$	$0.35^{+0.02}_{-0.01}$	$0.42^{+0.01}_{-0.02}$
v_A, [km/s]	$18.0^{+2.1}_{-1.4}$	$16.2^{+1.0}_{-2.5}$	$18.59^{+0.00}_{-3.25}$	$15.81^{+0.87}_{-1.99}$
$v_{0,\mathrm{c}}$, [km/s]	$0.08^{+9.09}_{-0.08}$	$0.52^{+2.32}_{-0.51}$	$0.35^{+4.94}_{-0.14}$	$0.79^{+2.19}_{-0.77}$
z_h, [kpc]	$6.45^{+0.30}_{-4.26}$	$3.58^{+2.36}_{-1.52}$	$3.36^{+3.47}_{-1.13}$	$2.47^{+1.58}_{-0.43}$
$\log(m_\mathrm{DM}/[\mathrm{GeV}])$	$1.89^{+0.03}_{-0.08}$		$1.88^{+0.05}_{-0.00}$	
$\log(\langle\sigma v\rangle/[\mathrm{s}/\mathrm{cm}^3])$	$-26.16^{+0.78}_{-0.04}$		$-25.56^{+0.20}_{-0.47}$	
δ_2			$0.23^{+0.01}_{-0.00}$	$0.30^{+0.02}_{-0.02}$
R_1, [GV]			344^{+26}_{-20}	338^{+49}_{-40}
$\varphi_{\mathrm{SM,AMS\text{-}02},p,\mathrm{He}}$, [MV]	616^{+71}_{-72}	625^{+55}_{-85}	566^{+19}_{-71}	567^{+19}_{-66}
$\varphi_{\mathrm{SM,AMS\text{-}02},\bar{p}}$, [MV]	604^{+112}_{-114}	561^{+135}_{-112}	577^{+43}_{-82}	561^{+35}_{-106}
$\chi^2_{\mathrm{AMS\text{-}02},p}$	3.2	2.6	4.9	7.0
$\chi^2_{\mathrm{AMS\text{-}02,He}}$	4.0	4.8	10.4	12.0
$\chi^2_{\mathrm{AMS\text{-}02},\bar{p}}$	11.1	22.1	12.2	20.0
$\chi^2_{\mathrm{Voager},p}$	3.2	3.8	2.7	3.6
$\chi^2_{\mathrm{Voager,He}}$	1.3	1.9	3.4	4.1
$\chi^2_{\mathrm{CREAM},p}$			1.0	1.0
$\chi^2_{\mathrm{CREAM,He}}$			1.0	2.9
$\chi^2_{\varphi_\mathrm{SM}}$	0.0	0.4	0.0	0.0
χ^2_CR	22.9	35.6	35.6	50.7
χ^2/dof	22.9/143	35.6/145	35.6/177	50.7/179
$\Delta\chi^2$	12.7		15.1	
DM significance	3.1σ		3.5σ	

Table 5.4: Fit quality without (second column) and with (third column) DM for for decreasing $R_{\rm cut}$. The last two columns contain the absolute $\Delta\chi^2$ between the fits with and without DM and the corresponding significance of the potential DM signal.

	χ^2/ndf			
$R_{\rm cut}$ [GV]	excl. DM	incl. DM	$\Delta\chi^2$	DM significance
5	$35.6/145 = 0.245$	$22.9/143 = 0.160$	12.7	3.1σ
3	$52.7/160 = 0.329$	$34.2/158 = 0.216$	18.5	3.9σ
2	$68.2/172 = 0.396$	$57.1/170 = 0.336$	11.1	2.9σ
1	$105.4/182 = 0.579$	$105.6/180 = 0.586$	-0.2	–

to 1 GV. We observe that the significance first increases to 3.9σ at $R_{\rm cut} = 3$ GV and then decreases again to 2.9σ and 0 at $R_{\rm cut} = 2$ GV and 1 GV, respectively. We note, however, that the fit quality, namely the χ^2/dof, increases gradually when decreasing $R_{\rm cut}$. The increase is particularly strong between 2 GV and 1 GV, hinting that there might be a more general problem of our CR propagation modeling or our solar modulation modeling at very low rigidities. All values are given in Tab. 5.4. In any case, we notice that our default cut rigidity is not tuned to maximize the significance for DM.

In summary, we have demonstrated that light nuclei (p, He, and antiprotons) precisely measured by AMS-02 can be used to derive solid bounds on the CR propagation parameters. This subset of light nuclei is independent from heavier nuclei and, thus, provides an important reference for the *standard* B/C analyses. In general, our bounds are compatible with expectations from B/C. A more detailed comparison between light nuclei and heavier nuclei, including B/C, is left to further studies. Compared to many previous studies of CR propagation we pushed the standards of the analysis to a new level. We consider CR antiprotons together with their parent nuclei, p and He, and present a consistent model for all of them. In order to better constrain solar modulation, we include at the same time VOYAGER and AMS-02 data. We treat solar modulation consistently for AMS-02 data sets which span slightly different measurement periods and consider the possibility of charge-sign dependent solar modulation. Furthermore, we have realized the importance of secondary antiproton production cross section to derive robust constrains on the spectral index of the diffusion coefficient. In a second step ,we have added a DM signal in CR antiproton. We find a hint for the annihilation of DM particles into $b\bar{b}$ final states with $m_{\rm DM} \sim 75$ GeV and a thermal annihilation cross section. We stress that we marginalize over a total of 15 parameters describing CR propagation in order to take uncertainties consistently into account. In the next section, we investigate two systematic uncertainties which can affect both, the derivation of CR propagation parameters and the DM hint in antiprotons.

5.2 Scrutinizing the evidence for DM in cosmic-ray antiprotons

In this section, we will study two sources of systematic uncertainties and their impact on the significance of the potential DM signal. We start with a discussion of the production cross sections for

secondary antiprotons. The derivation of these cross sections from collider data and its uncertainty was investigated in Chapter 4. In the second part of this section, we will discuss the impact of correlations in the AMS-02 data. Although the extremely precise data of AMS-02 is dominated by systematic uncertainty, a covariance matrix of these uncertainties is not provided by the experiment. We emphasize that the data the AMS-02 data of proton and helium fluxes are dominated by systematics in the whole energy range from 1 GV to 3 TV, while the antiproron-to-proton ratio is dominated by systematics only the intermediate energy range from 1.8 GV to 50 GV. We will first explain a data-driven method to obtain a covariance matrix of the CR data itself and then analyze the impact on our fit results

5.2.1 Antiproton production cross sections

Updating the GALPROP default cross sections to the latest parametrizations described in Chapter 4 reduces the significance of the potential DM signal to about 3σ. We propose two methods to incorporate the uncertainty of secondary antiproton production in the CR fit, namely, the *covariance matrix method* and the *joint fit method*.

Covariance matrix method

This methods relies on the propagation of errors in the cross-section parametrizations to the flux of CR antiprotons. It was first suggested and applied in [136]. The goal is to derive a covariance matrix from the cross-section fit which can be applied directly at the level of the antiproton flux. We use the covariance matrices of the cross-section fit (appendix of Ref. [3]) and sample $N = 1000$ random combinations of cross-section parameter sets. We denote a single realization of the parameter set with the index k. For each realization of cross-section parameters, we compute the source term of CR antiprotons, $q_{\bar{p}}^{(k)}(R_i)$, from Eq. (2.41). Here, R_i is the rigidity at the i-th data point. Finally, we extract the covariance matrix of the i-th and j-th data points by:

$$\mathcal{V}_{\mathrm{XS},ij}^{(q_{\bar{p},\mathrm{rel}})} = \frac{1}{N-1}\sum_{k=1}^{N}\left(\frac{q_{\bar{p}}^{(k)}(R_i)}{q_{\bar{p}}^{(\text{best fit})}(R_i)} - 1\right)\left(\frac{q_{\bar{p}}^{(k)}(R_j)}{q_{\bar{p}}^{(\text{best fit})}(R_j)} - 1\right) . \tag{5.4}$$

Note that in formulas, tables and figures *cross section* is abbreviated XS. If we assume that the relative uncertainties at source-term and flux level are identical,[9] the covariance matrix for the antiproton flux, $\phi_{\bar{p},i}^{(\text{AMS-02})}$, by:

$$\mathcal{V}_{\mathrm{XS},ij}^{\left(\phi_{\bar{p}/p}^{\text{AMS-02}}\right)} = \mathcal{V}_{\mathrm{XS},ij}^{(q_{\bar{p},\mathrm{rel}})}\,\phi_{\bar{p}/p,i}^{(\text{AMS-02})}\,\phi_{\bar{p}/p,j}^{(\text{AMS-02})} . \tag{5.5}$$

In the fit, we replace the covariance matrix in the log-likelihood definition of Eq. (5.3) by the sum of the AMS-02 measurement uncertainties and the cross-section covariance matrix.

$$\mathcal{V}_{ij}^{\left(\phi_{\bar{p}/p}^{\text{AMS-02}}\right)} = \mathcal{V}_{\mathrm{XS},ij}^{\left(\phi_{\bar{p}/p}^{\text{AMS-02}}\right)} + \delta_{ij}\left[\sigma_{\bar{p}/p,i}^{(\text{AMS-02})}\right]^2 . \tag{5.6}$$

[9] This is a very good approximation, confer to Chapter 4 for more details.

Finally, we stress that the covariance matrix method uses one disputable assumption. All uncertainties are propagated in terms of a covariance matrix, in other words, one assumes that the likelihood can be approximated by a multivariate Gaussian distribution. But the true likelihood could be much more complicated. Therefore, we propose a second method below.

Joint fit method

In the second method, we fit at the same time all the CR parameters and the parameters of the cross-section parametrization to, simultaneously, the CR flux measurements of AMS-02 and VOYAGER and the cross-section data from colliders. We will apply this method to the Param. MW (Eq. (4.2)). If we would take all 6 cross-section parameters into account, the already large parameter space of 11–13 MultiNest parameters would increase to 17–19. To avoid the challenge of such a large parameter space, we select 3 cross-section parameters which govern the main uncertainty in the shape and normalization of the cross-section parametrization: the over-all normalization, C_1, and the two parameters which change the shape of the cross section below $\sqrt{s} = 10$ GeV, C_5 and C_6 from Eq. (4.4). All other cross-section parameters are fixed to the best-fit values listed in Tabs. 4.3 and 4.7. The fit is performed to the same data sets as in Chapter 4. However, in contrast to the procedure in the previous chapter, we fit at the same time the data in the pp and the pA channels. As before, we use one nuisance ω for each data set with a Gaussian prior of width σ_ω as stated in Tabs. 4.1 and 4.5. The nuisance parameters are treated as linear parameters in the fit, namely, they are marginalized on-the-fly for each set of MultiNest parameters. The likelihood for the cross-section part is given by:

$$-2\log(\mathcal{L}_{\mathrm{XS}}) = \sum_e \sum_i \left(\frac{\omega_e \sigma^{(e)}_{\mathrm{inv},i} - \sigma^{(m)}_{\mathrm{inv}}(\sqrt{s}_i, x_{\mathrm{R}i}, p_{\mathrm{T}i})}{\omega_e \sigma_{\sigma^{(e)}_{\mathrm{inv},i}}} \right)^2 + \sum_e \left(\frac{1-\omega_e}{\sigma_{\omega_e}} \right)^2 , \tag{5.7}$$

where e denotes the experiments (this time of cross-section measurements) with data points i, and m denotes the cross-section parametrization. Furthermore, $\sigma^{(e)}_{\mathrm{inv}}$ and $\sigma_{\sigma^{(e)}_{\mathrm{inv}}}$ are the measured Lorentz-invariant cross section and its uncertainty, respectively. The total likelihood for the joint fit is given by the product of the likelihoods from Eqs. (5.3) and (5.7). Finally, we remind that this method correctly takes into account uncertainties beyond the Gaussian approximation, which is a clear advantage compared to the covariance matrix method. On the other hand, adding the 3 cross-section parameters significantly complicates the fit such that additional computation time is required. The number of likelihood evaluation of the fit in the default setup is roughly 200 000 while the joint fit requires approximately 500 000 likelihood evaluations to converge.

Results

In order to investigate the impact of cross-section uncertainties on the parameter estimation of CR propagation parameters and on the significance of the potential DM hint, we perform in total 8 fits. These fits correspond to 4 different setups concerning the antiproton production cross section. Then, each setup is fitted with and without a DM contribution. All results are summarized in Tab. 5.5.

Table 5.5: The best-fit parameters of various fits to investigate the impact of cross-section uncertainties. For details refer to Section 5.2.1.

parameter	**default setup, different XS**		**XS uncertainty by covariance matrix**				**Joint fit (CR+XS)**	
XS parametrization	Param. MD		Param. MW		Param. MD		Param. MW	
DM	incl.	excl.	incl.	excl.	incl.	excl.	incl.	excl.
γ_1	$1.55^{+0.11}_{-0.05}$	$1.65^{+0.09}_{-0.09}$	$1.65^{+0.07}_{-0.21}$	$1.68^{+0.07}_{-0.09}$	$1.52^{+0.08}_{-0.06}$	$1.64^{+0.09}_{-0.06}$	$1.57^{+0.06}_{-0.05}$	$1.67^{+0.09}_{-0.09}$
$\gamma_{1,p}$	$1.67^{+0.08}_{-0.02}$	$1.69^{+0.09}_{-0.07}$	$1.76^{+0.03}_{-0.17}$	$1.73^{+0.05}_{-0.08}$	$1.64^{+0.08}_{-0.05}$	$1.69^{+0.07}_{-0.05}$	$1.68^{+0.06}_{-0.05}$	$1.70^{+0.07}_{-0.05}$
γ_2	$2.43^{+0.01}_{-0.01}$	$2.39^{+0.01}_{-0.02}$	$2.43^{+0.02}_{-0.02}$	$2.37^{+0.02}_{-0.01}$	$2.43^{+0.02}_{-0.01}$	$2.28^{+0.01}_{-0.01}$	$2.44^{+0.01}_{-0.03}$	$2.38^{+0.01}_{-0.03}$
$\gamma_{2,p}$	$2.48^{+0.01}_{-0.01}$	$2.42^{+0.01}_{-0.02}$	$2.47^{+0.02}_{-0.02}$	$2.40^{+0.02}_{-0.01}$	$2.47^{+0.02}_{-0.01}$	$2.41^{+0.01}_{-0.01}$	$2.48^{+0.01}_{-0.03}$	$2.42^{+0.01}_{-0.03}$
R_0, [MV]	5860^{+870}_{-300}	6700^{+1490}_{-620}	6910^{+470}_{-1710}	6880^{+1200}_{-940}	5840^{+510}_{-430}	6830^{+730}_{-130}	5950^{+640}_{-370}	6910^{+970}_{-890}
s_0	$0.43^{+0.01}_{-0.08}$	$0.41^{+0.02}_{-0.06}$	$0.38^{+0.10}_{-0.02}$	$0.36^{+0.04}_{-0.06}$	$0.41^{+0.04}_{-0.03}$	$0.38^{+0.02}_{-0.04}$	$0.43^{+0.01}_{-0.08}$	$0.37^{+0.04}_{-0.05}$
D_0, [10^{28} cm^2/s]	$2.70^{+2.72}_{-0.25}$	$2.10^{+0.89}_{-0.50}$	$5.64^{+0.50}_{-3.60}$	$2.94^{+0.68}_{-1.06}$	$2.27^{+0.90}_{-0.13}$	$1.86^{+0.61}_{-0.19}$	$2.47^{+4.21}_{-0.01}$	$1.72^{+1.81}_{-0.26}$
δ	$0.35^{+0.02}_{-0.01}$	$0.41^{+0.02}_{-0.02}$	$0.35^{+0.03}_{-0.02}$	$0.43^{+0.01}_{-0.03}$	$0.35^{+0.02}_{-0.02}$	$0.42^{+0.02}_{-0.01}$	$0.35^{+0.04}_{-0.02}$	$0.42^{+0.02}_{-0.0004}$
v_A, [km/s]	$16.8^{+2.7}_{-1.8}$	$14.6^{+1.9}_{-1.7}$	$19.5^{+0.5}_{-4.9}$	$15.0^{+2.1}_{-0.6}$	$17.2^{+2.7}_{-2.2}$	$14.3^{+1.4}_{-1.8}$	$17.9^{+0.3}_{-2.2}$	$15.2^{+0.66}_{-1.38}$
$v_{0,\mathrm{c}}$, [km/s]	$4.80^{+2.44}_{-4.41}$	$1.97^{+4.11}_{-1.95}$	$2.63^{+6.21}_{-2.44}$	$0.66^{+1.65}_{-0.61}$	$4.22^{+3.67}_{-3.66}$	$2.78^{+1.01}_{-2.40}$	$1.17^{+5.39}_{-0.15}$	$0.27^{+2.02}_{-0.19}$
z_h, [kpc]	$2.62^{+2.49}_{-0.23}$	$2.54^{+1.24}_{-0.53}$	$5.76^{+0.50}_{-3.70}$	$3.72^{+0.82}_{-1.48}$	$2.20^{+0.81}_{-0.14}$	$2.28^{+0.86}_{-0.22}$	$2.46^{+4.21}_{-0.11}$	$2.15^{+2.61}_{-0.15}$
$\log(m_\mathrm{DM}/[\mathrm{GeV}])$	$1.85^{+0.02}_{-0.05}$		$1.88^{+0.07}_{-0.06}$		$1.82^{+0.04}_{-0.03}$		$1.89^{+0.03}_{-0.03}$	
$\log(\langle\sigma v\rangle/[\mathrm{s/cm}^3])$	$-25.50^{+0.01}_{-0.36}$		$-25.88^{+0.59}_{-0.09}$		$-25.32^{+0.01}_{-0.41}$		$-25.47^{+0.10}_{-0.42}$	
$\varphi_{\mathrm{SM,AMS\text{-}02},p,\mathrm{He}}$, [MV]	554^{+101}_{-13}	544^{+44}_{-58}	582^{+90}_{-64}	582^{+54}_{-25}	582^{+38}_{-46}	556^{+7}_{-28}	584^{+39}_{-80}	598^{+22}_{-61}
$\varphi_{\mathrm{SM,AMS\text{-}02},\bar{p}}$, [MV]	549^{+31}_{-45}	522^{+62}_{-115}	592^{+120}_{-90}	605^{+56}_{-114}	600^{+54}_{-56}	553^{+17}_{-55}	498^{+166}_{-81}	537^{+152}_{-61}
C_1, [10^{-3} (GeV)$^{-2}$]							$50.1^{+0.5}_{-1.0}$	$51.0^{+0.5}_{-1.7}$
C_5, [10^{-3}]							$0.32^{+0.24}_{-0.02}$	$0.27^{+0.08}_{-0.17}$
C_6							$3.82^{+0.27}_{-0.40}$	$3.73^{+0.81}_{-0.10}$
$\chi^2_{\mathrm{AMS\text{-}02},p}$	2.4	3.8	2.6	2.6	2.2	2.6	2.8	2.6
$\chi^2_{\mathrm{AMS\text{-}02,He}}$	4.4	4.6	4.1	5.1	4.1	4.3	3.9	4.7
$\chi^2_{\mathrm{AMS\text{-}02},\bar{p}}$	11.0	21.1	11.4	21.3	11.3	22.4	11.7	19.9
$\chi^2_{\mathrm{Voager},p}$	3.5	3.7	3.2	3.7	3.1	3.8	2.8	3.5
$\chi^2_{\mathrm{Voager,He}}$	0.9	1.0	1.7	1.1	1.1	1.0	1.1	1.9
$\chi^2_{\varphi_\mathrm{SM}}$	0.0	0.1	0.0	0.1	0.0	0.0	0.7	0.4
χ^2_CR	22.2	34.2	23.0	33.9	22.0	34.2	23.2	33.0
χ^2_XS							791.4	792.2
χ^2/dof	22.2/143	34.2/145	23.0/143	33.9/145	22.0/143	34.2/145	814.5/799	825.2/801
$\Delta\chi^2$	12.0		10.9		12.2		10.7	
DM significance	3.0σ		2.9σ		3.1σ		2.8σ	

In the first cross-section setup, we change the default parametrization from Param. MW to Param. MD. The results are very similar to the default setup, which is expected since the two cross-section parametrizations give similar results, see Chapter 4. The best-fit χ^2 of 34.2 is marginally smaller compared to the default fit which gives a χ^2 of 35.6. The residuals are shown in the first row of Fig. 5.4. They look very similar to the residuals of our default setup shown in Fig. 5.2. The best-fit propagation parameters (D_0, δ, v_A, $v_{0,c}$, and h_h) of both this fit are compatible with the results in the default setup. The contours in Fig. 5.5 (upper left panel) overlap in all parameters. Indeed, they look almost identical, except for the convection velocity. It converges to zero in both

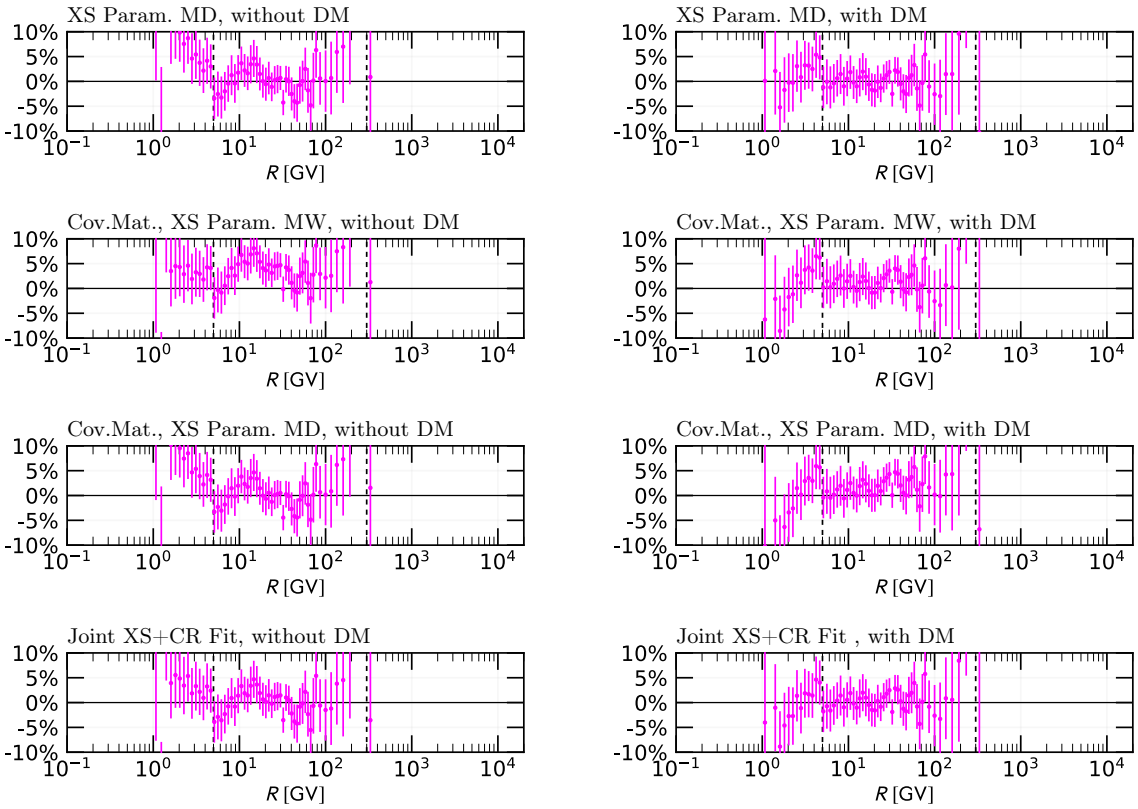

Figure 5.4: We display the residuals to the antiproton-to-proton flux ratio of AMS-02 for each of our 8 fits which are used to study the impact of cross-section uncertainties on the significance of the potential DM hint. The residuals plots on the left side contain 4 different cross-section setups. They do not incorporate any DM contribution, while the residual plots on the right-hand side corresponds to the same cross-section setup, but for them a DM signal is injected. Compared to the default setup we changed (top to bottom): (i) the default cross-section parametrization to Param. MD, (ii) applied the covariance matrix method with Param. MW, (iii) applied the covariance matrix method with Param. MD, and (iv) exploit the joint fit method using the Param. MW. The figure is taken from [2].

setups, but the upper constraint is a bit weaker when using the cross-section Param. MD. The significance for the DM signal reduces slightly from 3.1σ to 3.0σ.
The second and third setup, apply the covariance matrix method using the Param. MW and Param. MD as a baseline, respectively. For Param. MW the best-fit χ^2 without DM slightly reduces to 33.9, while the χ^2 in the fit with DM contribution remains constant at ~ 23. Consequently the significance for DM is reduced to 2.9σ. On the other hand, for Param. MD the covariance matrix method neither impacts the χ^2 of the fit with nor the one without DM contribution. The residuals in Fig. 5.4 look very similar to the default setup, however, we note one subtlety. Since the covariance matrix encodes a normalization uncertainty of the cross section, it is possible that the whole data are shifted up or down with respect to the best-fit. This is visible in particular for Param. MW

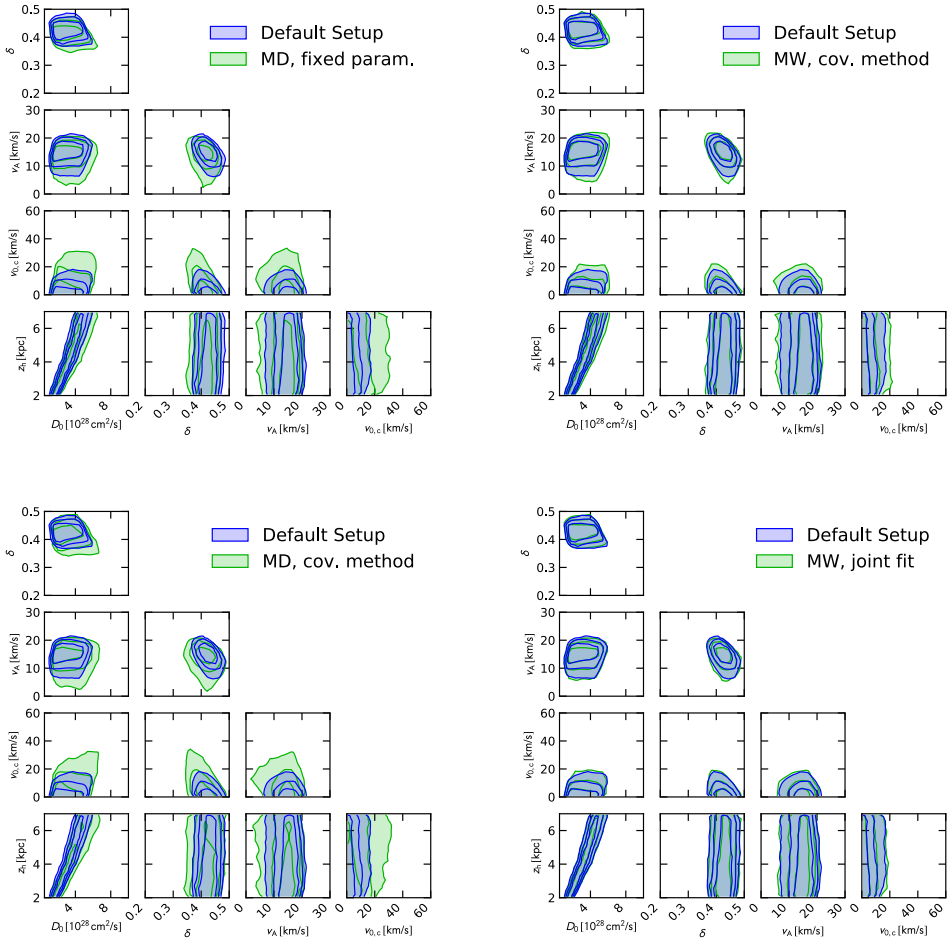

Figure 5.5: For each of our 4 different cross-section setups we compare the best-fit results for the propagation parameters with the default setup in a small triangle plot. The contours correspond to the 1σ, 2σ, and 3σ C.L. derived from the two-dimensional χ^2-distribution. The figure is taken from [2].

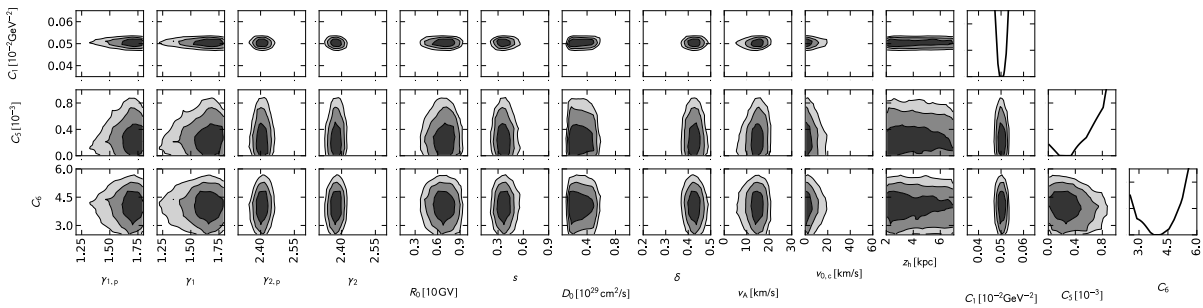

Figure 5.6: For the joint fit (without DM) we show the part of the triangle plot which contrasts the CR and cross-section parameters. The black contours display the 1σ, 2σ, and 3σ C.L. of the two-dimensional χ^2-distribution and the black lines in the panels on the very right show the χ^2 profile for the cross-section parameters (the y-axis ranges from 0–10). The figure is taken from [2].

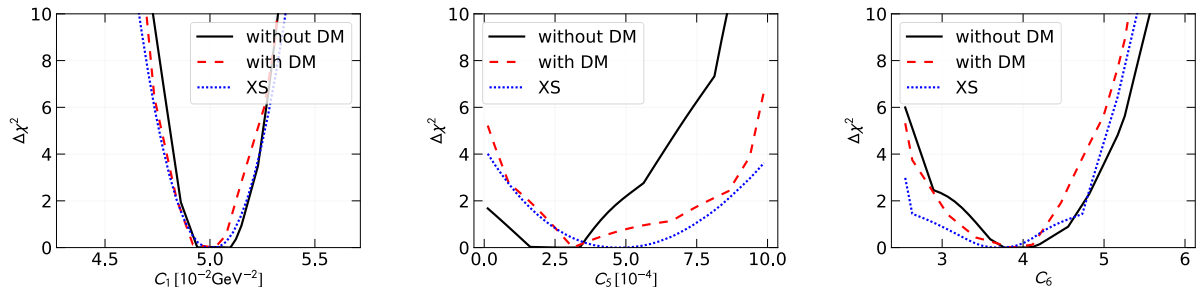

Figure 5.7: We compare the χ^2-profile of for the three cross-section parameters for the fit with (red dashed line) and without DM (black solid line). Furthermore, we display the χ^2-profile for the cross-section data only (blue dotted line), namely, the χ^2 is then defined by Eq. (5.7). The figure is taken from [2].

without DM and Param. MD with DM. Figure 5.5 shows that the propagation parameters are not affected by the covariance matrix approach which takes the cross-section uncertainties into account. Note that the effect of changing the cross-section parametrization (first setup) is larger than taking the cross-section uncertainty into account.

Finally, the fourth setup contains the joined fit based on Param. MW. The residuals in Fig. 5.4 are not affected by accounting for the cross-section uncertainties. The difference in the best-fit χ^2 with and without DM in this case reduces slightly compared to the other setups. We obtain $\Delta\chi^2 = 10.7$ which corresponds to a significance of 2.7σ for the potential DM signal. The propagation parameters in Fig. 5.5 (lower right panel) remains unchanged compared to the default setup. The joint fit allows to investigate whether there are degeneracies between CR propagation and the cross-section parametrization. In Fig. 5.6 we present the part of the triangle plot which contrasts the CR prop-

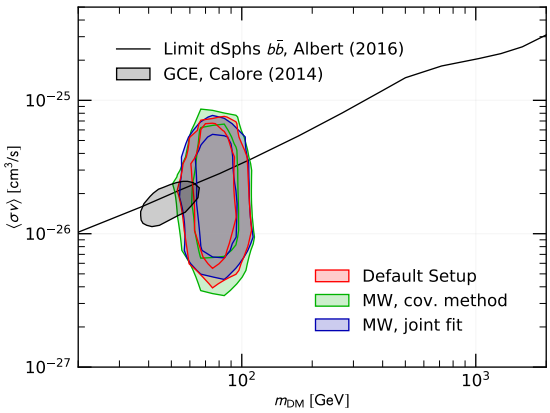

Figure 5.8: Best-fit contours in the plane of DM mass and velocity averaged annihilation cross section at the 1 and 2σ C.L. obtained from the different methods to include the uncertainties in the antiproton production cross section. For comparison we display the 2σ best-fit region of the GCE [214] and the current DM annihilation limits obtained from the observation of dwarf spheroidal galaxies [205]. The figure is taken from [2].

agation parameters and the parameters describing the antiproton production cross section. The triangle demonstrates that there are no strong or complicated degeneracies in the parameter space. We can investigate this conclusion a bit further by looking at the individual χ^2-profiles. Figure. 5.7 compares the χ^2-profiles of fitting only the cross section, $\chi^2_{\rm XS}$ is defined by Eq. (5.7), with the χ^2-profiles of the joint fit with and without DM contributions. We observe, that the χ^2-profiles for all three cross-section parameters are compatible. Especially, for the parameters C_1 and C_6 the agreement between the profile of the cross section and the joint fit profiles is very good, which means that C_1 and C_6 are entirely constrained by the cross-section data. For the parameter C_5 there is a very good agreement between the joint fit with DM and the cross-section χ^2-profile. The χ^2-profile of the fit without DM prefers slightly smaller values of C_5, so there is a small degeneracy. However, we remark that the χ^2-profile of the cross-section fit and the joint-fit without DM are very well compatible at the 1σ level.

We find a DM signal in all our setups and conclude that the DM hint is not related to underestimated uncertainties in the production cross section of secondary antiprotons. Taking the uncertainties into account decreases, however, slightly the significance of the DM signal from 3.1σ to 2.7σ. We compare the best-fit regions for the DM hint from our different cross-section setups in Fig. 5.8. We conclude that the best fit region does not depend on the cross-section uncertainties. All setups and methods converge to the same best-fit region around a DM mass of 70 GeV and an annihilation cross section between $\langle\sigma v\rangle = 3 \times 10^{-27}$ cm^3/s and 9×10^{-26} cm^3/s. We note the compatibility of the antiproton excess with the GCE [214] which will be explored in detail in Sec. 5.3. Furthermore, we display the current limit on the DM annihilation cross section derived from the observation of dwarf spheroidal galaxies with the Fermi-LAT detector [205]. Our potential DM signal is at the boundary of, but mostly below, the dwarf limits.

The results of this paragraph are somehow in tension with the analysis of [136] which finds a global significance of 1.1σ if cross-section uncertainties are considered. The origin of the different conclusion is not entirely clear. We note, however, some important differences between [136] and the analysis described in this Chapter:

- We perform a global fit of CR primaries and secondaries (p, He, and $\bar{p}/p$), while [136] exploits only the information of secondary fluxes ($\bar{p}$ and B). In this case, the primary fluxes are not fitted within the CR propagation model, but rather directly taken from the experimental measurements and then used calculate the source term of the secondaries. We note that fitting the primaries, especially protons, at the same time as fitting the secondaries gives tight constraints on reacceleration.
- The systematic uncertainties of the AMS-02 measurement partly cancel in the ratio leading to smaller relative uncertainties in the fit.
- The analysis of [136] relies on a CR propagation setup with a one-dimensional Galaxy. We, however, use a two-dimensional setup of the Galaxy and exploit the spatial dependence of CR fluxes in our Galaxy.
- We use a numerical solution of the diffusion equation of CRs while [136] relies on an analytic approximation. The treatment of reacceleration in the analytic model is different. It is confined to the Galactic Plane, while in the full numerical setup reacceleration occurs throughout the entire diffusion halo.

A more detailed exploration of the differences and their impact on the conclusion is under investigation.

5.2.2 Correlations in the systematic uncertainties of AMS-02 data

Space-based detectors measure CR fluxes at unpreceded precision with the immediate consequence that the systematic uncertainties in the measurement become more and more important. The proton and helium fluxes measured by AMS-02 are dominated by systematic uncertainties in the whole energy range from 1 GV to a few TV, while for the antiproton-to-proton ratio the statistical and systematic uncertainty have a similar weight, with a slightly larger systematic uncertainty between 2 GV and 50 GV. The commonly adopted treatment is to assume that systematic uncertainties are uncorrelated, namely, statistical and systematic uncertainties are added in quadrature. We also adopted this scheme in the previous section. As a result we obtain fit results with a χ^2/dof which are much smaller than one. In our standard setup, the χ^2/dof of protons is between 0.06 and 0.1 and the one of helium between 0.25 and 0.5. The problem with these small values of χ^2 is that we cannot say anything about the goodness of fit. Moreover, one might also wonder whether the significance of the potential DM signal can be affected by correlation in the AMS-02 data. We will investigate the impact of possible correlation scenarios in this chapter. However we stress that a proper and reliable treatment of systematic uncertainties would require a detailed analysis of the experimental collaboration which knows exactly the response and systematic uncertainties of the detector. So far, there is no such analysis by the AMS-02 collaboration, but recently there are attempts to model

the covariance matrixes of AMS-02 measurements from a theoretical perspective. Correlations are found to be one of the most important systematic uncertainties [95, 107, 152].

Methods to investigate the impact of correlated AMS-02 data

We will use two different strategies to take the effect of correlations in the AMS-02 data into account. In the first approach, we assume that the AMS-02 overestimated the uncorrelated systematic uncertainty. As a consequence, we fix the systematic uncertainty of the fluxes or flux ratios to 1%. Then we add this 1% uncertainty to the statistical uncertainty in quadrature. The remaining systematic uncertainty is assumed to be a pure normalization uncertainty. We remind that we marginalize over the normalization of proton and helium fluxes in our default fit setup, such that we can neglect any scale uncertainty in the data. This approach was already followed in [296][10]. This approach is, however, adhoc and its reliability is not entirely certain. Therefore, we suggest a second, data-driven method.

In the second approach, we try to derive constraints on the correlation in the AMS-02 data from the data itself, which is possible since the data establish one *sample realization* of the covariance matrix. For example, if we assume that the *true* CR flux is a smooth function but the flux measurement by AMS-02 introduces a systematic uncertainty with correlation of a few neighboring data points, we would expect to observe simultaneous upward or downward fluctuations of a few neighboring data points. In the following, we will use exactly this idea and derive limits on the correlation matrix.
We assume that the covariance matrix of the AMS-02 flux or flux ratio can be written as the sum of three components:

$$\mathcal{V} = \mathcal{V}_{\rm stat} + \mathcal{V}_{\rm short} + \mathcal{V}_{\rm long}\,. \tag{5.8}$$

The first term, $\mathcal{V}_{\rm stat}$, contains the statistical uncertainties provided by the AMS-02 collaboration and the remaining two terms contain the systematic uncertainties, which may exhibit two kind of correlations, one correlation on *short* energy scales (up to ~ 10 neighboring data points, *c.f* also Eq. (5.9)), $\mathcal{V}_{\rm short}$, and one on *long* energy scales (more than ~ 10 neighboring data points), $\mathcal{V}_{\rm long}$. We will only be able to constrain the correlations at short scales with the method presented below. But we stress that correlations at short energy scales are the most important concerning the significance of the potential DM signal. They could in principle be able to fake a sharp signal as the one expected from DM annihilation. On the other hand, long correlations are, for example, an overall normalization or a slope. We assume that the contribution of $\mathcal{V}_{\rm long}$ can be absorbed in our fit by the CR propagation parameters and the nuisance parameters, A_p and $A_{\rm He}$. For the covariance matrix with short correlation length, $\mathcal{V}_{\rm short}$, we take the following ansatz:

$$\mathcal{V}_{{\rm short},ij} = \exp\left(-\frac{|i-j|^\alpha}{{\ell_{\rm corr}}^\alpha}\right) f^2 \sigma_{{\rm sys},i}\sigma_{{\rm sys},j}\,, \tag{5.9}$$

where i and j are the i-th and j-th data point of the AMS-02 flux or ratio, and $\sigma_{{\rm sys},i}$ and $\sigma_{{\rm sys},j}$ are the respective systematic uncertainties. Finally, we have three free parameters which describe the

[10] This approach was suggested in a private conversation with the AMS-02 group in Aachen.

shape of the covariance matrix. They determine the length (in terms of neighboring data point) of correlation, $\ell_{\rm corr}$, the fraction of systematic uncertainty which exhibits short correlations, f, and one parameter which alters the shape of the correlation matrix, α. In order to determine $\mathcal{V}_{\rm short}$ we require a description of the *true* CR flux or ratio. We assume that this is can be obtained by fitting a smooth function to the measured CR flux or ratio. For the smooth function we adopt a broken power law with three smooth breaks[11] for the antiproton-to-proton ratio and the helium flux, and a power law with 4 breaks for the proton flux. We denote the difference of this smooth function and the measured AMS-02 flux or ratio at the rigidity R_i as x_i. Note that fitting a smooth function absorbs long correlations. So, we can neglect them when defining the likelihood to determine the short covariance matrix:

$$-\log(\mathcal{L}) = \frac{1}{2}\log\left(\det\left[\mathcal{V}_{\rm stat}+\mathcal{V}_{\rm short}(\ell_{\rm corr},f,\alpha)\right]\right)+\frac{1}{2}\boldsymbol{x}\cdot\left[\mathcal{V}_{\rm stat}+\mathcal{V}_{\rm short}(\ell_{\rm corr},f,\alpha)\right]^{-1}\boldsymbol{x}+\text{const}\,. \quad (5.10)$$

The first term arises from the normalization of the multivariate Gaussian while the second term corresponds to the usual χ^2 definition. The reliability of the constraints from our method is verified in a toy MC. We apply the method on the AMS-02 data, separately to protons, helium, and the antiproton-to-proton ratio, since, in principle, the correlation of different measurements may change.

[11] The functional form is the generalization of Eq. (5.1).

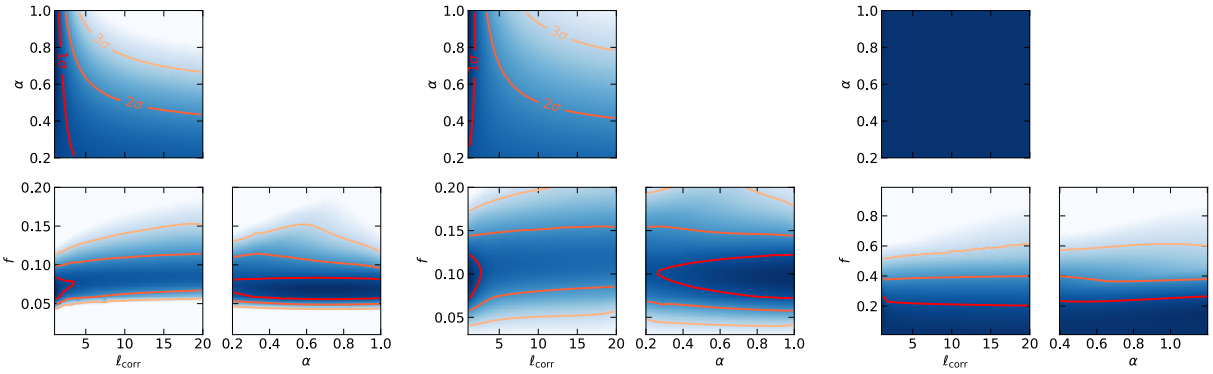

Figure 5.9: Triangle plots for the fit of the covariance matrices using Eq. (5.10) for the proton flux (left panel), the helium flux (central panel), and antiproton-over-proton flux ratio (right panel). The figure is taken from [2].

Table 5.6: Based on the fit results of Fig. 5.9 we use three benchmark scenarios summarized in this table to investigate the impact of correlations in the AMS-02 data.

	$\ell_{\rm corr}=\mathbf{0}$			$\ell_{\rm corr}=\mathbf{5}$			$\ell_{\rm corr}=\mathbf{10}$		
data set	p	He	$\bar{p}/p$	p	He	$\bar{p}/p$	p	He	$\bar{p}/p$
f	0.062	0.080	0.30	0.079	0.103	0.30	0.082	0.101	0.30
α	0.63	0.81	1.00	0.20	0.21	1.00	0.20	0.20	1.00

Our results are presented in in Fig. 5.9. The constraints on the covariance matrix of protons and helium are very similar. In both cases, there is a preference for a small value of α and a slight preference for a small correlation length, $\ell_{\rm corr}$. However, at 2σ the value of $\ell_{\rm corr}$ is not constrained for both fluxes. We obtain good constraints on the fraction of the systematic uncertainty which is allowed to have a small correlation length. For protons this fraction is restricted between 5% and 10% while for helium it is restricted between 5% and 15%. For the antiproton-to-proton ratio we obtain less strict constraints from the data since statistical uncertainties are non-negligible. But we conclude that the fraction of a correlated systematic uncertainty should be below $\sim 30\%$ at a 90% C.L. Since, we cannot point to a single preferred covariance matrix with our data-driven method we will explore three benchmark scenarios with $\ell_{\rm corr}$ fixed to 0, 5, and 10, respectively. The other two parameters are obtained as follows. For proton and helium we adopt the best-fit values of α and f at the specific choice of $\ell_{\rm corr}$. In the case of the antiproton-to-proton ratio we proceed differently. Here the preferred value of f would converge to 0. But we want to test the impact of correlation on our DM signal. Therefore, we adopt values of f at the upper bound of the 90% C.L. We adopt $f = 0.3$ for each benchmark scenario. The parameter alpha is fixed to 1. The three benchmark scenarios and the adopted parameters are summarized in Tab. 5.6.

Results

We perform 8 fits to investigate the impact of correlation in the AMS-02 data. These 8 fits correspond to 4 different choices of the covariance matrices. Then, for each choice we perform one fit with and one without DM contribution. We have described the 4 different setups of covariance matrices in the previous section. In the first setup, we fix the systematic uncertainty of all AMS-02 data sets to 1%. The remaining three setups exploit the covariance matrices obtained from our data-driven method with benchmarks of the correlation lenght chosen set to $\ell_{\rm corr} = 0$, 5, and 10. The results of all the fits are summarized in Figs. 5.10 and 5.11, and in Tab. 5.7.

First, we have a look at the results of the fit where we fix the systematic uncertainties to 1%, which effectively reduces all uncertainties in the fit. In this setup, the fit without DM converges at a χ^2/dof of 77.4/143 which is still significantly smaller than one. The contribution from the antiproton-over-proton ratio to this χ^2 is 44.0 which matches very well the number of data points of 42. So, the problem arises from the proton and helium fits, which converge to a χ^2 of 7.6 and 9.8, respectively, which is far too small for a number of about 50 data points each. The best-fit region of the propagation parameters is compatible with the default setup. The comparison of the best-fit propagation parameters to the default setup is shown in Fig. 5.10 (upper left panel). The fit with DM converges to a best-fit χ^2 of 47.4, hence, we obtain a $\Delta\chi^2$ of 30 or, equivalently, a significance of 5.1σ. The best-fit values of the DM mass and the annihilation cross section are consistent with the default setup as shown in Fig. 5.11.

We now discuss the results of the three benchmark scenarios taken from the data-driven method. A DM signal improves the $\Delta\chi^2$s of the fits by 34.1, 17.6, and 18.0 for the benchmarks at $\ell_{\rm corr} = 0$, 5 and 10, respectively. These values correspond to a significance of 5.5σ for $\ell_{\rm corr} = 0$ and 3.8σ for the other two benchmarks. We note, however, that in all three cases the best-fit χ^2/dof is significantly larger than 1. It varies between 1.6 and 2.0. The contribution of the antiproton-over-proton to the χ^2 is reasonable while a too large contribution comes from the proton and helium fit. So, now we

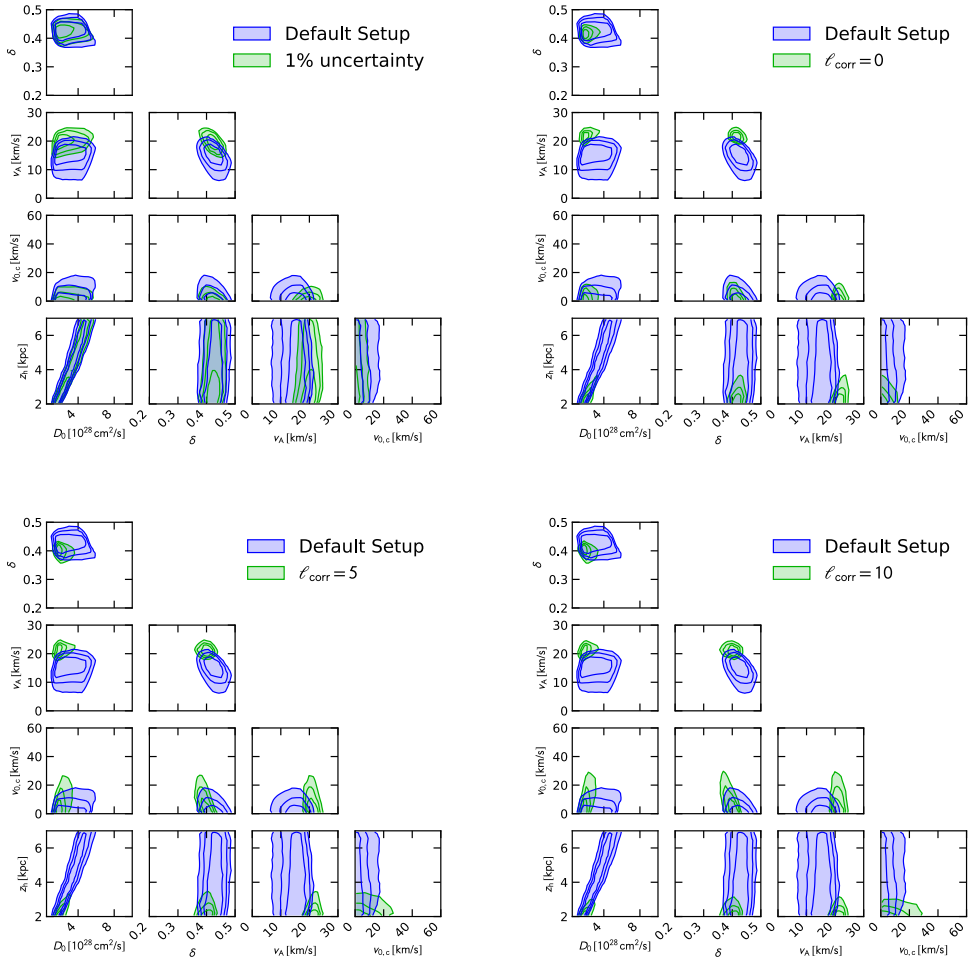

Figure 5.10: Similar to Fig. 5.4. We display the 1–3σ contours of the 2-dimensional χ^2-distribution for a choice of propagation parameters. The panels display the comparison of our default setup and the 4 different choices of correlation matrices for the treatment of systematic uncertainties. The upper left panel corresponds to the setup where we fix systematic uncertainties to 1%. The remaining three panels show the comparison with our data-driven method with a benchmark correlation length of $\ell_{\rm corr} = 0$ (upper right), 5 (lower left), 10 (lower right). The figure is taken from [2].

seem to underestimate their uncertainties. Indeed, the relative uncertainties of proton and helium are very small now. The relative uncertainty of the systematic uncertainty in the AMS-02 proton flux measurement is approximately 2%. Our data-driven method, shows that only about 10% of this uncertainty should be considered in the fit. In other words, we reduce the effective uncertainty of the proton flux to 0.2%, which seems to be slightly underestimating. Nevertheless, we observe a few interesting results. When we compare the benchmark setup with $\ell_{\rm corr} = 0$ with the two setups of $\ell_{\rm corr} = 5$ and 10 we observe that the correlation of a few neighboring bins reduces the significance

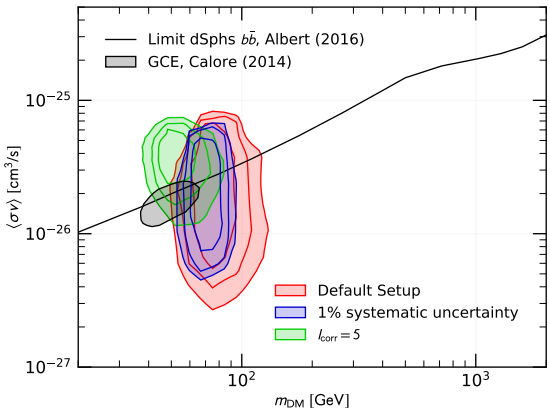

Figure 5.11: Similar to Fig. 5.8. We show the 1–3σ best-fit contours in the plane of DM mass and velocity averaged annihilation cross section of the default setup and two cross checks with different correlation assumption. First, the scenario where we fix systematic uncertainties to 1% and, second, the benchmark setup with $\ell_{\rm corr} = 5$. The contour of the DM interpretation of the GCE [214] and the DM limit from dwarf spheroidal galaxies [205] are shown for comparison. The figure is taken from [2].

of the potential DM from 5.5σ to 3.8σ. So, the effect of correlation works as anticipated in the introduction of this chapter. The best-fit contours of the CR propagation parameters shrink with respect to our default setup. Especially, we observe that the preferred value of the halo half-height converges to very small values of $z_h \lesssim 3$ kpc, which are disfavored from the observation of leptons at low energies [115, 297, 298] and the recent analysis of the beryllium-to-boron ratio [110]. The best-fit region for the corresponding DM signal is shown in Fig. 5.11 for $\ell_{\rm corr} = 5$. The contours for $\ell_{\rm corr} = 0$ and 10 look very similar to $\ell_{\rm corr} = 5$. So, in all three benchmark scenarios the preferred DM mass shifts to slightly smaller values. The fact that the fits prefer only slightly larger values of $\langle \sigma v \rangle$ is directly related to the preferred region of z_h. We remind that z_h and $\langle \sigma v \rangle$ are anticorrelated.

Finally, we stress that all results of this paragraph should be taken with caution. We use educated guessing and some data constraints in order to obtain four different benchmark scenarios for the correlation of uncertainties in the AMS-02 data. By no means do we claim that our benchmarks establish a full representation of the all allowed covariance matrices or that the *true* covariance matrix is contained in our benchmarks. We consider this chapter as a proof of concept. Correlations in the AMS-02 data can have an important effect on the parameter estimation and the significance of the potential DM signal. We conclude nonetheless, if we adopt the realistic assumption that only a fraction of the systematic uncertainty is correlated on short energy scales, we rather seem to increase the significance of the DM hint.

Table 5.7: The best-fit parameters of various fit setups to investigate the impact of correlated AMS-02 uncertainties.

parameter	**1% σ_{sys}**		**$\ell_{\mathrm{corr}} = 0$**		**$\ell_{\mathrm{corr}} = 5$**		**$\ell_{\mathrm{corr}} = 10$**	
XS parametrization	Param. MW		Param. MW		Param. MW		Param. MW	
DM	incl.	excl.	incl.	excl.	incl.	excl.	incl.	excl.
γ_1	$1.62^{+0.08}_{-0.10}$	$1.77^{+0.02}_{-0.08}$	$1.65^{+0.02}_{-0.03}$	$1.70^{+0.03}_{-0.05}$	$1.61^{+0.10}_{-0.12}$	$1.72^{+0.02}_{-0.06}$	$1.65^{+0.07}_{-0.11}$	$1.67^{+0.03}_{-0.06}$
$\gamma_{1,p}$	$1.70^{+0.08}_{-0.07}$	$1.74^{+0.02}_{-0.07}$	$1.67^{+0.01}_{-0.04}$	$1.66^{+0.02}_{-0.04}$	$1.64^{+0.09}_{-0.13}$	$1.69^{+0.02}_{-0.06}$	$1.66^{+0.04}_{-0.13}$	$1.65^{+0.02}_{-0.06}$
γ_2	$2.43^{+0.01}_{-0.01}$	$2.37^{+0.02}_{-0.002}$	$2.42^{+0.00}_{-0.01}$	$2.39^{+0.01}_{-0.00}$	$2.43^{+0.00}_{-0.01}$	$2.40^{+0.00}_{-0.00}$	$2.42^{+0.01}_{-0.01}$	$2.39^{+0.01}_{-0.00}$
$\gamma_{2,p}$	$2.47^{+0.01}_{-0.01}$	$2.40^{+0.02}_{-0.001}$	$2.45^{+0.00}_{-0.01}$	$2.41^{+0.01}_{-0.00}$	$2.46^{+0.00}_{-0.02}$	$2.42^{+0.00}_{-0.00}$	$2.45^{+0.01}_{-0.01}$	$2.42^{+0.01}_{-0.00}$
R_0, [MV]	6600^{+720}_{-1090}	9180^{+50}_{-1270}	6869^{+200}_{-173}	7844^{+575}_{-512}	6519^{+1300}_{-793}	7983^{+340}_{-707}	6743^{+1103}_{-743}	7290^{+262}_{-582}
s_0	$0.42^{+0.03}_{-0.05}$	$0.32^{+0.06}_{-0.01}$	$0.45^{+0.01}_{-0.01}$	$0.40^{+0.02}_{-0.01}$	$0.47^{+0.01}_{-0.04}$	$0.41^{+0.02}_{-0.01}$	$0.46^{+0.02}_{-0.03}$	$0.41^{+0.02}_{-0.01}$
D_0, [10^{28} cm^2/s]	$2.80^{+2.35}_{-0.85}$	$2.19^{+0.36}_{-0.58}$	$1.99^{+0.05}_{-0.02}$	$1.79^{+0.34}_{-0.013}$	$1.94^{+0.22}_{-0.20}$	$1.90^{+0.05}_{-0.03}$	$1.84^{+0.22}_{-0.02}$	$1.66^{+0.25}_{-0.00}$
δ	$0.36^{+0.02}_{-0.01}$	$0.43^{+0.002}_{-0.02}$	$0.37^{+0.01}_{-0.01}$	$0.42^{+0.00}_{-0.01}$	$0.36^{+0.02}_{-0.00}$	$0.40^{+0.00}_{-0.00}$	$0.37^{+0.01}_{-0.01}$	$0.41^{+0.00}_{-0.01}$
v_{A}, [km/s]	$21.1^{+0.4}_{-3.4}$	$19.6^{+1.2}_{-1.4}$	$21.87^{+0.17}_{-0.17}$	$20.93^{+1.50}_{-0.45}$	$22.23^{+1.89}_{-1.77}$	$22.15^{+0.15}_{-0.93}$	$21.37^{+1.51}_{-0.79}$	$20.25^{+1.41}_{-0.17}$
$v_{0,\mathrm{c}}$, [km/s]	$0.52^{+4.62}_{-0.27}$	$0.06^{+0.79}_{-1.36}$	$0.53^{+2.75}_{-0.27}$	$0.37^{+1.51}_{-0.26}$	$3.69^{+10.95}_{-3.66}$	$0.24^{+2.65}_{-0.21}$	$2.01^{+9.99}_{-1.92}$	$0.25^{+3.96}_{-0.00}$
z_{h}, [kpc]	$2.76^{+2.68}_{-0.75}$	$2.72^{+0.44}_{-0.70}$	$2.03^{+0.08}_{-0.00}$	$2.05^{+0.41}_{-0.02}$	$2.00^{+0.29}_{-0.00}$	$2.11^{+0.03}_{-0.01}$	$2.01^{+0.12}_{-0.00}$	$2.02^{+0.13}_{-0.02}$
$\log(m_{\mathrm{DM}}/[\mathrm{GeV}])$	$1.82^{+0.05}_{-0.02}$		$1.70^{+0.04}_{-0.01}$		$1.74^{+0.01}_{-0.06}$		$1.71^{+0.05}_{-0.06}$	
$\log(\langle\sigma v\rangle/[\mathrm{s/cm}^3])$	$-25.57^{+0.26}_{-0.37}$		$-25.49^{+0.07}_{-0.12}$		$-25.41^{+0.10}_{-0.10}$		$-25.38^{+0.05}_{-0.14}$	
$\varphi_{\mathrm{SM,AMS\text{-}02},p,\mathrm{He}}$, [MV]	674^{+9}_{-138}	738^{+58}_{-39}	819^{+14}_{-0}	857^{+16}_{-25}	839^{+20}_{-43}	844^{+14}_{-26}	837^{+18}_{-12}	832^{+26}_{-2}
$\varphi_{\mathrm{SM,AMS\text{-}02},\bar{p}}$, [MV]	601^{+146}_{-138}	613^{+69}_{-94}	741^{+71}_{-81}	568^{+30}_{-55}	743^{+190}_{-43}	534^{+57}_{-26}	791^{+92}_{-99}	556^{+42}_{-34}
$\chi^2_{\mathrm{AMS\text{-}02},p}$	3.3	7.6	83.5	81.0	74.4	75.9	79.4	84.3
$\chi^2_{\mathrm{AMS\text{-}02,He}}$	7.6	9.8	97.4	98.9	96.5	94.5	96.7	89.7
$\chi^2_{\mathrm{AMS\text{-}02},\bar{p}}$	30.3	44.0	52.2	69.2	42.3	50.1	47.4	53.9
$\chi^2_{\mathrm{Voager},p}$	3.4	7.5	8.8	14.7	7.7	9.5	6.8	13.4
$\chi^2_{\mathrm{Voager,He}}$	2.1	6.8	7.3	11.4	9.3	10.1	10.4	10.0
$\chi^2_{\varphi_{\mathrm{SM}}}$	0.6	1.7	0.9	8.8	2.4	10.0	0.6	8.0
χ^2/dof	47.4/145	77.4/143	250.0/143	284.1/145	232.6/143	250.2/145	241.3/143	259.3/145
$\Delta\chi^2$	30.0		34.1		17.6		18.0	
DM significance	5.1σ		5.5σ		3.8σ		3.8σ	

5.3 Probing dark matter annihilation with antiprotons and gamma rays

In Secs. 5.1 and 5.2, we have investigated a possible hint of DM annihilation in CR antiprotons. Here, we will explore the compatibility of this potential CR antiproton excess with the GCE. Moreover, we will extend the study of Sec. 5.2, where we presented results for $b\bar{b}$ final states, to further SM final states. This section is structured as follows. In Sec. 5.3.1 we briefly recap the setup of our global CR fits and present their results. Then, in Sec. 5.3.2 we explain the setup of the GCE fit and limits form dSphs. We present the results of a joint fit to CR antiprotons and gamma rays. Finally, in Sec. 5.3.3 we interpret our results within the singlet scalar Higgs portal model. This section is based on the paper [6].

5.3.1 Cosmic-ray fits for individual dark matter annihilation channels

We perform global fits to CR proton, helium, and antiproton data, allowing for a DM contribution in antiprotons which gives rise to a characteristic signal as described in Eq. (2.51). The setup of the CR is the same as in [8] and very similar to the one described in Sec. 5.4.1. The only small difference is that in this section we exploit the production cross section of secondary antiprotons from [123], which is the default cross section implemented in the GALPROP package. We take the DM energy spectra, $\mathrm{d}N_{\bar{p}}^{f}/\mathrm{d}R$, which are tabulated in [292]. However, these tables are only provided for on-shell production of the W- or Z-bosons. We extend the tables to lower masses and allow off-shell production of one gauge boson. This off-shell production can be relevant because the decay widths of the two gauge bosons are relatively large. Off-shell gauge bosons are denoted with an asterisk superscript. We generated the spectra of ZZ^* and WW^* final states with MADGRAPH5_AMC@NLO [299] and PYTHIA 8.215 [300], where we adopt the default settings and choose a scale of $Q = m_{\mathrm{DM}}$. We note that the choice of scale introduces an uncertainty on the energy spectra of 15% to 30%, which, however, does not significantly affects our final results. Furthermore, we have checked that our spectra for on-shell WW and ZZ production, *i.e.* for $m_{\mathrm{DM}}{>}m_W$ and $m_{\mathrm{DM}}{>}m_Z$, respectively, are in agreement with the tables of [292]. Off-shell production is typically not relevant for the Higgs boson or top-quark production because the respective decay widths are very small. We assume an NFW profile (see Eq. 1.4) for the DM distribution in our Galaxy with a characteristic halo radius $r_h = 20$ kpc, and a characteristic halo density ρ_h, such that the local DM density is normalized to 0.43 GeV/cm^3 [41] at the solar position of 8 kpc distance from the Galactic Center.

The results of the CR fits are presented in Fig. 5.12. We find that a DM signal can improve the CR fit for all the considered SM final states. The best fit without DM contribution converges to a χ^2/dof of 71/165 (see Ref. [8]) while the fits with DM contribution give a best-fit χ^2/dof of 46/163 ($b\bar{b}$), 48/163 (hh), 50/163 (gluons and/or light quarks), 50/163 (WW^*), 46/163 (ZZ^*), and 59/163 ($t\bar{t}$), respectively. The fits show an improvement in $\Delta\chi^2$ between 20 an 25 which, formally, corresponds to a significance of 4 to 4.5σ. The $t\bar{t}$ channel forms the only exception. It is gives a slightly smaller $\Delta\chi^2$ of 12 which corresponds to a significance 3σ. All values are summarized in Tab. 5.8. We note that these results are affected by systematic uncertainties. We have discussed

the impact of the antiproton production cross section and correlations in the AMS-02 data in Chapter 5. Especially, a more recent description of the antiproton production cross section and its uncertainties can reduce the significance of the potential DM signal to about 3σ in the $b\bar{b}$ channel. We expect that all channels are affected by this systematics similarly. However, we do not expect the smaller significance to change the general conclusions of this section. The best-fit region for the potential DM signal depends on the SM final state: In general, lighter SM final states prefer a lighter DM particle. The best-fit DM mass for annihiliation into two gluons or a pair of light quarks converges to $m_{\mathrm{DM}} \sim 35$ GeV, while the $t\bar{t}$ final state requires a DM masse close to the production threshold of the top quark pair at 173 GeV. The required DM annihilation cross sections varies between $\langle\sigma v\rangle = 2 \times 10^{-27}$ cm^3/s and 2×10^{-25} cm^3/s. The annihilation cross sections depends on the DM mass: the lager the DM mass the larger $\langle\sigma v\rangle$. This trend is in agreement with the DM interpretation of the GCE [226].

5.3.2 Joint fit of antiprotons and gamma rays

In the joint fit of CRs and gamma-rays, we aim to fit simultaneously the excess in CR antiprotons and the GCE. Furthermore, we will include DM limits of dSphs. The GCE is a excess in the gamma-ray spectrum around the Galactic center at a few GeV [213–215]. Despite viable astrophysical explanations a DM origin of the excess is not excluded. For more details we refer to Sec. 3.2. We exploit the energy spectrum of the GCE and the correlated uncertainties provided in [226]. The

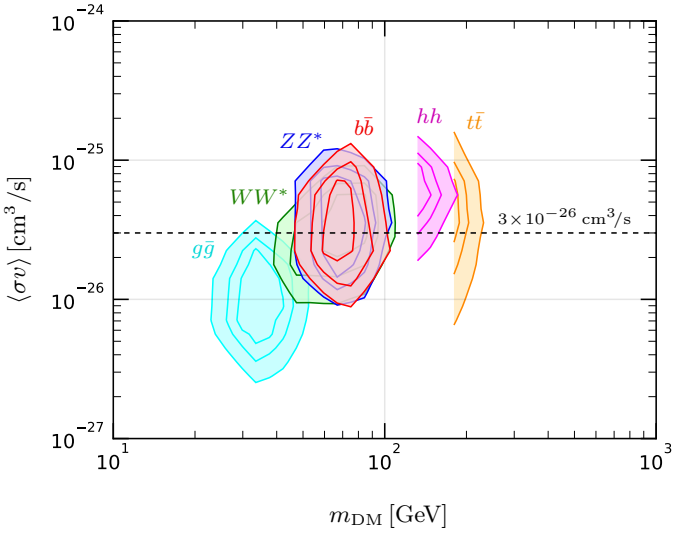

Figure 5.12: Hint for DM annihilation in the antiproton spectrum derived from a global fit of CRs. We exploit different SM final states: gg (cyan), WW^* (green), $b\bar{b}$ (red), ZZ^* (blue), hh (pink) and $t\bar{t}$ (orange). The results are presented in the plane of DM mass and velocity averaged annihilation cross section. The contours denote the 1, 2, and 3σ C.L. of the preferred DM mass and the annihilation cross section. The figure is taken from [6].

fit takes into account an uncertainty on the J-factor of the ROI analyzed in [226], J_{40°. The ROI of [226] extends over a $40^\circ \times 40^\circ$ square centered around the Galactic Center. The Galactic plane is masked for latitudes of $|b| < 2^\circ$. We take into account an uncertainty on our model of $\sigma_{\rm rel} = 10\%$. The uncertainty on the model comes from systematic differences in the gamma-ray energy spectra from DM annihilation derived with different Pythia versions. The likelihood of the GCE fit is defined by:

$$\begin{aligned} -2\log(\mathcal{L}_{\rm GCE}) &= \log\left(\det\left[\mathcal{V}_{ij}^{\rm GCE} + \delta_{ij}[\sigma_{\rm rel}\, S^{(m)}(E_i)]^2\right]\right) \\ &+ \sum_{ij}\left(S_i^{(\rm GCE)} - S^{(m)}(E_i)\right)\left(\mathcal{V}_{ij}^{\rm GCE} + \delta_{ij}[\sigma_{\rm rel}\, S^{(m)}(E_i)]^2\right)^{-1}\left(S_j^{(\rm GCE)} - S^{(m)}(E_j)\right) \\ &+ \frac{[\log(J_{40^\circ}) - \log(J_{40^\circ,\rm norm})]^2}{[\sigma_{\log J}]^2} + \text{const}\,. \end{aligned} \tag{5.11}$$

Here $S_i^{(\rm GCE)}$ is the gamma-ray flux in the i-th energy bin as provided by [226] and $\mathcal{V}^{\rm GCE}$ is the corresponding covariance matrix, while $S^{(m)}(E_i)$ is the flux calculated in our model:

$$S^{(m)}\left(E_i, m_{\rm DM}, \langle\sigma v\rangle, J_{40^\circ}\right) = \int_{E_{{\rm min},i}}^{E_{{\rm max},i}} {\rm d}E\, \frac{{\rm d}S}{{\rm d}E}\left(E, m_{\rm DM}, \langle\sigma v\rangle, J_{40^\circ}\right) \tag{5.12}$$

with ${\rm d}S/{\rm d}E$ defined in Eq. (3.1). The energy spectra of gamma-rays are obtained with the Pythia 8.209 event generator [300]. The difference of these spectra compared to spectra generated with Pythia 6 [301] is of the order of 10%. We incorporate this uncertainty in the likelihood by setting $\sigma_{\rm rel}$ to 0.1. Finally, we marginalize over the uncertainty in the J-factor. The uncertainty on $\log(J_{40^\circ})$ was derived in [302]. We use this result and adopt a Gaussian distribution for $\log(J_{40^\circ})$ (log-normal in J_{40°) with a mean value of $\log(J_{40^\circ,\rm norm}) = 53.54$ and a width of $\sigma_J = 0.43$. For more

Table 5.8: Summary of the best-fit χ^2s of the individual fits of CRs and the GCE as well as the joint fits The number of dof for the CR and GCE fit are 163 and 22, respectively.

	individual fits		joint fit	
channel	$\chi^2_{\rm CR}$	$\chi^2_{\rm GCE}$	$\chi^2_{\rm CR}$	$\chi^2_{\rm GCE}$
gg	50.3	20.8	52.0	31.6
$b\bar{b}$	45.8	21.2	47.9	23.5
$WW^{(*)}$	50.4	25.6	54.6	25.6
$ZZ^{(*)}$	45.6	25.0	45.8	25.9
hh	47.6	25.8	48.4	25.8
$t\bar{t}$	59.5	41.1	59.5	41.1

details, we refer to [302]. All in all, the fit of the GCE contains 3 free parameters: the DM mass, $m_{\rm DM}$, the annihilation cross section, $\langle\sigma v\rangle$, and the J-factor, J_{40°.
In order to join the CR fit with the GCE fit we proceed as follows. We use the results of the CR fits performed in Sec. 5.3.1 and extract the χ^2-profile in $m_{\rm DM}$ and $\langle\sigma v\rangle$, which we denote $\tilde{\chi}^2_{\rm CR}(m_{\rm DM}, \langle\sigma v\rangle)$. Note that by extracting the profile we marginalize over a total of 11 CR propagation parameters. In Sec. 5.3.1, we fixed the local DM density to $\rho_{\rm sun,norm} = 0.43$ GeV/cm^3. Now, we want to marginalize over the uncertainty of the local DM density. Thus, we *re-interpret* the extracted CR χ^2-profile and define the final CR likelihood by:

$$-2\,\log(\mathcal{L}_{\rm CR})\Big(m_{\rm DM}, \langle\sigma v\rangle, \rho_{\rm sun}\Big) = \tilde{\chi}^2_{\rm CR}\left(m_{\rm DM}\,,\ \langle\sigma v\rangle\,\frac{\rho^2_{\rm sun}}{\rho^2_{\rm sun,norm}}\right) + \left(\frac{\rho_{\rm sun}-\rho_{\rm sun,norm})}{\sigma_{\rho_{\rm sun}}}\right)^2 . \quad (5.13)$$

We adopt an uncertainty on the local DM density of $\sigma_{\rho_{\rm sun}} = 0.15$ GeV/cm^3. In the joint fit of CRs (p, He, and $\bar{p}/p$) and the GCE, there is one subtlety concerning the DM density profile. When calculating J_{40°, we assume a gNFW DM density profile (see Eq. 1.5) with $\gamma = 1.2 \pm 0.08$ while in the CR we use the normal NFW profile ($\gamma = 1.0$). However, the CR flux is virtually not affected by difference of an NFW and a gNFW profile. In Sec. 5.4, we investigated impact of the DM density profile on the CR limits by changing the cuspy NFW profile to a cored Burkert profile with core radius of $r_c = 5$ kpc and we found that the limits where affected by less than 30%. The differences between NFW and gNFW are much smaller. In this sense, it is justified to explore an NFW profile in the CR fit, while using a gNFW profile in the GCE fit.

Finally, we take into account the constraints on DM annihilation from the observation of dSphs. We proceed as described in Sec. 3.2 and use the likelihoods defined in Eqs. (3.3) to (3.5). We exploit the information of eleven dSphs: the seven brightest confirmed dwarfs from [205] as well as Willman 1, Tucana III, Tucana IV and Indus II. We note that four of these dSphs exhibit small DM excesses at the level of 2σ. These excesses are compatible with DM annihilation at a thermal cross section [205, 209, 210]. We remind that we marginalize the likelihood over the measured J-factor of each dSph. The joint likelihood is the product of the individual likelihoods of Eqs. (3.5),(5.11) and (5.13): $\mathcal{L}_{\rm joint} = \mathcal{L}_{\rm CR} \cdot \mathcal{L}_{\rm GCE} \cdot \mathcal{L}_{\rm dSphs}$.

The results are summarized in Fig. 5.13 and Tab. 5.8. The best-fit region of the CR fit for each SM final state is presented by the red contours. These contours span a slightly larger range in $\langle\sigma v\rangle$ compared to the contours in Fig. 5.12 since here we additionally marginalize over the local DM density. The blue contours show the best-fit region of the GCE fit. Combining the CR and GCE likelihoods results in the green contours. Finally, adding the constraints from dSphs we obtain the black contours. We observe that, in principle, all hadronic channels provide a good fit and, thus, are able to explain, at the same time, the CR antiproton excess and the GCE. However, looking at the χ^2s in Tab. 5.8, the best results are achieved for the $b\bar{b}$, WW^*, ZZ^*, and hh channels, while the annihilation into two gluons (or a pair of light quarks) and a top-quark pair are slightly disfavored. Finally, we note that the joint fit prefers values for the local DM density of $\rho_{\rm sun} = 0.55 \pm 0.15$ GeV/cm^3, which is slightly larger than our prior. Values of $\rho_{\rm sun} < 0.3$ GeV/cm^3 would make it more difficult to explain simultaneously the GCE and the antiproton excess. We note, however, that our setup constrains the half-height of the diffusion halo to a range between 2 and 7 kpc in the fit. A larger value of z_h, which is still allowed, would boost the DM signal in CR

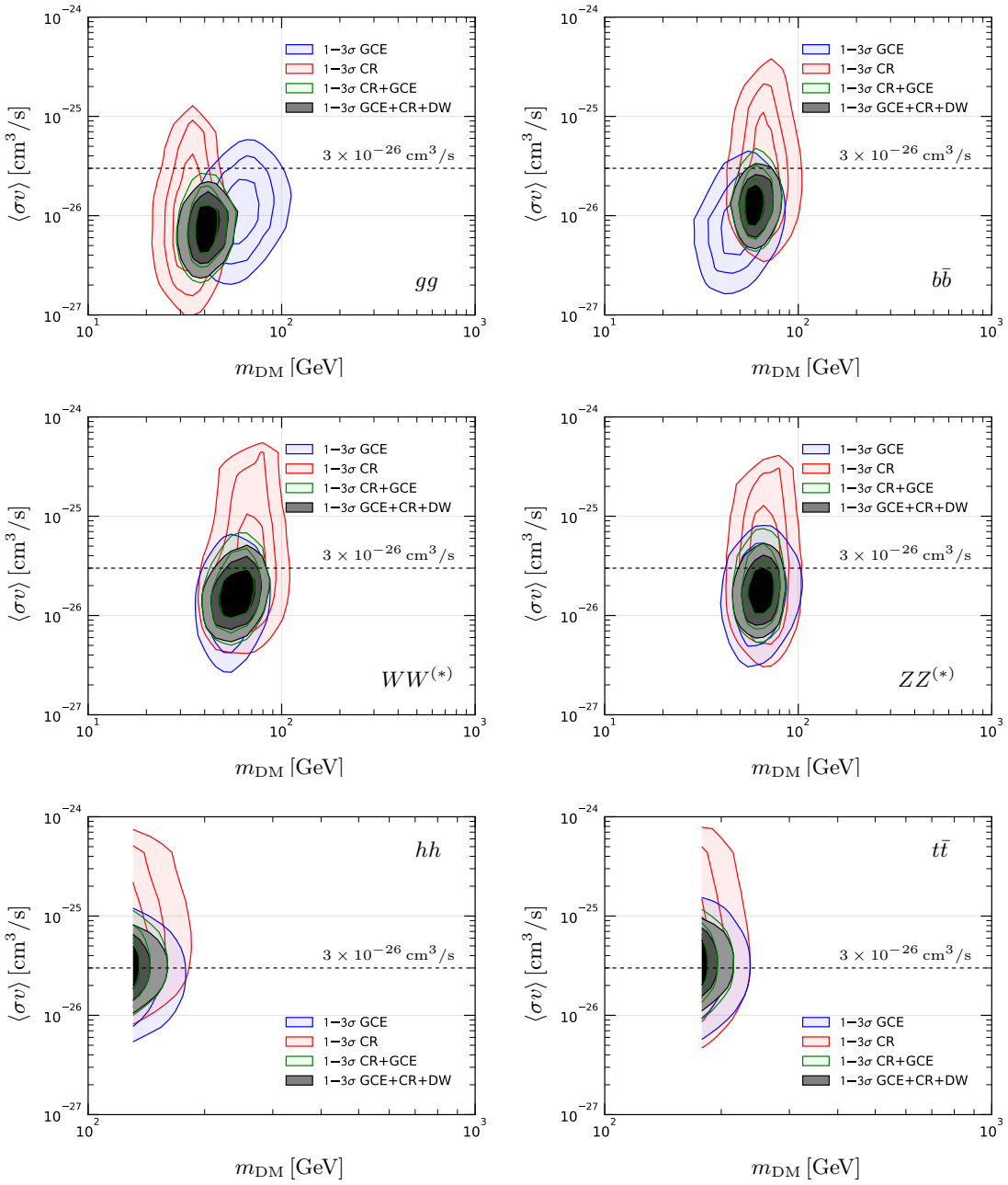

Figure 5.13: Results of the joint fit of the CR antiproton excess and the GCE. We display the best-fit region for the individual CR (red) and GCE (blue) fits as well as the joint fit with (black) and without (green) limits from dSphs. The contours refer to the 1, 2, and 3σ C.L. The figure is taken from [6].

antiprotons compared to the secondary background. This could also be used to push $\rho_{\rm sun}$ again to smaller values.

5.3.3 Interpretation within the singlet scalar Higgs portal model

We now turn to a specific BSM model which provides a suitable DM candidate: the singlet scalar Higgs portal model [303–305].[12] In addition to the SM there is only one scalar field S. The analysis in this section is very similar to Ref. [302], to which we refer for more detailed description. The main difference of this section and [302] is that here we include the DM hint in CR antiprotons. In order to make S stable we have to impose the Z_2 symmetry $S \to -S$. Then the Lagrangian of the Higgs portal model before electroweak symmetry breaking is given by:

$$\mathcal{L} = \mathcal{L}_{\rm SM} + \frac{1}{2}\partial_\mu S \partial^\mu S - \frac{1}{2} m_{S,0}^2 S^2 - \frac{1}{4}\lambda_S S^4 - \frac{1}{2}\lambda_{HS}\, S^2 H^\dagger H \,. \tag{5.14}$$

A short calculation yields

$$\mathcal{L} \supset -\frac{1}{2} m_S^2\, S^2 - \frac{1}{4}\lambda_S\, S^4 - \frac{1}{4}\lambda_{HS}\, h^2 S^2 - \frac{1}{2}\lambda_{HS}\, v h S^2 \tag{5.15}$$

after electroweak symmetry breaking. Here we assume $H = (h+v,0)/\sqrt{2}$ and $v = 246$ GeV. The physical mass of the scalar particle is given by $m_S^2 = m_{S,0}^2 + \lambda_{HS}\, v^2/2$. From Eq. (5.15) we see that, in principle, our model exhibits three free parameters: m_S, λ_S, and λ_{HS}. However, the DM phenomenology is not affected by the quartic self-coupling term $\frac{1}{4}\lambda_S\, S^4$.[13] So, we can focus on the two parameter $m_S = m_{\rm DM}$ and λ_{HS} describing the DM mass and coupling to SM Higgs, respectively.

In principle, the Lagrangian in Eq. (5.15) gives rise to two possible annihilation channels. First, two scalars S may annihilate into two Higgs bosons, which is possible through a four-point vertex and with an intermediate S in a p-wave process. This channel is only available if $m_S > m_h$. However, the DM masses, which describe well the GCE and the DM hint in CR antiprotons, are below 100 GeV. In this case, the only option is the second channel, where two scalars annihilate into two SM final states via s-wave annihilation with an intermediate Higgs boson. The branching ratios for this reaction depend only on the mass of the scalar particles. As shown in [302] (their Fig. 2), for m_S up to about 65 GeV the dominant annihilation channel is $b\bar{b}$. For larger masses (up to $m_S = m_h$) the scalars annihilate mostly into W- and Z-boson pairs. We implement the mass-dependent branching ratios in our fit setup.

In the following, we perform a fit of the singlet scalar Higgs portal model. Thus, the free fit parameters are two parameters $m_S = m_{\rm DM}$ and λ_{HS} defined in eq. (5.15). They can be related to the velocity averaged annihilation cross section required in the GCE, CR, and dSph likelihoods. As in the previous section, we include the local DM density, $\rho_{\rm sun}$, and the J-factor of the GCE analysis, J_{40°, as nuisance parameters. Furthermore, we consider the possibility that the scalar S exhibits only a fraction R of the total DM content in the Universe, $R = \Omega_S/\Omega_{\rm DM}$. This might be the case

[12] For a more detailed and recent review of the singlet Higgs portal model, which is studied extensively in literature, we refer to [306, 307].

[13] We note that is term is important for the stability of the electroweak vacuum.

if the phenomenology of a dark sector is richer than the simple scalar field discussed here. In more detail, if the parameter R is equal to 1, S explains the entire DM content in the Universe. For $R < 1$, we assume that the clustering of S follows the clustering of the remaining DM, namely, today and in our Galaxy we require $\rho_S(\vec{x}) = R \cdot \rho_{\rm DM}(\vec{x})$.

The Higgs portal model can be constrained with additional observations from particle physics, cosmology, and direct detection. The final likelihood of the fit is given by the product of the individual likelihoods: $\mathcal{L}_{\rm HP} = \mathcal{L}_{\rm CR} \cdot \mathcal{L}_{\rm GCE} \cdot \mathcal{L}_{\rm constraints}$.[14] We take into account constraints from the Higgs invisible decay width, direct detection searches, the DM relic density, and searches for gamma-ray lines in the inner Galaxy. The individual constraints are briefly summarized below:[15]

- We are interested in the mass regime $m_{\rm DM} < m_h/2$, where the Higgs can decay into two scalars, $h \to SS$. The branching ratio for the invisible Higgs decay is constraint by LHC measurements to ${\rm BR}_{\rm inv} \lesssim 0.23$ [308]. This constraint leads to an upper limit on the Higgs-scalar coupling λ_{HS} as function of m_S.

- The scalar particle can scatter off nuclei via a spin-independent cross section, which is proportional to $\lambda_{HS}^2/m_{\rm DM}^2$. Thus, we can consider upper bounds on the scattering cross section from direct detection experiments. We exploit the limits from LUX [309].[16] The local energy density of the scalar is given by $\rho_{S,\rm sun} = R\,\rho_{\rm sun}$.

- The Higgs portal model predicts gamma-ray lines from the annihilation of two scalars. We derived the annihilation cross section $\langle\sigma v\rangle_{\gamma\gamma}$ from an Higgs effective Lagrangian as detailed in [302]. Then, we use the constraints on gamma-ray lines from the Galactic halo published by the Fermi-LAT collaboration [312].

- We require that our model provides the correct DM relic density of $\Omega_{\rm DM}h^2 = 0.1198 \pm 0.0015$ [37]. In order to calculate the relic density as function of m_S and λ_{HS} we use MICROMEGAs [313] which is linked to CALCHEP [314]. If the scalar S only establishes a fraction $R < 1$ of the total DM density we require: $\Omega_{\rm DM}h^2 = \Omega_S h^2 / R$.

We present the results of the fit in Fig. 5.14. It includes the CR antiproton flux, the GCE, and constraints from dSphs, invisible Higgs decays, direct detection, gamma-ray lines, and the DM relic density. There are two regions in the parameter space which are able to explain the potential CR excess and the GCE equally well. These two regions comply with all the constraints mentioned above. In the first region, the scalar requires a mass of 62.5 GeV to 63 GeV and a coupling of $\lambda_{HS} \sim 2 \times 10^{-2}$. The small values for λ_{HS} are required to in order to fit the GCE and antiproton signals. The values required in our fit are smaller than recent limits derived from vector-boson fusion at LHC [315]. However, in the first region the singlet scalar is not able to reproduce the entire DM content in the Universe. The maximal fraction of S to DM is about 30%. We note

[14] We note that $\mathcal{L}_{\rm constraints}$ contains also the dwarf limits $\mathcal{L}_{\rm dSphs}$.
[15] More details are provided in [302].
[16] We note that there are more recent and slightly more constraining limits by [310,311]. However, we do not expect this to change the general conclusions of this section.

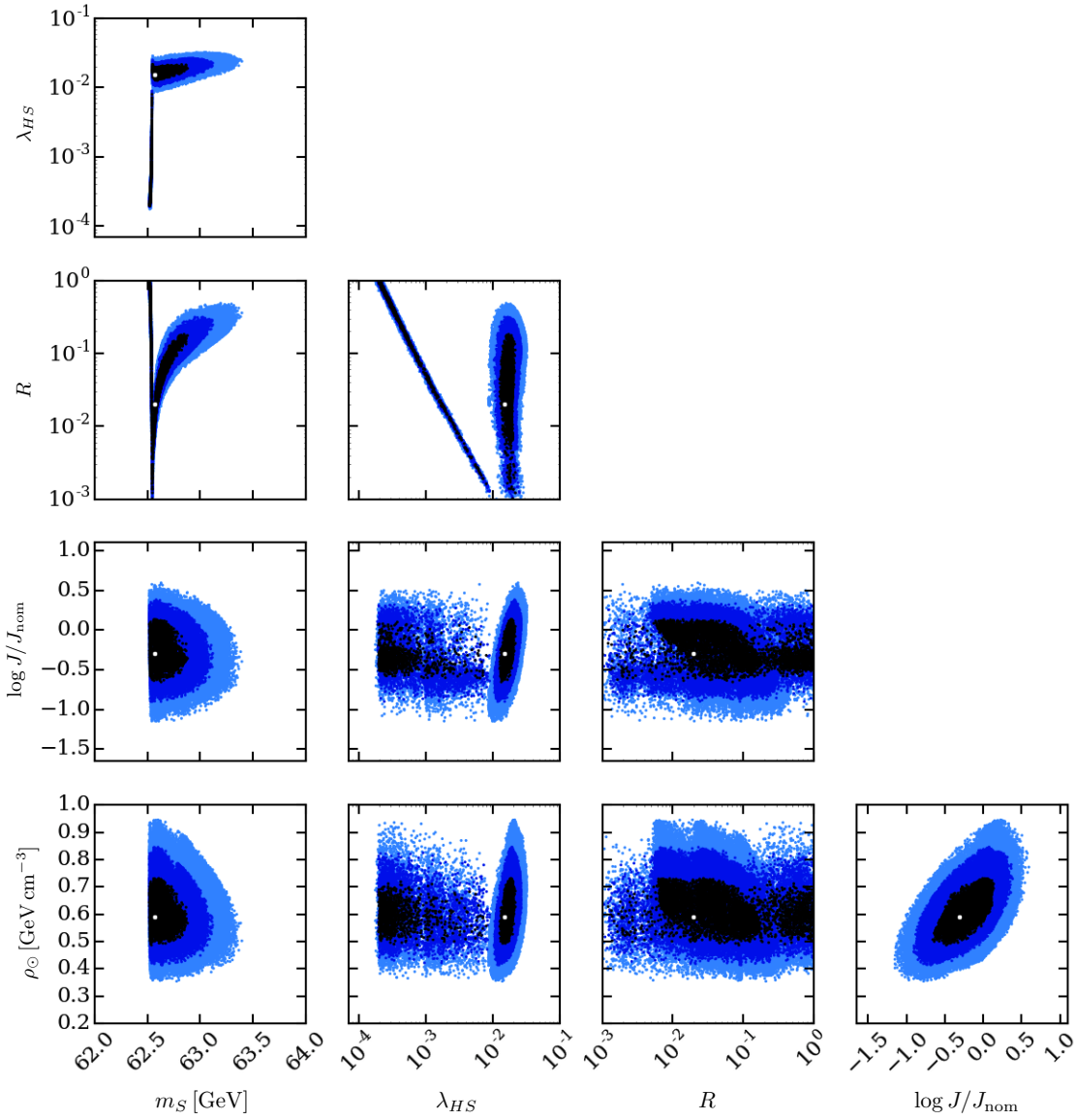

Figure 5.14: Triangle plot of the fit to CR antiprotons, the GCE, and all other constraints on the parameter space within the Higgs portal singlet scalar model. The black, blue and light blue points lie within the 1, 2, and 3σ region around the best-fit point (denoted by a white dot), respectively. The figure is taken from [6]. We note that $r_\odot = r_{\rm sun}$ and $J = J_{40^\circ}$.

Table 5.9: Fit parameters and $\langle\sigma v\rangle R^2$ for the best-fit points of the Higgs portal model in the regions 1 and 2. We take into account the log-likelihood contributions from GCE+constraints, CR+constraints and CR+GCE+constraints. We show also the individual contribution on the χ^2 from GCE and CRs.

	region 1			region 2		
$\log L$ contribution	GCE+constr.	CR+constr.	GCE+CR+constr.	GCE+constr.	CR+constr.	GCE+CR+constr.
m_S [GeV]	$62.58^{+0.76}_{-0.04}$	$62.60^{+0.21}_{-0.06}$	$62.58^{+0.18}_{-0.03}$	$62.541^{+0.003}_{-0.016}$	$62.532^{+0.012}_{-0.009}$	$62.533^{+0.011}_{-0.011}$
λ_{HS}	$0.017^{+0.015}_{-0.003}$	$0.015^{+0.006}_{-0.002}$	$0.015^{+0.004}_{-0.001}$	$0.0016^{+0.0060}_{-0.0013}$	$0.00032^{+0.00815}_{-0.00012}$	$0.00039^{+0.00561}_{-0.00017}$
R	$0.019^{+0.204}_{-0.018}$	$0.041^{+0.124}_{-0.040}$	$0.020^{+0.100}_{-0.018}$	$0.021^{+0.979}_{-0.019}$	$0.39^{+0.61}_{-0.38}$	$0.29^{+0.71}_{-0.28}$
$\log J_{40^\circ}/J_{40^\circ,\mathrm{nom}}$	$-0.065^{+0.341}_{-0.295}$	$-0.280^{+0.351}_{-0.793}$	$-0.303^{+0.304}_{-0.205}$	$-0.099^{+0.377}_{-0.275}$	$-0.415^{+0.468}_{-0.590}$	$-0.316^{+0.238}_{-0.201}$
ρ_{sun} [GeVcm^{-3}]	$0.43^{+0.15}_{-0.15}$	$0.56^{+0.09}_{-0.08}$	$0.59^{+0.1}_{-0.05}$	$0.43^{+0.15}_{-0.15}$	$0.56^{+0.09}_{-0.09}$	$0.59^{+0.09}_{-0.06}$
$\langle\sigma v\rangle R^2$ [10^{-26} cm^3/s]	$1.36^{+0.45}_{-0.44}$	$1.89^{+0.72}_{-0.53}$	$1.73^{+0.38}_{-0.47}$	$1.36^{+0.46}_{-0.45}$	$1.87^{+0.72}_{-0.51}$	$1.70^{+0.39}_{-0.32}$
χ^2_{GCE}	26.22	26.49	26.69	26.47	27.35	26.88
χ^2_{CR}	52.32	48.08	48.42	57.14	48.07	48.42

that the parameter R introduces a non-trivial interplay between the GCE and CR antiproton signal which scale with R^2 and the constraint from direct detection which scales with R.

In the second region, it is possible to have $R = 1$. Thus, S could be the only DM particle. In order to achieve this we require a scalar mass strictly at the Higgs resonance, $m_S \approx m_h/2$, and a coupling λ_{HS} of the order of $\mathcal{O}(10^{-3})$ to $\mathcal{O}(10^{-4})$. The even smaller values of λ_{HS} with respect to the first region are required in order to comply with the constraints from the DM relic density. As observed in the previous section, there is a slight preference to decrease the J-factor of the Galactic center and to enhance the local DM density. The best fit-values and 1σ uncertainties of the two regions are summarized in Tab. 5.9.

In summary, we present a UV-complete BSM model which is able to explain, at the same time, the DM hint in CR antiproton and the GCE. It is compatible with all current constraints from direct detection and collider experiments. BSM models with a Higgs portal are attractive since they are the only renormalizable theories where DM directly couples to the SM.

5.4 Limits on heavy dark matter from cosmic-ray antiprotons

In this section, we will take the more conservative approach and interpret the results of our fit to CR proton, helium, and the antiproton-over-proton ratio in terms of upper limits on the annihilation cross section of DM. Therefore, we concentrate on DM masses above 200 GeV. This section is structured as follows. In Sec. 5.4.1 we describe the technical details and differences to the setup discussed in Sec. 5.1 and, then, we present model-independent results for different SM final states in Sec. 5.4.2. Finally, we briefly discuss the application of our limits in the context of *minimal DM* models in Sec. 5.4.3.

5.4.1 Technical setup to derive dark matter limits from cosmic-ray antiprotons

The technical details of the fits performed in this section resemble the *extended setup* described above in Sec. 5.1.1. However, there are a few small differences which we list in the following.

- We fix the solar modulation potential of AMS-02 antiprotons to the same value as for protons and helium. This has only a very small effect since we exclude data below 5 GV in the fits. Furthermore, we use the unmodified AMS-02 data for proton and helium, so the proton and helium data correspond to a slightly different measurement period compared to antiprotons.

- The fits include the CREAM data of protons and helium, but we do not allow an individual free normalization (nuisance parameter) for the CREAM data. Instead the normalizations are fixed to the AMS-02 values.

- Our standard cross-section parametrization for secondary antiproton production in the pp channel is [117]. We scale to the pA channels with the parametrization suggested in [121]. In some cases, we will additionally test the cross-section parametrization of [119, 123, 128] and compare the results.

In order to estimate the uncertainties of the DM limits due to the adopted CR propagation scenario, we will slightly modify our standard setup and additionally derive the DM limits in these modified setups. In particular, we will investigate a diffusion model without convection and two setups where we fix z_h to 2 kpc and 10 kpc, respectively. Furthermore, we vary the rigidity cut on AMS-02 data, which, in the standard setup, is set to 5 GV, and we try different parametrizations of the secondary antiproton production cross section. The DM component is described with two free parameters, the DM mass, $m_{\rm DM}$ and the velocity averaged cross section, $\langle\sigma v\rangle$. We investigate different SM final states, thereby, assuming generic models where the DM particles annihilate with a branching ratio of 100% into one pair of SM final states. We consider the following final states in Eq. (2.51): $f = q, c, b, t, g, W, Z, h, \ell$, and ν, where $q = u, d, s$, $\ell = e, \mu, \tau$, and $\nu = \nu_e, \nu_\mu, \nu_\tau$, and use the energy spectra tabulated in [292]. These tables take into account electroweak processes in a model-independent way by using electroweak splitting functions [316, 317]. Because of the electroweak processes also leptonic DM annihilations produce antiprotons and can be constrained from our setup.

In order to calculate the upper limit on $\langle\sigma v\rangle$ as function of DM mass and for each SM final state we perform a fit with MultiNest and include $\langle\sigma v\rangle$ and $m_{\rm DM}$ as free parameters. We divided the final MultiNest sample points into 20 bins in DM mass range from 200 GeV to 50 TeV, which are equally-spaced in $\log(m_{\rm DM})$. Then, we deduce the profile likelihood of $\langle\sigma v\rangle$ in each bin and define our limit at the 95% C.L. from the condition $\Delta\chi^2 = 3.84$. Compared to the previous analysis of [6] we exploit two strategies to improve the coverage of our parameter space. First, we exploit the fact that the annihilation cross section, $\langle\sigma v\rangle$, affects the DM flux linearly, namely, if we increase $\langle\sigma v\rangle$ by a factor 2 also the DM flux of CR antiprotons is increased by a factor 2. We reevaluate the likelihood on a grid in $\langle\sigma v\rangle$ with 41 points logarithmically spaced between $\langle\sigma v\rangle = 10^{-27}{\rm cm}^3{\rm s}^{-1}$ to $\langle\sigma v\rangle = 10^{-23}{\rm cm}^3{\rm s}^{-1}$. Effectively this increases our coverage by a factor of 40. Secondly, we combine the information of different MulitNest scans. The idea is that a good-fit point for one final state can be a good fit point also for another final states since the energy spectra for example of all hadronic final states are very similar for large $m_{\rm DM}$. So, we reevaluate the good fit points of each scan also for all other final states. Together, these two strategies significantly improve our coverage and, hence, make our results more robust.

5.4.2 Results and discussion

Figure 5.15 shows the upper limits on the DM annihilation cross section, $\langle\sigma v\rangle$, obtained from a global fit of CR protons, helium, and antiprotons as detailed in Sec. 5.4.1. We present the results for annihilation into all possible pairs of SM final states. We note that the DM energy spectra of some final states are indistinguishable for $m_{\rm DM} > 200$ GeV. Therefore, we present only one limit for W/Z and for g/c final states. Furthermore, we find that the antiproton production from leptonic channels is flavor-independent and the limit from neutrinos and charged leptons only differs by a constant factor $\nu/\ell \simeq 0.4$. We compare our limits from CR antiprotons with those from dSph observations by the Fermi-LAT. The limits on $\langle\sigma v\rangle$ from dSphs are derived from the likelihood defined in Eqs. (3.3) to (3.5). In particular, we exploit the likelihood of the nine dSphs with the largest confirmed J-factors as given in [207]. We remind that we marginalize over the J-factor of each dSph according to its uncertainty given in [207]. We find that the limits from CR antiprotons in

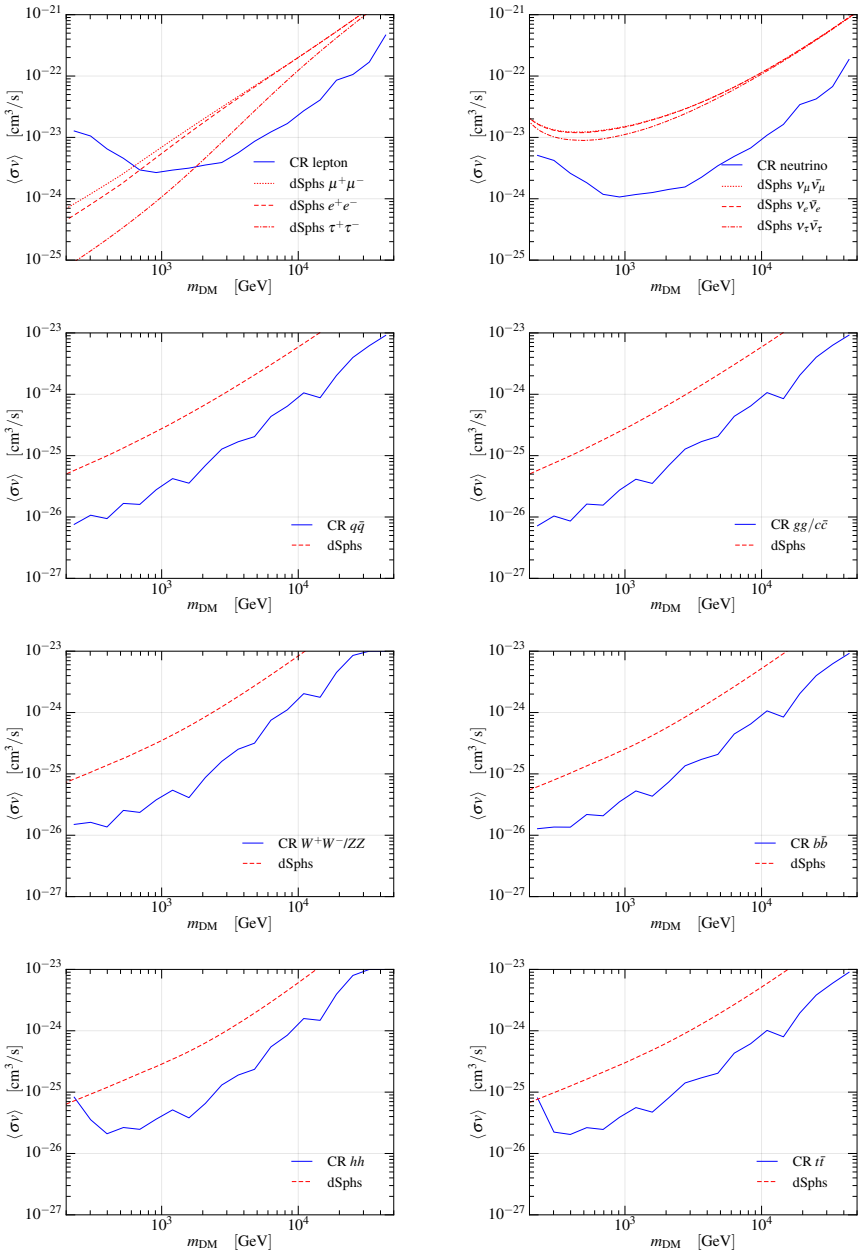

Figure 5.15: We present the upper limits on the DM annihilation cross section, $\langle\sigma v\rangle$, at the 95% C.L. for all annihilation channels into pairs of SM particles. The limits are derived from our global fit of CR with a DM contribution in CR antiprotons (blue solid line) which we compare to the limits from dSphs (red dashed lines). We note the different scales on the y-axis for leptonic and hadronic annihilation channels. The figure is taken from [5].

the hadronic channels are more constraining for heavy DM than the limits from dSph observations by the Fermi-LAT. We notice that the limits in the Higgs and top-quark channels exhibit an increase at $m_{\rm DM} \sim 200$ GeV. The origin of this increase is that for those two channels a DM mass of 200 GeV finds a small evidence for the DM signal discussed in Sec. 5.1, *c.f.* also to Fig. 5.12. The charged lepton channel provides competitive limits for $m_{\rm DM} \gtrsim 1$ TeV. The reason that the limit from CR antiprotons improves between 200 GeV and 1 TeV is related to the fact that electroweak corrections are enhanced logarithmically for large DM masses [296]. The same argument applies for the neutrino channels. However, we note that our limits in the leptonic channels are significantly weaker than the limits in the hadronic channels.

Finally, we quantify the systematic uncertainty on the CR limit arising from our choice of the CR propagation setup. The discussion is focussed on W/Z final states but we note that the conclusions are true for all (hadronic) channels. We use the same methodology as before but slightly modify the setup for CR propagation changing the following assumption from the standard setup:

- We remove convection from our standard setup (labeled: no $v_{\rm c}$).
- Instead of varying half-height of the diffusion halo in the fit we fixed it to two benchmark scenarios of $z_h = 2$ kpc and 10 kpc, respectively.
- We include AMS-02 data down to rigidities of 1 GV in the fit.
- We investigate the impact of the antiproton production cross section by changing the standard parametrization [117] to the parametrizations suggested in [119, 123, 128].
- We change the DM density profile from a cuspy NFW profile to a cored Burkert profile. For the Burkert profile we adopt two different values for the core radius. We test $r_c = 5$ kpc and $r_c = 10$ kpc.

Our results are summarized in Fig. 5.16. The upper left panel displays the various limits obtained in different CR propagation setups. We observe that the uncertainties are bracketed between the setups with fixed half-height of the diffusion halo at $z_h = 2$ kpc and 10 kpc. The setup with $z_h = 10$ kpc provides the most constraining limit while the small halo half-height of 2 kpc corresponds to the most conservative limits. In the following, we show the envelope of these limits as systematic

Table 5.10: J-factors for different DM density profiles. The ROI corresponds to the analysis by H.E.S.S. to constrain DM annihilation from the Galactic DM halo [318].

density profile	$\log_{10}\left(J_{\rm HESS}/(\mathrm{GeV}^2\,\mathrm{cm}^{-5})\right)$
Einasto	21.66
NFW	21.41
Burkert ($r_{\rm c} = 5\,$kpc)	20.05
Burkert ($r_{\rm c} = 10\,$kpc)	19.34

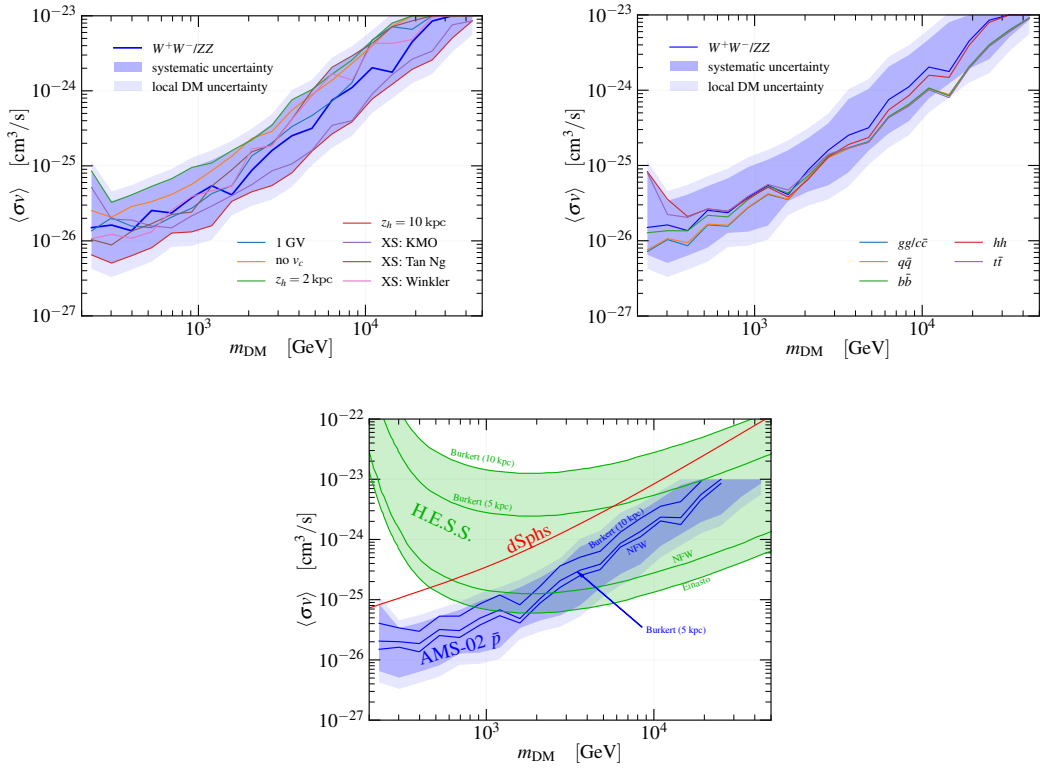

Figure 5.16: Similar to Fig. 5.15. We present the limits on the DM annihilation cross section, $\langle\sigma v\rangle$, at the 95% C.L. In the upper left panel we show the systematic uncertainty due to different setups of the CR propagation and the additional uncertainty from the local DM density. The lines with different cross-section parametrizations are labeled Tan&Ng [123], KMO [128], and Winkler [119]. In the upper right panel we compare all the hadronic annihilation channels and in the lower panel we investigate the impact of the DM density profile on our results. We compare the CR limit with the gamma-ray limits of dSphs and the Galactic center (H.E.S.S.). The figure is taken from [5].

uncertainty. Furthermore, we note that our setup assumes a fixed value for the local DM density of 0.43 GeV/cm^3. If we allow for an uncertainty in the local DM density of ± 0.15 GeV/cm^3 we obtain the additional uncertainty shown in the light-blue band. In the upper right panel we compare the DM limits of the various hadronic final states. As already mentioned, they give very similar results. Finally, in the lower panel of Fig. 5.16 we show the impact of changing the DM density profile. The CR limits are only mildly affected by the shape of the DM density profile at the Galactic center. The limit derived with a Burkert profile and a core radius of $r_c = 5$ kpc weakens the limits by 20% to 30% compared to the NFW density profile, while a core radius of $r_c = 10$ kpc would weaken the limit by about a factor of 3. We compare the CR limits with the limits from dSph observation by the Fermi-LAT and with the limits obtained from DM searches by the H.E.S.S. experiment in the region around the Galactic center. In particular, heavy DM can be constrained from the non-observations of gamma-ray of the H.E.S.S. experiment [318] which analyzed a circular ROI of 1° centered around the Galactic center excluding the Galactic plane at latitudes $|b| < 0.3°$. The H.E.S.S. analysis assumes that the DM in our Galaxy follows the Einasto profile [40]. We can compute and compare the J-factor in the H.E.S.S. ROI for different DM density profiles. The values are summarized in Tab. 5.10. The results show that the J-factors and subsequently the limits on the DM annihilation cross section crucially depend on the choice of the DM density profile. Assuming a Burkert profile with $r_c = 10$ kpc instead of the Einasto profile changes the J-factor and, thus, the limit by more than two orders of magnitude. In this sense, our CR limits provide important complementary information.

5.4.3 Constraints on minimal dark matter models

We now apply our limits to specific BSM models. We use the framework of so-called *minimal DM*, where we add an electroweak fermion multiplet χ to the Lagrangian of the SM. The coupling of the additional multiplet and the SM is determined by the covariant derivative D_μ. Then, the mass M of the multiplet χ is the only free parameter. The Lagrangian is given by:

$$\mathcal{L} = \mathcal{L}_{\mathrm{SM}} + \bar{\chi}\,(i\not{D} + M)\,\chi\,. \tag{5.16}$$

The hypercharge Y of the multiplet is fixed by the requirement that a suitable DM candidate has to be electrically neutral [319]. The currently best constraints on electroweak fermions in minimal DM scenarios are provided by indirect detection, making the antiproton limits derived in the previous paragraph particularly interesting. The reason for the importance of the indirect detection is related to the Sommerfeld enhancement of the DM annihilation cross section [320–334].

In the following, we will present results for three cases of different multiplets. Here we briefly summarize the key properties and refer to [5] and references therein for more details.

- **A fermion doublet:** In this case, minimal DM represents the limit of a supersymmetric theory with a higgsino DM candidate. The hypercharge of the doublet must be $Y = 1/2$. The mass splitting between the neutral and charged particle, which is induced by loop effects, is of the order of 340 MeV [335]. The neutral particle of the fermion doublet makes up the observed relic density of DM for a mass of $m_\chi \approx 1050$ GeV [335]. For smaller masses the

thermal contribution of χ to the energy content of the Universe, $\Omega_{\rm therm}$, is smaller than the measured abundance, $\Omega_{\rm meas}$. We define the ratio of the Ω_χ to the measured abundance as $R = \Omega_\chi/\Omega_{\rm meas}$. The pure minimal DM model of a fermion doublet is excluded by direct detection experiments, since the Dirac fermions have a large spin-independent nucleon scattering cross section. However in a complete supersymmetric model these limits can be circumvented due to a mixing of the higgsino with its SM superpartners [336]. Our limits from indirect detection presented below should be understood in such a supersymmetric model, as for example discussed in [334,337]. Higgsino DM can be constrained by the non-observation of disappearing charged tracks at the LHC. The 13 TeV run excludes DM masses up to 120 GeV [338–341]. In the following, we use the cross section and relic density prediction from [335]. The dominant annihilation of the higgsino occurs in the WW and ZZ channel. Furthermore, there are is loop induced annihilations into $\gamma\gamma$ and γZ final states giving rise to gamma-ray lines.

- **A fermion triplet:** The fermion triplet corresponds to the limit of a supersymmetric model with wino DM which is extensively studied in literature [325,332,334,335,342–345]. We assume that everything except for the wino multiplet is decoupled from the SM. The fermion triplet requires a hypercharge of $Y = 0$. For $Y = 0$ the nucleon scattering cross section disappears at tree-level rendering current direct-detection constraints unimportant. The mass splitting between the neutral and charged particles due to loop effects is about 160 MeV [346–350]. LHC constraints on wino DM by disappearing charged tracks are sensitive up to masses of about 460 GeV [338]. The relic density predicted in the wino model matches the observed DM relic density for $m_\chi \approx 2.8$ TeV [322, 323, 335]. We use the relic density prediction from [335] and the prediction of the annihilation cross section for indirect detection into the channels of WW (tree level) and ZZ, $Z\gamma$, $\gamma\gamma$ (loop-induced) from [324].

- **A fermion quintuplet:** As in the wino case, we require a hypercharge of $Y = 0$. The observed relic density is reproduced for a pure quintuplet fermion of $m_\chi \approx 9.4$ TeV [351]. We use the cross section and relic density predictions from [351].

In Fig. 5.17 we compare the DM limits from CR antiproton to the three scenarios of minimal DM. As a first step, we consider that the entire amount of DM comes from the minimal DM particle, $\Omega_\chi h^2 = \Omega_{\rm meas} h^2 = 0.1198$ [37]. We note that this requires either a non thermal production mechanism or a non standard cosmological evolution of the Universe. Then, we compare the limits on the annihilation cross section of the previous section with the predicted annihilation cross section in the wino, higgsino, and quintuplet model. We define the cross section for annihilation in any pair of vector bosons as $\langle\sigma v\rangle_{VV} = \langle\sigma v\rangle_{WW} + \langle\sigma v\rangle_{ZZ} + \frac{1}{2}\langle\sigma v\rangle_{Z\gamma}$. Since the antiproton DM limits on the annihilation cross section into WW and ZZ are identical, we can directly take this limit from Fig. 5.16 and apply it to VV. This interpretation of the results is shown in the left column of Fig. 5.17. For comparison the limits from dSphs are also displayed. We can exclude wino DM up to the thermal mass of 2.8 TeV, while higgsino DM is only excluded up to about 600 GeV. Quintuplet DM is excluded in our benchmark scenario of CR propagation, but due to systematic uncertainties, in a more conservative interpretation of the CR antiproton limit some mass regions might still be allowed.

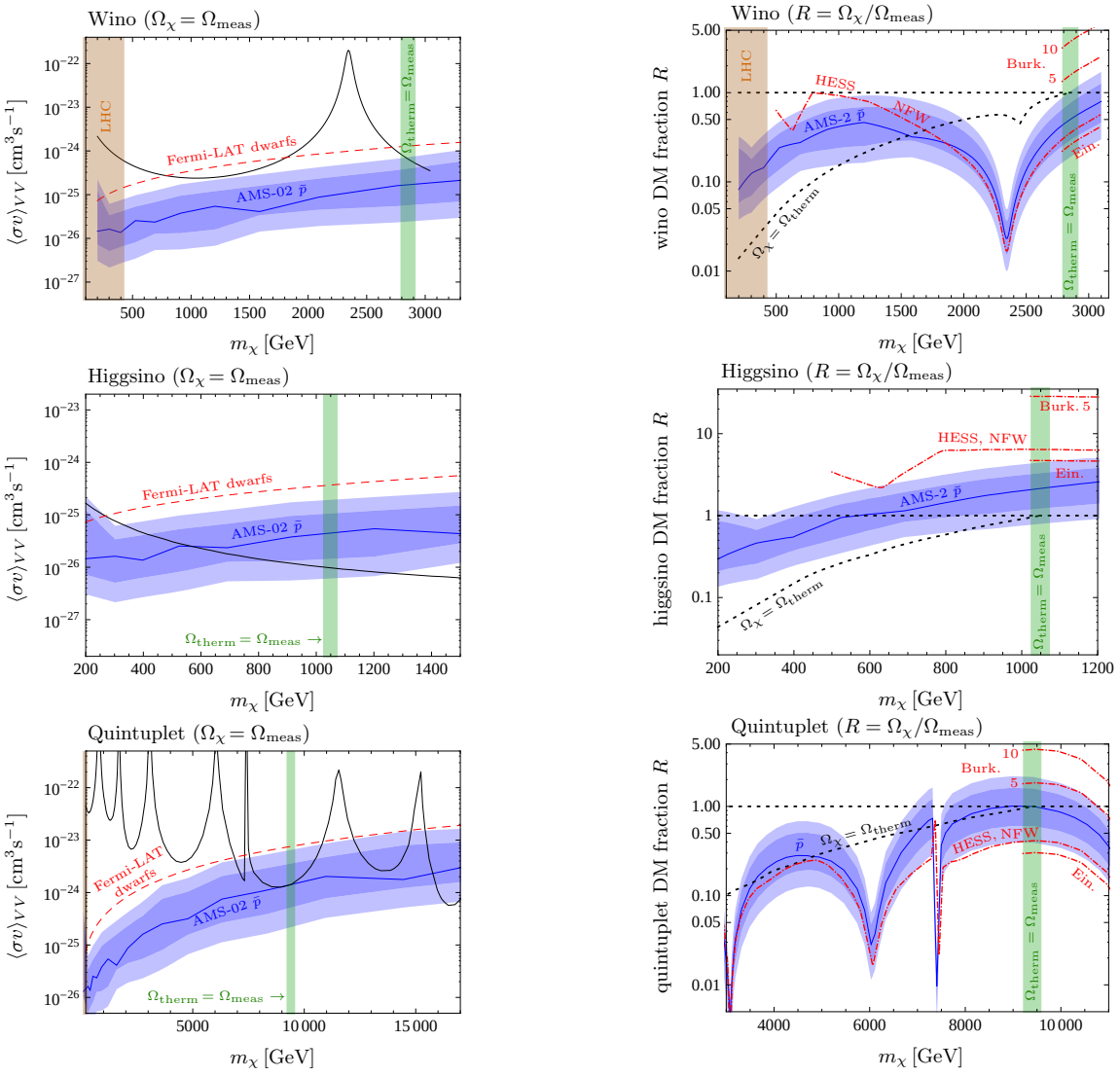

Figure 5.17: We show the upper limits on the DM annihilation cross section (left column) at the 95% C.L. for three cases of minimal DM models. The rows correspond to a wino (upper row), higgsino (central row), and quintuplet (bottom row) DM model. The blue band display the upper limit from AMS-02 antiprotons, which is compared to the limit from dSph observations by the Fermi-LAT. The solid black line shows the predicted annihilation cross section into vector bosons pairs VV. LHC excluded regions are marked in brown and the masses at which at which the abundance of χ matches thermal production is marked with a green shaded band. In the right column, we display the upper limits on the ratio $R = \Omega_\chi/\Omega_{\rm meas}$. The dashed line represents the prediction of the thermal abundance of χ. We show the limits from gamma-ray line searches by H.E.S.S. for different assumptions on the DM density profile. For more details we refer to the text. The figure is taken from [5].

We turn now to the second interpretation of the limits. Here we assume that the minimal DM candidate makes up only a fraction $R = \Omega_\chi/\Omega_{\rm meas}$ of the total DM content in the Universe. Thus, we interpret our limits as an upper bound on the ratio R as shown in the right column of Fig. 5.17. The remaining DM density is assumed to decouple completely from the minimal DM candidate, but to have the same clustering properties ($\rho_\chi(\vec{x}) = R \cdot \rho_{\rm DM}(\vec{x})$). We show additionally the constraints from dSphs and from the non-observation of gamma-ray lines [352]. These limits are taken from an analysis at the Galactic center and, therefore, strongly depend on the assumption on the DM density profile (see also Tab. 5.10). Thus, the CR antiproton limits provide very important complementary information. In this interpretation, we can exclude thermal DM winos with masses of $m_\chi \gtrsim 1.6$ TeV. Thermal higgsinos are not excluded and thermal quintuplet fermions are only excluded in a few mass ranges, but not at $m_\chi = 9.4$ TeV, *i.e.* for $\Omega_{\rm therm} = \Omega_{\rm meas}$.

Chapter 6

Prospects to detect antideuteron or antihelium in cosmic rays

In Chapter 5 we have explored a potential signal for DM annihilation in CR antiprotons. Its existence and significance are, however, still discussed controversially in literature. Indeed the analysis suffers from large systematic uncertainties such as the correlation of uncertainties in the AMS-02 data, Galactic propagation, and the antiproton production cross section. All of these systematic uncertainties should be understood better in the future. In the meantime, the search for a low-energy antinucleus in CRs offers direct option to cross-check the DM interpretation, since naturally the production of antinucelons will result in the production of heavier antinuclei by coalescence. The observation of a low-energy antinucleus, in particular antideuteron, would provide additional information although its production from DM annihilation is highly suppressed compared to antiprotons. The reason is that the secondary production is suppressed kinematically even further, see Sec. 2.6. So, antideuteron is expected to have a favorable signal-to-background. However, it is experimentally very challenging to explore the extremely low fluxes at which DM signals or secondary fluxes are expected. On the other hand, the AMS-02 experiment and the future experiment GAPS are expected to (partly) explore the interesting parameter space. For more details we refer to Sec. 2.6.

In this chapter, we will calculate the antideuteron and antihelium signal arising from the potential DM hint in CR antiprotons and discuss the implications. Baseline for this calculation is the analysis [8] (abbreviated CuKrKo in figures). Then, we will adopt a more conservative approach and calculate the maximal antideuteron flux which is compatible with the DM limits from CR antiprotons from the same analysis [8]. The results are compared with the expected sensitivities of GAPS and AMS-02. This chapter is based on the paper [6].

6.1 Technical specification of the analysis

For our calculations we adopt the analytic coalescence model which is presented in Sec. 2.6 to obtain the source terms of secondary and DM antideuteron or antihelium. Then, the source terms are

propagated to the antinuclei fluxes by solving the diffusion equation for CRs, Eq. (2.20), using the GALPROP code. Furthermore, we compare with the approximate analytic solution of the diffusion equation discussed in Sec. 2.3.2. In the following of this section, we state the technical details of the calculation, but we do not repeat any formulas. For a more general overview, we refer to the respective section in Chapter 2.

Finally, we remark that in this chapter whenever we say antihelium we imply antihelium three. If, instead, we mean antihelium four we will denote this explicitly.

6.1.1 Determination of the antideuteron and anithelium source terms

The secondary source term is given by Eq. (2.41), if we replace the antiproton production cross section by the antinuclei production cross sections for antideuteron and antihelium given by Eq. (2.59) and Eq. (2.60), respectively. The energy threshold for the projectile to produce antideuteron (anihelium) in a pp collision is $T_{\rm thr} = 16m_p$ ($T_{\rm thr} = 30m_p$). Antiproton and antineutron production is described with the analytic parametrization taken from [117]. This takes into account a 30% enhancement of antineutron production with respect to antiprotons. The parametrization is given for pp collisions. For heavier projectiles or targets we scale with mass number to the power 0.7, in other words, a factor $A^{0.7}$. We include the contributions of the four most important channels: pp, pHe, Hep, and HeHe. The contribution of heavier projectiles and targets is at the percent level and can be neglected. Furthermore, we consider the contribution from $\bar{p}+p \to \bar{D}+X$ and $\bar{p}+\mathrm{He} \to \bar{D}+X$, which requires a parametrization of the fully differential cross section of the reaction $\bar{p}+p \to \bar{p}+X$. In the absence of good measurements and parametrization, we approximate this cross section with the one of $p+p \to p+X$ and use the parametrization of [353]. The source term for antideuteron, separately for each the individual channel, was already shown in Fig. 2.13. The corresponding figure for antihelium looks very similar (see Ref. [4]).

Next to the secondary production there is also a so-called tertiary which becomes important at low energies. Tertiaries are inelastically scattered secondaries. The source term is again given by Eq. (2.41), however, now the cross section describes the inelastic but non-annihilating interaction of the antinucleus on the ISM. This cross section is purely measured. For antideuteron we follow the procedure suggested in [155]. We use the data from [354] for the scattering of antiprotons on deuteron with additional meson production. From this we extract the total inelastic, but non-annihlating, cross section of the reaction $\bar{D}+p \to \bar{D}+X$. Then we assume that the functional form of the fully-differential cross section is given by the $p+p \to p+X$ cross section parametrized by [353]. For ISM component of helium in the initial state we scale this cross sections by $4^{0.8}$. For antihelium production we assume that the tertiary production cross section of antideuteron can be scaled with a factor $3/2$.

The source term for DM is calculated from Eq. (2.51), adapted for antideuteron or antihelium, respectively, and the energy spectra are calculated in the analytic coalescence model from the Eqs. (2.64) and (2.65). The energy-spectra for antiprotons are taken from the tables provided in [292]. We assume that antiproton and antineutron production from DM is equal. Our baseline scenario is that DM annihilates to 100% into a pair of $b\bar{b}$ quarks. However, we will investigate also other pure SM final states in the results section below. In principle, one can imagine that there

is also a tertiary contribution for the DM flux. We take this into account but notice that it is negligible compared to the primary DM flux. For the secondaries the situation is different because of the very different shape in energy compared to the DM flux. The spatial distribution of DM is assumed to follow an NFW density profile [39], (see Eq. 1.4), with a scale radius $r_h = 20$ kpc. The halo density, ρ_h, is normalized such that the local DM density at $r = r_\odot = 8$ kpc is given by 0.43 GeV/cm^3 [41]. We remind that CRs mostly probe the local DM density while they are not very sensitive to a change of the DM density profile at the Galactic Center [5, 132, 133], see also Sec. 2.5.6. For example, changing the cuspy NFW profile to a cored Burkert profile (see Eq. 1.3) only changes the antinuclei fluxes from DM by an overall normalization of about 30%. This effect is, however, degenerate with $\langle\sigma v\rangle$ in the following sense: the normalization of antiprotons and antideuteron/antihelium is changed simultaneously by the same amount. So, changing the NFW profile to a Burkert profile decreases the antiproton signal in [8] such that a larger value of $\langle\sigma v\rangle$ is required. All in all, the effects cancel in our calculations.

As a benchmark, in this chapter we use a coalescence momentum which is tuned to the antideuteron production in Z-boson decays at the ALEPH experiment [172]. This is expected to be very close to the situation of DM annihilation because the initial state is non-hadronic. We adopt the value of $p_\mathcal{C} = (160 \pm 19)$ MeV which was found in the analysis of [159]. Recently, the ALICE experiment measured the production of antideuteron, antihelium, and antitritium in pp collisions [355]. The results are presented in terms of the B_2 and B_3 parameters defined in Eq. (2.62). Explicitly, they are given by:

$$B_2 = \frac{m_D}{m_p m_n}\frac{\pi p_\mathcal{C}^3}{6} \qquad \text{and} \qquad B_3 = \frac{m_{\rm He}}{m_p^2 m_n}\left(\frac{\pi}{6}p_\mathcal{C}^3\right)^2 . \tag{6.1}$$

ALICE provided the B_2 factor at different CM energies, $\sqrt{s} = 0.9$, 2.76, and 7 TeV, and as function of transverse momentum. Taking into account that in CRs the dominant contribution of secondaries originates from small $p_{\rm T}$, we estimate that B_2 should be taken between 0.01 and 0.02 GeV^2. On the other hand, the factor B_3 is only provided at $\sqrt{s} = 7$ TeV. At small transverse momenta B_3 varies between 1×10^{-4} and 3×10^{-4} GeV^4. We can translate these B_A factors into coalescence momenta. Then, we obtain $p_\mathcal{C}$ between 208 and 262 MeV for antideuteron (B_2) and $p_\mathcal{C}$ between 218 and 261 MeV for antihelium and antitritium (B_3). We note that the coalescence momenta from B_2 and B_3 are very similar. This is a very interesting and actually non-trivial result because $p_\mathcal{C}$ is a phenomenological parameters. We take this result as confirmation that the analytic coalescence model correctly describes the scaling between antinuclei with different masses. In our default setup, we will adopt the more conservative coalescence momentum of $p_\mathcal{C} = 160$ MeV. All results are additionally also presented for the larger coalescence momentum inferred from the ALICE measurement of $p_\mathcal{C} = 248$ MeV.

Finally, we note that antihelium can be produced in two ways: first directly by the fusion of two antiprotons and one antineutron. The second option is to produce tritium from one antiproton and two antineutrons. Tritium will decay subsequently into antihelium during propagation. This subtlety concerns only antihelium. Antideuteron can only be produced in a single way, by coalescence of one antiproton and one antineutron.

6.1.2 Propagation of antideuteron and anithelium

Numerical solution of the diffusion equation

In the standard setup, we use GALPROP to solve the diffusion equation and to calculate the antideuteron and antihelium fluxes. Note that GALPROP does not calculate antideuteron and antihelium in its standard configuration. We have, therefore, implemented the relevant extensions and consider the secondary, tertiary, and DM contribution for each antinucleus. We adopt the same setup which is used in [8] and also described in Chapter 5. More specifically, we adopt a 2-dimensional Galaxy with cylindrical symmetry and a maximal radial extension of 20 kpc. We use homogeneous and isotropic diffusion which is assumed to be a power law in rigidity. Furthermore, we allow for reacceleration which is described by the speed of Alfven magnetic waves, v_A, and a constant convection velocity perpendicular to the Galactic plane, v_c. We include DM annihilation which is fully described with two free parameters, the DM mass, m_DM, and the annihilation cross section, $\langle\sigma v\rangle$. We adopt the best fit parameters from the fit including DM from [8]. The values of the propagation parameters are repeated in Tab. 6.1. We take into account the effect of solar modulation. In the standard setup, we use the force-field approximation, Eq. (2.66), with a solar modulation potential of 400 MV.

Analytic solution of the diffusion equation

We compare the results obtained with GALPROP with the analytic diffusion model of [94]. Note that this solution was already exploited for antideuteron [165] and antihelium [164]. The solution of this model is stated in Chapter 2 in Eqs. (2.31) to (2.33). We adopt a maximal radial extension, $r_\mathrm{max} = 20$ kpc. The half-height of the Galactic disk is taken to be $h = 0.1$ kpc and the densities of hydrogen and helium in the Galactic disc are 1 cm^{-3} and 0.1 cm^{-3}, respectively. In contrast to the numerical setup we do not propagate the parent nuclei p, He, and $\bar{p}$, which is required to calculate the secondary source terms of $\bar{D}$ and $\overline{\mathrm{He}}$. Instead, we take these fluxes directly from AMS-02 data [58, 59, 75]. We reverse the effect of solar modulation within the force-field approximation assuming a solar modulation potential of 600 MV. The annihilation cross section of antideuteron on the ISM is the difference of the total and elastic antideuteron cross section: $\sigma_\mathrm{ann} = \sigma_\mathrm{tot} - \sigma_\mathrm{el}$. There is, however, only a measurement of the total deuteron-antiproton cross section [356]. By symmetry

[1] We note that D_0 is normalized at 4 GV in GALPROP and at 1 GV in the MED and MAX configuration.

Table 6.1: Summary of the propagation parameters for different setups.

Parameter	CuKrKo	MED	MAX
D_0 [kpc^2/Myr][1]	0.326	0.0112	0.0765
δ	0.25	0.70	0.46
v_c [km/s]	45	12	5
v_A [km/s]	29		
L [kpc]	5.4	4	15

this has to be equal to the total antideuteron-proton cross section. Finally, we approximate the annihilation cross section by assuming that it can be scaled from the $\bar{p}p$ cross section according to:

$$\sigma_{\rm ann}^{\bar{D}p} \approx \frac{\sigma_{\rm tot}^{\bar{D}p}}{\sigma_{\rm tot}^{\bar{p}p}} (\sigma_{\rm tot}^{\bar{p}p} - \sigma_{\rm el}^{\bar{p}p}). \tag{6.2}$$

Furthermore, we adopt a scaling factor of $4^{0.7}$ for helium targets and 3/2 for the antihelium annihilation cross section. The remaining propagation parameters are fixed to two benchmark scenarios which are taken from [133]. This analysis has identified three sets of propagation parameters, commonly known as MIN, MED, and MAX. All of them are tuned to B/C data, but they give quite different results for antiprotons from DM annihilation. We note that the MIN scenario is disfavored by recent data from AMS-02 [110,115,297,298]. Therefore, we test only the MED and MAX setups, whose parameters are stated in Tab. 6.1.

6.2 Results for secondary, tertiary and dark matter fluxes

We start by presenting the results on antideuteron and, then, in the second part of this section comment on antihelium.

6.2.1 Predictions and limits for antideuterons

Figure 6.1 shows the antideuteron fluxes derived as specified in the previous section. We exploit the analytic coalescence model to calculate separately the fluxes of secondaries, tertiaries, and DM. Two scenarios are explored: our baseline scenario assumes a coalescence momentum of 160 MeV (left panel) which is tuned to the Z-boson decay measured by ALEPH. On the other hand, we explore also the larger coalescence momentum of 248 MeV (right panel) which is suggested by recent measurements of ALICE in pp collisions. The DM flux corresponds to annihilation of a potential DM particle into a pair of $b\bar{b}$ quarks. The DM mass is set to 71 GeV and the annihilation cross section to $2.6{\times}10^{-26}$ cm^3/s, which matches the hint from CR antiprotons found in [8]. In the standard setup we use the GALPROP code (solid) lines. These results are cross checked against the analytic propagation models in the MED and MAX configuration (shaded bands). Solar modulation is taken into account within the force-field approximation. We assume a Fisk potential of 400 MeV, which is a realistic value since the GAPS experiment is expected to take data during a period of low solar activity. The secondary fluxes peak around 3–4 GeV/n and quickly decrease at smaller energies due to the kinematic suppression discussed above. We note the difference between the GALPROP propagation setup and the MED/MAX setup in the secondary flux. The GALPROP setup lies significantly above the analytic setups at low energies, while there is a very good agreement at higher energies. The origin of the difference is that continuous energy losses and reacceleration is neglected in our analytic setups. Hence, the GALPROP results are more reliable at low energies. At very low energies of about 0.4 GeV/n the tertiary flux becomes important and dominates over the secondary flux. So, this tertiary flux is the true background for DM searches in GAPS energy bin. The DM fluxes peaks at 0.1–0.2 GeV/n. In the conservative coalescence setup with a coalescence momentum of 160 MeV the flux reaches a maximum of 3×10^{-6} (GeV/n)$^{-1}$m^{-2}s^{-1}sr^{-1} and, therefore, lies within the

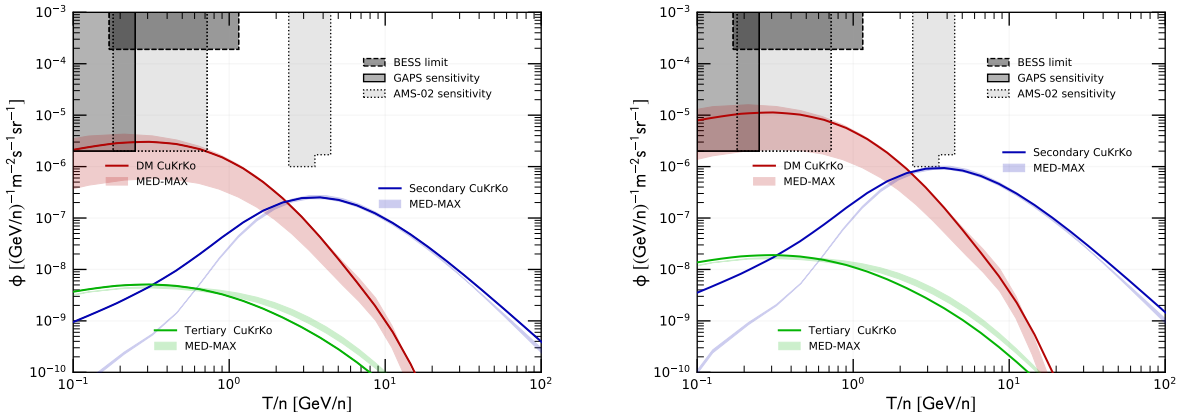

Figure 6.1: Antideuteron fluxes as function of kinetic energy-per-nucleon. We show separately the contribution from secondaries, tertiaries, and a potential DM signal. The DM flux corresponds to the DM hint from CR antiprotons found in [8] (abbreviated CuKrKo), The putative signal corresponds to the annihilation of a DM particle with a mass of $m_{\rm DM} = 71$ GeV and an annihilation cross section of $\langle\sigma v\rangle = 2.6 \times 10^{-26}$ cm^3/s into a pair of $b\bar{b}$ quarks. The diffusion equation for CR propagation is solved using GALPROP (solid lines) with the propagation parameters found in [8] (best-fit with DM). For comparison, we show the solution of the analytic propagation setup of [133]. The shaded band comprises the MED and MAX scenarios. We investigate two values for the coalescence momentum: $p_{\mathcal{C}} = 160$ GeV (left panel) and $p_{\mathcal{C}} = 248$ GeV (right panel). Finally, we show the current antideuteron flux limit by BESS (95% CL) [166] and the expected sensitivities of AMS-02 [168] and GAPS (99% CL) [357]. The figure is taken from [4].

sensitivities of both GAPS and AMS-02 which are expected at 2×10^{-6} (GeV/n)$^{-1}$m^{-2}s^{-1}sr^{-1}. In the analytic propagation setup, the MAX scenario lies within the experimental sensitivities while the MED scenario lies slightly below. If, however, we assume that the larger coalescence momentum of 248 MeV is applicable also for DM we increase the DM flux by approximately a factor 4. In this case, also the MED propagation scenario is within the experimental range.

We perform various cross checks in order to investigate how our results are affected by systematic uncertainties. For this we consider the whole best-fit region of the DM hint from [4]. The 2σ best-fit contour is transferred into a contour in $m_{\rm DM}$ and the average $\bar{D}$ flux in the GAPS bin divided by GAPS sensitivity. This average $\bar{D}$ flux divided by GAPS sensitivity can be understood as follows. If this quantity is larger than 1 GAPS will be able to detect the antideuteron flux while it will not be sensitive to the flux if this quantity is smaller than 1. The results for the 2σ contours are shown in Fig. 6.2. The blue contour in each panel corresponds to our baseline setup, namely, the analytic coalescence model, a coalescence momentum of $p_{\mathcal{C}} = 160$ MeV, solar modulation with a Fisk potential of 400 MV and CR propagation with GALPROP. Almost the entire blue contour lies within the expected experimental sensitive of GAPS. In the following, we will change each of these four assumptions. We start by changing the coalescence model from the analytic to a MC-based

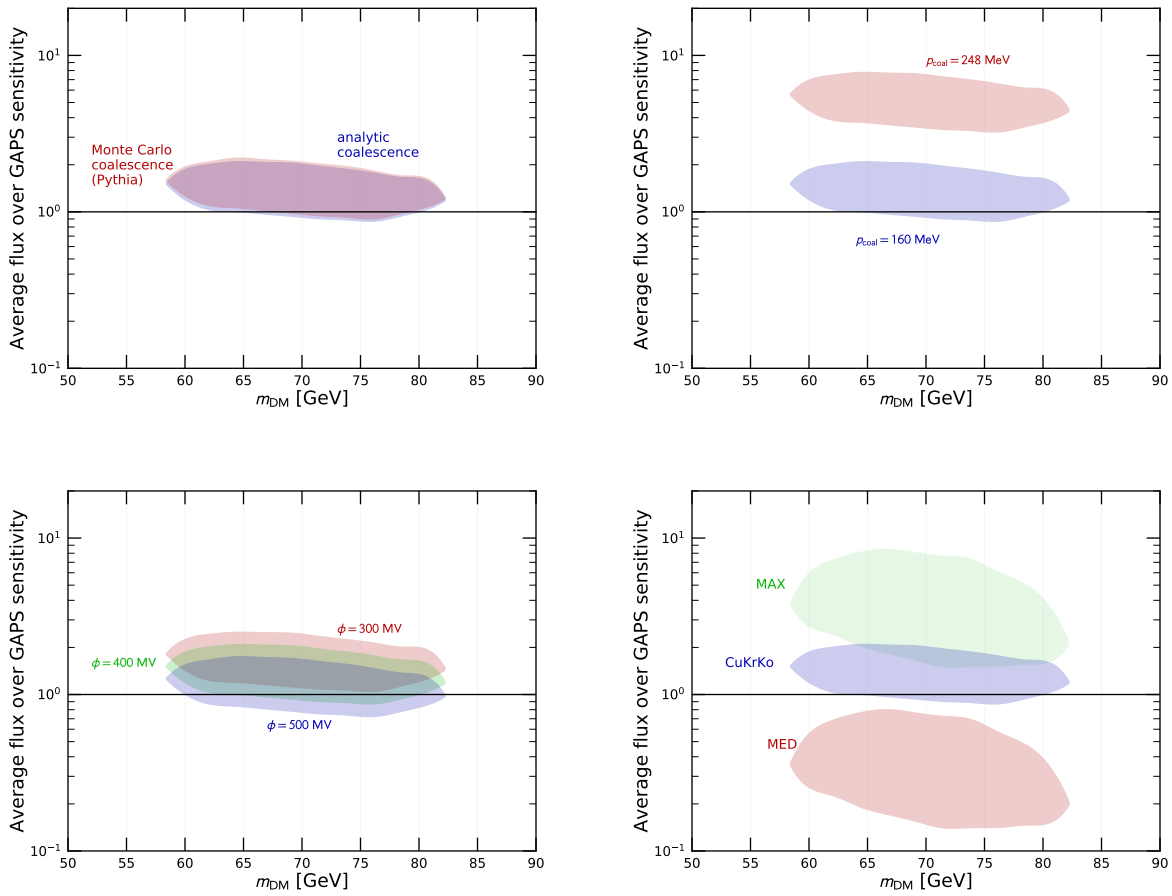

Figure 6.2: The four panels display the average antideuteron flux in the GAPS energy range divided by GAPS sensitivity of 2.0×10^{-6} $\mathrm{m^{-2}s^{-1}sr^{-1}(GeV/n)^{-1}}$ [357] as function of DM mass. We perform four different cross checks of systematic uncertainties arising from the choice of the coalescence model (upper left), the coalescence momentum (upper right), solar modulation (lower left), and the propagation setup (lower right). The blue contour corresponds to our standard setup and refers to the 2σ best-fit region of the DM hint from [8]. More details are provided in the text. The figure is taken from [4].

approach. The energy spectrum of the MC-based approach is taken from [159]. We note that this MC-based is tuned to ALEPH data. We observe that the analytic and MC-based coalescence models give very similar results (upper left panel of Fig. 6.2). This result was already hinted in Sec. 2.6. It is expected since both coalescence models are tuned to ALEPH data. We remind that the energy bin of ALEPH and GAPS approximately coincide and, therefore, our prediction for the antideuteron yield in GAPS does not depend on the coalescence model. The situation will change

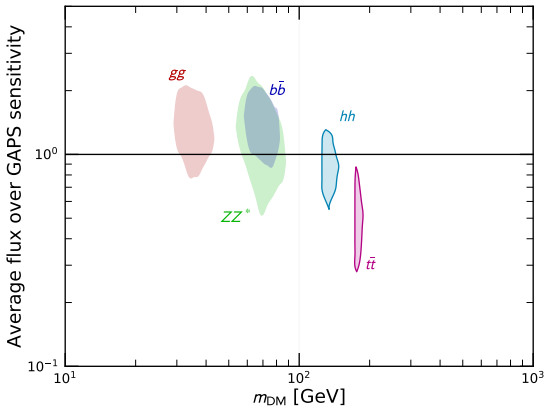

Figure 6.3: This figure is very similar to Fig. 6.2. The blue contour shows our standard setup for DM annihilation into $b\bar{b}$ final states. We compare this with the results of DM annihilation in different hadronic SM final states: gg, ZZ^*, hh, and $t\bar{t}$. The 2σ best-fit regions are taken from Fig. 5.12. The figure is taken from [6].

for different energy bins. For example, a MC-based coalescence model typically predicts higher $\bar{D}$ yields at higher energies and slightly lower yields at lower energies. Changing the coalescence momentum from 160 to 248 MeV results in an increase of the $\bar{D}$ yield by approximately a factor of 4 (upper left panel). This behavior is easily seen from Eq. (2.59): the production cross section (and finally the flux) scales with p_C^3. We remind that the situation of DM annihilation is expected to be more similar to Z-boson decay which has a non-hadronic initial state. In this sense, the smaller coalescence momentum of 160 MeV might be more appropriate for our prediction. Changing the solar modulation potential between 300 and 500 MV only has a very small effect on the result (lower left panel). The reason is that the DM flux is very flat around 0.1 GeV/n. On the other hand, the propagation setup can significantly impact the result. If we change to the analytic propagation model and use the MAX scenario, the entire contour is within the GAPS sensitivity range, while the MED configuration would be entirely below. However, we do not investigate the antiproton

Table 6.2: Summary of the best-fit DM mass and the velocity averaged cross section for various SM final states from [6] and [8].

Final state	m_{DM} [GeV]	$\langle\sigma v\rangle$ [10^{-26} cm^3/s]
gg	34	1.9
$b\bar{b}$	71	2.6
ZZ^*	66	2.4
hh	128	5.7
$t\bar{t}$	173	3.8

yield of the MED and MAX propagation setup. Probably, in the MED scenario we would obtain an antiproton yield below current DM limits and in the MAX scenario we would overproduce CR antiprotons. Therefore, we stress that the GALPROP setup provides the most reliable result.

So far we have always assumed pure annihilation of the DM particles into a pair of $b\bar{b}$ final state. But our results are not specific to this final states. It was shown in Sec 5.3 that the putative CR antiproton excess can be fitted well with DM annihilation into basically any hadronic SM final state. We use the results of [6] and transfer the 2σ best-fit contours of various hadronic final states into the plane of DM mass and GAPS sensitivity. The results for the final states gg, ZZ^*, hh, and $t\bar{t}$ are compared with our standard assumption of $b\bar{b}$ final states in Fig. 6.3. All final states, except $t\bar{t}$, are at least partly within the detection range of GAPS.

Finally, we remark the compatibility of the potential CR antiproton excess and the GCE [213, 214, 226, 358] in gamma rays. Although, there are possible astrophysical explanations, like for example a population of unresolved millisecond pulsars, the DM hypothesis at the Galactic Center is not yet excluded. The DM interpretation of the GCE points to very similar values for DM mass and velocity averaged cross section as the DM hint in CR antiprotons. In this sense, our analysis shows that antideuterons might also probe the DM interpretation of the GCE.

Now we take a more conservative perspective and calculate the maximal antidueteron flux which

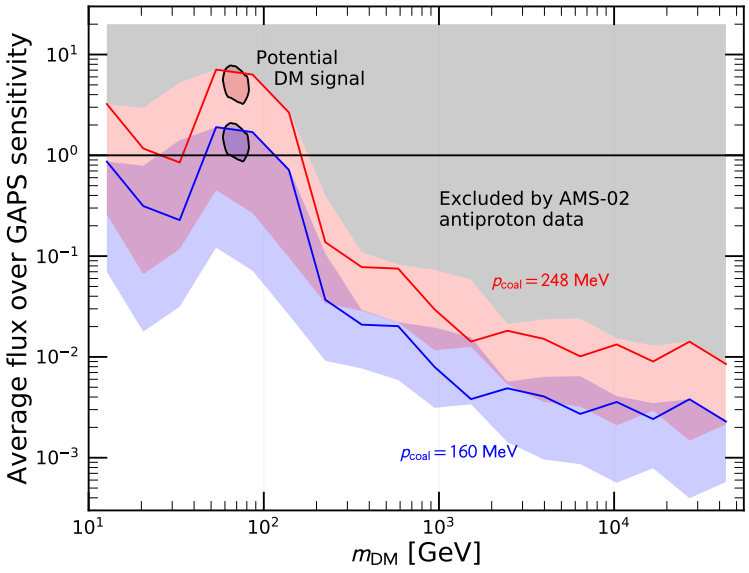

Figure 6.4: We transfer the DM limit from CR antiprotons derived in [6] to the maximal allowed antideuteron flux. The y-axis shows the maximal allowed flux in the GAPS energy bin divided by the GAPS sensitivity. For comparison, we show the contours of the potential DM signal (contours surrounded with black line) from Fig. 6.2 (upper right panel).

can be expected without violating recent DM limits from CR antiprotons. We adopt our standard setup and transfer the DM limit from [8] into the plane of DM mass and GAPS sensitivity. The DM limit in [8] is derived from a MultiNest scan with free parameters of CR propagation and two free parameters for DM, the DM mass and the velocity averaged cross section. We calculate the antideuteron flux for each point in the MultiNest chain which is below the DM limit. Then, we search in each slice of DM mass for the maximal antideuteron flux in the GAPS energy bin. In Fig. 6.4, we report this maximal flux divided by the GAPS sensitivity. We provide the two curves, one curve for $p_{\mathcal{C}} = 160$ MeV and a second curve for $p_{\mathcal{C}} = 248$ MeV. The shaded band represents the systematic uncertainty arising from the adopted CR propagation setup (*c.f.* to the different lines in Fig. 3 of Ref. [8]). The result shows that GAPS will explore a new parameter space for $m_{\rm DM} \lesssim 200$ GeV, while at higher DM masses the detection of antideuterons by GAPS is already excluded by CR antiprotons measured by AMS-02.

6.2.2 Predictions for antihelium

Finally, we apply all our tools on antihelium and calculate the fluxes from secondaries, tertiaries, and DM sources. They are shown separately in Fig. 6.5. The role of the coalescence momentum is even more important for antihelium than for antideuteron, since the production cross section and, subsequently, the flux scales with $p_{\mathcal{C}}$ to the sixth power. Therefore, the larger coalescence momentum of 248 MeV implies a significant increase of the antihelium flux with respect to the

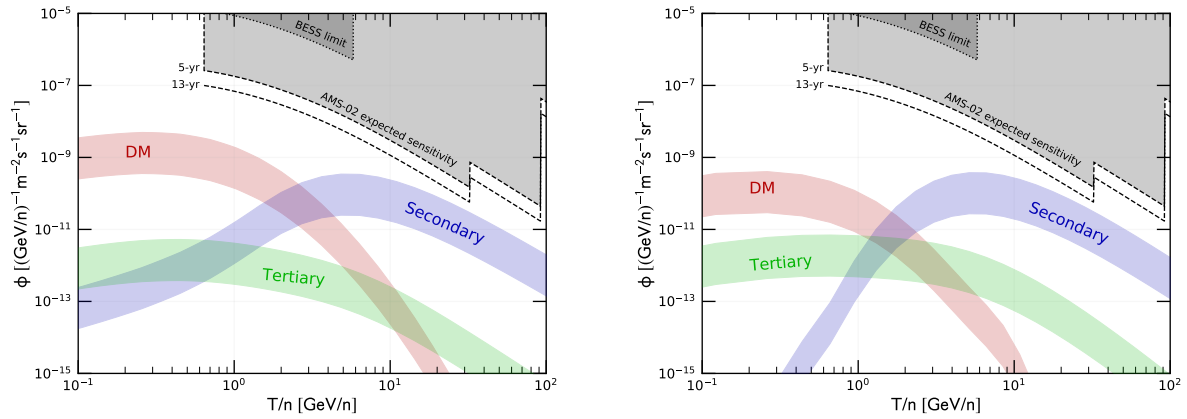

Figure 6.5: Fluxes of $^3\overline{\rm He}$ as function of kinetic energy per nucleon. We explore two different propagation setups. The first is based on Galprop adopting the best fit parameters of [8] (left panel). The second scenario is based on [133] in the MED configuration (right panel). The bands display the uncertainty on the coalescence momentum which is varied between 160 MeV to 248 MeV. We apply a correction due to solar modulation using the force-field approximation with a solar modulation potential of $\phi = 600$ MV. For comparison, we show the BESS limit (95% CL) [167] and AMS-02 sensitivity (95% CL, scaled to 5 and 13 years) [359]. The figure is taken from [4].

smaller coalescence momentum of 160 MeV. The difference is a factor of 14 as can be seen from the width of the bands in Fig. 6.5. Note that previous publications typically relied on the smaller coalescence momentum [164, 360]. We observe that in the GALPROP propagation setup (left panel) the DM component seems to be enhanced with respect to the MED configuration (right panel). Probably, this is due to the enhancement of antihelium in a diffusion setup with reacceleration which was noted in [361]. We remind that we neglect reacceleration in the analytic propagation setup. Our results show that the antihelium flux of secondaries and DM are significantly below the current AMS-02 sensitivities. This is particularly interesting since AMS-02 observed a few particles which are compatible with a $^3\overline{\mathrm{He}}$ and $^4\overline{\mathrm{He}}$ interpretation in the detector. If these candidates were confirmed, the theoretical interpretation would depend on the isotope and the energy regime. At low energies of 1 GeV/n the observation of $^3\overline{\mathrm{He}}$ would strongly indicate a DM origin, while an observation of $^3\overline{\mathrm{He}}$ above a few GeV/n would point towards a secondary origin. A putative observation of $^4\overline{\mathrm{He}}$ could not be explained in our current models. Antihelium four should be suppressed compared to antihelium three by approximately 3 orders of magnitude. If indeed the observation of $^4\overline{\mathrm{He}}$ was confirmed, this would challenge our current understanding of the Universe [362].

Chapter 7

Testing blazar models with angular correlations and photon-count statistics

Blazars represent the dominant population of resolved, *i.e.* individually detected by the Fermi-LAT, extragalactic point sources in the gamma-ray sky [363]. In order to detect an individual source a minimal flux of this source is required. If we continue to smaller individual fluxes per source, further populations are expected to show up. These populations are, for example, mAGN and SFG. Moreover, if we assume that DM particles can annihilate or decay and produce gamma-rays, the corresponding signals from extragalactic DM halos could establish an additional population of point-like sources. However, one can estimate the fluxes at which SFG and mAGN would contribute significantly to the source-count distribution of gamma-ray sources. From these estimations neither the 1pPDF method [265] nor the APS [281] are expected to be sensitive to SFG and mAGN. A similar conclusion is true for DM. Therefore, it is reasonable to assume that our signals of the 1pPDF method [265] and the APS [269] in the unresolved flux regime are dominated by blazars. In this sense, the 1pPDF method and the APS can be used to constrain the distribution of blazars in the unresolved flux regime. We note that the sensitivity of the 1pPDF method to probe the source-count distribution of blazar models was already hinted in [265]. In this chapter, we use the GLF and SED model of blazars from [201]. In this model, we derive constraints on the blazar populations from the unresolved flux regime by exploiting the 1pPDF method and the APS of gamma rays. We compare these results with the constraints we obtained by refitting the blazar model to the latest Fermi-LAT source catalog [363], *i.e.* in the resolved flux regime.

This chapter is structured as follows. In Sec. 7.1 we describe the technical specification to fit the blazar model to our observables. In Sec. 7.2 we present our results individually for each observable and, finally, in Sec. 7.3 we discuss the compatibility and complementarity of our results.

7.1 Model for the blazar populations

The GLF and SED model from [201] was already described in detail in Sec. 3.3.1. This model contains a large number (17) of free parameters. In [201] these are fitted to data from the Fermi-LAT

catalog which is complemented with some additional redshift information from spectroscopic and photometric measurements as detailed in [364]. In other words, the model is constrained by the information of individually resolved sources. Our goal is to constrain the model with additional information in the unresolved regime, *i.e.* below the current detection threshold of the Fermi-LAT for point sources. Therefore, we fit the blazar model with the 1pPDF method and to the APS. In these fits, we will vary the parameters which control the general behavior of the GLF, so the five free parameters are the normalization A of the GLF, the central value μ^* of the distribution of the photon spectral index Γ, the power-law index γ_1 of the luminosity dependence at small L, and the central values p_1^* and p_2^* which govern the redshift dependence of the LDDE model. The remaining values are fixed to the best-fit values of [201]. Finally, we refit the blazar model to the 4FGL catalog data varying the same five free parameters. The technical details for each of the three fits is provided in the following subsections.

7.1.1 The technique of the one-point probability distribution function

Our analysis is focussed on the energy range from 1 GeV to 10 GeV, where we have large statistics and a good angular resolution of the Fermi-LAT detector. We assume that the total $\mathrm{d}N/\mathrm{d}S$ is given by blazars. Other sources are expected to be subdominant at the fluxes tested with the 1pPDF. The $\mathrm{d}N/\mathrm{d}S$ is computed from Eq. (3.35). We restrict the redshift integration between 0.01 and 5.0, since there are no blazars at smaller distance and blazars at larger distances are below the sensitivity of the 1pPDF method. The integration bounds of the photon spectral index, Γ, are chosen between 1.0 and 3.5. These bounds properly cover the range of observed blazars [363]. Our model includes the diffuse gamma-ray emission from Galactic foregrounds and a generic isotropic distribution. The normalization of the Galactic foreground emission, A_{gal}, and the total isotropic flux, F_{iso}, serve as nuisance parameters in the fit. Specifically, $x_{\mathrm{diff}}^{(p)}$ is defined as

$$x_{\mathrm{diff}}^{(p)} = A_{\mathrm{gal}}\, x_{\mathrm{gal}}^{(p)} + x_{\mathrm{iso}}^{(p)}(F_{\mathrm{iso}}) \tag{7.1}$$

with

$$x_{\mathrm{gal}}^{(p)} = \int_{\Omega_{\mathrm{pix}}} \mathrm{d}\Omega \int_{E_{\mathrm{min}}}^{E_{\mathrm{max}}} \mathrm{d}E\, \frac{\mathrm{d}S_{\mathrm{gal}}^{(p)}(E)}{\mathrm{d}E} \cdot \mathcal{E}^{(p)}(E), \tag{7.2}$$

$$\begin{aligned} x_{\mathrm{iso}}^{(p)} &= \int_{\Omega_{\mathrm{pix}}} \mathrm{d}\Omega \int_{E_{\mathrm{min}}}^{E_{\mathrm{max}}} \mathrm{d}E\, \frac{\mathrm{d}S_{\mathrm{iso}}(E)}{\mathrm{d}E} \cdot \mathcal{E}^{(p)}(E) \\ &= F_{\mathrm{iso}} \cdot \int_{\Omega_{\mathrm{pix}}} \mathrm{d}\Omega \int_{E_{\mathrm{min}}}^{E_{\mathrm{max}}} \mathrm{d}E\, \frac{E^{\Gamma_{\mathrm{iso}}}\,(1-\Gamma_{\mathrm{iso}})}{E_{\mathrm{max}}^{1-\Gamma_{\mathrm{iso}}} - E_{\mathrm{min}}^{1-\Gamma_{\mathrm{iso}}}} \cdot \mathcal{E}^{(p)}(E). \end{aligned} \tag{7.3}$$

Here, $\mathrm{d}S_{\mathrm{gal}}^{(p)}/\mathrm{d}E$ is the energy-differential flux of the Galactic foreground emission. and the flux of the isotropic component is modeled as power law, $\mathrm{d}S_{\mathrm{iso}}/\mathrm{d}E \propto E^{-\Gamma_{\mathrm{iso}}}$. We remind that the total

isotropic flux is defined as $F_{\rm iso} = \int_{E_{\rm min}}^{E_{\rm max}} {\rm d}E\, S_{\rm iso}/{\rm d}E$. The parameter $\Gamma_{\rm iso}$ is fixed to 2.3, which is the measured index of the diffuse isotropic background [365].

We exploit the Fermi-LAT gamma-ray data from 2008 August 4 (239,557,417 s MET) until 2018 December 10 (566,097,546 s MET) which are released at `Pass 8`[1]. The event selection and data processing was performed using the Fermi Science Tools (v10r0p5) [2]. We select data passing the standard quality selection criteria (`DATA_QUAL==1` and `LAT_CONFIG==1`). We require events to comply with the `ULTRACLEANVETO` cut and use the corresponding instrument response functions. The corresponding PSF is used to determine the average distribution function of the fractional photon flux, $\rho(f)$, *c.f.* Eq. (3.31). In order to avoid significant PSF smoothing, the event sample is restricted to the `PSF3` quartile following [258, 265]. The data is binned according to the `HEALPix` equal-area pixelization scheme [366] with a resolution parameter $\kappa = 7$. This corresponds to a total number of pixels given by $N_{\rm pix} = 12N_{\rm side}^2$ and $N_{\rm side} = 2^\kappa$. To avoid unnecessary contamination of the diffuse emission from the Galactic plane, we restrict the analysis to high latitudes, $|b| > 30$ deg. We use the official spatial and spectral template of the Interstellar Emission Model (IEM) as provided by the Fermi-LAT Collaboration for `Pass 8`, `gll_iem_v06.fits` [367], to obtain ${\rm d}S_{\rm gal}^{(p)}/{\rm d}E$.

The likelihood is defined as $\mathcal{L}(\vec{\Theta}) = \prod_{p=1}^{N_{\rm pix}} p_k^{(p)}$, where $\vec{\Theta}$ denotes the fit parameters and $p_k^{(p)}$ is defined in Sec. 3.4. We not that this likelihood corresponds to the method L2 in [258]. To sample the likelihood we exploit the MultiNest package in a configuration with 1500 live points and a stopping parameter of `tol=0.2`. All results in the following will be presented within the frequentist framework.

7.1.2 The angular power spectrum technique

We define the APS of intensity fluctuations in gamma rays as $C_\ell^{ij} = \frac{1}{2\ell+1}\sum_m a_{\ell m}^i a_{\ell m}^{j*}$. This sum is an estimator for the expectation value $\langle a_{\ell m}^i a_{\ell m}^{j*}\rangle$ discussed in Sec. 3.5. The indices i and j denote different energy bins. Furthermore, $a_{\ell m}$ are the coefficients of the expansion of the gamma-ray intensity fluctuations in spherical harmonics: $\delta S^i(\vec{n}) = \sum_{\ell m} a_{\ell m}^i Y_{\ell m}(\vec{n})$, with $\delta S^i(\vec{n}) = S^i(\vec{n}) - \langle S^i\rangle$. We note that this definition differs from Eq. (3.40) by a normalization factor $\langle S^i\rangle$. For $i = j$ we refer to the APS as energy auto-correlation, while for $i \neq j$ we call it cross-correlation of the intensity fluctuations in two different energy bins (short: energy cross-correlation).

For blazars, which are point-like and bright astrophysical sources, the APS signal is dominated by the Poisson noise [269]. The Poisson noise is independent of ℓ. In concordance with Eq. (3.53) we define

$$C_{\rm P}^{ij} = \frac{1}{4\pi}\int_{0.01}^{5.0} dz \frac{dV}{dz}\int_1^{3.5} d\Gamma \int_{L_{\rm min}}^{L_{\rm max}} dL\, \Phi(L,z,\Gamma) S_s^i(L,z,\Gamma)\, S_s^j(L,z,\Gamma) \times [1-\Omega(S_{\rm thr}(\Gamma))]\ . \tag{7.4}$$

[1] Publicly available at `https://heasarc.gsfc.nasa.gov/\FTP/fermi/data/lat/weekly/photon/`. More details are found at `https://fermi.gsfc.nasa.gov/ssc/data/analysis/documentation/Cicerone/Cicerone_Data/LAT_DP.html`

[2] `https://fermi.gsfc.nasa.gov/ssc/data/analysis/software/`

We adopt the integration bounds in luminosity of $L_{\rm min} = 10^{43}$ erg/s and $L_{\rm max} = 10^{52}$ erg/s from [201]. Equation (7.4) resembles the definition of $C_{\rm P}$ in Sec. 3.5 apart from the factor $(1 - \Omega(S_{\rm thr}(\Gamma))$ which takes into account that resolved point sources are masked in the $C_{\rm P}$ measurement. Hence, Ω is the Fermi-LAT sensitivity to resolve a point source. This sensitivity depends on the photon flux, S_s, of the source and its spectral index, Γ. Our benchmark model for Ω is a step function, which is equal to 0 for $S_s < S_{\rm thr}(\Gamma)$ and 1 otherwise. We determine the flux threshold, $S_{\rm thr}(\Gamma)$, separately for the 4FGL [193] and the Third Catalog of Hard Fermi-LAT sources (3FHL) [368] catalog. For each value of Γ we define $S_{\rm thr}(\Gamma)$ such that 98% of the sources in the respective catalog are above the flux threshold. We cross-check, as discussed in more detail below, that the choice of Ω does not impact our result. Furthermore, we stress that the Γ-dependence of $S_{\rm thr}$ is an improvement compared to previous analyses(e.g. [270]). We use the $C_{\rm P}$ measurement of [274] which is performed on 8 years of Fermi-LAT. The data is binned into 12 energy bins between 524 MeV and 1 TeV. The measurement is based on `Pass 8` data and events are selected from the event class `P8R3_SOURCEVETO_V2` and with `PSF1+2+3`. The masking procedure of resolved point sources is energy dependent: In the energy range from 0.5–14.5 GeV all sources from the FL8Y[3] catalog are masked, while from 14.5–120 GeV sources are masked both from the FL8Y and 3FHL catalogs. Above 120 GeV sources are only masked if they are in the 3FHL catalog. Low Galactic latitudes are masked to avoid a strong bias from the Galactic plane. The remainder of the Galactic diffuse emission at high latitudes is modeled using the official IEM template, `gll_iem_v6.fits` [367]. For a more detailed description of the analysis we refer to [274].

We perform the χ^2-fit of the APS on the auto- and cross-correlation energy bins and define:

$$\chi^2_{\rm APS} = \sum_{i \leq j} \frac{\left[\left(C_{\rm P}^{ij}\right)_{\rm meas} - \left(C_{\rm P}^{ij}\right)_{\rm th}\right]^2}{\sigma^2_{C_{\rm P}^{ij}}}, \tag{7.5}$$

where the subscripts *meas* denotes the measured $C_{\rm P}$ from [274] and the subscript *th* denotes the theoretical $C_{\rm P}$ which is calculated from Eq. (7.4). Moreover, $\sigma^2_{C_P^{ij}}$ is the measurement uncertainty of the $C_{\rm P}$. The corresponding likelihood, $\mathcal{L} = \exp(-\chi^2_{\rm APS}/2)$, is sampled with the `MultiNest` package. We use a configuration with 2000 live points, an enlargement factor of `efr=0.7`, and a stopping parameter of `tol=0.1`.

7.1.3 The 4FGL and 4LAC catalogs for resolved blazars

We aim to compare the result in the unresolved regime with those from resolved sources. Therefore, we analyze the most recent source catalog, the 4FGL catalog, complemented with redshift information from the Fourth Catalog of Active Galactic Nuclei (4LAC) catalog [363]. Both catalogs are based on 8 years of Fermi-LAT data. In the following, whenever we mention *4FGL* we rather mean *4FGL complemented with redshift information from 4LAC*. We note that the resolved sources in the 4FGL catalog are the only observable in our setup with explicit redshift information. Since the statistical methods of the 1pPDF and APS do not identify individual sources, they cannot directly

[3]The FL8Y is a preliminary version of the 4FGL catalog. We assume that the flux thresholds of the preliminary FL8Y and the final 4FGL are identical.

constrain the redshift-dependence encoded in the LDDE model. The source-count distributions extracted from the 4FGL catalog is fitted varying the same five GLF parameters as above: A, μ^*, γ_1, p_1^*, and p_2^*. The total $\chi^2_{\rm 4FGL}$ may be split into three contributions which arise from (i) the total number of observed point sources, (ii) the number of associated[4] blazars, and (iii) blazars with redshift measurements:

$$\chi^2_{\rm 4FGL} = \chi^2_{\rm all} + \chi^2_{\rm as} + \chi^2_z. \tag{7.6}$$

The first term serves as upper limit of the source-count distribution. In detail, we extract the source-count distribution of all sources, $({\rm d}N/{\rm d}S)_{{\rm all},i}$, in 12 flux bins i. The bins are equally spaced in $\log(S)$ and range from $10^{-12} \times {\rm cm}^{-2}{\rm s}^{-1}$ to $10^{-7} \times {\rm cm}^{-2}{\rm s}^{-1}$. In the context of the catalog fit, S is always the flux in the energy bin from 1 GeV to 100 GeV. As before, we restrict the analysis to high latitudes $|b| > 30$ deg. Here, the point sources are dominated by blazars, but some of the unassociated sources could fall into a different source class. Therefore, when we fit the catalog ${\rm d}N/{\rm d}S$ of associated sources to our theoretical model we take it as an upper limit, formally defined as:

$$\chi^2_{\rm all} = \sum_i \begin{cases} \frac{\left[\left(\frac{{\rm d}N}{{\rm d}S}\right)_{{\rm all},i} - \left\langle\frac{{\rm d}N}{{\rm d}S}\right\rangle_{{\rm th},i}\right]^2}{\sigma^2_{{\rm all},i}} & , \text{if } \left\langle\frac{{\rm d}N}{{\rm d}S}\right\rangle_{{\rm th},i} > \left(\frac{{\rm d}N}{{\rm d}S}\right)_{{\rm all},i} \\ 0 & , \text{otherwise.} \end{cases} \tag{7.7}$$

Here $\langle {\rm d}N/{\rm d}S\rangle_{{\rm th},i}$ is the source-count distribution predicted by our GLF model. The $\langle ... \rangle$ denote the average ${\rm d}N/{\rm d}S$ in each bin, *i.e.* the integral of the ${\rm d}N/{\rm d}S$ (see Eq. (3.35)) in each flux bin i divided by the bin width ΔS_i.

In analogy to the first term, we define the second term which constrains the contribution of the associated sources. However, instead of extracting the total source-count distribution, we count only the ${\rm d}N/{\rm d}S$ of associated blazars, denoted $({\rm d}N/{\rm d}S)_{{\rm as},i}$. In contrast to the first term, $({\rm d}N/{\rm d}S)_{{\rm as},i}$ serves as a lower limit in the fit, because we know that the association in the catalog is incomplete. We define:

$$\chi^2_{\rm as} = \sum_i \begin{cases} \frac{\left[\left(\frac{{\rm d}N}{{\rm d}S}\right)_{{\rm as},i} - \left\langle\frac{{\rm d}N}{{\rm d}S}\right\rangle_{{\rm th},i}\right]^2}{\sigma^2_{{\rm as},i}} & , \text{if } \left\langle\frac{{\rm d}N}{{\rm d}S}\right\rangle_{{\rm th},i} < \left(\frac{{\rm d}N}{{\rm d}S}\right)_{{\rm as},i} \\ 0 & , \text{otherwise.} \end{cases} \tag{7.8}$$

Note that by taking $\chi^2_{\rm all}$ as an upper limit and $\chi^2_{\rm as}$ as a lower limit, we avoid double counting in Eq. (7.6).

The last term of Eq. (7.6) exploits the redshift information which is important to constrain the LDDE model. In addition to binning our data in flux, we now also bin into 4 redshift bins, j: [0, 0.5], [0.5, 1.2], [1.2, 2.3] and [2.3,4]. The source-count distribution extracted from the 4FGL catalog is denoted $({\rm d}N/{\rm d}S)_{z,ij}$. To obtain the corresponding source-count distribution of our model, $\langle {\rm d}N/{\rm d}S\rangle_{{\rm th},ij}$, we simply restrict the integration range of z in Eq. (3.35) to the respectived redshift bin. We note

[4] In this chapter, *associated* means the sum of identified and associated blazars, more precisely, the 4FGL source classes are `BLL, BCU, FSRQ, bll, bcu, fsrq`.

Table 7.1: Best-fit parameters for each of the three applied techniques. For reference, in the last column we report the values from [201].

Parameter	1pPDF	$C_{\rm P}$	4FGL	$C_{\rm P}$+4FGL	Ref. [201]
$\log_{10}(A/\mathrm{Mpc}^{-3})$	$-8.98^{+0.86}_{-0.49}$	$-7.55^{+0.54}_{-5.60}$	$-9.01^{+0.08}_{-0.19}$	$-8.91^{+0.05}_{-0.16}$	$-8.71^{+0.36}_{-0.47}$
γ_1	$0.652^{+0.44}_{-0.02}$	$0.36^{+0.17}_{-0.23}$	$0.65^{+0.16}_{-0.02}$	$0.60^{+0.04}_{-0.01}$	$0.50^{+0.14}_{-0.12}$
p_1^*	$3.26^{+2.74}_{-2.26}$	$4.89^{+0.11}_{-0.75}$	$2.80^{+1.37}_{-1.25}$	$3.74^{+0.65}_{-1.47}$	$3.39^{+0.89}_{-0.70}$
p_2^*	$-17.5^{+8.60}_{-2.54}$	$-19.5^{+7.36}_{-0.50}$	$-5.28^{+2.38}_{-0.67}$	$-5.31^{+1.57}_{-0.68}$	$-4.96^{+2.25}_{-4.76}$
μ^*	$1.78^{+0.34}_{-0.22}$	$2.32^{+0.05}_{-0.09}$	$1.79^{+0.32}_{-0.79}$	$2.31^{+0.04}_{-0.02}$	$2.22^{+0.03}_{-0.02}$
$A_{\rm gal}$	$1.05^{+0.01}_{-0.01}$	-	-	-	-
$F_{\rm iso}$ $[10^{-7}\mathrm{cm}^{-1}\mathrm{s}^{-1}\mathrm{sr}^{-1}]$	$1.18^{+0.11}_{-0.12}$	-	-	-	-
k	-	$0.59^{+0.82}_{-0.09}$	-	$1.13^{+0.06}_{-0.05}$	-
-	$\ln(\mathcal{L})$= -245276.1	χ^2/dof =80.2/72	χ^2/dof = 5.5/2 [5]	χ^2/dof = 94.5/79	-

that the redshift measurements of the catalog are incomplete. Consequently, the χ^2_z contribution is taken as a lower limit:

$$\chi^2_z = \sum_{i,j} \begin{cases} \frac{\left[\left(\frac{\mathrm{d}N}{\mathrm{d}S}\right)_{z,ij} - \left\langle\frac{\mathrm{d}N}{\mathrm{d}S}\right\rangle_{\mathrm{th},ij}\right]^2}{\sigma^2_{\mathrm{z},ij}} & , \text{if } \left\langle\frac{\mathrm{d}N}{\mathrm{d}S}\right\rangle_{\mathrm{th},ij} < \left(\frac{\mathrm{d}N}{\mathrm{d}S}\right)_{z,ij} \\ 0 & , \text{otherwise.} \end{cases} \tag{7.9}$$

We observe that the sum of $\chi^2_{\rm all}+\chi^2_z$, which contains redshift information, mostly constrains the two parameters p_1^* and p_2^*, while the remaining three parameters, A, γ_1 and, μ^*, are mostly constrained by $\chi^2_{\rm all}+\chi^2_{\rm as}$. We have explicitly verified this expectation by performing two additional fits, where either we use only $\chi^2_{\rm all}+\chi^2_{\rm as}$ or we use only $\chi^2_{\rm all}+\chi^2_{\rm z}$. In this sense, effectively, we avoid double counting in the $\chi^2_{\rm 4FGL}$ definition.

Below the flux threshold, $S_{\rm thr}$, the detection efficiency of point sources quickly drops to zero, meaning that the catalog becomes incomplete. If the catalog is incomplete, the $\chi^2_{\rm all}$ cannot serve as an upper limit. Hence, we exclude data points below the threshold of $S_{\rm thr} = 1.1\times10^{-10}$ cm^{-2}s^{-1}. In other words, the sum over i in Eq. (7.7) is restricted to those flux bins which are above $S_{\rm thr}$. The likelihood parameters space is sampled again with the MultiNest package, using 2000 live points, an enlargement factor of `efr=0.7`, and a stopping parameter of `tol=0.1`.

7.2 Results of fitting the blazar model

7.2.1 Results from the photon-count statistics analysis

We apply the 1pPDF technique discussed in Sec. 3.4 with the specifications from Sec. 7.1.1. The results are shown in Fig. 7.1. The red solid line shows the best-fit model of the blazar model, while the grey dashed line corresponds to a fit where the $\mathrm{d}N/\mathrm{d}S$ is modeled as a multiple-broken power law with three breaks as defined in (3.34). In both cases, the shaded bands mark the 1σ uncertainty level. In the case of the blazar model, the fit contains the five model parameters, A, μ^*, γ_1, p_1^*, and p_2^*, and two nuisance parameters, $A_{\rm gal}$ and $F_{\rm iso}$. Their best-fit values and uncertainties are summarized in Tab. 7.1. The best-fit parameters obtained with the 1pPDF technique are consistent at the 2σ

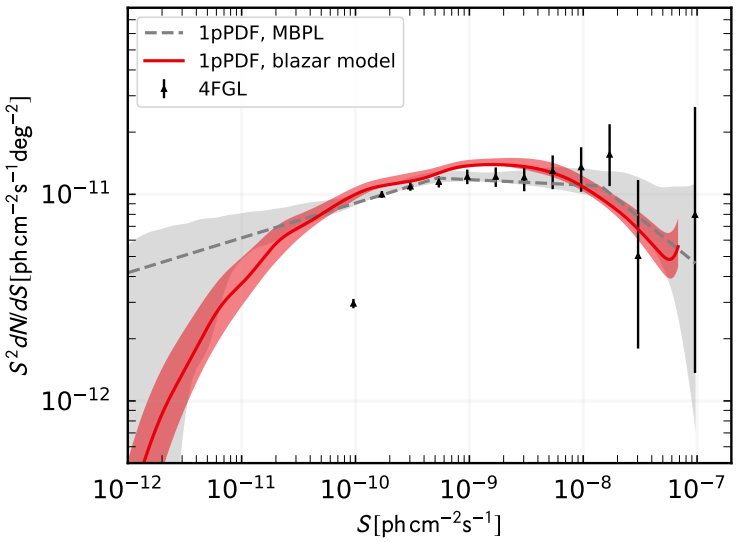

Figure 7.1: Source-count distribution, $\mathrm{d}N/\mathrm{d}S$, obtained with the 1pPDF technique. We overlay the results of fitting the blazar model form [201] (red solid line) with the results of fitting a multiple-broken power law parametrization (grey dashed line) in the energy range from 1 GeV to 10 GeV. The shaded bands correspond to the 1σ uncertainty, frequentist interpretation. For comparison, we display the $\mathrm{d}N/\mathrm{d}S$ of the resolved sources from the 4FGL catalog. The figure is taken from [1].

C.L. with the reference model [201] and at the 1σ C.L. with our refit of the model on 4FGL catalog data, see Sec. 7.2.3. The best-fit of the multiple-broken power law converges to a normalization parameter $A_\mathrm{S} = 2.31^{+7.67}_{-1.22} \times 10^9$ cm^{2}ssr^{-1}; position of the breaks at $S_{b1} = 1.43^{+3.57}_{-0.93} \times 10^{-8}$ cm^{-2}s^{-1}, $S_{b2} = 5.2^{+8.08}_{-2.94} \times 10^{-10}$ cm^{-2}s^{-1}, and $S_{b3} = 2.21^{+97.7}_{-1.18} \times 10^{-13}$ cm^{-2}s^{-1}; and power-law indices of $n_1 = 2.45^{+0.78}_{-0.48}$, $n_2 = 2.03^{+0.10}_{-0.10}$, $n_3 = 1.83^{+0.14}_{-0.15}$, and $n_4 = -0.32^{+2.18}_{-1.68}$. The reference flux is chosen to be $S_0 = 5 \times 10^{-9}$ cm^{-2}s^{-1}. The 1pPDF method with a multiple-broken power law is well-tested [258, 265]. Hence, the good agreement between the $\mathrm{d}N/\mathrm{d}S$ of the multiple-broken law and the physical blazar model confirms our new technique. Both results are in good agreement with the $\mathrm{d}N/\mathrm{d}S$ data points extracted from the 4FGL catalog. So, our blazar model describes at the same time the $\mathrm{d}N/\mathrm{d}S$ in the resolved and unresolved flux regime, indicating that blazars are indeed the dominating point sources in the flux regime tested by the 1pPDF. Finally, we note that the fit of the multiple-broken power law provides important information concerning the sensitivity of the 1pPDF technique. The source count distribution (grey band) is well constrained down to fluxes of about 8×10^{-12} cm^{-2}s^{-1}, while the threshold of the catalog for resolved sources is at the order of 2–3×10^{-10} cm^{-2}s^{-1}. So, in the energy bin from 1 GeV to 10 GeV the 1pPDF measures the $\mathrm{d}N/\mathrm{d}S$ more than one order of magnitude below the catalog threshold. This sensitivity cannot be seen from the blazar model fit.

[5] We mention here a subtlety connected to the counting of the dof in the fit of the blazar model to the 4FGL catalog. We adopt an upper limits (χ^2_all) in 7 flux bins. With a total of 5 free parameters we obtain a dof of 2. The subtlety is that in addition we use the redshift information as lower limit in the fit (effectively) 28 bins. Since the χ^2

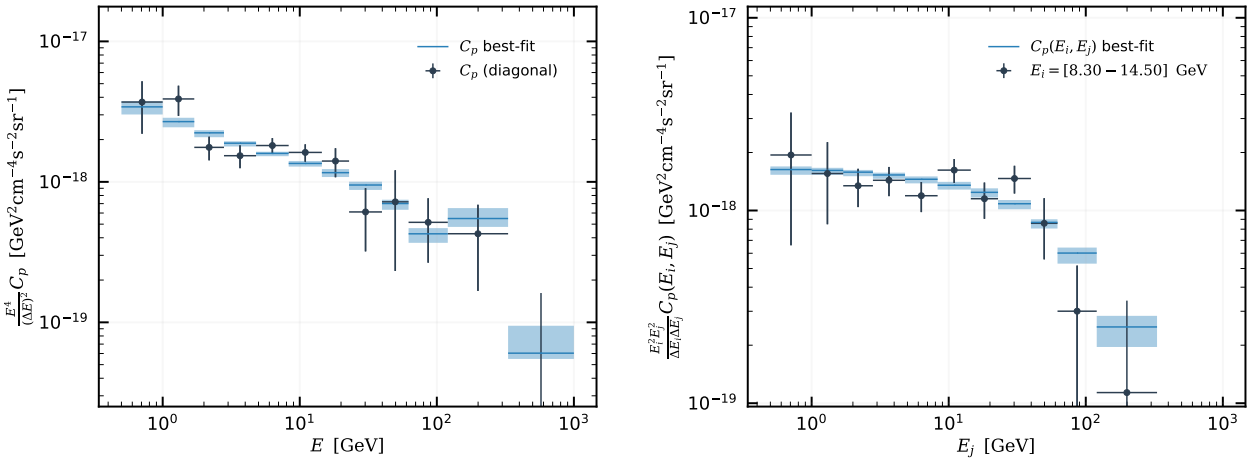

Figure 7.2: Best-fit result of the blazar model to the C_{P} as a function of the energy. The data is taken from [274]. In the left panel we display the energy auto-correlation, while the right panel shows the energy cross-correlation in one selected energy bin from 8.3 GeV to 14.5 GeV with all others bins. The shaded bands correspond to the 1σ C.L. This figure is taken from [1].

7.2.2 Results from the angular correlation analysis

In the APS analysis, we use the same blazar model and setup as in the 1pPDF fit described above, but the treatment of nuisance parameter changes. The uncertainty of Galactic foreground emission is already marginalized in [274] and, hence, included in the uncertainty of the data points. However, there is one important systematic uncertainty which is introduced in the C_{P} measurement. It is related to the fact that the threshold for masking point sources is only approximately known. We take the uncertainty on S_{thr} into account by introducing the nuisance parameter k, which allows to vary the value of S_{thr} by a factor between 0.5 to 2.0. Further cross-checks concerning the S_{thr} are discussed later. In summary, the free fit parameters are A, μ^*, γ_1, p_1^*, and p_2^*, and the nuisance parameter k.
The results of our fit are shown in Fig. 7.2. We compare the measured C_{P} data point with the blazar model (light-blue lines) for the energy auto-correlation and all cross-correlation bins. In Fig. 7.2 we only show the energy auto-correlation (left panel) and one example for the energy cross correlation of the 8.3 GeV to 14.5 GeV bin with all others bins (right panel). The corresponding best-fit values are summarized again in Tab. 7.1. They are well-compatible with the values obtained from the 1pPDF analysis above as well as with the reference values from [201]. Only the parameter p_2^* seems to show a small tension between the 1pPDF and APS fits, one the one hand, and the reference values from [201] and the 4FGL fit, on the other hand. We will comment on this again in the next paragraph, but note already here that the significance of this tension is below 2σ.

of the best-fit point is only marginally affected by the lower limits, we decided not to count these dof in the table.

In the context of the $C_{\rm P}$ fit we have performed two cross checks. First, we have studied the effect of the cut threshold, $S_{\rm thr}$, and, second, we have investigated the possibility of a second population in the APS. The catalog efficiency, Ω, in our benchmark model is assumed to be a Θ-like cut. But certainly this is only an approximation. What actually occurs in reality is that the efficiency of the Fermi-LAT detector to detect point sources gradually increases from 0 to 1 with increasing flux of the sources. However, the exact shape and Γ dependence of the efficiency is not provided for the 4FGL catalog. We test the impact of a smooth efficiency function on the results of the fit. In order to do this we adopt a functional form of the efficiency, which then depends on one additional parameters η:

$$\Omega_{\rm smooth}(\Gamma, \eta) = 1 - \frac{1}{1 + [S/S_{\rm thr(\Gamma)}]^{\eta}} \,. \tag{7.10}$$

The new parameter allows to control how quickly the efficiency grows from 0 to 1: the larger η the steeper the growth. We have varied η between 2.5 and 4 and verified that our physical results (A, γ_1, p_1^*, p_2^*, μ^*) are stable against these changes of the functional form of the efficiency. In all our fits the nuisance parameter k converges to a value close to 1.
Previous analyses have claimed evidence for two populations in the APS instead of a single population [270, 274, 276]. We explicitly test this hypothesis by adding an additional component in our fit. We assume that this additional component is governed by a power-law $\mathrm{d}N/\mathrm{d}S$ and a power-law SED. Explicitly, we parameterize $\mathrm{d}N/\mathrm{d}S = A_{\rm PWL}(S/S_0)^{-\beta_{\rm PWL}}$ and $\mathrm{d}N/\mathrm{d}E \sim E^{-\Gamma_{\rm PWL}}$. Then, we varied the three parameters of the power-law component ($A_{\rm PWL}$, $\beta_{\rm PWL}$, $\Gamma_{\rm PWL}$) on top of our six parameter of the benchmark setup. We find no evidence for the additional component. The extended fit leads only to an small improvement of the χ^2 which is below the 2σ C.L. This result justifies a posteriori our initial assumption to base the analysis solely on one component, blazars. We note, in particular, the difference between our setup and the analysis in [274]. We use a physical model which allows for a distribution of Γ, while [274] assumes a single, fixed value of Γ. The evidence for two populations in [274] probably originates from the fact that the effect of a distribution in Γ is not investigated. The evidence for two population then mimics the fact that in reality there is a distribution in Γ.

7.2.3 Results from the analysis of the 4FGL catalog

We fit the blazar model to the 4FGL catalog as described in Sec. 7.1.3. The free parameters in this fit are again A, μ^*, γ_1, p_1^*, and p_2^*.

The results are shown in Fig. 7.3. The lower black triangles refer to the source-count distribution of all point sources $(\mathrm{d}N/\mathrm{d}S)_{{\rm all},i}$. They are included as upper limits in the fit, *c.f.* Eq. 7.7. The upper black triangles mark the associated blazars, $(\mathrm{d}N/\mathrm{d}S)_{{\rm as},i}$, and serve as a lower limit, *c.f.* Eq. 7.8. Finally, the colored upper triangles display the source-count distribution in each redshift bin, $(\mathrm{d}N/\mathrm{d}S)_{z,ij}$. Those data point have to be understood again as lower limit, *c.f.* Eq. 7.9. The best-fit blazar model is represented by the solid lines. We note that, as expected, the model passes between the upper and lower black triangles and lies above the colored data points. This fit is unique in the sense that, in contrast to 1pPDF method and APS, it contains explicit redshift information. It is therefore expected to provide the most reliable constraint on the LDDE model. The best-fit

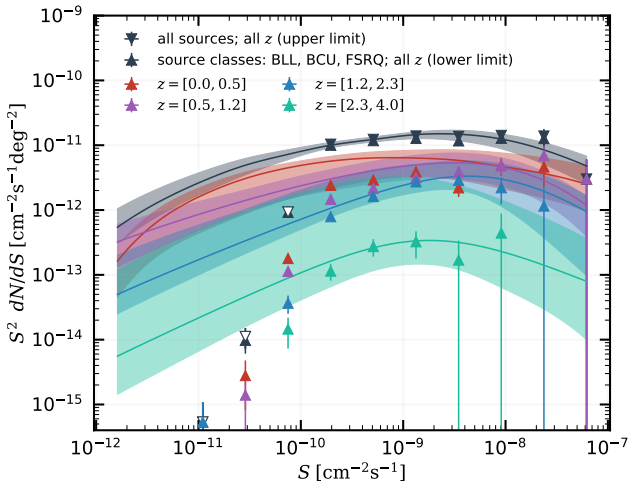

Figure 7.3: Results of fitting the blazar model using the 4FGL catalog. The shaded bands mark the 1σ uncertainty. The data points with triangles pointing upwards and downwards correspond to lower and upper limits, respectively. Open white data points are not considered in the fit since they are below the flux threshold. The flux, S, refers to the energy range from 1 GeV to 100 GeV. Further details are provided in the text. This figure is taken from [1].

parameters and uncertainties are summarized in Tab. 7.1. We observe indeed a better constraint on the parameter p_2^*. We mentioned before that there is a slight tension between the best-fit value of the 4FGL at $p_2^* = -5.28^{+2.38}_{-0.67}$ and smaller values which are slightly preferred by the 1pPDF and APS fits. In this case, the value of the 4FGL fit should be more trusted because of the argument hinted above.

7.3 Complementarity of the observables

The compatibly and complementarity of all the techniques to constrain the blazar model is best shown in Fig. 7.4. The triangle plot displays the comparison the best-fit parameter regions for the three methods. The various panels in the lower half of the triangle plot show contours of the 2-dimensional χ^2-distribution for each combination of two fit parameters. The three contours in each color mark the 1σ, 2σ, and 3σ C.L., which correspond to a $\Delta\chi^2$ of 2.30, 6.18, and 11.83, respectively. On the diagonal, we display the χ^2-profile for each of the five fit parameters. The figure shows that the three techniques are compatible at the 2σ level. The largest tension concerns the parameter p_2^* which we have already commented above. The complementarity of the different observables is, in particular, visible in the two lower left panels. While the APS fit constrains very well the parameter μ^*, the normalization, A, and slope of the luminosity dependence, γ_1, are mostly constrained by the 1pPDF and the 4FGL catalog. This result is expected since the APS is the only

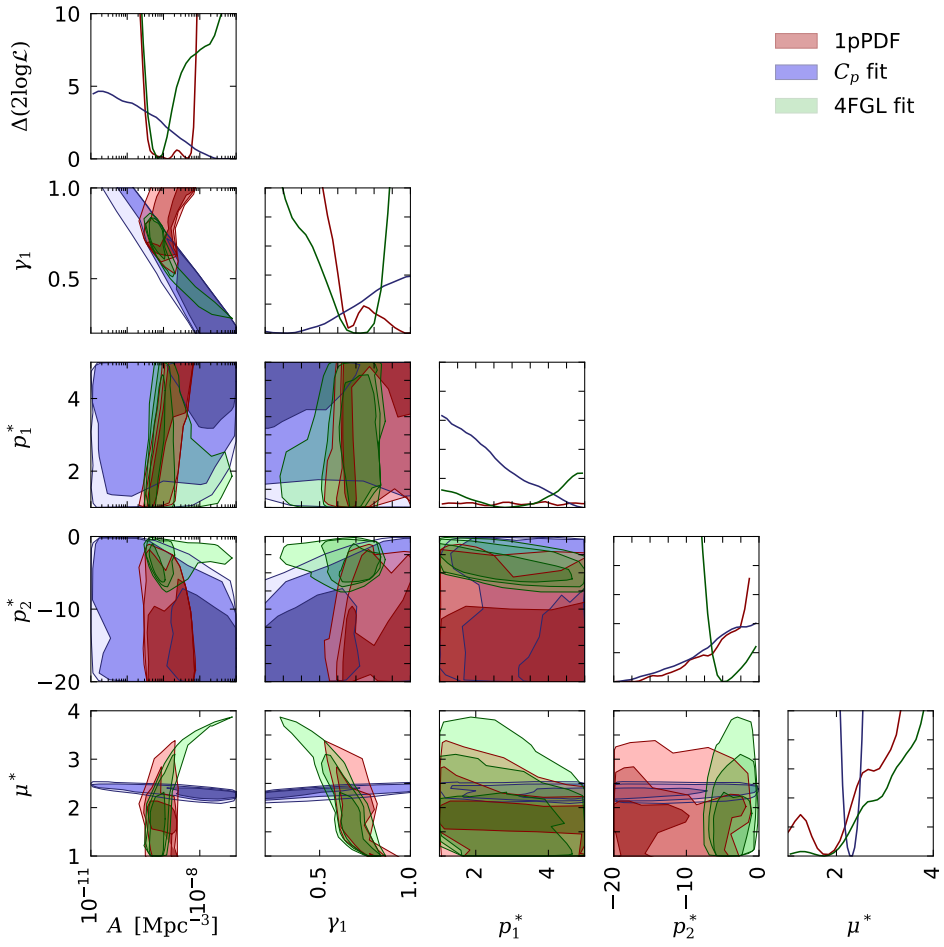

Figure 7.4: Constraints on the blazar model parameters obtained with the 1pPDF method (red), the APS (blue), and the 4FGL catalog (green). The panels on the diagonal show the likelihood profile for each fit parameters (the y-axis of each panel ranges linearly from 0 to 10). The remaining panels in the lower triangle show the 1, 2, and 3σ C.L. contours for each combination of the fit parameters. This figure is taken from [1].

observable which includes explicit information about the behavior as a function of energy. Because of this energy binning it constrains very well the overall behavior of the SED. On the other hand, the 1pPDF and 4FGL directly measure the source count distribution. Thus, they are very sensitive

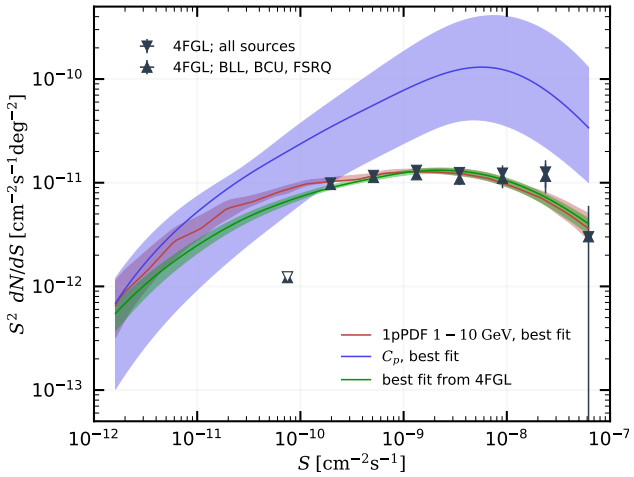

Figure 7.5: Comparison of the dN/dS prediction from the individual observables: 1pPDF, APS, and 4FGL catalog. The solid lines show the best-fit model of each individual fit while the shaded bands refer to the 1σ uncertainty level. The data points of the dN/dS are determined from the 4FGL catalog. The notation follows Fig. 7.3: lower triangles contain all source classes while upper triangles are restricted to the source classes BBL, BCU, and FSRQ. The flux in this figure refers to the energy bin from 1 GeV to 10 GeV. This figure is taken from [1].

to the normalization and flux- or luminosity-dependence[6].

We can push the comparison of the three fits even one step further, namely, we can predict for each fit the observables of the respective other methods. The results are shown in Figs. 7.5 and 7.6. Figure 7.5 shows the dN/dS provided by the best fits of the 1pPDF method, the APS, and the 4FGL catalog. It is particularly interesting to have a closer look at the dN/dS prediction of the APS results (blue band). The APS can be understood as second moment of the dN/dS distribution. Therefore, it is the integral over the source-count distribution and does not directly constrain its functional behavior. Nonetheless, the C_P fit provides a good agreement to the 1pPDF fit and 4FGL fit at small fluxes. We remind that the APS is measured only for $S < S_\mathrm{thr}$ and note that the agreement of all three methods in this flux range is very good. We have explicitly checked that at larger fluxes, $S > S_\mathrm{thr}$ the APS prediction agrees with the expectation (4FGL data points) at the 3σ level. The agreement of 1pPDF method and 4FGL catalog with the expected dN/dS is a trivial result since both are direct sensitive to measure the dN/dS. Furthermore, we have checked that the APS and 1pPDF predictions do not violate the redshift constraints of the 4FGL catalog. Now, we invert the idea and predict the APS from the best-fit models of the 1pPDF and 4FGL catalog fits. The results are presented in Fig. 7.6. The uncertainty bands of the 1pPDF and 4FGL are very large and agree (at 3σ) with the expectation (C_P data points). The fact that some of

[6]We remind the flux-luminosity relation, dL/d$S = L/S$, as discussed at the end of Sec. 3.4.

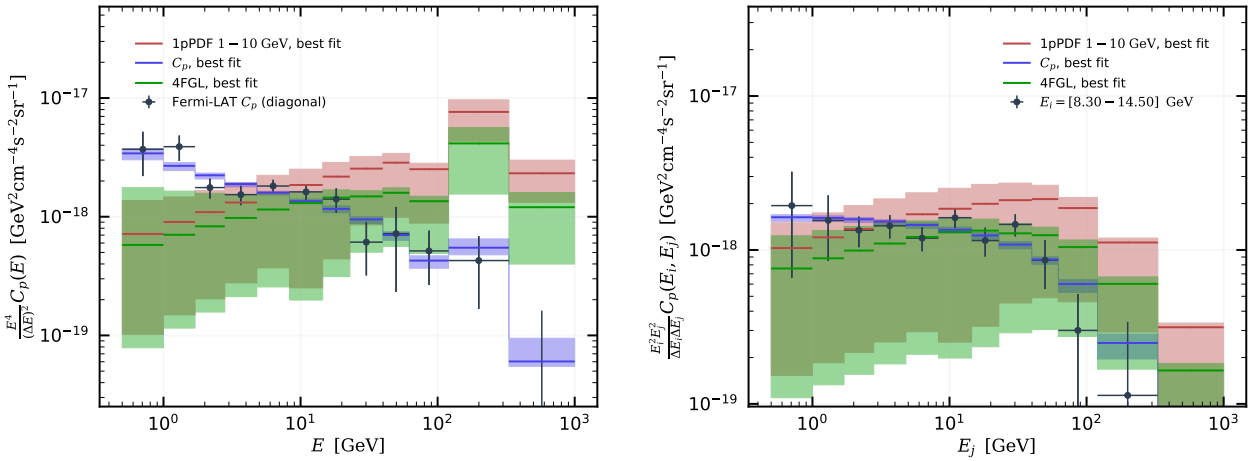

Figure 7.6: Comparison of the APS prediction from the individual observables: 1pPDF, APS, and 4FGL catalog. The solid lines show the best-fit model of each individual fit while the shaded bands refer to the 1σ uncertainty level. The C_P data points are taken from [274]. In analogy to Fig. 7.2 we display in the left panel the energy auto-correlation and in the right panel the energy cross-correlation for one specific energy bin. This figure is taken from [1].

the predictions lead to a fairly large uncertainty band is another indication for the complementary information of our observables.

Finally, we combine the contours of the APS and the 4FGL fits by performing a joint fit. The information of the 1pPDF fit cannot simply be included in a joint fit, since this would lead to a double-counting of the underlying data. In the case of APS and 4FGL, the 4FGL catalog contains exactly the information of the gamma-ray sky which is masked in the APS measurement. So, there is no double counting. The joint fit includes the usual five parameters of the blazar model and the nuisance parameter k from the APS fit. The χ^2 of the joint fit is the sum of the two individual χ^2s defined in Eqs. (7.5) and (7.6), respectively. The fit results are displayed in Fig. 7.7, which visualizes the striking complementarity of the two observables. The best-fit contours of the joint fit shrink, as expected, to the overlap of the two individual fits. The fit quality of the joint fit is reasonable with a χ^2/dof of 94.5/79. The separate contributions of the APS and 4FGL fits are 86.2 and 8.3, respectively. The best-fit parameters and 1σ uncertainties are summarized in Tab. 7.1.

In summary, we have used two statistical methods in order to constrain the gamma-ray emission of point sources. These analyses are based on the recently provided Fermi-LAT data. We interpret our results within the blazar model of [201] and demonstrate the complementarity of the different techniques. Most importantly, we have used two techniques, which are sensitive to probe gamma-ray point sources in the unresolved flux regime, the 1pPDF method and the APS of gamma rays. We remind that these two techniques provide complementary information. While the first directly

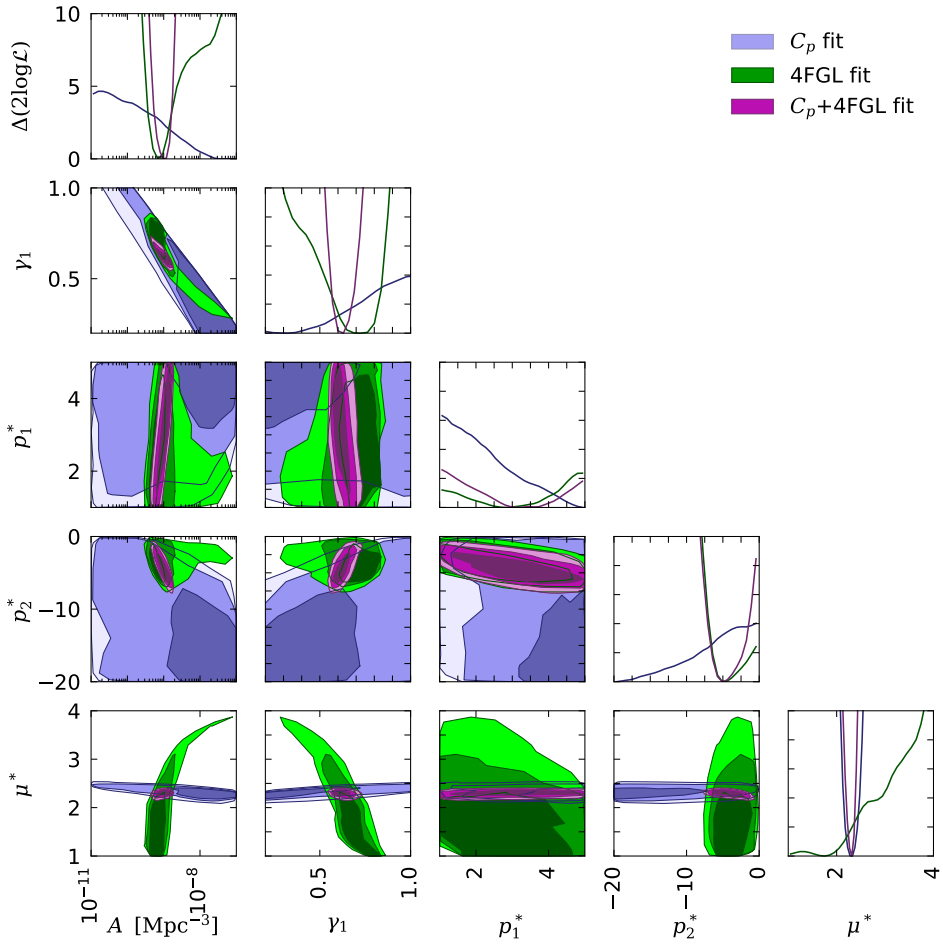

Figure 7.7: Triangle plot to compare the joint fit of C_P+4FGL with the individual fits of the C_P and the 4FGL catalog. The blue and green contours are exactly the same as those shown in Fig. 7.4.

measures the source-count distribution, the latter can be understood as the second moment of the source-count distribution. The blazar model of [201] is able to explain self-consistently and with consistent parameters our observables in the unresolved (1pPDF and APS techniques) and the resolved (4FGL catalog) flux regime. We take this as an indication that blazars are the only important population of point sources in the flux regime probed by the 1pPDF method and APS. Finally, we stress again that these statistical methods exploit gamma-ray information of faint sources which are more than one order of magnitude below the flux threshold for individual detection in

the 4FGL source catalog.

Part III

Conclusions and perspectives

Conclusions and perspectives

In this thesis, we have used recent precise measurements of CRs and gamma rays to understand the Galactic and extragalactic Universe. Our main motivation to study these messengers is the indirect search for DM, which often requires a better understanding of pure astrophysical phenomena.

We have investigated CR propagation with a particular focus on antiprotons and their primary parents, proton and helium. The precise measurement of their fluxes by the AMS-02 experiment allows to perform analyses at a new level of accuracy. We used the AMS-02 data of protons, helium, and the antiproton-over-proton ratio to understand CR propagation of light nuclei and derive constraints on the key parameters of the CR model which includes diffusion, reacceleration, and convection. In particular, we find that the parameter δ, which describes the energy dependence of magnetic turbulence in our Galaxy, is well constrained around a value of 0.4. The next logical step will be to extend the methods developed and applied in this thesis to heavier nuclei. AMS-02 provides the primary fluxes of carbon, nitrogen, and oxygen, as well as the secondary fluxes of helium three, lithium, beryllium and boron. The comparison of the results from antiprotons and light nuclei with those of heavier nuclei might help to answer open questions in CR physics. It might be possible to investigate better the behavior of the diffusion coefficient, for example, whether there are deviations from a pure power law at small rigidities and whether the approximation of homogeneous and isotropic diffusion is justified. Related questions concern the robustness of our conclusions on reacceleration and convection. More generally, one might even challenge common assumption on the importance reacceleration for CR propagation. Furthermore, the combination of various CR nuclei should allow to test the universality of CR injection, which is broken for proton and helium, for helium and heavier primary nuclei. This might help to better understand the sources of primary CR nuclei.

We have discussed the importance of the precise predictions of the secondary antiproton production cross sections for the correct interpretation of CR antiproton data. We have updated and compared the two most recent analytic cross-section parametrizations of antiproton production in proton-proton and proton-nucleus interactions exploiting newly available data from the high-energy experiments NA61 and LHCb. We found that the uncertainty of cross sections on the source term prediction exceeds the uncertainty in the antiproton flux measurement by AMS-02 and, consequently, provided guidelines for potential future measurements of antiproton production at collider or fixed-target experiments. Other production cross sections in CRs face similar or even larger uncertainties compared to antiprotons. It would hence be interesting to reinvestigate the secondary production of leptons which in many cases relies on MC prediction and is not data driven. The

situation for the production of secondary CR nuclei is even more involved. There is a huge number of cross sections for different isotopes in the projectile initial states and the final state products. A theoretical modeling is extremely challenging and data for many reactions is scarce. Therefore, the robustness of results derived from CR nuclei heavier than helium will be closely related to the understanding of nuclei inelastic and fragmentation cross sections.

Global fits to AMS-02 data of protons, helium, and the antiproton-over-proton ratio provide a powerful tool to search for DM in our Galaxy. We assume that DM annihilation produces antiprotons with an energy spectrum depending on the elementary annihilation process. In our fits we found a hint for DM annihilation into hadronic SM final states. The potential DM particle requires a mass between 30 and 200 GeV, and an annihilation cross section of the order of 3×10^{-26} cm^3/s. The significance of this putative signal in CR antiprotons is found to be at the level of 2.7σ after accounting for uncertainties in the antiproton production cross section. Moreover, we have quantified the impact of correlations in the systematic uncertainties of the AMS-02 flux data. Realistic assumptions for the correlation seem to increase the significance. As the statistical precision of long-term, space-based CR experiments increases, systematic uncertainties become more relevant. These uncertainties are expected to exhibit strong correlations for all nuclei and leptons, which are typically not stated by the CR experiments. Modeling correctly the correlations in the CR data will be crucial to fully exploit the potential of the precise data and to prevent biased conclusions. A more robust assessment of the potential DM signal in the future should rely on a more detailed study of solar modulation. The time-dependent flux data of various leptons and nuclei by AMS-02 is expected to lead to better modeling of solar modulation beyond the force-field approximation. Also, a consistent picture of CR propagation of the light and heavier nuclei, as mentioned in the previous paragraph, would be important to increase the confidence in the putative signal.
If we interpret the results of our global fits to CR protons, helium, and the antiproton-over-proton ratio in terms of upper limits on the annihilation cross section, we obtain strong bounds for hadronic SM final states and DM masses above 200 GeV. The bounds are competitive and complementary to constraints on DM from gamma-ray observation of dSphs and the Galactic center.

The search for low-energy antideuteron or antihelium in CRs is the most direct and complementary strategy to search indirectly for DM. We have derived the expected antinuclei fluxes which correspond to the DM hint in CR antiprotons. This is the largest possible flux of antinuclei which is consistent with CR antiproton data of AMS-02. We found that the expected antideuteron flux is within the sensitivity of AMS-02 and the future experiment GAPS, while the antihelium flux stays always below the AMS-02 sensitivity. Moreover, we have updated the predictions of the secondary and tertiary fluxes of both antinuclei. They are out of reach for both experiments. The largest uncertainty in the prediction of antinuclei fluxes are the coalescence models for the formation of antinuclei from antiprotons and antineutrons. One important challenge, from the experimental point of view, will be a measurement of the correlations in the simultaneous production of an antiproton and an antineutron in proton-proton collisions or Z-boson decays, which could be used to improve the coalescence models.

Furthermore, gamma rays provide an excellent prospect to search for potential DM signals. In contrast to charged CRs, the indirect DM search in gamma rays can be concentrated on regions with either a large DM density or a low astrophysical background, as for example the Galactic center

or dSphs, respectively. Also gamma rays at high galactic latitude can be used to search for DM. In any case, the expected DM signals are very small and challenging to detect. One interesting approach is to correlate the extragalactic gamma-ray sky with gravitational tracers of matter, such as provided by on-going and future experiments of galaxy surveys, weak lensing, or HI intensity mapping. We have studied the properties of the extragalactic gamma-ray sky exploiting two unique tools which provide information about gamma-ray sources with very small fluxes. More explicitly, we have applied the technique of the one-point statistics of photon counts on recent Fermi-LAT data at high latitudes and we have used the latest Fermi-LAT measurement of the angular correlations in the UGRB to learn more about the properties of point sources at very small fluxes, which are below the detection threshold of the Fermi-LAT. Comparing these properties to a model of the GLF of blazars, we found that the emission of gamma rays at high latitudes and small fluxes is consistent with a pure blazar population. A further refinement of the statistical tools, as for example a study of the one-point statistics of photon counts in different energy bins, might allow an even better understanding of blazar models at small fluxes. We can also imagine a comprehensive fit of the one-point statistics, angular correlations, and cross correlations in the future.

The search for DM is an interdisciplinary effort and an unambiguous answer concerning the nature of DM can only be achieved by combining the information of different observations. This thesis is focussed on different signatures and strategies for indirect detection of DM with CRs and gamma rays. These messengers from astrophysics provide complementary informations and constraints. Finally, they have to be completed with information from particle physics and cosmology.

Acknowledgements

I am thankful to Prof. Fiorenza Donato and Prof. Dr. Michael Krämer for supervising this work. They gave me the opportunity to investigate interesting topics and always supported my work. Their great experience and enthusiasm for physics inspired me and pushed this work to what is presented in this thesis. Furthermore, I would like to thank my colleagues: Silvia Manconi, Alessandro Cuoco, Mattia Di Mauro, Nicolao Fornengo, Jan Heisig, Lukas Klamt, Marco Regis, and Hannes Zechlin for many discussions and a lot of assistance during various projects.

My special gratitude goes to Fiorenza. She was always available to answer countless questions with patience. In difficult situations, she always had excellent advice. Thank you so very much.

I would like to thank all members of the astroparticle group Turin and TTK in Aachen for support and fruitful discussions. I acknowledge the translation of my abstract to Italian by Marco Taoso and the careful reading of the manuscript by Fiorenza, Silvia, Alessandro, Jan, Marco, and Sandro. I am thankful to Philip Mertsch, Pasquale Serpico, and Andrew Strong for examining this work.

Finally, I would like to thank all the theoretical PhD fellows from the *Bunker* for warmly welcoming me to Torino. You helped me a lot to find my way in the new environment. Many thanks to all my friends, who succeeded to distract me from my challenges at work and, thus, allowed me to gather new motivation. My family deserves a special gratitude. You always showed great interest in my work and found comforting words in challenging times. Insbesondere danke ich an dieser Stelle auch meinen Eltern und meiner Schwester. Ohne Eure Unterstüzung wäre ich nie so weit gekommen.

Eidesstattliche Erklärung

Michael Korsmeier erklärt hiermit, dass diese Dissertation und die darin dargelegten Inhalte die eigenen sind und selbstständig, als Ergebnis der eigenen originären Forschung, generiert wurden.

Hiermit erkläre ich an Eides statt:

1. Diese Arbeit wurde vollständig in der Phase als Doktorand dieser Fakultät und Universität angefertigt;
2. Sofern irgendein Bestandteil dieser Dissertation zuvor für einen akademischen Abschluss oder eine andere Qualifikation an dieser oder einer anderen Institution verwendet wurde, wurde dies klar angezeigt;
3. Wenn immer andere eigene oder Veröffentlichungen Dritter herangezogen wurden, wurden diese klar benannt;
4. Wenn aus anderen eigenen oder Veröffentlichungen Dritter zitiert wurde, wurde stets die Quelle hierfür angegeben. Diese Dissertation ist vollständig meine eigene Arbeit, mit der Ausnahme solcher Zitate;
5. Alle wesentlichen Quellen von Unterstützung wurden benannt;
6. Wenn immer ein Teil dieser Dissertation auf der Zusammenarbeit mit anderen basiert, wurde von mir klar gekennzeichnet, was von anderen und was von mir selbst erarbeitet wurde;
7. Kein Teil dieser Arbeit wurde vor deren Einreichung veröffentlicht.

September 9, 2022

Michael Korsmeier

Bibliography

[1] S. Manconi, M. Korsmeier, F. Donato, N. Fornengo, M. Regis and H. Zechlin, *Testing gamma-ray models of blazars in the extragalactic sky*, 1912.01622. (Cited on pages v, 157, 158, 160, 161, 162, and 163.)

[2] A. Cuoco, J. Heisig, L. Klamt, M. Korsmeier and M. Krämer, *Scrutinizing the evidence for dark matter in cosmic-ray antiprotons*, *Phys. Rev.* **D99** (2019) 103014 [1903.01472]. (Cited on pages v, 38, 94, 99, 100, 101, 102, 109, 110, 111, 112, 115, 117, and 118.)

[3] M. Korsmeier, F. Donato and M. Di Mauro, *Production cross sections of cosmic antiprotons in the light of new data from the NA61 and LHCb experiments*, *Phys. Rev.* **D97** (2018) 103019 [1802.03030]. (Cited on pages v, 30, 34, 67, 71, 72, 73, 74, 78, 79, 80, 81, 83, 91, and 106.)

[4] M. Korsmeier, F. Donato and N. Fornengo, *Prospects to verify a possible dark matter hint in cosmic antiprotons with antideuterons and antihelium*, *Phys. Rev.* **D97** (2018) 103011 [1711.08465]. (Cited on pages v, 42, 140, 144, 145, and 148.)

[5] A. Cuoco, J. Heisig, M. Korsmeier and M. Krämer, *Constraining heavy dark matter with cosmic-ray antiprotons*, *JCAP* **1804** (2018) 004 [1711.05274]. (Cited on pages v, 37, 38, 94, 131, 133, 134, 136, and 141.)

[6] A. Cuoco, J. Heisig, M. Korsmeier and M. Krämer, *Probing dark matter annihilation in the Galaxy with antiprotons and gamma rays*, *JCAP* **1710** (2017) 053 [1704.08258]. (Cited on pages v, 93, 94, 120, 121, 124, 127, 130, 139, 146, and 147.)

[7] F. Donato, M. Korsmeier and M. Di Mauro, *Prescriptions on antiproton cross section data for precise theoretical antiproton flux predictions*, *Phys. Rev.* **D96** (2017) 043007 [1704.03663]. (Cited on pages v, 31, 32, 33, 36, 67, 85, 87, 88, 89, and 90.)

[8] A. Cuoco, M. Krämer and M. Korsmeier, *Novel Dark Matter Constraints from Antiprotons in Light of AMS-02*, *Phys. Rev. Lett.* **118** (2017) 191102 [1610.03071]. (Cited on pages v, 38, 93, 97, 103, 120, 139, 141, 142, 143, 144, 145, 146, and 148.)

[9] M. Korsmeier and A. Cuoco, *Galactic cosmic-ray propagation in the light of AMS-02: Analysis of protons, helium, and antiprotons*, *Phys. Rev.* **D94** (2016) 123019 [1607.06093]. (Cited on pages v, 94, 95, 97, and 99.)

[10] C. N. Yang and R. L. Mills, *Conservation of Isotopic Spin and Isotopic Gauge Invariance*, *Physical Review* **96** (1954) 191. (Cited on page 3.)

[11] S. L. Glashow, *Partial-symmetries of weak interactions*, *Nuclear Physics* **22** (1961) 579. (Cited on page 3.)

[12] F. Englert and R. Brout, *Broken Symmetry and the Mass of Gauge Vector Mesons*, *Physical Review Letters* **13** (1964) 321. (Cited on page 3.)

[13] P. W. Higgs, *Broken Symmetries and the Masses of Gauge Bosons*, *Physical Review Letters* **13** (1964) 508. (Cited on page 3.)

[14] S. Weinberg, *A Model of Leptons*, *Physical Review Letters* **19** (1967) 1264. (Cited on page 3.)

[15] A. Salam, *Weak and Electromagnetic Interactions*, *Conf. Proc.* **C680519** (1968) 367. (Cited on page 3.)

[16] A. Einstein, *Die Grundlage der allgemeinen Relativitätstheorie [AdP 49, 769 (1916)]*, *Annalen der Physik* **517** (2005) 517. (Cited on page 3.)

[17] A. Einstein, *Kosmologische Betrachtungen zur allgemeinen Relativitätstheorie*, *Sitzungsberichte der Königlich Preußischen Akademie der Wissenschaften (Berlin* (1917) 142. (Cited on page 3.)

[18] A. Friedmann, *Über die Krümmung des Raumes*, *Zeitschrift fur Physik* **10** (1922) 377. (Cited on page 3.)

[19] A. Friedmann, *Über die Möglichkeit einer Welt mit konstanter negativer Krümmung des Raumes*, *Zeitschrift fur Physik* **21** (1924) 326. (Cited on page 3.)

[20] G. Lemaître, *Expansion of the universe, A homogeneous universe of constant mass and increasing radius accounting for the radial velocity of extra-galactic nebulae*, *Monthly Notices of the RAS* **91** (1931) 483. (Cited on page 3.)

[21] H. P. Robertson, *Kinematics and World-Structure*, *Astrophysical Journal* **82** (1935) 284. (Cited on page 3.)

[22] H. P. Robertson, *Kinematics and World-Structure II.*, *Astrophysical Journal* **83** (1936) 187. (Cited on page 3.)

[23] H. P. Robertson, *Kinematics and World-Structure III.*, *Astrophysical Journal* **83** (1936) 257. (Cited on page 3.)

[24] A. G. Walker, *On Milne's Theory of World-Structure*, *Proceedings of the London Mathematical Society* **42** (1937) 90. (Cited on page 3.)

[25] Planck collaboration, *Planck 2018 results. VI. Cosmological parameters*, 1807.06209. (Cited on pages 4, 5, 10, and 60.)

[26] E. W. Kolb and M. S. Turner, *The early universe*, vol. 69. 1990. (Cited on pages 4 and 7.)

[27] S. Weinberg, *Cosmology*. 2008. (Cited on page 4.)

[28] G. Bertone et al., *Particle Dark Matter*. Cambridge University Press, 2013. (Cited on page 4.)

[29] F. Zwicky, *Die Rotverschiebung von extragalaktischen Nebeln*, *Helv. Phys. Acta* **6** (1933) 110. (Cited on page 4.)

[30] E. Hubble and M. L. Humason, *The Velocity-Distance Relation among Extra-Galactic Nebulae*, *Astrophys. J.* **74** (1931) 43. (Cited on page 4.)

[31] V. C. Rubin and W. K. Ford, Jr., *Rotation of the Andromeda Nebula from a Spectroscopic Survey of Emission Regions*, *Astrophys. J.* **159** (1970) 379. (Cited on page 4.)

[32] D. Clowe, A. Gonzalez and M. Markevitch, *Weak lensing mass reconstruction of the interacting cluster 1E0657-558: Direct evidence for the existence of dark matter*, *Astrophys. J.* **604** (2004) 596 [astro-ph/0312273]. (Cited on page 5.)

[33] M. Tegmark and M. Zaldarriaga, *Separating the early universe from the late universe: Cosmological parameter estimation beyond the black box*, *Phys. Rev.* **D66** (2002) 103508 [astro-ph/0207047]. (Cited on page 5.)

[34] E. Di Dio, F. Montanari, J. Lesgourgues and R. Durrer, *The CLASSgal code for Relativistic Cosmological Large Scale Structure*, *JCAP* **1311** (2013) 044 [1307.1459]. (Cited on page 5.)

[35] V. Springel, C. S. Frenk and S. D. M. White, *The large-scale structure of the Universe*, *Nature* **440** (2006) 1137 [astro-ph/0604561]. (Cited on pages 5 and 6.)

[36] M. Vogelsberger, S. Genel, V. Springel, P. Torrey, D. Sijacki, D. Xu et al., *Introducing the Illustris Project: Simulating the coevolution of dark and visible matter in the Universe*, *Mon. Not. Roy. Astron. Soc.* **444** (2014) 1518 [1405.2921]. (Cited on pages 5 and 6.)

[37] Planck collaboration, *Planck 2015 results. XIII. Cosmological parameters*, *Astron. Astrophys.* **594** (2016) A13 [1502.01589]. (Cited on pages 5, 126, and 135.)

[38] A. Burkert, *The Structure of dark matter halos in dwarf galaxies*, *IAU Symp.* **171** (1996) 175 [astro-ph/9504041]. (Cited on page 5.)

[39] J. F. Navarro, C. S. Frenk and S. D. M. White, *The Structure of cold dark matter halos*, *Astrophys. J.* **462** (1996) 563 [astro-ph/9508025]. (Cited on pages 6 and 141.)

[40] J. Einasto, *On the Construction of a Composite Model for the Galaxy and on the Determination of the System of Galactic Parameters*, *Trudy Astrofizicheskogo Instituta Alma-Ata* **5** (1965) 87. (Cited on pages 6 and 134.)

[41] P. Salucci, F. Nesti, G. Gentile and C. F. Martins, *The dark matter density at the Sun's location*, *Astron. Astrophys.* **523** (2010) A83 [1003.3101]. (Cited on pages 6, 96, 120, and 141.)

[42] R. D. Peccei and H. R. Quinn, *CP Conservation in the Presence of Instantons*, *Phys. Rev. Lett.* **38** (1977) 1440. (Cited on page 6.)

[43] D. J. E. Marsh, *Axion Cosmology*, *Phys. Rept.* **643** (2016) 1 [1510.07633]. (Cited on page 6.)

[44] P. W. Graham, I. G. Irastorza, S. K. Lamoreaux, A. Lindner and K. A. van Bibber, *Experimental Searches for the Axion and Axion-Like Particles*, *Ann. Rev. Nucl. Part. Sci.* **65** (2015) 485 [1602.00039]. (Cited on page 6.)

[45] Particle Data Group collaboration, *Review of Particle Physics, Chapter 111. Axions and Other Similar Particles, (Revised by A. Ringwald, L.J Rosenberg and G. Rybka)*, *Phys. Rev.* **D98** (2018) 030001. (Cited on page 6.)

[46] G. Jungman, M. Kamionkowski and K. Griest, *Supersymmetric dark matter*, *Phys. Rept.* **267** (1996) 195 [hep-ph/9506380]. (Cited on page 6.)

[47] S. P. Martin, *A Supersymmetry primer*, hep-ph/9709356. (Cited on page 6.)

[48] G. Bertone, D. Hooper and J. Silk, *Particle dark matter: Evidence, candidates and constraints*, *Phys. Rept.* **405** (2005) 279 [hep-ph/0404175]. (Cited on page 7.)

[49] J. L. Feng, *Dark Matter Candidates from Particle Physics and Methods of Detection*, *Ann. Rev. Astron. Astrophys.* **48** (2010) 495 [1003.0904]. (Cited on page 7.)

[50] M. Bauer and T. Plehn, *Yet Another Introduction to Dark Matter*, *Lect. Notes Phys.* **959** (2019) pp. [1705.01987]. (Cited on page 7.)

[51] V. F. Hess, *Über Beobachtungen der durchdringenden Strahlung bei sieben Freiballonfahrten*, *Phys. Z.* **13** (1912) 1084. (Cited on page 13.)

[52] A. H. Compton, *Variation of the Cosmic Rays with Latitude*, *Physical Review* **41** (1932) 111. (Cited on page 13.)

[53] C. D. Anderson, *The Positive Electron*, *Physical Review* **43** (1933) 491. (Cited on page 13.)

[54] S. H. Neddermeyer and C. D. Anderson, *Note on the Nature of Cosmic-Ray Particles*, *Physical Review* **51** (1937) 884. (Cited on page 13.)

[55] C. M. G. Lattes, G. P. S. Occhialini and C. F. Powell, *Observations on the Tracks of Slow Mesons in Photographic Emulsions*, *Nature* **160** (1947) 453. (Cited on page 13.)

[56] G. D. Rochester and C. C. Butler, *Evidence for the Existence of New Unstable Elementary Particles*, *Nature* **160** (1947) 855. (Cited on page 13.)

[57] PAMELA collaboration, *PAMELA Measurements of Cosmic-ray Proton and helium Spectra*, *Science* **332** (2011) 69 [1103.4055]. (Cited on pages 14, 15, and 29.)

[58] AMS collaboration, *Precision Measurement of the Proton Flux in Primary Cosmic Rays from Rigidity 1 GV to 1.8 TV with the Alpha Magnetic Spectrometer on the International Space Station*, *Phys. Rev. Lett.* **114** (2015) 171103. (Cited on pages 14, 15, 29, 72, 94, 97, and 142.)

[59] AMS collaboration, *Precision Measurement of the helium Flux in Primary Cosmic Rays of Rigidities 1.9 GV to 3 TV with the Alpha Magnetic Spectrometer on the International Space Station*, *Phys. Rev. Lett.* **115** (2015) 211101. (Cited on pages 14, 15, 29, 80, 94, 97, and 142.)

[60] AMS collaboration, *Electron and Positron Fluxes in Primary Cosmic Rays Measured with the Alpha Magnetic Spectrometer on the International Space Station*, *Phys. Rev. Lett.* **113** (2014) 121102. (Cited on pages 14 and 15.)

[61] DAMPE Collaboration, G. Ambrosi, Q. An, R. Asfand iyarov, P. Azzarello, P. Bernardini et al., *Direct detection of a break in the teraelectronvolt cosmic-ray spectrum of electrons and positrons*, *Nature* **552** (2017) 63 [1711.10981]. (Cited on page 14.)

[62] T. K. Gaisser, T. Stanev and S. Tilav, *Cosmic Ray Energy Spectrum from Measurements of Air Showers*, *Front. Phys.(Beijing)* **8** (2013) 748 [1303.3565]. (Cited on page 14.)

[63] S. Manconi, *Unveiling Universes's cosmic messengers*, Ph.D. thesis, Scuola di Dottorato Universitá di Torino, 2019. (Cited on page 14.)

[64] K. Greisen, *End to the cosmic-ray spectrum?*, *Phys. Rev. Lett.* **16** (1966) 748. (Cited on page 15.)

[65] G. T. Zatsepin and V. A. Kuzmin, *Upper limit of the spectrum of cosmic rays*, *Journal of Experimental and Theoretical Physics Letters* **4** (1966) 78. (Cited on page 15.)

[66] PAMELA collaboration, *An anomalous positron abundance in cosmic rays with energies 1.5-100 GeV*, *Nature* **458** (2009) 607 [0810.4995]. (Cited on page 15.)

[67] PAMELA collaboration, *The cosmic-ray electron flux measured by the PAMELA experiment between 1 and 625 GeV*, *Phys. Rev. Lett.* **106** (2011) 201101 [1103.2880]. (Cited on page 15.)

[68] AMS collaboration, *First Result from the Alpha Magnetic Spectrometer on the International Space Station: Precision Measurement of the Positron Fraction in Primary Cosmic Rays of 0.5–350 GeV*, *Phys. Rev. Lett.* **110** (2013) 141102. (Cited on page 15.)

[69] AMS collaboration, *Precision Measurement of the $(e^+ + e^-)$ Flux in Primary Cosmic Rays from 0.5 GeV to 1 TeV with the Alpha Magnetic Spectrometer on the International Space Station*, *Phys. Rev. Lett.* **113** (2014) 221102. (Cited on page 15.)

[70] AMS collaboration, *Towards Understanding the Origin of Cosmic-Ray Electrons*, *Phys. Rev. Lett.* **122** (2019) 101101. (Cited on page 15.)

[71] O. Adriani et al., *Measurement of boron and carbon fluxes in cosmic rays with the PAMELA experiment*, *Astrophys. J.* **791** (2014) 93 [1407.1657]. (Cited on page 15.)

[72] AMS collaboration, *Precision Measurement of the Boron to Carbon Flux Ratio in Cosmic Rays from 1.9 GV to 2.6 TV with the Alpha Magnetic Spectrometer on the International Space Station*, *Phys. Rev. Lett.* **117** (2016) 231102. (Cited on pages 15, 28, and 29.)

[73] AMS collaboration, *Observation of the Identical Rigidity Dependence of He, C, and O Cosmic Rays at High Rigidities by the Alpha Magnetic Spectrometer on the International Space Station*, *Phys. Rev. Lett.* **119** (2017) 251101. (Cited on pages 15, 29, and 80.)

[74] AMS collaboration, *Observation of New Properties of Secondary Cosmic Rays Lithium, Beryllium, and Boron by the Alpha Magnetic Spectrometer on the International Space Station*, *Phys. Rev. Lett.* **120** (2018) 021101. (Cited on pages 15, 25, and 80.)

[75] AMS collaboration, *Antiproton Flux, Antiproton-to-Proton Flux Ratio, and Properties of Elementary Particle Fluxes in Primary Cosmic Rays Measured with the Alpha Magnetic Spectrometer on the International Space Station*, *Phys. Rev. Lett.* **117** (2016) 091103. (Cited on pages 16, 85, 94, 97, 99, and 142.)

[76] E. Fermi, *On the Origin of the Cosmic Radiation*, *Phys. Rev.* **75** (1949) 1169. (Cited on page 17.)

[77] A. R. Bell, *The acceleration of cosmic rays in shock fronts - I.*, *Monthly Notices of the RAS* **182** (1978) 147. (Cited on page 19.)

[78] A. R. Bell, *The acceleration of cosmic rays in shock fronts - II.*, *Monthly Notices of the RAS* **182** (1978) 443. (Cited on page 19.)

[79] L. O. Drury, *An introduction to the theory of diffusive shock acceleration of energetic particles in tenuous plasmas*, *Rept. Prog. Phys.* **46** (1983) 973. (Cited on page 19.)

[80] V. L. Ginzburg and S. I. Syrovatskii, *The Origin of Cosmic Rays*. 1964. (Cited on page 21.)

[81] A. W. Strong, I. V. Moskalenko and V. S. Ptuskin, *Cosmic-ray propagation and interactions in the Galaxy*, *Ann. Rev. Nucl. Part. Sci.* **57** (2007) 285 [astro-ph/0701517]. (Cited on page 21.)

[82] V. S. Berezinskii, S. V. Bulanov, V. A. Dogiel and V. S. Ptuskin, *Astrophysics of cosmic rays*. 1990. (Cited on pages 21 and 24.)

[83] V. A. Dogiel, V. S. Berezinsky, S. V. Bulanov and V. S. Ptuskin, *Astrophysics of cosmic rays*. Elsevier Since Publischers B.V., 1990. (Cited on page 21.)

[84] E. S. Seo and V. S. Ptuskin, *Stochastic reacceleration of cosmic rays in the interstellar medium*, *Astrophys. J.* **431** (1994) 705. (Cited on page 21.)

[85] L. O. Drury and A. W. Strong, *Power requirements for cosmic ray propagation models involving diffusive reacceleration; estimates and implications for the damping of interstellar turbulence*, *Astron. Astrophys.* **597** (2017) A117 [1608.04227]. (Cited on page 22.)

[86] V. S. Ptuskin, I. V. Moskalenko, F. C. Jones, A. W. Strong and V. N. Zirakashvili, *Dissipation of magnetohydrodynamic waves on energetic particles: impact on interstellar turbulence and cosmic ray transport*, *Astrophys. J.* **642** (2006) 902 [astro-ph/0510335]. (Cited on page 22.)

[87] A. W. Strong, I. V. Moskalenko and O. Reimer, *Diffuse continuum gamma-rays from the galaxy*, *Astrophys. J.* **537** (2000) 763 [astro-ph/9811296]. (Cited on pages 22 and 85.)

[88] A. W. Strong, *Recent extensions to GALPROP*, 1507.05020. (Cited on pages 22 and 85.)

[89] C. Evoli, D. Gaggero, A. Vittino, G. Di Bernardo, M. Di Mauro, A. Ligorini et al., *Cosmic-ray propagation with DRAGON2: I. numerical solver and astrophysical ingredients*, *JCAP* **1702** (2017) 015 [1607.07886]. (Cited on page 22.)

[90] R. Kissmann, *PICARD: A novel code for the Galactic Cosmic Ray propagation problem*, *Astroparticle Physics* **55** (2014) 37 [1401.4035]. (Cited on page 22.)

[91] D. Maurin, *USINE: semi-analytical models for Galactic cosmic-ray propagation*, 1807.02968. (Cited on page 22.)

[92] R. Taillet and D. Maurin, *Spatial origin of galactic cosmic rays in diffusion models: 1. Standard sources in the galactic disk*, *Astron. Astrophys.* **402** (2003) 971 [astro-ph/0212112]. (Cited on page 24.)

[93] A. Putze, L. Derome, D. Maurin, L. Perotto and R. Taillet, *A Markov Chain Monte Carlo for Galactic Cosmic Ray physics: I. Method and results for the Leaky Box Model*, *Astron. Astrophys.* **497** (2009) 991 [0808.2437]. (Cited on page 24.)

[94] D. Maurin, R. Taillet, F. Donato, P. Salati, A. Barrau and G. Boudoul, *Galactic cosmic ray nuclei as a tool for astroparticle physics*, astro-ph/0212111. (Cited on pages 24 and 142.)

[95] L. Derome, D. Maurin, P. Salati, M. Boudaud, Y. Génolini and P. Kunzé, *Fitting B/C cosmic-ray data in the AMS-02 era: A cookbook*, *Astron. Astrophys.* **627** (2019) A158 [1904.08210]. (Cited on pages 25, 26, 28, and 114.)

[96] G. L. Case and D. Bhattacharya, *A new sigma-d relation and its application to the galactic supernova remnant distribution*, *Astrophys. J.* **504** (1998) 761 [astro-ph/9807162]. (Cited on pages 26 and 95.)

[97] D. A. Green, *Constraints on the distribution of supernova remnants with Galactocentric radius*, *Mon. Not. Roy. Astron. Soc.* **454** (2015) 1517 [1508.02931]. (Cited on pages 26 and 95.)

[98] J. S. George, K. A. Lave, M. E. Wiedenbeck, W. R. Binns, A. C. Cummings, A. J. Davis et al., *Elemental Composition and Energy Spectra of Galactic Cosmic Rays During Solar Cycle 23*, *Astrophys. J.* **698** (2009) 1666. (Cited on page 27.)

[99] C. H. Tsao, R. Silberberg, A. F. Barghouty and L. Sihver, *Energy Degradation in Cosmic-Ray Nuclear Spallation Reactions: Relaxing the Straight-ahead Approximation*, *Astrophys. J.* **451** (1995) 275. (Cited on page 27.)

[100] Y. Genolini, D. Maurin, I. V. Moskalenko and M. Unger, *Current status and desired precision of the isotopic production cross sections relevant to astrophysics of cosmic rays: Li, Be, B, C, and N*, *Phys. Rev.* **C98** (2018) 034611 [1803.04686]. (Cited on page 27.)

[101] E. G. Berezhko, L. T. Ksenofontov, V. S. Ptuskin, V. N. Zirakashvili and H. J. Völk, *Cosmic ray production in supernova remnants including reacceleration: The secondary to primary ratio*, *Astronomy and Astrophysics* **410** (2003) 189 [astro-ph/0308199]. (Cited on page 27.)

[102] P. Blasi and P. D. Serpico, *High-energy antiprotons from old supernova remnants*, *Phys. Rev. Lett.* **103** (2009) 081103 [0904.0871]. (Cited on page 27.)

[103] P. Mertsch and S. Sarkar, *AMS-02 data confront acceleration of cosmic ray secondaries in nearby sources*, *Phys. Rev.* **D90** (2014) 061301 [1402.0855]. (Cited on page 27.)

[104] V. Bresci, E. Amato, P. Blasi and G. Morlino, *Effects of re-acceleration and source grammage on secondary cosmic rays spectra*, *Mon. Not. Roy. Astron. Soc.* **488** (2019) 2068 [1904.10282]. (Cited on page 27.)

[105] N. Tomassetti and F. Donato, *Secondary cosmic-ray nuclei from supernova remnants and constraints on the propagation parameters*, *Astronomy and Astrophysics* **544** (2012) A16 [1203.6094]. (Cited on page 28.)

[106] I. Cholis and D. Hooper, *Constraining the origin of the rising cosmic ray positron fraction with the boron-to-carbon ratio*, *Phys. Rev.* **D89** (2014) 043013 [1312.2952]. (Cited on page 28.)

[107] Y. Génolini et al., *Cosmic-ray transport from AMS-02 boron to carbon ratio data: Benchmark models and interpretation*, *Phys. Rev.* **D99** (2019) 123028 [1904.08917]. (Cited on pages 28, 101, and 114.)

[108] I. V. Moskalenko, S. G. Mashnik and A. W. Strong, *New calculation of radioactive secondaries in cosmic rays*, in *27th International Cosmic Ray Conference (ICRC 2001) Hamburg, Germany, August 7-15, 2001*, p. 1836, 2001, astro-ph/0106502. (Cited on page 29.)

[109] A. Putze, L. Derome and D. Maurin, *A Markov Chain Monte Carlo technique to sample transport and source parameters of Galactic cosmic rays: II. Results for the diffusion model combining B/C and radioactive nuclei*, *Astron. Astrophys.* **516** (2010) A66 [1001.0551]. (Cited on page 29.)

[110] C. Evoli, G. Morlino, P. Blasi and R. Aloisio, *The AMS-02 beryllium and its implication for Cosmic Ray transport*, 1910.04113. (Cited on pages 29, 118, and 143.)

[111] Y. Génolini et al., *Indications for a high-rigidity break in the cosmic-ray diffusion coefficient*, *Phys. Rev. Lett.* **119** (2017) 241101 [1706.09812]. (Cited on page 29.)

[112] P. Blasi, E. Amato and P. D. Serpico, *Spectral breaks as a signature of cosmic ray induced turbulence in the Galaxy*, *Phys. Rev. Lett.* **109** (2012) 061101 [1207.3706]. (Cited on page 29.)

[113] R. Aloisio, P. Blasi and P. Serpico, *Nonlinear cosmic ray Galactic transport in the light of AMS-02 and Voyager data*, *Astron. Astrophys.* **583** (2015) A95 [1507.00594]. (Cited on page 29.)

[114] C. Evoli, P. Blasi, G. Morlino and R. Aloisio, *Origin of the Cosmic Ray Galactic Halo Driven by Advected Turbulence and Self-Generated Waves*, *Phys. Rev. Lett.* **121** (2018) 021102 [1806.04153]. (Cited on page 29.)

[115] M. Di Mauro, F. Donato, N. Fornengo, R. Lineros and A. Vittino, *Interpretation of AMS-02 electrons and positrons data*, *JCAP* **1404** (2014) 006 [1402.0321]. (Cited on pages 31, 118, and 143.)

[116] R. Kappl and M. W. Winkler, *The Cosmic Ray Antiproton Background for AMS-02*, *JCAP* **1409** (2014) 051 [1408.0299]. (Cited on pages 31, 35, and 36.)

[117] M. di Mauro, F. Donato, A. Goudelis and P. D. Serpico, *New evaluation of the antiproton production cross section for cosmic ray studies*, *Phys. Rev.* **D90** (2014) 085017 [1408.0288]. (Cited on pages 32, 33, 35, 36, 67, 71, 73, 86, 89, 96, 129, 132, and 140.)

[118] NA49 collaboration, *Baryon yields, isospin effects and strangeness production in elementary hadronic interactions*, *Acta Phys. Hung.* **A17** (2003) 369. (Cited on page 32.)

[119] M. W. Winkler, *Cosmic Ray Antiprotons at High Energies*, *JCAP* **1702** (2017) 048 [1701.04866]. (Cited on pages 33, 34, 35, 36, 37, 67, 68, 69, 71, 73, 75, 79, 81, 83, 89, 96, 103, 129, 132, and 133.)

[120] LHCb collaboration, *Measurement of antiproton production in pHe collisions at sqrts = 110 GeV*, in *52nd Rencontres de Moriond*, 2017, https://cds.cern.ch/record/2260835/files/LHCb-CONF-2017-002.pdf. (Cited on pages 34, 35, 67, and 76.)

[121] R. P. Duperray, C. Y. Huang, K. V. Protasov and M. Buenerd, *Parameterization of the antiproton inclusive production cross-section on nuclei*, *Phys. Rev.* **D68** (2003) 094017 [astro-ph/0305274]. (Cited on pages 34, 35, 36, 74, 89, and 129.)

[122] NA49 collaboration, *Inclusive production of protons, anti-protons, neutrons, deuterons and tritons in p+C collisions at 158 GeV/c beam momentum*, *Eur. Phys. J.* **C73** (2013) 2364 [1207.6520]. (Cited on pages 34, 75, and 76.)

[123] L. C. Tan and L. K. Ng, *Calculation of the equilibrium anti-proton spectrum*, *J. Phys.* **G9** (1983) 227. (Cited on pages 35, 36, 103, 120, 129, 132, and 133.)

[124] NA49 collaboration, *Inclusive production of protons, anti-protons and neutrons in p+p collisions at 158-GeV/c beam momentum*, *Eur. Phys. J.* **C65** (2010) 9 [0904.2708]. (Cited on pages 35, 69, 70, and 90.)

[125] NA61/SHINE collaboration, *Measurements of $\pi^{\pm}$, $K^{\pm}$, p and $\bar{p}$ spectra in proton-proton interactions at 20, 31, 40, 80 and 158 GeV/c with the NA61/SHINE spectrometer at the CERN SPS*, *Eur. Phys. J.* **C77** (2017) 671 [1705.02467]. (Cited on pages 35, 67, 69, and 70.)

[126] M. Simon, A. Molnar and S. Roesler, *A New Calculation of the Interstellar Secondary Cosmic-Ray Antiprotons*, *Astrophysical Journal* **499** (1998) 250. (Cited on page 35.)

[127] F. Donato, D. Maurin, P. Salati, A. Barrau, G. Boudoul and R. Taillet, *Anti-protons from spallations of cosmic rays on interstellar matter*, *Astrophys. J.* **563** (2001) 172 [astro-ph/0103150]. (Cited on page 35.)

[128] M. Kachelriess, I. V. Moskalenko and S. S. Ostapchenko, *New calculation of antiproton production by cosmic ray protons and nuclei*, *Astrophys. J.* **803** (2015) 54 [1502.04158]. (Cited on pages 35, 36, 71, 73, 79, 129, 132, and 133.)

[129] M. Kachelrieß, I. V. Moskalenko and S. Ostapchenko, *AAfrag: Interpolation routines for Monte Carlo results on secondary production in proton-proton, proton-nucleus and nucleus-nucleus interactions*, 1904.05129. (Cited on page 35.)

[130] F. E. Taylor, D. C. Carey, J. R. Johnson, R. Kammerud, D. J. Ritchie, A. Roberts et al., *An Analysis of Radial Scaling in Single Particle Inclusive Reactions*, *Phys. Rev.* **D14** (1976) 1217. (Cited on page 36.)

[131] R. P. Feynman, *Very high-energy collisions of hadrons*, *Phys. Rev. Lett.* **23** (1969) 1415. (Cited on page 36.)

[132] D. Maurin and R. Taillet, *Spatial origin of galactic cosmic rays in diffusion models: ii-exotic primary cosmic rays*, *Astron. Astrophys.* **404** (2003) 949 [astro-ph/0212113]. (Cited on pages 37 and 141.)

[133] F. Donato, N. Fornengo, D. Maurin and P. Salati, *Antiprotons in cosmic rays from neutralino annihilation*, *Phys. Rev.* **D69** (2004) 063501 [astro-ph/0306207]. (Cited on pages 37, 38, 141, 143, 144, and 148.)

[134] M.-Y. Cui, X. Pan, Q. Yuan, Y.-Z. Fan and H.-S. Zong, *Revisit of cosmic ray antiprotons from dark matter annihilation with updated constraints on the background model from AMS-02 and collider data*, *JCAP* **1806** (2018) 024 [1803.02163]. (Cited on page 38.)

[135] I. Cholis, T. Linden and D. Hooper, *A Robust Excess in the Cosmic-Ray Antiproton Spectrum: Implications for Annihilating Dark Matter*, *Phys. Rev.* **D99** (2019) 103026 [1903.02549]. (Cited on page 38.)

[136] A. Reinert and M. W. Winkler, *A Precision Search for WIMPs with Charged Cosmic Rays*, *JCAP* **1801** (2018) 055 [1712.00002]. (Cited on pages 38, 101, 106, and 113.)

[137] P. von Doetinchem et al., *Cosmic-ray Antinuclei as Messengers of New Physics: Status and Outlook for the New Decade*, 2002.04163. (Cited on page 38.)

[138] L. Bergstrom, J. Edsjo and P. Ullio, *Cosmic anti-protons as a probe for supersymmetric dark matter?*, *Astrophys. J.* **526** (1999) 215 [astro-ph/9902012]. (Cited on page 38.)

[139] T. Bringmann and P. Salati, *The galactic antiproton spectrum at high energies: Background expectation vs. exotic contributions*, *Phys. Rev.* **D75** (2007) 083006 [astro-ph/0612514]. (Cited on page 38.)

[140] F. Donato, D. Maurin, P. Brun, T. Delahaye and P. Salati, *Constraints on WIMP Dark Matter from the High Energy PAMELA $\bar{p}/p$ data*, *Phys. Rev. Lett.* **102** (2009) 071301 [0810.5292]. (Cited on page 38.)

[141] C. Evoli, I. Cholis, D. Grasso, L. Maccione and P. Ullio, *Antiprotons from dark matter annihilation in the Galaxy: astrophysical uncertainties*, *Phys. Rev.* **D85** (2012) 123511 [1108.0664]. (Cited on page 38.)

[142] N. Fornengo, L. Maccione and A. Vittino, *Constraints on particle dark matter from cosmic-ray antiprotons*, *JCAP* **1404** (2014) 003 [1312.3579]. (Cited on page 38.)

[143] D. Hooper, T. Linden and P. Mertsch, *What Does The PAMELA Antiproton Spectrum Tell Us About Dark Matter?*, *JCAP* **1503** (2015) 021 [1410.1527]. (Cited on page 38.)

[144] V. Pettorino, G. Busoni, A. De Simone, E. Morgante, A. Riotto and W. Xue, *Can AMS-02 discriminate the origin of an anti-proton signal?*, *JCAP* **1410** (2014) 078 [1406.5377]. (Cited on page 38.)

[145] M. Boudaud, M. Cirelli, G. Giesen and P. Salati, *A fussy revisitation of antiprotons as a tool for Dark Matter searches*, *JCAP* **1505** (2015) 013 [1412.5696]. (Cited on page 38.)

[146] J. A. R. Cembranos, V. Gammaldi and A. L. Maroto, *Antiproton signatures from astrophysical and dark matter sources at the galactic center*, *JCAP* **1503** (2015) 041 [1410.6689]. (Cited on page 38.)

[147] M. Cirelli, D. Gaggero, G. Giesen, M. Taoso and A. Urbano, *Antiproton constraints on the GeV gamma-ray excess: a comprehensive analysis*, *JCAP* **1412** (2014) 045 [1407.2173]. (Cited on page 38.)

[148] T. Bringmann, M. Vollmann and C. Weniger, *Updated cosmic-ray and radio constraints on light dark matter: Implications for the GeV gamma-ray excess at the Galactic center*, *Phys. Rev.* **D90** (2014) 123001 [1406.6027]. (Cited on page 38.)

[149] G. Giesen, M. Boudaud, Y. Genolini, V. Poulin, M. Cirelli, P. Salati et al., *AMS-02 antiprotons, at last! Secondary astrophysical component and immediate implications for Dark Matter*, *JCAP* **1509** (2015) 023 [1504.04276]. (Cited on pages 38 and 93.)

[150] C. Evoli, D. Gaggero and D. Grasso, *Secondary antiprotons as a Galactic Dark Matter probe*, *JCAP* **1512** (2015) 039 [1504.05175]. (Cited on page 38.)

[151] M.-Y. Cui, Q. Yuan, Y.-L. S. Tsai and Y.-Z. Fan, *Possible dark matter annihilation signal in the AMS-02 antiproton data*, *Phys. Rev. Lett.* **118** (2017) 191101 [1610.03840]. (Cited on pages 38 and 93.)

[152] M. Boudaud, Y. Génolini, L. Derome, J. Lavalle, D. Maurin, P. Salati et al., *AMS-02 antiprotons are consistent with a secondary astrophysical origin*, 1906.07119. (Cited on pages 39, 93, and 114.)

[153] P. Chardonnet, J. Orloff and P. Salati, *The Production of antimatter in our galaxy*, *Phys. Lett.* **B409** (1997) 313 [astro-ph/9705110]. (Cited on page 39.)

[154] F. Donato, N. Fornengo and P. Salati, *Anti-deuterons as a signature of supersymmetric dark matter*, *Phys. Rev.* **D62** (2000) 043003 [hep-ph/9904481]. (Cited on page 39.)

[155] R. Duperray, B. Baret, D. Maurin, G. Boudoul, A. Barrau, L. Derome et al., *Flux of light antimatter nuclei near Earth, induced by cosmic rays in the Galaxy and in the atmosphere*, *Phys. Rev.* **D71** (2005) 083013 [astro-ph/0503544]. (Cited on pages 39 and 140.)

[156] M. Kadastik, M. Raidal and A. Strumia, *Enhanced anti-deuteron Dark Matter signal and the implications of PAMELA*, *Phys. Lett.* **B683** (2010) 248 [0908.1578]. (Cited on page 39.)

[157] A. Ibarra and S. Wild, *Determination of the Cosmic Antideuteron Flux in a Monte Carlo approach*, *Phys. Rev.* **D88** (2013) 023014 [1301.3820]. (Cited on page 39.)

[158] C. B. Brauninger and M. Cirelli, *Anti-deuterons from heavy Dark Matter*, *Phys. Lett.* **B678** (2009) 20 [0904.1165]. (Cited on page 39.)

[159] N. Fornengo, L. Maccione and A. Vittino, *Dark matter searches with cosmic antideuterons: status and perspectives*, *JCAP* **1309** (2013) 031 [1306.4171]. (Cited on pages 39, 44, 45, 141, and 145.)

[160] L. A. Dal and A. R. Raklev, *Antideuteron Limits on Decaying Dark Matter with a Tuned Formation Model*, *Phys. Rev.* **D89** (2014) 103504 [1402.6259]. (Cited on page 39.)

[161] J. Herms, A. Ibarra, A. Vittino and S. Wild, *Antideuterons in cosmic rays: sources and discovery potential*, *JCAP* **1702** (2017) 018 [1610.00699]. (Cited on page 39.)

[162] K. Blum, K. C. Y. Ng, R. Sato and M. Takimoto, *Cosmic rays, antihelium, and an old navy spotlight*, *Phys. Rev.* **D96** (2017) 103021 [1704.05431]. (Cited on page 39.)

[163] M. Kachelrieß, S. Ostapchenko and J. Tjemsland, *Alternative coalescence model for deuteron, tritium, helium-3 and their antinuclei*, *Eur. Phys. J.* **A56** (2020) 4 [1905.01192]. (Cited on page 39.)

[164] M. Cirelli, N. Fornengo, M. Taoso and A. Vittino, *Anti-helium from Dark Matter annihilations*, *JHEP* **08** (2014) 009 [1401.4017]. (Cited on pages 39, 142, and 149.)

[165] F. Donato, N. Fornengo and D. Maurin, *Antideuteron fluxes from dark matter annihilation in diffusion models*, *Phys. Rev.* **D78** (2008) 043506 [0803.2640]. (Cited on pages 39 and 142.)

[166] H. Fuke et al., *Search for cosmic-ray antideuterons*, *Phys. Rev. Lett.* **95** (2005) 081101 [astro-ph/0504361]. (Cited on pages 39 and 144.)

[167] K. Abe et al., *Search for Antihelium with the BESS-Polar Spectrometer*, *Phys. Rev. Lett.* **108** (2012) 131301 [1201.2967]. (Cited on pages 39 and 148.)

[168] T. Aramaki et al., *Review of the theoretical and experimental status of dark matter identification with cosmic-ray antideuterons*, *Phys. Rept.* **618** (2016) 1 [1505.07785]. (Cited on pages 39 and 144.)

[169] GAPS collaboration, *GAPS - Dark matter search with low-energy cosmic-ray antideuterons and antiprotons*, *PoS* **ICRC2015** (2016) 1219 [1507.02717]. (Cited on page 39.)

[170] GAPS collaboration, *The GAPS Experiment to Search for Dark Matter using Low-energy Antimatter*, *PoS* **ICRC2017** (2018) 914 [1710.00452]. (Cited on page 39.)

[171] D.-M. Gomez-Coral, A. Menchaca Rocha, V. Grabski, A. Datta, P. von Doetinchem and A. Shukla, *Deuteron and Antideuteron Production Simulation in Cosmic-Ray Interactions*, *Phys. Rev.* **D98** (2018) 023012 [1806.09303]. (Cited on pages 42 and 43.)

[172] ALEPH collaboration, *Deuteron and anti-deuteron production in e+ e- collisions at the Z resonance*, *Phys. Lett.* **B639** (2006) 192 [hep-ex/0604023]. (Cited on pages 45 and 141.)

[173] L. A. Dal and M. Kachelriess, *Antideuterons from dark matter annihilations and hadronization model dependence*, *Phys. Rev.* **D86** (2012) 103536 [1207.4560]. (Cited on page 45.)

[174] M. Potgieter, *Solar Modulation of Cosmic Rays*, *Living Rev. Solar Phys.* **10** (2013) 3 [1306.4421]. (Cited on page 45.)

[175] R. Kappl, *Charge-sign dependent solar modulation for everyone*, *J. Phys. Conf. Ser.* **718** (2016) 052020 [1601.02832]. (Cited on page 45.)

[176] M. J. Boschini, S. Della Torre, M. Gervasi, G. La Vacca and P. G. Rancoita, *Propagation of cosmic rays in heliosphere: The HELMOD model*, *Adv. Space Res.* **62** (2018) 2859 [1704.03733]. (Cited on page 45.)

[177] O. Adriani et al., *Time dependence of the proton flux measured by PAMELA during the July 2006 - December 2009 solar minimum*, *Astrophys. J.* **765** (2013) 91 [1301.4108]. (Cited on page 45.)

[178] O. Adriani et al., *Time Dependence of the Electron and Positron Components of the Cosmic Radiation Measured by the PAMELA Experiment between July 2006 and December 2015*, *Phys. Rev. Lett.* **116** (2016) 241105 [1606.08626]. (Cited on page 45.)

[179] AMS collaboration, *Observation of Fine Time Structures in the Cosmic Proton and helium Fluxes with the Alpha Magnetic Spectrometer on the International Space Station*, *Phys. Rev. Lett.* **121** (2018) 051101. (Cited on page 45.)

[180] AMS collaboration, *Observation of Complex Time Structures in the Cosmic-Ray Electron and Positron Fluxes with the Alpha Magnetic Spectrometer on the International Space Station*, *Phys. Rev. Lett.* **121** (2018) 051102. (Cited on page 45.)

[181] L. A. Fisk, *Solar Modulation and a Galactic Origin for the Anomalous Component Observed in Low-Energy Cosmic Rays*, *Astrophys. J.* **206** (1976) 333. (Cited on page 45.)

[182] I. G. Usoskin, G. A. Bazilevskaya and G. A. Kovaltsov, *Solar modulation parameter for cosmic rays since 1936 reconstructed from ground-based neutron monitors and ionization chambers*, *Journal of Geophysical Research (Space Physics)* **116** (2011) A02104. (Cited on page 46.)

[183] D. Maurin, A. Cheminet, L. Derome, A. Ghelfi and G. Hubert, *Neutron monitors and muon detectors for solar modulation studies: Interstellar flux, yield function, and assessment of critical parameters in count rate calculations*, *Adv. Space Res.* **55** (2015) 363 [1403.1612]. (Cited on page 46.)

[184] M. Kuhlen and P. Mertsch, *Time-dependent AMS-02 electron-positron fluxes in an extended force-field model*, 1909.01154. (Cited on page 46.)

[185] C. E. Fichtel, R. C. Hartman, D. A. Kniffen, D. J. Thompson, G. F. Bignami, H. Ögelman et al., *High-energy gamma-ray results from the second Small Astronomy Satellite.*, *Astrophysical Journal* **198** (1975) 163. (Cited on page 47.)

[186] G. F. Bignami, G. Boella, J. J. Burger, P. Keirle, H. A. Mayer-Hasselwander, J. A. Paul et al., *The COS-B experiment for gamma-ray astronomy.*, *Space Science Instrumentation* **1** (1975) 245. (Cited on page 47.)

[187] D. J. Thompson, D. L. Bertsch, C. E. Fichtel, R. C. Hartman, R. Hofstadter, E. B. Hughes et al., *Calibration of the Energetic Gamma-Ray Experiment Telescope (EGRET) for the Compton Gamma-Ray Observatory*, *Astrophysical Journal, Supplement* **86** (1993) 629. (Cited on page 47.)

[188] Fermi-LAT collaboration, *The Large Area Telescope on the Fermi Gamma-ray Space Telescope Mission*, *Astrophys. J.* **697** (2009) 1071 [0902.1089]. (Cited on page 47.)

[189] H.E.S.S. collaboration, *The Status of the H.E.S.S. project*, *New Astron. Rev.* **48** (2004) 331 [astro-ph/0403052]. (Cited on page 47.)

[190] VERITAS collaboration, *Recent results from VERITAS*, *J. Phys. Conf. Ser.* **1342** (2020) 012011. (Cited on page 47.)

[191] MAGIC collaboration, *The major upgrade of the MAGIC telescopes, Part II: A performance study using observations of the Crab Nebula*, *Astropart. Phys.* **72** (2016) 76 [1409.5594]. (Cited on page 47.)

[192] Fermi-LAT collaboration, *Fermi-LAT Observations of the Diffuse Gamma-Ray Emission: Implications for Cosmic Rays and the Interstellar Medium*, *Astrophys. J.* **750** (2012) 3 [1202.4039]. (Cited on page 47.)

[193] Fermi-LAT Collab. collaboration, *Fermi Large Area Telescope Fourth Source Catalog*, 1902.10045. (Cited on pages 47, 51, and 154.)

[194] Fermi-LAT collaboration, *Fermi Large Area Telescope Third Source Catalog*, *Astrophys. J. Suppl.* **218** (2015) 23 [1501.02003]. (Cited on page 47.)

[195] Y. Inoue, *Contribution of the Gamma-ray Loud Radio Galaxies Core Emissions to the Cosmic MeV and GeV Gamma-Ray Background Radiation*, *Astrophys. J.* **733** (2011) 66 [1103.3946]. (Cited on page 47.)

[196] J. Singal, V. Petrosian and M. Ajello, *Flux and Photon Spectral Index Distributions of Fermi-LAT Blazars And Contribution To The Extragalactic Gamma-ray Background*, *Astrophys. J.* **753** (2012) 45 [1106.3111]. (Cited on pages 47 and 51.)

[197] M. Di Mauro, F. Donato, G. Lamanna, D. A. Sanchez and P. D. Serpico, *Diffuse γ-ray emission from unresolved BL Lac objects*, *Astrophys. J.* **786** (2014) 129 [1311.5708]. (Cited on page 47.)

[198] M. Di Mauro, F. Calore, F. Donato, M. Ajello and L. Latronico, *Diffuse γ-ray emission from misaligned active galactic nuclei*, *Astrophys. J.* **780** (2014) 161 [1304.0908]. (Cited on pages 47 and 51.)

[199] I. Tamborra, S. Ando and K. Murase, *Star-forming galaxies as the origin of diffuse high-energy backgrounds: Gamma-ray and neutrino connections, and implications for starburst history*, *JCAP* **1409** (2014) 043 [1404.1189]. (Cited on page 47.)

[200] M. Di Mauro and F. Donato, *Composition of the Fermi-LAT isotropic gamma-ray background intensity: Emission from extragalactic point sources and dark matter annihilations*, *Phys. Rev.* **D91** (2015) 123001 [1501.05316]. (Cited on page 47.)

[201] M. Ajello et al., *The Origin of the Extragalactic Gamma-Ray Background and Implications for Dark-Matter Annihilation*, *Astrophys. J.* **800** (2015) L27 [1501.05301]. (Cited on pages 47, 51, 52, 53, 151, 152, 154, 156, 157, 158, and 163.)

[202] Fermi-LAT collaboration, *Dark Matter Constraints from Observations of 25 Milky Way Satellite Galaxies with the Fermi Large Area Telescope*, *Phys. Rev.* **D89** (2014) 042001 [1310.0828]. (Cited on page 49.)

[203] Fermi-LAT, DES collaboration, *Search for Gamma-Ray Emission from DES Dwarf Spheroidal Galaxy Candidates with Fermi-LAT Data*, *Astrophys. J.* **809** (2015) L4 [1503.02632]. (Cited on page 49.)

[204] Fermi-LAT collaboration, *Searching for Dark Matter Annihilation from Milky Way Dwarf Spheroidal Galaxies with Six Years of Fermi Large Area Telescope Data*, *Phys. Rev. Lett.* **115** (2015) 231301 [1503.02641]. (Cited on page 49.)

[205] Fermi-LAT, DES collaboration, *Searching for Dark Matter Annihilation in Recently Discovered Milky Way Satellites with Fermi-LAT*, *Astrophys. J.* **834** (2017) 110 [1611.03184]. (Cited on pages 49, 50, 112, 118, and 123.)

[206] G. D. Martinez, *A robust determination of Milky Way satellite properties using hierarchical mass modelling*, *Mon. Not. Roy. Astron. Soc.* **451** (2015) 2524 [1309.2641]. (Cited on page 49.)

[207] A. Geringer-Sameth, S. M. Koushiappas and M. Walker, *Dwarf galaxy annihilation and decay emission profiles for dark matter experiments*, *Astrophys. J.* **801** (2015) 74 [1408.0002]. (Cited on pages 49 and 130.)

[208] V. Bonnivard et al., *Dark matter annihilation and decay in dwarf spheroidal galaxies: The classical and ultrafaint dSphs*, *Mon. Not. Roy. Astron. Soc.* **453** (2015) 849 [1504.02048]. (Cited on page 49.)

[209] A. Geringer-Sameth, M. G. Walker, S. M. Koushiappas, S. E. Koposov, V. Belokurov, G. Torrealba et al., *Indication of Gamma-ray Emission from the Newly Discovered Dwarf Galaxy Reticulum II*, *Phys. Rev. Lett.* **115** (2015) 081101 [1503.02320]. (Cited on pages 50 and 123.)

[210] S. Li, Y.-F. Liang, K.-K. Duan, Z.-Q. Shen, X. Huang, X. Li et al., *Search for gamma-ray emission from eight dwarf spheroidal galaxy candidates discovered in Year Two of Dark Energy Survey with Fermi-LAT data*, *Phys. Rev.* **D93** (2016) 043518 [1511.09252]. (Cited on pages 50 and 123.)

[211] F. Calore, P. D. Serpico and B. Zaldivar, *Dark matter constraints from dwarf galaxies: a data-driven analysis*, *JCAP* **1810** (2018) 029 [1803.05508]. (Cited on page 50.)

[212] F. Calore, A. Cuoco, T. Regimbau, S. Sachdev and P. Serpico, *Cross-correlating galaxy catalogs and gravitational waves: a tomographic approach*, 2002.02466. (Cited on page 50.)

[213] L. Goodenough and D. Hooper, *Possible Evidence For Dark Matter Annihilation In The Inner Milky Way From The Fermi Gamma Ray Space Telescope*, 0910.2998. (Cited on pages 50, 121, and 147.)

[214] F. Calore, I. Cholis, C. McCabe and C. Weniger, *A Tale of Tails: Dark Matter Interpretations of the Fermi GeV Excess in Light of Background Model Systematics*, *Phys. Rev.* **D91** (2015) 063003 [1411.4647]. (Cited on pages 50, 112, 118, 121, and 147.)

[215] Fermi-LAT collaboration, *The Fermi Galactic Center GeV Excess and Implications for Dark Matter*, *Astrophys. J.* **840** (2017) 43 [1704.03910]. (Cited on pages 50 and 121.)

[216] Fermi-LAT collaboration, *Indirect Search for Dark Matter from the center of the Milky Way with the Fermi-Large Area Telescope*, in *Fermi gamma-ray space telescope. Proceedings, 2nd Fermi Symposium, Washington, USA, November 2-5, 2009*, 2009, 0912.3828. (Cited on page 50.)

[217] D. Hooper and L. Goodenough, *Dark Matter Annihilation in The Galactic Center As Seen by the Fermi Gamma Ray Space Telescope*, *Phys. Lett.* **B697** (2011) 412 [1010.2752]. (Cited on page 50.)

[218] K. N. Abazajian and M. Kaplinghat, *Detection of a Gamma-Ray Source in the Galactic Center Consistent with Extended Emission from Dark Matter Annihilation and Concentrated Astrophysical Emission*, *Phys. Rev.* **D86** (2012) 083511 [1207.6047]. (Cited on page 50.)

[219] D. Hooper and T. Linden, *On The Origin Of The Gamma Rays From The Galactic Center*, *Phys. Rev.* **D84** (2011) 123005 [1110.0006]. (Cited on page 50.)

[220] D. Hooper and T. R. Slatyer, *Two Emission Mechanisms in the Fermi Bubbles: A Possible Signal of Annihilating Dark Matter*, *Phys. Dark Univ.* **2** (2013) 118 [1302.6589]. (Cited on page 50.)

[221] W.-C. Huang, A. Urbano and W. Xue, *Fermi Bubbles under Dark Matter Scrutiny Part II: Particle Physics Analysis*, *JCAP* **1404** (2014) 020 [1310.7609]. (Cited on page 50.)

[222] C. Gordon and O. Macias, *Dark Matter and Pulsar Model Constraints from Galactic Center Fermi-LAT Gamma Ray Observations*, *Phys. Rev.* **D88** (2013) 083521 [1306.5725]. (Cited on page 50.)

[223] K. N. Abazajian, N. Canac, S. Horiuchi and M. Kaplinghat, *Astrophysical and Dark Matter Interpretations of Extended Gamma-Ray Emission from the Galactic Center*, *Phys. Rev.* **D90** (2014) 023526 [1402.4090]. (Cited on page 50.)

[224] B. Zhou, Y.-F. Liang, X. Huang, X. Li, Y.-Z. Fan, L. Feng et al., *GeV excess in the Milky Way: The role of diffuse galactic gamma-ray emission templates*, *Phys. Rev.* **D91** (2015) 123010 [1406.6948]. (Cited on page 50.)

[225] T. Daylan, D. P. Finkbeiner, D. Hooper, T. Linden, S. K. N. Portillo, N. L. Rodd et al., *The characterization of the gamma-ray signal from the central Milky Way: A case for annihilating dark matter*, *Phys. Dark Univ.* **12** (2016) 1 [1402.6703]. (Cited on page 50.)

[226] F. Calore, I. Cholis and C. Weniger, *Background Model Systematics for the Fermi GeV Excess*, *JCAP* **1503** (2015) 038 [1409.0042]. (Cited on pages 50, 121, 122, and 147.)

[227] Fermi-LAT collaboration, *Fermi-LAT Observations of High-Energy γ-Ray Emission Toward the Galactic Center*, *Astrophys. J.* **819** (2016) 44 [1511.02938]. (Cited on page 50.)

[228] C. Karwin, S. Murgia, T. M. P. Tait, T. A. Porter and P. Tanedo, *Dark Matter Interpretation of the Fermi-LAT Observation Toward the Galactic Center*, *Phys. Rev.* **D95** (2017) 103005 [1612.05687]. (Cited on page 50.)

[229] I. Cholis, D. Hooper and T. Linden, *Challenges in Explaining the Galactic Center Gamma-Ray Excess with Millisecond Pulsars*, *JCAP* **1506** (2015) 043 [1407.5625]. (Cited on page 50.)

[230] J. Petrović, P. D. Serpico and G. Zaharijas, *Millisecond pulsars and the Galactic Center gamma-ray excess: the importance of luminosity function and secondary emission*, *JCAP* **1502** (2015) 023 [1411.2980]. (Cited on page 50.)

[231] T. Linden, N. L. Rodd, B. R. Safdi and T. R. Slatyer, *High-energy tail of the Galactic Center gamma-ray excess*, *Phys. Rev.* **D94** (2016) 103013 [1604.01026]. (Cited on page 50.)

[232] X. Huang, T. Enßlin and M. Selig, *Galactic dark matter search via phenomenological astrophysics modeling*, *JCAP* **1604** (2016) 030 [1511.02621]. (Cited on page 50.)

[233] D. Hooper and T. Linden, *The Gamma-Ray Pulsar Population of Globular Clusters: Implications for the GeV Excess*, *JCAP* **1608** (2016) 018 [1606.09250]. (Cited on page 50.)

[234] C. Eckner et al., *Millisecond pulsar origin of the Galactic center excess and extended gamma-ray emission from Andromeda - a closer look*, *Astrophys. J.* **862** (2018) 79 [1711.05127]. (Cited on page 50.)

[235] R. Bartels, F. Calore, E. Storm and C. Weniger, *Galactic binaries can explain the Fermi Galactic centre excess and 511 keV emission*, *Mon. Not. Roy. Astron. Soc.* **480** (2018) 3826 [1803.04370]. (Cited on page 50.)

[236] R. Bartels, S. Krishnamurthy and C. Weniger, *Strong support for the millisecond pulsar origin of the Galactic center GeV excess*, *Phys. Rev. Lett.* **116** (2016) 051102 [1506.05104]. (Cited on page 50.)

[237] S. K. Lee, M. Lisanti, B. R. Safdi, T. R. Slatyer and W. Xue, *Evidence for Unresolved γ-Ray Point Sources in the Inner Galaxy*, *Phys. Rev. Lett.* **116** (2016) 051103 [1506.05124]. (Cited on pages 50 and 55.)

[238] R. K. Leane and T. R. Slatyer, *Revival of the Dark Matter Hypothesis for the Galactic Center Gamma-Ray Excess*, *Phys. Rev. Lett.* **123** (2019) 241101 [1904.08430]. (Cited on page 51.)

[239] L. J. Chang, S. Mishra-Sharma, M. Lisanti, M. Buschmann, N. L. Rodd and B. R. Safdi, *Characterizing the Nature of the Unresolved Point Sources in the Galactic Center*, 1908.10874. (Cited on pages 51 and 55.)

[240] F. Calore, M. Di Mauro, F. Donato, J. W. T. Hessels and C. Weniger, *Radio detection prospects for a bulge population of millisecond pulsars as suggested by Fermi LAT observations of the inner Galaxy*, *Astrophys. J.* **827** (2016) 143 [1512.06825]. (Cited on page 51.)

[241] F. Calore, T. Regimbau and P. D. Serpico, *Probing the Fermi-LAT GeV excess with gravitational waves*, *Phys. Rev. Lett.* **122** (2019) 081103 [1812.05094]. (Cited on page 51.)

[242] E. Storm, C. Weniger and F. Calore, *SkyFACT: High-dimensional modeling of gamma-ray emission with adaptive templates and penalized likelihoods*, *JCAP* **1708** (2017) 022 [1705.04065]. (Cited on page 51.)

[243] R. Bartels, E. Storm, C. Weniger and F. Calore, *The Fermi-LAT GeV excess as a tracer of stellar mass in the Galactic bulge*, *Nat. Astron.* **2** (2018) 819 [1711.04778]. (Cited on page 51.)

[244] J. Petrović, P. D. Serpico and G. Zaharijaš, *Galactic Center gamma-ray "excess" from an active past of the Galactic Centre?*, *JCAP* **1410** (2014) 052 [1405.7928]. (Cited on page 51.)

[245] I. Cholis, C. Evoli, F. Calore, T. Linden, C. Weniger and D. Hooper, *The Galactic Center GeV Excess from a Series of Leptonic Cosmic-Ray Outbursts*, *JCAP* **1512** (2015) 005 [1506.05119]. (Cited on page 51.)

[246] T. Lacroix, O. Macias, C. Gordon, P. Panci, C. Bœhm and J. Silk, *Spatial morphology of the secondary emission in the Galactic Center gamma-ray excess*, *Phys. Rev.* **D93** (2016) 103004 [1512.01846]. (Cited on page 51.)

[247] D. Gaggero, M. Taoso, A. Urbano, M. Valli and P. Ullio, *Towards a realistic astrophysical interpretation of the gamma-ray Galactic center excess*, *JCAP* **1512** (2015) 056 [1507.06129]. (Cited on page 51.)

[248] E. Carlson, T. Linden and S. Profumo, *Improved Cosmic-Ray Injection Models and the Galactic Center Gamma-Ray Excess*, *Phys. Rev.* **D94** (2016) 063504 [1603.06584]. (Cited on page 51.)

[249] W. de Boer, L. Bosse, I. Gebauer, A. Neumann and P. L. Biermann, *Molecular clouds as origin of the Fermi gamma-ray GeV excess*, *Phys. Rev.* **D96** (2017) 043012 [1707.08653]. (Cited on page 51.)

[250] Y. Inoue and T. Totani, *The Blazar Sequence and the Cosmic Gamma-Ray Background Radiation in the Fermi Era*, *Astrophys. J.* **702** (2009) 523 [0810.3580]. (Cited on page 51.)

[251] Fermi-LAT collaboration, *The Second Catalog of Active Galactic Nuclei Detected by the Fermi Large Area Telescope*, *Astrophys. J.* **743** (2011) 171 [1108.1420]. (Cited on page 51.)

[252] K. N. Abazajian, S. Blanchet and J. P. Harding, *The Contribution of Blazars to the Extragalactic Diffuse Gamma-ray Background and Their Future Spatial Resolution*, *Phys. Rev.* **D84** (2011) 103007 [1012.1247]. (Cited on page 51.)

[253] M. Ajello et al., *The Luminosity Function of Fermi-detected Flat-Spectrum Radio Quasars*, *Astrophys. J.* **751** (2012) 108 [1110.3787]. (Cited on page 51.)

[254] C. M. Urry and P. Padovani, *Unified schemes for radio-loud active galactic nuclei*, *Publ. Astron. Soc. Pac.* **107** (1995) 803 [astro-ph/9506063]. (Cited on page 51.)

[255] P. Padovani et al., *Active galactic nuclei: what's in a name?*, *Astron. Astrophys. Rev.* **25** (2017) 2 [1707.07134]. (Cited on page 51.)

[256] M. Fornasa and M. A. Sánchez-Conde, *The nature of the Diffuse Gamma-Ray Background*, *Phys. Rept.* **598** (2015) 1 [1502.02866]. (Cited on page 53.)

[257] D. Malyshev and D. W. Hogg, *Statistics of gamma-ray point sources below the Fermi detection limit*, *Astrophys. J.* **738** (2011) 181 [1104.0010]. (Cited on pages 54 and 55.)

[258] H.-S. Zechlin, A. Cuoco, F. Donato, N. Fornengo and A. Vittino, *Unveiling the Gamma-ray Source Count Distribution Below the Fermi Detection Limit with Photon Statistics*, *Astrophys. J. Suppl.* **225** (2016) 18 [1512.07190]. (Cited on pages 54, 55, 153, and 157.)

[259] P. A. G. Scheuer, *A statistical method for analysing observations of faint radio stars*, *Proceedings of the Cambridge Philosophical Society* **53** (1957) 764. (Cited on page 54.)

[260] J. J. Condon, *Confusion and Flux-Density Error Distributions*, *Astrophysical Journal* **188** (1974) 279. (Cited on page 54.)

[261] P. A. G. Scheuer, *Fluctuations in the X-ray background*, *Monthly Notices of the RAS* **166** (1974) 329. (Cited on page 54.)

[262] G. Hasinger, R. Burg, R. Giacconi, G. Hartner, M. Schmidt, J. Trumper et al., *A deep X-ray survey in the Lockman hole and the soft X-ray log N-log S.*, *Astronomy and Astrophysics* **275** (1993) 1. (Cited on page 54.)

[263] T. Miyaji and R. E. Griffiths, *Faint source counts from off-source fluctuation analysis on chandra observations of the hubble deep field-north*, *Astrophys. J.* **564** (2002) L5 [astro-ph/0111393]. (Cited on page 54.)

[264] S. Dodelson, A. V. Belikov, D. Hooper and P. Serpico, *Identifying Dark Matter Annihilation Products In The Diffuse Gamma Ray Background*, *Phys. Rev.* **D80** (2009) 083504 [0903.2829]. (Cited on page 54.)

[265] H.-S. Zechlin, A. Cuoco, F. Donato, N. Fornengo and M. Regis, *Statistical Measurement of the Gamma-ray Source-count Distribution as a Function of Energy*, *Astrophys. J.* **826** (2016) L31 [1605.04256]. (Cited on pages 54, 55, 151, 153, and 157.)

[266] R. K. Leane and T. R. Slatyer, *Revival of the Dark Matter Hypothesis for the Galactic Center Gamma-Ray Excess*, *Phys. Rev. Lett.* **123** (2019) 241101 [1904.08430]. (Cited on page 55.)

[267] H.-S. Zechlin, S. Manconi and F. Donato, *Constraining Galactic dark matter with gamma-ray pixel counts statistics*, *Phys. Rev.* **D98** (2018) 083022 [1710.01506]. (Cited on page 55.)

[268] S. Ando and E. Komatsu, *Anisotropy of the cosmic gamma-ray background from dark matter annihilation*, *Phys. Rev.* **D73** (2006) 023521 [astro-ph/0512217]. (Cited on page 60.)

[269] S. Ando, E. Komatsu, T. Narumoto and T. Totani, *Dark matter annihilation or unresolved astrophysical sources? Anisotropy probe of the origin of cosmic gamma-ray background*, *Phys. Rev.* **D75** (2007) 063519 [astro-ph/0612467]. (Cited on pages 60, 151, and 153.)

[270] S. Ando, M. Fornasa, N. Fornengo, M. Regis and H.-S. Zechlin, *Astrophysical interpretation of the anisotropies in the unresolved gamma-ray background*, *Phys. Rev.* **D95** (2017) 123006 [1701.06988]. (Cited on pages 60, 154, and 159.)

[271] A. Cooray and R. K. Sheth, *Halo Models of Large Scale Structure*, *Phys. Rept.* **372** (2002) 1 [astro-ph/0206508]. (Cited on page 60.)

[272] R. J. Scherrer and E. Bertschinger, *Statistics of Primordial Density Perturbations from Discrete Seed Masses*, *Astrophysical Journal* **381** (1991) 349. (Cited on page 60.)

[273] S. Ando and E. Komatsu, *Constraints on the annihilation cross section of dark matter particles from anisotropies in the diffuse gamma-ray background measured with Fermi-LAT*, *Phys. Rev.* **D87** (2013) 123539 [1301.5901]. (Cited on page 60.)

[274] Fermi-LAT collaboration, *Unresolved Gamma-Ray Sky through its Angular Power Spectrum*, *Phys. Rev. Lett.* **121** (2018) 241101 [1812.02079]. (Cited on pages 60, 154, 158, 159, and 163.)

[275] Fermi-LAT collaboration, *Anisotropies in the diffuse gamma-ray background measured by the Fermi LAT*, *Phys. Rev.* **D85** (2012) 083007 [1202.2856]. (Cited on page 60.)

[276] M. Fornasa et al., *Angular power spectrum of the diffuse gamma-ray emission as measured by the Fermi Large Area Telescope and constraints on its dark matter interpretation*, *Phys. Rev.* **D94** (2016) 123005 [1608.07289]. (Cited on pages 60 and 159.)

[277] N. Fornengo and M. Regis, *Particle dark matter searches in the anisotropic sky*, *Front. Physics* **2** (2014) 6 [1312.4835]. (Cited on pages 60 and 64.)

[278] S. Camera, M. Fornasa, N. Fornengo and M. Regis, *A Novel Approach in the Weakly Interacting Massive Particle Quest: Cross-correlation of Gamma-Ray Anisotropies and Cosmic Shear*, *Astrophys. J.* **771** (2013) L5 [1212.5018]. (Cited on page 60.)

[279] S. Ammazzalorso, N. Fornengo, S. Horiuchi and M. Regis, *Characterizing the local gamma-ray Universe via angular cross-correlations*, *Phys. Rev.* **D98** (2018) 103007 [1808.09225]. (Cited on page 60.)

[280] S. Ammazzalorso et al., *Detection of Cross-Correlation between Gravitational Lensing and Gamma Rays*, 1907.13484. (Cited on page 60.)

[281] E. Pinetti, S. Camera, N. Fornengo and M. Regis, *Synergies across the spectrum for particle dark matter indirect detection: how HI intensity mapping meets gamma rays*, 1911.04989. (Cited on pages 60 and 151.)

[282] M. LoVerde and N. Afshordi, *Extended Limber Approximation*, *Phys. Rev.* **D78** (2008) 123506 [0809.5112]. (Cited on page 62.)

[283] LHCb collaboration, *Measurement of Antiproton Production in* pHe *Collisions at* $\sqrt{s_{NN}} = 110$ *GeV*, *Phys. Rev. Lett.* **121** (2018) 222001 [1808.06127]. (Cited on page 67.)

[284] D. Dekkers, J. A. Geibel, R. Mermod, G. Weber, T. R. Willitts, K. Winter et al., *Experimental Study of Particle Production at Small Angles in Nucleon-Nucleon Collisions at 19 and 23 GeV/c*, *Phys. Rev.* **137** (1965) B962. (Cited on pages 69 and 70.)

[285] BRAHMS collaboration, *Production of mesons and baryons at high rapidity and high P(T) in proton-proton collisions at s**(1/2) = 200-GeV*, *Phys. Rev. Lett.* **98** (2007) 252001 [hep-ex/0701041]. (Cited on pages 69 and 70.)

[286] AMS collaboration, *Precision Measurement of Cosmic-Ray Nitrogen and its Primary and Secondary Components with the Alpha Magnetic Spectrometer on the International Space Station*, *Phys. Rev. Lett.* **121** (2018) 051103. (Cited on page 80.)

[287] J. J. Engelmann, P. Ferrando, A. Soutoul, P. Goret and E. Juliusson, *Charge composition and energy spectra of cosmic-ray nuclei for elements from Be to NI - Results from HEAO-3-C2*, *Astronomy and Astrophysics* **233** (1990) 96. (Cited on page 81.)

[288] N. Przybilla, M. F. Nieva and K. Butler, *A cosmic abundance standard: chemical homogeneity of the solar neighbourhood & the ISM dust-phase composition*, *Astrophys. J.* **688** (2008) L103 [0809.2403]. (Cited on page 81.)

[289] G. Jóhannesson et al., *Bayesian analysis of cosmic-ray propagation: evidence against homogeneous diffusion*, *Astrophys. J.* **824** (2016) 16 [1602.02243]. (Cited on pages 94 and 101.)

[290] E. C. Stone, A. C. Cummings, F. B. McDonald, B. C. Heikkila, N. Lal and W. R. Webber, *Voyager 1 Observes Low-Energy Galactic Cosmic Rays in a Region Depleted of Heliospheric Ions*, *Science* **341** (2013) 150. (Cited on pages 94 and 97.)

[291] Y. S. Yoon et al., *Cosmic-Ray Proton and helium Spectra from the First CREAM Flight*, *Astrophys. J.* **728** (2011) 122 [1102.2575]. (Cited on pages 94 and 97.)

[292] M. Cirelli, G. Corcella, A. Hektor, G. Hutsi, M. Kadastik, P. Panci et al., *PPPC 4 DM ID: A Poor Particle Physicist Cookbook for Dark Matter Indirect Detection*, *JCAP* **1103** (2011) 051 [1012.4515]. (Cited on pages 96, 120, 130, and 140.)

[293] F. Feroz, M. P. Hobson and M. Bridges, *MultiNest: an efficient and robust Bayesian inference tool for cosmology and particle physics*, *Mon. Not. Roy. Astron. Soc.* **398** (2009) 1601 [0809.3437]. (Cited on page 97.)

[294] Y. Genolini, A. Putze, P. Salati and P. D. Serpico, *Theoretical uncertainties in extracting cosmic-ray diffusion parameters: the boron-to-carbon ratio*, *Astron. Astrophys.* **580** (2015) A9 [1504.03134]. (Cited on page 101.)

[295] R. Kappl, A. Reinert and M. W. Winkler, *AMS-02 Antiprotons Reloaded*, *JCAP* **1510** (2015) 034 [1506.04145]. (Cited on page 101.)

[296] L. A. Cavasonza, H. Gast, M. Krämer, M. Pellen and S. Schael, *Constraints on leptophilic dark matter from the AMS-02 experiment*, *Astrophys. J.* **839** (2017) 36 [1612.06634]. (Cited on pages 114 and 132.)

[297] J. Lavalle, D. Maurin and A. Putze, *Direct constraints on diffusion models from cosmic-ray positron data: Excluding the minimal model for dark matter searches*, *Phys. Rev.* **D90** (2014) 081301 [1407.2540]. (Cited on pages 118 and 143.)

[298] M. Boudaud, E. F. Bueno, S. Caroff, Y. Genolini, V. Poulin, V. Poireau et al., *The pinching method for Galactic cosmic ray positrons: implications in the light of precision measurements*, *Astron. Astrophys.* **605** (2017) A17 [1612.03924]. (Cited on pages 118 and 143.)

[299] J. Alwall, R. Frederix, S. Frixione, V. Hirschi, F. Maltoni, O. Mattelaer et al., *The automated computation of tree-level and next-to-leading order differential cross sections, and their matching to parton shower simulations*, *JHEP* **07** (2014) 079 [1405.0301]. (Cited on page 120.)

[300] T. Sjostrand, S. Mrenna and P. Z. Skands, *A Brief Introduction to PYTHIA 8.1*, *Comput. Phys. Commun.* **178** (2008) 852 [0710.3820]. (Cited on pages 120 and 122.)

[301] T. Sjostrand, S. Mrenna and P. Z. Skands, *PYTHIA 6.4 Physics and Manual*, *JHEP* **05** (2006) 026 [hep-ph/0603175]. (Cited on page 122.)

[302] A. Cuoco, B. Eiteneuer, J. Heisig and M. Krämer, *A global fit of the γ-ray galactic center excess within the scalar singlet Higgs portal model*, *JCAP* **1606** (2016) 050 [1603.08228]. (Cited on pages 122, 125, and 126.)

[303] V. Silveira and A. Zee, *SCALAR PHANTOMS*, *Phys. Lett.* **161B** (1985) 136. (Cited on page 125.)

[304] J. McDonald, *Gauge singlet scalars as cold dark matter*, *Phys. Rev.* **D50** (1994) 3637 [hep-ph/0702143]. (Cited on page 125.)

[305] C. P. Burgess, M. Pospelov and T. ter Veldhuis, *The Minimal model of nonbaryonic dark matter: A Singlet scalar*, *Nucl. Phys.* **B619** (2001) 709 [hep-ph/0011335]. (Cited on page 125.)

[306] J. M. Cline, K. Kainulainen, P. Scott and C. Weniger, *Update on scalar singlet dark matter*, *Phys. Rev.* **D88** (2013) 055025 [1306.4710]. (Cited on page 125.)

[307] A. Beniwal, F. Rajec, C. Savage, P. Scott, C. Weniger, M. White et al., *Combined analysis of effective Higgs portal dark matter models*, *Phys. Rev.* **D93** (2016) 115016 [1512.06458]. (Cited on page 125.)

[308] ATLAS collaboration, *Constraints on new phenomena via Higgs boson couplings and invisible decays with the ATLAS detector*, *JHEP* **11** (2015) 206 [1509.00672]. (Cited on page 126.)

[309] LUX collaboration, *Results from a search for dark matter in the complete LUX exposure*, *Phys. Rev. Lett.* **118** (2017) 021303 [1608.07648]. (Cited on page 126.)

[310] XENON collaboration, *Dark Matter Search Results from a One Ton-Year Exposure of XENON1T*, *Phys. Rev. Lett.* **121** (2018) 111302 [1805.12562]. (Cited on page 126.)

[311] PandaX-II collaboration, *Dark Matter Results From 54-Ton-Day Exposure of PandaX-II Experiment*, *Phys. Rev. Lett.* **119** (2017) 181302 [1708.06917]. (Cited on page 126.)

[312] Fermi-LAT collaboration, *Updated search for spectral lines from Galactic dark matter interactions with pass 8 data from the Fermi Large Area Telescope*, *Phys. Rev.* **D91** (2015) 122002 [1506.00013]. (Cited on page 126.)

[313] G. Bélanger, F. Boudjema, A. Pukhov and A. Semenov, *micrOMEGAs4.1: two dark matter candidates*, *Comput. Phys. Commun.* **192** (2015) 322 [1407.6129]. (Cited on page 126.)

[314] A. Belyaev, N. D. Christensen and A. Pukhov, *CalcHEP 3.4 for collider physics within and beyond the Standard Model*, *Comput. Phys. Commun.* **184** (2013) 1729 [1207.6082]. (Cited on page 126.)

[315] J. Heisig, M. Krämer, E. Madge and A. Mück, *Probing Higgs-portal dark matter with vector-boson fusion*, 1912.08472. (Cited on page 126.)

[316] M. Ciafaloni, P. Ciafaloni and D. Comelli, *Towards collinear evolution equations in electroweak theory*, *Phys. Rev. Lett.* **88** (2002) 102001 [hep-ph/0111109]. (Cited on page 130.)

[317] P. Ciafaloni and D. Comelli, *Electroweak evolution equations*, *JHEP* **11** (2005) 022 [hep-ph/0505047]. (Cited on page 130.)

[318] H.E.S.S. collaboration, *Search for dark matter annihilations towards the inner Galactic halo from 10 years of observations with H.E.S.S*, *Phys. Rev. Lett.* **117** (2016) 111301 [1607.08142]. (Cited on pages 132 and 134.)

[319] M. Cirelli, N. Fornengo and A. Strumia, *Minimal dark matter*, *Nucl. Phys.* **B753** (2006) 178 [hep-ph/0512090]. (Cited on page 134.)

[320] J. Hisano, S. Matsumoto and M. M. Nojiri, *Explosive dark matter annihilation*, *Phys. Rev. Lett.* **92** (2004) 031303 [hep-ph/0307216]. (Cited on page 134.)

[321] J. Hisano, S. Matsumoto, M. M. Nojiri and O. Saito, *Non-perturbative effect on dark matter annihilation and gamma ray signature from galactic center*, *Phys. Rev.* **D71** (2005) 063528 [hep-ph/0412403]. (Cited on page 134.)

[322] J. Hisano, S. Matsumoto, M. Nagai, O. Saito and M. Senami, *Non-perturbative effect on thermal relic abundance of dark matter*, *Phys. Lett.* **B646** (2007) 34 [hep-ph/0610249]. (Cited on pages 134 and 135.)

[323] A. Hryczuk, R. Iengo and P. Ullio, *Relic densities including Sommerfeld enhancements in the MSSM*, *JHEP* **03** (2011) 069 [1010.2172]. (Cited on pages 134 and 135.)

[324] A. Hryczuk and R. Iengo, *The one-loop and Sommerfeld electroweak corrections to the Wino dark matter annihilation*, *JHEP* **01** (2012) 163 [1111.2916]. (Cited on pages 134 and 135.)

[325] E. J. Chun, J.-C. Park and S. Scopel, *Non-perturbative Effect and PAMELA Limit on Electro-Weak Dark Matter*, *JCAP* **1212** (2012) 022 [1210.6104]. (Cited on pages 134 and 135.)

[326] A. Hryczuk, I. Cholis, R. Iengo, M. Tavakoli and P. Ullio, *Indirect Detection Analysis: Wino Dark Matter Case Study*, *JCAP* **1407** (2014) 031 [1401.6212]. (Cited on page 134.)

[327] M. Baumgart, I. Z. Rothstein and V. Vaidya, *Calculating the Annihilation Rate of Weakly Interacting Massive Particles*, *Phys. Rev. Lett.* **114** (2015) 211301 [1409.4415]. (Cited on page 134.)

[328] M. Bauer, T. Cohen, R. J. Hill and M. P. Solon, *Soft Collinear Effective Theory for Heavy WIMP Annihilation*, *JHEP* **01** (2015) 099 [1409.7392]. (Cited on page 134.)

[329] G. Ovanesyan, T. R. Slatyer and I. W. Stewart, *Heavy Dark Matter Annihilation from Effective Field Theory*, *Phys. Rev. Lett.* **114** (2015) 211302 [1409.8294]. (Cited on page 134.)

[330] M. Baumgart, I. Z. Rothstein and V. Vaidya, *Constraints on Galactic Wino Densities from Gamma Ray Lines*, *JHEP* **04** (2015) 106 [1412.8698]. (Cited on page 134.)

[331] M. Baumgart and V. Vaidya, *Semi-inclusive wino and higgsino annihilation to LL'*, *JHEP* **03** (2016) 213 [1510.02470]. (Cited on page 134.)

[332] E. J. Chun and J.-C. Park, *Electro-Weak Dark Matter: non-perturbative effect confronting indirect detections*, *Phys. Lett.* **B750** (2015) 372 [1506.07522]. (Cited on pages 134 and 135.)

[333] G. Ovanesyan, N. L. Rodd, T. R. Slatyer and I. W. Stewart, *One-loop correction to heavy dark matter annihilation*, *Phys. Rev.* **D95** (2017) 055001 [1612.04814]. (Cited on page 134.)

[334] M. Beneke, A. Bharucha, A. Hryczuk, S. Recksiegel and P. Ruiz-Femenia, *The last refuge of mixed wino-Higgsino dark matter*, *JHEP* **01** (2017) 002 [1611.00804]. (Cited on pages 134 and 135.)

[335] M. Cirelli, A. Strumia and M. Tamburini, *Cosmology and Astrophysics of Minimal Dark Matter*, *Nucl. Phys.* **B787** (2007) 152 [0706.4071]. (Cited on pages 134 and 135.)

[336] J. Hisano, K. Ishiwata and N. Nagata, *QCD Effects on Direct Detection of Wino Dark Matter*, *JHEP* **06** (2015) 097 [1504.00915]. (Cited on page 135.)

[337] J. Bramante, N. Desai, P. Fox, A. Martin, B. Ostdiek and T. Plehn, *Towards the Final Word on Neutralino Dark Matter*, *Phys. Rev.* **D93** (2016) 063525 [1510.03460]. (Cited on page 135.)

[338] ATLAS collaboration, *Search for long-lived charginos based on a disappearing-track signature in pp collisions at* $\sqrt{s} = 13$ *TeV with the ATLAS detector*, *JHEP* **06** (2018) 022 [1712.02118]. (Cited on page 135.)

[339] H. Fukuda, N. Nagata, H. Otono and S. Shirai, *Higgsino Dark Matter or Not: Role of Disappearing Track Searches at the LHC and Future Colliders*, *Phys. Lett.* **B781** (2018) 306 [1703.09675]. (Cited on page 135.)

[340] R. Mahbubani, P. Schwaller and J. Zurita, *Closing the window for compressed Dark Sectors with disappearing charged tracks*, *JHEP* **06** (2017) 119 [1703.05327]. (Cited on page 135.)

[341] B. Ostdiek, *Constraining the minimal dark matter fiveplet with LHC searches*, *Phys. Rev.* **D92** (2015) 055008 [1506.03445]. (Cited on page 135.)

[342] T. Cohen, M. Lisanti, A. Pierce and T. R. Slatyer, *Wino Dark Matter Under Siege*, *JCAP* **1310** (2013) 061 [1307.4082]. (Cited on page 135.)

[343] J. Fan and M. Reece, *In Wino Veritas? Indirect Searches Shed Light on Neutralino Dark Matter*, *JHEP* **10** (2013) 124 [1307.4400]. (Cited on page 135.)

[344] B. Bhattacherjee, M. Ibe, K. Ichikawa, S. Matsumoto and K. Nishiyama, *Wino Dark Matter and Future dSph Observations*, *JHEP* **07** (2014) 080 [1405.4914]. (Cited on page 135.)

[345] M. Beneke, A. Bharucha, F. Dighera, C. Hellmann, A. Hryczuk, S. Recksiegel et al., *Relic density of wino-like dark matter in the MSSM*, *JHEP* **03** (2016) 119 [1601.04718]. (Cited on page 135.)

[346] H.-C. Cheng, B. A. Dobrescu and K. T. Matchev, *Generic and chiral extensions of the supersymmetric standard model*, *Nucl. Phys.* **B543** (1999) 47 [hep-ph/9811316]. (Cited on page 135.)

[347] J. L. Feng, T. Moroi, L. Randall, M. Strassler and S.-f. Su, *Discovering supersymmetry at the Tevatron in wino LSP scenarios*, *Phys. Rev. Lett.* **83** (1999) 1731 [hep-ph/9904250]. (Cited on page 135.)

[348] T. Gherghetta, G. F. Giudice and J. D. Wells, *Phenomenological consequences of supersymmetry with anomaly induced masses*, *Nucl. Phys.* **B559** (1999) 27 [hep-ph/9904378]. (Cited on page 135.)

[349] Y. Yamada, *Electroweak two-loop contribution to the mass splitting within a new heavy SU(2)(L) fermion multiplet*, *Phys. Lett.* **B682** (2010) 435 [0906.5207]. (Cited on page 135.)

[350] M. Ibe, S. Matsumoto and R. Sato, *Mass Splitting between Charged and Neutral Winos at Two-Loop Level*, *Phys. Lett.* **B721** (2013) 252 [1212.5989]. (Cited on page 135.)

[351] M. Cirelli, T. Hambye, P. Panci, F. Sala and M. Taoso, *Gamma ray tests of Minimal Dark Matter*, *JCAP* **1510** (2015) 026 [1507.05519]. (Cited on page 135.)

[352] H.E.S.S. collaboration, *Search for Photon-Linelike Signatures from Dark Matter Annihilations with H.E.S.S.*, *Phys. Rev. Lett.* **110** (2013) 041301 [1301.1173]. (Cited on page 137.)

[353] E. W. Anderson et al., *Proton and Pion Spectra from Proton-Proton Interactions at 10, 20, and 30 BeV/c*, *Phys. Rev. Lett.* **19** (1967) 198. (Cited on page 140.)

[354] A. Baldini, V. Flaminio, W. G. Moorhead and D. R. O. Morrison, *Total Cross-Sections for Reactions of High Energy Particles*, vol. 12B. SpringerMaterials, The address, 1988, 10.1007/10367917. (Cited on page 140.)

[355] ALICE collaboration, *Production of deuterons, tritons, ^{3}He nuclei and their anti-nuclei in pp collisions at $\sqrt{s}$ = 0.9, 2.76 and 7 TeV*, 1709.08522. (Cited on page 141.)

[356] Particle Data Group collaboration, *Review of Particle Physics*, *Chin. Phys.* **C38** (2014) 090001. (Cited on page 142.)

[357] GAPS collaboration, *Antideuteron Sensitivity for the GAPS Experiment*, *Astropart. Phys.* **74** (2016) 6 [1506.02513]. (Cited on pages 144 and 145.)

[358] Fermi-LAT collaboration, *Characterizing the population of pulsars in the inner Galaxy with the Fermi Large Area Telescope*, *Submitted to: Astrophys. J.* (2017) [1705.00009]. (Cited on page 147.)

[359] AMS collaboration, *AMS Experiment on the International Space Station*, in *Proceedings, 32nd ICRC 2011*, vol. c, p. 5, 2011, DOI. (Cited on page 148.)

[360] E. Carlson, A. Coogan, T. Linden, S. Profumo, A. Ibarra and S. Wild, *Antihelium from Dark Matter*, *Phys. Rev.* **D89** (2014) 076005 [1401.2461]. (Cited on page 149.)

[361] I. Cholis, T. Linden and D. Hooper, *Anti-Deuterons and Anti-Helium Nuclei from Annihilating Dark Matter*, 2001.08749. (Cited on page 149.)

[362] V. Poulin, P. Salati, I. Cholis, M. Kamionkowski and J. Silk, *Where do the AMS-02 antihelium events come from?*, *Phys. Rev.* **D99** (2019) 023016 [1808.08961]. (Cited on page 149.)

[363] The Fermi-LAT Collaboration, *The Fourth Catalog of Active Galactic Nuclei Detected by the Fermi Large Area Telescope*, arXiv:1905.10771. (Cited on pages 151, 152, and 154.)

[364] M. Ajello et al., *The cosmic evolution of fermi bl lacertae objects*, *Astrophys.J.* **780** (2014) 73 [1310.0006]. (Cited on page 152.)

[365] Fermi-LAT collaboration, *The spectrum of isotropic diffuse gamma-ray emission between 100 mev and 820 gev*, *Astrophys.J.* **799** (2015) 86 [1410.3696]. (Cited on page 153.)

[366] K. M. Górski, E. Hivon, A. J. Banday, B. D. Wand elt, F. K. Hansen, M. Reinecke et al., *HEALPix: A Framework for High-Resolution Discretization and Fast Analysis of Data Distributed on the Sphere*, *Astrophysical Journal* **622** (2005) 759 [astro-ph/0409513]. (Cited on page 153.)

[367] Fermi-LAT collaboration, *Development of the Model of Galactic Interstellar Emission for Standard Point-Source Analysis of Fermi Large Area Telescope Data*, *Astrophys. J. Suppl.* **223** (2016) 26 [1602.07246]. (Cited on pages 153 and 154.)

[368] Fermi-LAT collaboration, *3FHL: The Third Catalog of Hard Fermi-LAT Sources*, *Astrophys. J. Suppl.* **232** (2017) 18 [1702.00664]. (Cited on page 154.)